

Chapter 1 Introduction

Models that treat three-dimensional (3-D) radiative transfer processes are needed for the detailed computation of the spatial and angular distributions of the radiative energy in an atmosphere-ocean-land system with clouds and in forest and city canopies. Such a radiation model is especially important for realistic simulations of the 3-D distribution of radiative heating in cloud fields simulated by cloud-resolving dynamical models. In addition, for the purpose of wide-area observation of the atmosphere and land using satellite remote sensing data, it is important to understand the relationships between satellite-observed signals (radiance) and the properties of clouds, vegetation, and land surfaces. Although simplified treatments have been used conventionally, more detailed, realistic treatments are becoming possible with the aid of improved computational power.

There are several complicated problems related to modern radiative transfer calculation methods in geophysical research, including 3-D radiative transfer in a cloudy atmosphere and plant/city canopy, light scattering by leaves and non-spherical particles, polarization, radiative transfer in a spherical atmosphere, and scattering of a laser beam. Most of these can be modeled by Monte Carlo (MC) methods. In particular, the MC methods for 3-D radiative transfer problems are popular not only in geophysics but also in astrophysics, medical sensing, mechanical engineering, and many other fields (Taniguchi et al., 1994).

The MC method is widely used as a method for numerical integration. Its advantage is that it can be applied very easily to solving complicated problems that are difficult to solve with other deterministic (analytical/numerical) methods. In general, deterministic methods work more efficiently for rather simple problems than the MC method, but the merit of the MC method increases with increasing problem complexity (e.g., for problems with higher dimensions of integration). The deterministic methods require larger computational resources (computation time and memory) for a complicated problem, while the computational resources needed for the MC method do not strongly depend on the complexity of the problem.

Deterministic solvers for one-dimensional (1-D) radiative transfer were established in the 1980s. Accurate 3-D radiative transfer calculations were very difficult without the MC method, which has a long history of application to radiative transfer. The MC method was used with even smaller computational resources in the 1970s for 3-D radiative transfer calculations in a simple 3-D geometry (McKee and Cox, 1974; Aida, 1977; Oikawa and Saeki, 1977; Davies, 1984). The rapid growth of computational power enabled researchers to deal with the problem using a more complicated atmosphere (Barker and Davies, 1992; Cahalan et al., 1994a; Barker et al., 1998; O'Hirok and Gautier, 1998; Macke et al., 1999; Fu et al., 2000; Barker et al., 2003; Iwabuchi and Tsuboki, 2004). In the 1970s, plant ecologists tried to develop MC models for the radiative transfer in the plant canopy (Oikawa and Saeki, 1977). Subsequently, advances in modeling studies were made by researchers in geophysics and planetary physics (Ross and Marshak, 1988; Antyufeev and Marshak, 1990; North, 1996; Govaerts and Verstraete, 1998). As a result, similar theories and methods have been used in recent MC-based models for the

atmosphere and plant canopy.

The development of deterministic (analytical/numerical) models for 3-D radiative transfer began in the 1990s, and several models are mature enough for actual applications with reasonable computation time (Gastellu-Etchegorry et al., 1996; Evans, 1998; Marshak and Davis, 2005). However, MC models are often more efficient, especially for complicated problems. One of the advantages of the MC model is that the model treats the non-approximate physical processes behind the radiative transfer and can simulate very accurately the physical processes.

The authors have developed MC-based 3-D radiative transfer models that can be used for various applications such as for the radiative energy budget in the atmosphere and plant canopy and in simulations for remote sensing using optical measurements. This technical report describes the basic theory simply and uses algorithms to provide details. In writing this report, we gave special attention to covering various possible algorithms in great detail, to enable readers to write the computation code by themselves. Due to this effort, explanations of the fundamental theories of radiative transfer are not the main focus of the report, since they can be found in many textbooks and in the literature.

In the following, Chapter 2 describes briefly the basic theory and algorithms of the MC model. Chapter 2 also describes the radiative properties of atmospheric components and plant canopies. Chapter 3, the main part of this report, describes the respective algorithms used in the MC models. The fundamental processes of radiative transfer are fully described, including source emissions, scattering and absorption in the atmosphere and plant canopy, reflection from the land surface and ocean, and computation methods for estimating the radiative quantities of interest. Chapter 4 presents methods and techniques for improving computational efficiency. In some cases, the acceleration methods presented here enable significantly faster computation. Chapter 5 introduces three actually-working models for the atmosphere and plant canopy and presents several examples of their applications. Chapter 6 presents conclusions.

Chapter 2 Physical principle of the radiative transfer model

2.1 Theory of radiative transfer method

Here, we summarize the theory of the photon transport simulation based on the MC method. We then introduce the fundamental concept of the MC algorithm and simple code for MC radiative transfer simulation.

2.1.1 Basic radiative transfer equations for MC method

The differential equation for 3-D radiative transfer under the steady state is expressed as the radiation I ($\text{W m}^{-2} \text{sr}^{-1}$) budget of an infinitesimally small arbitrary area:

$$\mathbf{\Omega} \cdot \nabla I(\mathbf{r}, \mathbf{\Omega}) = -\beta_e(\mathbf{r})I(\mathbf{r}, \mathbf{\Omega}) + \frac{\beta_s(\mathbf{r})}{4\pi} \int_{4\pi} I(\mathbf{r}, \mathbf{\Omega}') P(\mathbf{r}, \mathbf{\Omega}', \mathbf{\Omega}) d\Omega' + \beta_a(\mathbf{r}) B_T(\mathbf{r}) \quad (2.1.1)$$

The first term on the right side of (2.1.1) is an attenuation of $I(\mathbf{r}, \mathbf{\Omega})$ in the photon path (unit vector $\mathbf{\Omega}$), and the second term is the incoming radiation toward the direction $\mathbf{\Omega}$ via a scattering from the direction $\mathbf{\Omega}'$ with $I(\mathbf{r}, \mathbf{\Omega}')$. The third term is the contribution of the thermal radiation. β_e and β_s (m^{-1}) are extinction and scattering coefficients for the unit volume, respectively, and P is a scattering phase function, which is defined as the scattering ratio of the radiation with the direction $\mathbf{\Omega}$ to $\mathbf{\Omega}'$.

The radiative transfer equation is also expressed by the integral equation (Marchuk et al., 1980):

$$f(x) = \int_x k(x', x) f(x') dx' + \psi(x) \quad (2.1.2)$$

$x = (\mathbf{r}, \mathbf{\Omega})$ and $k(x', x)$ is a kernel for photon transport, which is a product of the collision (collision kernel) at point x' and the state transition (transition kernel) from point x' to point x , and is expressed as

$$k(x', x) = \frac{\beta_s(\mathbf{r}') P(\mu) \exp[-\tau(\mathbf{r}', \mathbf{r})] \beta_e(\mathbf{r})}{2\pi \beta_e(\mathbf{r}') |\mathbf{r} - \mathbf{r}'|^2} \delta\left(\mathbf{\Omega} - \frac{\mathbf{r} - \mathbf{r}'}{|\mathbf{r} - \mathbf{r}'|}\right) \quad (2.1.3)$$

μ is a cosine between $(\mathbf{r} - \mathbf{r}')/|\mathbf{r} - \mathbf{r}'|$ and the scattering direction $\mathbf{\Omega}$. By substituting $f(x)$ to (2.1.2), the integral equation of the radiative transfer can be formulated as a von Neumann series:

$$f(x) = \sum_{n=0}^{\infty} \int_X k_n(x', x) f(x') dx' \quad (2.1.4)$$

As shown in (2.1.4), the collision density in the focused area is a summation of the contribution of radiation from zero to infinite orders of scattering.

The MC radiative transfer calculation is an integration technique based on the MC method. The radiation is sampled by simulating the physical processes described in (2.1.1) and (2.1.4), such as the emission, collision, and scattering of photons. MC radiative transfer simulation does not directly solve the above sets of equations, but rather traces the trajectories of the “modeled photon” in the simulated space, where the modeled photon is defined as a sampling unit in the MC radiative transfer simulation and is not identical to an actual light photon defined as a quantum unit. The modeled photon corresponds to a group containing a number of photons.

The MC radiative transfer calculation has two different approaches: forward-type and backward-type MC. While the forward type simulates the photon trajectory along the actual light path, the backward type simulates the photon trajectory in reverse, following the actual light path from the local point to the light source. The backward type is superior to the forward type when we would like to accurately determine the radiative quantity in the focused point with costless time. On the other hand, the forward type is useful in simulating many physical quantities over the simulated space in a one-time simulation. Hereafter, we mainly focus on the description for the forward-type MC method. Some of the algorithms and simulation techniques are common to both approaches.

2.1.2 Basic algorithm for MC radiative transfer simulation

In the MC simulation, the spatial distribution of radiative quantities such as irradiance, radiance, and heating rate are sampled by tracing the modeled photon, the position, direction, and weight of which are modified by the physical laws governing the radiative transfer theory (Fig. 2.1.1.). The fundamental flow of the algorithm is depicted in Fig. 2.1.2. The procedure is as follows:

- i) Start the photon tracing at the given light source. Solar radiation or thermal radiation from the earth could be a natural source of light energy. An artificial source, such as a laser, could also be a potential source of light.
- ii) Obtain a random number, simulate the path of photon travel using the random number, and move the photon ahead by the determined path length.
- iii) After the photon travel, if the photon has gone outside the simulation space, stop the photon tracing and return to procedure i). If the photon still exists in the simulation space, return to ii) and continue the photon tracing.

Here, the path for photon travel is determined using the random number ρ :

$$\tau = -\ln \rho \quad (2.1.5)$$

The traveling path of the modeled photon is described in 3.4 in detail. When the modeled

photon collides with the media, it is scattered or absorbed. The partition of the scattering and absorption depends on the optical properties of the media. Although the MC radiative transfer model could perform these processes via various numerical techniques, the scattering direction must be determined following the statistical distribution of the phase function P . The determination of the scattering direction is described in 3.5 in detail.

Radiative quantities such as irradiance, radiance, and heating rate are sampled by tracing the modeled photon. In general, these quantities are calculated by

$$F = \sum_i \Psi_i \Xi(\mathbf{r}_i) \quad \Xi(\mathbf{r}) = \begin{cases} 1 & \mathbf{r} \in \mathbf{A} \\ 0 & \mathbf{r} \notin \mathbf{A} \end{cases} \quad (2.1.6)$$

where \mathbf{A} is the sampling area and $\Psi(\mathbf{r})$ is a contribution function of these quantities. In the actual simulation, these quantities are evaluated using various methods based on (2.1.6).

For example, when we want to know the irradiance at a certain surface in the focused area, we can calculate it by counting the weight of the modeled photons that pass through that surface. Also, when we want to know the radiance, we can calculate it by sampling the contribution of the modeled photon at every scattering event using the local estimation method (LEM). The heating rate can be sampled from the change in the weight of photons after every scattering. A detailed description of the sampling method is provided in the following chapter.

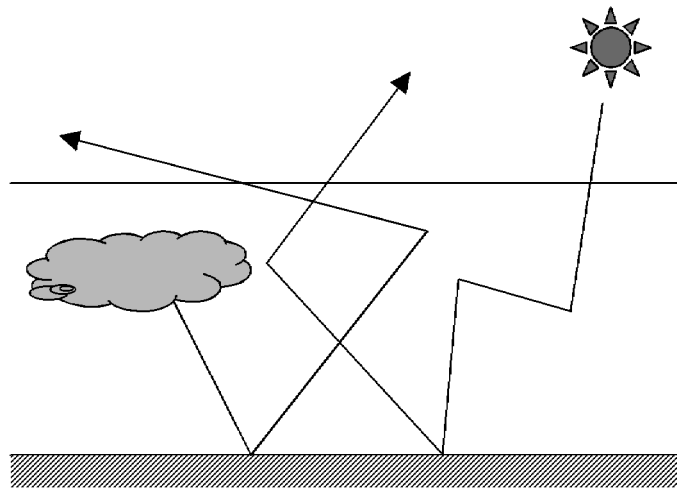


Fig. 2.1.1 Basic concept of photon tracing in the MC method.

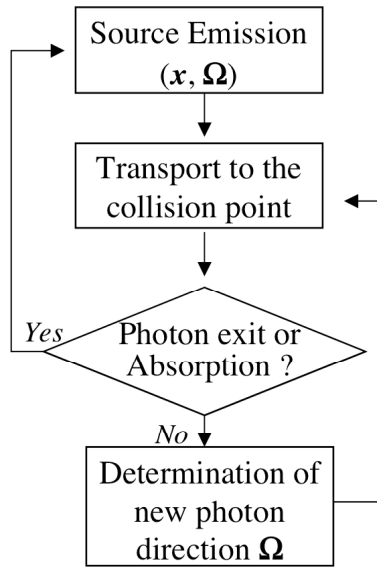


Fig. 2.1.2 Flowchart of the MC radiative transfer algorithm.

2.1.3 Example of a simple MC radiative transfer simulation

We introduce a simple MC simulation as shown in Fig. 2.1.2. Let us consider a 1-D rod-like atmosphere (Fig. 2.1.3), in which a photon can move only along the z-axis. A photon enters from the top of the rod, and photon tracing starts. The entering photon travels the path length determined by (2.1.5) and collides with a medium. Figure 2.1.4 shows an example of the simulation results.

The results (Fig. 2.1.4) are obtained from the atmospheric medium under isotropic scattering (50% forward and 50% backward scattering) and no absorption. As the atmospheric optical thickness gradually increases, the reflectance at the top of the rod-like atmosphere gradually increases and the transmittance at the bottom of the atmosphere decreases. In addition to atmospheric optical thickness, these results (reflectance and transmittance) depend on an atmospheric scattering phase function and absorption.

The simulation code is shown on the next page. This source code of just 40 lines enables us to simulate the conceptual behavior of the atmospheric reflected and transmitted flux under various atmospheric conditions (under various quantities of single scattering albedo, surface reflectance, etc.).

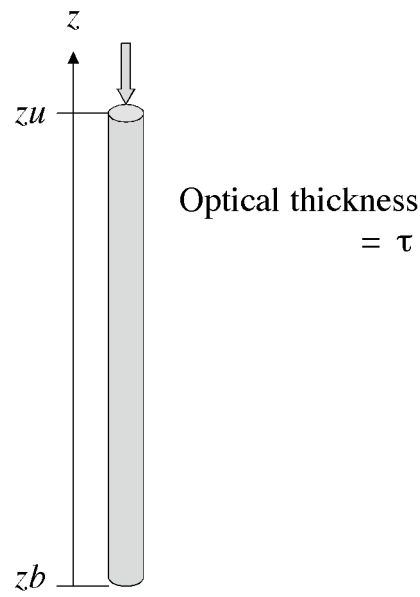


Fig. 2.1.3 Radiative transfer in 1-D rod-like atmosphere.

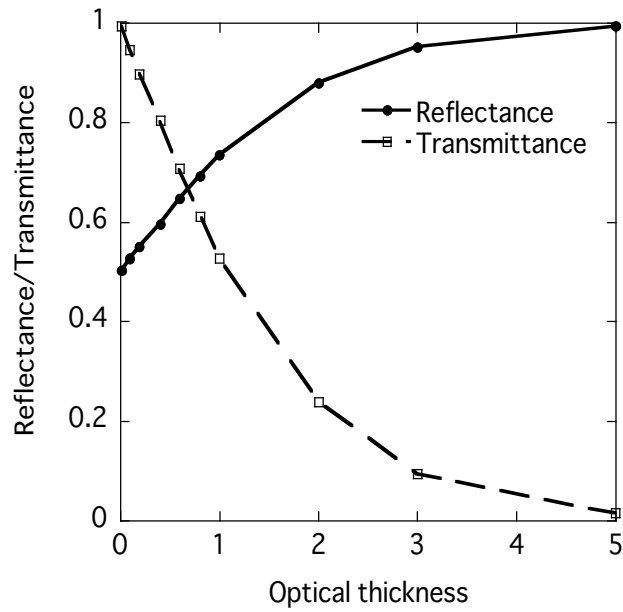


Fig. 2.1.4 Relationship between reflectance/transmittance and optical thickness derived from the MC simulation.

Fortran 77 simulation code

```
c Simple one-dimensional monte carlo simulation
implicit none
integer i,np
real rand,zu,zb,z,tau,sr,path,w,dir,omg,sumr,sumt

np=10000          ! total photon
tau=1.0          ! optical thickness
sr=0.5           ! surface reflectance
omg=1.0          ! single scattering albedo
zu=tau           ! upper boundary
zb=0.0           ! lower boundary
sumr=0.0         ! summation of reflectance
sumt=0.0         ! summation of transmittance

do i=1,np        ! photon loop
  w=1.0          ! initial photon weight
  z=zu           ! photon set in the upper boundary
  dir=-1.0       ! photon direction (+1 upward -1 downward)
  do            ! single photon interaction loop
    path=-log(rand(0)) ! photon free path
    z=zu+dir*path      ! determination of next position z
    if(z.le.zb)then    ! if next position of z is lower than lower boundary
      z=zb             ! z is set to the lower boundary
      dir=1.0          ! upward photon direction
      sumt=sumt+w      ! transmittance sampling
      w=w*sr           ! new photon weight
    elseif(z.gt.zu)then ! if z is larger than upper boundary
      sumr=sumr+w      ! reflectance sampling
      exit             ! exit do loop
    else               ! else case scattering occurs
      if(rand(0).gt.0.5)then ! random number [0,1] is larger than 0.5
        dir=1.0*dir    ! photon direction unchanged (forward scattering)
      else              ! random number [0,1] is less than 0.5
        dir=-1.0*dir   ! photon direction change (backscattering)
      end if
      w=w*omg          ! new photon weight
    end if
  end do
end do

write(*,*) "Reflectance top & Transmittance bottom"
write(*,*) sumr/np,sumt/np
stop
end
```

2.2 Radiative properties in the atmosphere

We describe the optical properties in an atmosphere-surface system. In particular, we emphasize the optical properties of Rayleigh scattering and Mie scattering.

2.2.1 Coordinate system and atmosphere-surface model

In the MC method, various kinds of coordinate systems are potentially available. The typical coordinate systems are

- 1) Cartesian coordinate system, which is conventionally expressed by (x, y, z)
- 2) Spherical coordinate system, which is usually employed when considering the spherical shape of the planetary surface
- 3) Coordinate system fitted in a topographical shape, which uses a rectangular grid in the (x, y) direction. The gridding of the vertical direction (z) depends on the (x, y) grid system and is determined along the shape of the surface topography.

A constant optical property is assumed as a single voxel, but it consists of a mixture of several atmospheric media. The typical compounds are

- 1) Absorbing gases: H_2O , CO_2 , O_3 , CH_4 , O_2 , other uniformly mixed gases
- 2) Scattering gases (Rayleigh scattering): O_2 , N_2 , CO_2
- 3) Aerosols: water-soluble species, dust, soot, organic carbon, etc.
- 4) Cloud particles: cloud water, cloud ice

In each grid, extinction, single scattering albedo, and phase function are given based on these compounds. In addition, since aerosol and cloud particles have a particle size distribution, it is possible to divide these particles into “bins” for each size distribution. In this case, each bin is dealt with as one compound of the media. However, this method requires massive amounts of computational memory and, in most cases, the single parameter of the so-called “effective particle” works well as a representative of the particle size distribution. Therefore, detailed particle size information is not usually necessary.

The surface properties are provided as a surface elevation and normal vector at each (x, y) point of the grid. The surface reflectance is modeled as a Lambertian or bidirectional reflectance distribution function (BRDF). Physical descriptions of these models are given in 3.6.

2.2.2 Gaseous absorption

The spectra of gas absorptions have strong and spike-like peaks, which are determined by the energy level transitions of the gases. The frequent oscillation of these spike-like peaks spreads over a certain waveband, forming the spectral distribution of the absorption coefficient as an aggregation of such spike-like peaks. The absorption peaks are collected in the HITRAN

database and are available to the public. In the actual atmosphere, since the width of an absorption peak varies with the atmospheric temperature and pressure, the absorption coefficients are computed as a function of the temperature and pressure.

In the radiative transfer simulation, a line-by-line calculation within a specific waveband is ideally necessary; however, wavelength band models such as the correlated k -distribution (CKD) method are usually used due to the computational limitation (Shibata, 1999). So far, several waveband models have been developed for climate/meteorological and remote sensing purposes. MODTRAN (a later version of LOWTRAN, Kneizys et al., 1988) was developed for the latter purpose. The modeling for climate/meteorology is dedicated to achieving the required accuracy with fewer bands (Fu and Liou, 1992; Chou and Lee, 1996; Kato et al., 1999; Nakajima et al., 2000).

The CKD method calculates the radiative quantity in a single waveband by the weighted average of the radiative calculation in multiple terms. For the given k th absorption coefficient $\beta_a(\mathbf{r}, k)$ and weight $w(k)$, $w(k)$ is normalized as

$$\sum_{k=1}^K w(k) = 1 \quad (2.2.1)$$

When $F(k)$ is defined as a radiative quantity of the k th term, the waveband-integrated radiative quantity is calculated as

$$\bar{F} = \sum_{k=1}^K w(k)F(k) \quad (2.2.2)$$

In the MC modeling, there are two approaches to solve the CKD method: the approach to distribute the number of photons proportionally to the weight of each CKD term and the approach to distribute the number of photons with arbitrary rules (e.g., equal distribution) and Eq. (2.2.2).

2.2.3 Rayleigh scattering

a. Scattering cross section

The scattering cross section for Rayleigh scattering by atmospheric molecules is expressed as (Thomas and Stamnes, 1999)

$$\sigma = \frac{24\pi^3(n_s^2 - 1)^2}{\lambda^4 N_s^2(n_s^2 + 2)^2} F(\text{air}) \quad (2.2.3)$$

where λ is a wavelength (cm). σ is nearly proportional to λ^{-4} . N_s , which is a number representing molecular density (molecules cm^{-3}) in the standard atmosphere (288.15 K, 1013.25 hPa), is derived from Avogadro's number A ($= 6.0221367 \times 10^{23} \text{ mol}^{-1}$) and molar volume.

$$N_s = \frac{6.0221367 \times 10^{23}}{22.4141 \times 1000} \times \frac{273.15}{288.15} \quad (2.2.4)$$

$$= 2.546899 \times 10^{19}$$

n_s is a refractive index (see 3.7). F is called a depolarization term or King factor:

$$F(\text{air}) = \frac{6 + 3\rho}{6 - 7\rho} \quad (2.2.5)$$

The parameter ρ is a depolarization factor, which is an anisotropy indicator of the molecular structure. The King factor is the most uncertain parameter and the following values have been proposed:

$$\text{Penndorf (1957): } F(\text{air}) = 1.0608 \quad (2.2.6a)$$

$$\text{Young (1981): } F(\text{air}) = 1.048 \quad (2.2.6b)$$

Of the two, the value given by Young (1981) has been the most widely used. However, in theory, F is related to the wavelength λ . According to Bodhaine et al. (1999), the weighted average of the depolarization of the molecules proposed by Bates (1984) has the best accuracy. Bates (1984) proposed the following equations:

$$F(\text{N}_2) = 1.034 + 3.17 \times 10^{-4} \frac{1}{\lambda^4} \quad (2.2.7a)$$

$$F(\text{O}_2) = 1.096 + 1.385 \times 10^{-3} \frac{1}{\lambda^2} + 1.448 \times 10^{-4} \frac{1}{\lambda^4} \quad (2.2.7b)$$

$$F(\text{Ar}) = 1.0 \quad (2.2.7c)$$

$$F(\text{CO}_2) = 1.15 \quad (2.2.7d)$$

Bodhaine et al. (1999) recommended using the following equation based on the equations given by Bates (1984):

$$F(\text{air}, \text{CO}_2) = \frac{78.084F(\text{N}_2) + 20.946F(\text{O}_2) + 0.934 \times 1.0 + C_{\text{CO}_2} \times 1.15}{78.084 + 20.946 + 0.934 + C_{\text{CO}_2}} \quad (2.2.8)$$

C_{CO_2} is the CO_2 concentration (parts per volume, e.g., 360×10^{-6} for 360 ppm).

Finally, σ is determined by substituting it for the King factor derived from (2.2.8) and N_s derived from (2.2.4). The refractive index of the atmosphere is calculated using the equation mentioned in 3.7. These sets of equations are the most accurate procedure for σ determination at present. In these equations, it is possible to calculate σ under a change in the CO_2 concentration.

Bodhaine et al. (1999) also proposed a simpler empirical equation for σ (10^{-32} m^2) under a constant CO_2 concentration (360 ppm, λ (μm)):

$$\sigma = \frac{1.0455996 - 341.29061\lambda^{-2} - 0.90230850\lambda^2}{1 + 0.0027059889\lambda^{-2} - 85.968563\lambda^2} \quad (2.2.9)$$

The error for this equation is less than 0.01% in 0.25–0.85 μm and 0.05% in 0.85–1.0 μm ,

which is still accurate compared with what has so far been proposed.

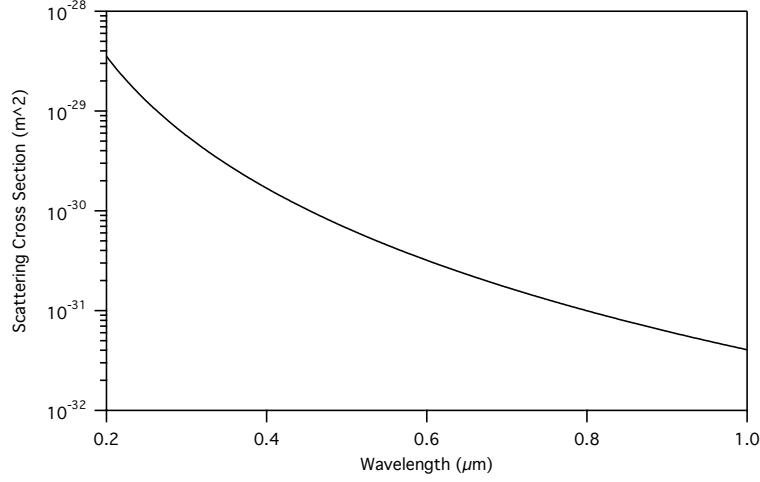


Fig. 2.2.1 Scattering cross section of Rayleigh scattering.

b. Scattering coefficient and optical thickness

Under hydrostatic equilibrium, it is easy to calculate the vertically integrated optical thickness when the scattering coefficient is given. The optical thickness is a function of atmospheric pressure:

$$\tau(\lambda) = \sigma \frac{PA}{M_{\text{dry}}g} \quad (2.2.10)$$

P , M_{dry} , and g are pressure, average molecular weight, and gravitational acceleration, respectively. According to Bodhaine et al. (1999), when we assume C_{CO_2} to be 360 ppm,

$$\begin{aligned} M_{\text{dry}}(0 \text{ ppm CO}_2) &= 28.95949 \text{ gm mol}^{-1} \\ M_{\text{dry}}(360 \text{ ppm CO}_2) &= 28.96491 \text{ gm mol}^{-1} \\ M_{\text{dry}} &\cong 28.9595 + 15.0556(\text{CO}_2) \end{aligned}$$

g is a function of the latitude ϕ and elevation z (m). In Bodhaine et al. (1999), g (cm s^{-1}) was calculated by following the method given by List (1968):

$$\begin{aligned} g &= g_0 - (3.085462 \times 10^{-4} + 2.27 \times 10^{-7} \cos 2\phi)z \\ &\quad + (7.254 \times 10^{-11} + 1.0 \times 10^{-13} \cos 2\phi)z^2 \\ &\quad - (1.517 \times 10^{-17} + 6.0 \times 10^{-20} \cos 2\phi)z^3 \end{aligned} \quad (2.2.11)$$

g_0 is the gravitational acceleration at $z = 0$ m.

$$g_0 = 980.616(1 - 0.0026373 \cos 2\phi) + 0.0000059 \cos^2 2\phi \quad (2.2.12)$$

According to Bodhaine et al. (1999), z_c (m), which provides the height for effective g in (2.2.10), is a useful parameter and computed by

$$z_c = 0.73737z + 5517.56 \quad (2.2.13)$$

Once the optical thickness is derived from (2.2.10), the scattering coefficient can be calculated as

$$\beta_s(\lambda, z) = \frac{d\tau(\lambda)}{dz} = -\sigma \frac{A}{M_{\text{dry}} g} \frac{dP}{dz} \quad (2.2.14)$$

When the atmosphere is far from the hydrostatic equilibrium condition, the scattering coefficient can be computed under the given vertical profiles of the temperature and pressure. The scattering coefficient is then a function of the molecular density N :

$$\beta_s(\lambda, z) = \sigma N \quad (2.2.15)$$

N is calculated as

$$N = \frac{A}{R^*} \cdot \frac{P}{T} \quad (2.2.16)$$

where R^* ($= 8.3143 \text{ J K}^{-1} \text{ mol}^{-1}$) is the universal gas constant. When N_b and N_t are the density values at heights z_b and z_t , respectively, $N(z)$ is formulated under the assumption of an exponential vertical profile:

$$N(z) = N_b \exp\left[-\frac{z - z_b}{z_t - z_b} (\ln N_b - \ln N_t)\right] \quad (2.2.17)$$

Hence, the optical thickness between z_b and z_t is calculated as

$$\begin{aligned} \tau(z_b, z_t) &= \int_{z_b}^{z_t} \sigma N(z) dz \\ &= \sigma N_b \int_{z_b}^{z_t} \exp\left[-\frac{z - z_b}{z_t - z_b} (\ln N_b - \ln N_t)\right] dz \\ &= \sigma \frac{N_b}{N_t} \frac{N_b - N_t}{\ln N_b - \ln N_t} (z_t - z_b) \end{aligned} \quad (2.2.18)$$

2.2.4 Mie scattering: Aerosol and cloud particles

The aerosol and cloud particles are usually approximated as having a spherical shape with a size of 0.005–100 μm . In this case, a scattering event can be mathematically formulated by Mie theory (Mie scattering). The optical properties of Mie scattering are characterized by the wavelength λ , particle radius r , and complex refractive index \mathbf{n} . The complex refractive indices

of water, ice, ammonium sulfate, soot, soil particles, etc., were investigated based on laboratory measurements and observations (Hale and Querry, 1973; Palmer and Williams, 1974; Downing and Williams, 1975; Shettle and Fenn, 1979; d’Almeida et al., 1991). The refractive index of particles such as water weakly depend on the temperature. A method to calculate the single sphere extinction coefficient, scattering cross section, and scattering phase function was provided by Bohren and Huffman (1983) or elsewhere. Nowadays, we can use state-of-the-art simulation code that can calculate not only spherical particles but also non-spherical particle cases.

Various sizes of aerosol and cloud particles are generally mixed together in the atmosphere. Let the number density be N ($\#/m^3$) and particle size distribution be $n(r)$ ($m^{-3} \mu m^{-1}$).

$$n(r) = \frac{dN}{dr} \tag{2.2.19a}$$

$$N = \int_0^{\infty} n(r) dr \tag{2.2.19b}$$

The particle size distribution can be approximated by an analytical function (Appendix A1), or a simulated distribution by the bin method and the observed distribution are also used.

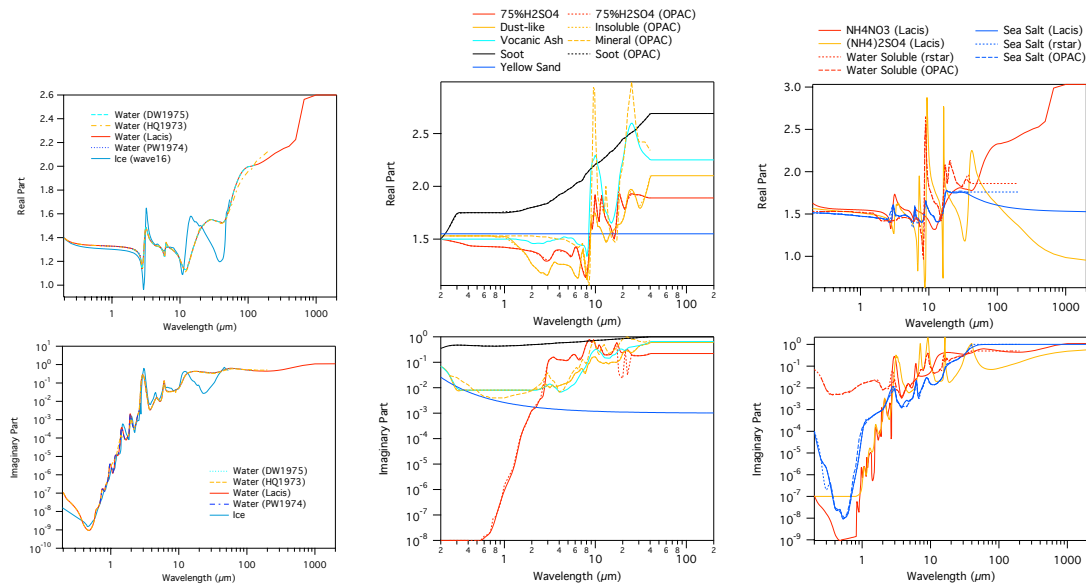


Fig. 2.2.2 Reflective indices of various materials.

2.2.5 Moment of particle size distribution and volume mixing ratio

The geometric average radius, and cross-section-mean and volume-mean radii are defined by

$$r_{geo} = \frac{1}{N} \int r n(r) dr \quad (2.2.20a)$$

$$r_{sec} = \left(\frac{1}{N} \int r^2 n(r) dr \right)^{1/2} \quad (2.2.20b)$$

$$r_{vol} = \left(\frac{1}{N} \int r^3 n(r) dr \right)^{1/3} \quad (2.2.20c)$$

The most important parameters for particle size distribution are the effective radius r_{eff} and the effective dispersion v_{eff} (Hansen and Travis, 1974):

$$r_{eff} = \frac{\int r \cdot \pi r^2 n(r) dr}{\int \pi r^2 n(r) dr} = \frac{r_{vol}^3}{r_{sec}^2} \quad (2.2.21)$$

$$v_{eff} = \frac{\int (r - r_{eff})^2 \cdot \pi r^2 n(r) dr}{r_{eff}^2 \int \pi r^2 n(r) dr} = \frac{1}{r_{eff}^3 r_{vol}^3} \frac{\int r^4 n(r) dr}{N} - 1 \quad (2.2.22)$$

These parameters are the weighted average and dispersion of the particle size distribution. The relationships between the effective radius, cross-section-mean radius, and volume-mean radius can be expressed by

$$\kappa = \left(\frac{r_{sec}}{r_{eff}} \right)^2 = \left(\frac{r_{vol}}{r_{eff}} \right)^3 \quad (2.2.23)$$

Here, κ is a coefficient related to the width of the particle size distribution. According to the field observation of the particle size distribution by Martin et al. (1994), κ in maritime boundary layer clouds is 0.8 and in continental ones is 0.67.

The atmospheric particle volume in a unit volume V (volume mixing ratio in m^3/m^3) and the mass density M (kg m^{-3}) are expressed by

$$V = \int \frac{4}{3} \pi r^3 n(r) dr = \frac{4\pi}{3} r_{vol}^3 N \quad (2.2.24a)$$

$$M = \rho V \quad (2.2.24b)$$

ρ is a density (kg m^{-3}). If V or M and N are given as a priori knowledge, the effective radius can be derived from (2.2.23a) and (2.2.24a,b):

$$r_{eff} = \left[\frac{3}{4\pi\kappa N} V \right]^{1/3} = \left[\frac{3}{4\pi\kappa N} \frac{M}{\rho} \right]^{1/3} \quad (2.2.25)$$

Thus, the parameter κ is related to V or M and N . From (2.2.20) and (2.2.24), the geometric cross section ($\text{m}^2 \text{m}^{-3}$) of particles contained in the unit atmospheric volume is calculated by

$$\int \pi r^2 n(r) dr = N \pi r_{sec}^2 = \frac{3}{4} \frac{V}{r_{eff}} = \frac{3}{4} \frac{M}{r_{eff} \rho} \quad (2.2.26)$$

The particle size distribution is usually approximated by an analytical function. Clouds and aerosols can be widely approximated by the power-law, gamma, and lognormal distributions (Hess et al., 1998). The characteristics of the typical distribution function and its relationship to M , V , and N are summarized in Appendix A1.

2.2.6 Weighted average optical properties by particle size distribution

The extinction coefficient, scattering coefficient, and scattering phase function, which are averaged with the weighting of the particle size distribution, are

$$\beta_e = \int \tilde{Q}_e(r) \pi r^2 n(r) dr \quad (2.2.27a)$$

$$\beta_s = \int \tilde{Q}_s(r) \pi r^2 n(r) dr \quad (2.2.27b)$$

$$P(\Theta) = \frac{\int \tilde{P}(\Theta, r) \tilde{Q}_s(r) \pi r^2 n(r) dr}{\int \tilde{Q}_s(r) \pi r^2 n(r) dr} \quad (2.2.27c)$$

The extinction/scattering efficiency factor, which is defined by the extinction cross section in a unit cross section, and phase function can be calculated by Mie theory. When the average extinction/scattering efficiency factor weighted by the particle size distribution is formulated by

$$Q_e = \frac{\int \tilde{Q}_e(r) \pi r^2 n(r) dr}{\int \pi r^2 n(r) dr}, \quad Q_s = \frac{\int \tilde{Q}_s(r) \pi r^2 n(r) dr}{\int \pi r^2 n(r) dr} \quad (2.2.28)$$

the average extinction cross section, scattering cross section, and single scattering albedo of the single particle are calculated from (2.2.23b):

$$\sigma_e = Q_e \pi r_{sec}^2 = Q_e \pi \frac{r_{vol}^3}{r_{eff}} \quad (2.2.29a)$$

$$\sigma_s = Q_s \pi r_{sec}^2 = Q_s \pi \frac{r_{vol}^3}{r_{eff}} \quad (2.2.29b)$$

$$\omega = \frac{\sigma_s}{\sigma_e} = \frac{Q_s}{Q_e} \quad (2.2.29c)$$

In summary, when the particle size distribution is given in a scattering particle medium, the required parameters for the optical parameter to be determined are

$(Q_e, Q_s, P(\Theta))$ and (N, r_{sec})

Note that this can be rewritten in a different form expressed by M and V when using (2.2.23–24).

As shown in the above description, the average optical properties weighted by the particle size distribution are usually required to integrate using the weight of the particle size distribution and geometric cross section (see (2.2.27–28)). That is,

$$Y = \int_0^\infty \tilde{Y}(r) \pi r^2 n(r) dr \cong \int_{r_{\min}}^{r_{\max}} \tilde{Y}(r) \pi r^2 n(r) dr \quad (2.2.30)$$

Here, $Y(r)$ does not strongly depend on r and irregularly varies (e.g., scattering efficiency factor). $n(r)$ is generally distorted toward the positive direction. Therefore, the transformation given below is useful:

$$\frac{dN}{d \ln r} = r \frac{dN}{dr} = rn(r) \quad (2.2.31)$$

$$Y = \int_{-\infty}^{\infty} \tilde{Y}(r) \pi r^3 n(r) d \ln r \cong \int_{\ln r_{\min}}^{\ln r_{\max}} \tilde{Y}(r) \pi r^3 n(r) d \ln r \quad (2.2.32)$$

Here, it should be emphasized that it is not recommended to refer to $n(r)$ when determining the integral domain. The maximum r_{\max} and minimum r_{\min} of the integral domain should be determined by minimizing $r^3 n(r)$.

Generally, it is necessary to consider a mixture of several aerosols and cloud water/cloud ice for an atmospheric medium. The optical properties of the mixing media are described in Appendix A2. In the radiative transfer simulation, waveband average parameters are usually employed. Appendix A3 summarizes the method to derive the waveband average parameters. Furthermore, an example of the determination of the aerosol vertical profile is described in Appendix A4.

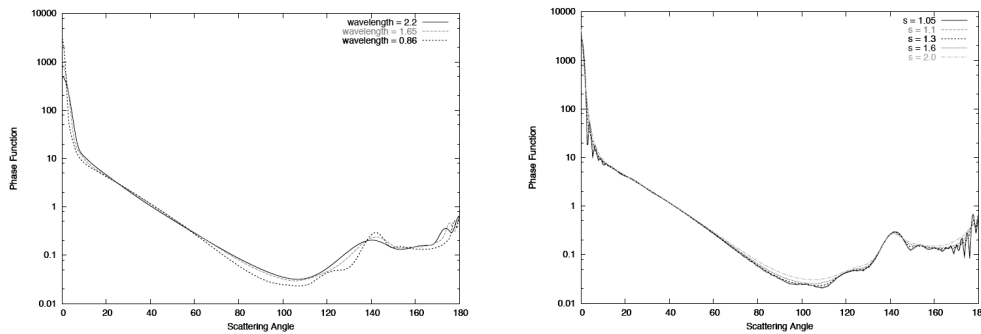


Fig. 2.2.3 Cloud water phase function (left) under the assumption of a lognormal distribution for the particle volume. Phase function (right) for various widths of the lognormal distribution for the particle volume. $10 \mu\text{m}$ is assumed for the effective radius.

2.2.7 Hygroscopic growth of aerosol

There are two types of aerosols: hygroscopic aerosols (e.g., $(\text{NH}_4)_2\text{SO}_4$, NH_4NO_3 , NaCl) and non-hygroscopic aerosols (e.g., soil, desert dust, black carbon). The size of an hygroscopic aerosol increases when absorbing atmospheric water vapor. Then, the density and refractive index approach the parameters for water. Hygroscopic growth with an increase in relative humidity does not begin until the relative humidity reaches a critical point (RHD). When the relative humidity rises above the RHD, hygroscopic growth begins and follows a curve determined by the relative humidity. On the other hand, when the aerosols release their contained water with a decrease in the relative humidity, all of the water is released at a critical point (RHC). Generally, the RHC is less than the RHD. Due to such hysteresis of the hygroscopic aerosol, the increase ratio and mixing ratio cannot be determined simply by the relative humidity: they depend on the pathway of the aerosol particles. In the actual atmosphere, most particles lay above the hysteresis curve of the relative humidity (Hess et al., 1998).

The growth factor (radius increase ratio) B and mixing ratio are defined by

$$B = \frac{r}{r_0} \quad (2.2.33a)$$

$$x = \frac{m_0}{m} \quad (2.2.33b)$$

where m is the mass of particles and the subscript 0 indicates the dissolved substance under a dry condition. Here, the relationship between B and ρ is

$$B^3 = \frac{m}{m_0} \frac{\rho_0}{\rho} = \frac{\rho_0}{\rho x} \quad (2.2.34)$$

The maximum B is approximately 4 at a relative humidity = 0.99. Strictly speaking, the relative humidity η (between 0 and 1) of the equilibrium state increases slightly due to the Kelvin effect (surface tension). However, since this phenomenon is negligibly small, the relative humidity approximately becomes equal to water activity:

$$\eta \cong a_w \quad (2.2.35)$$

Tang and Munkelwitz (1994, 1996) derived empirical formulae for the various materials:

$$a_w = 1.0 + \sum_i C_i x^i \quad (2.2.36a)$$

$$\rho = 0.9971 + \sum_i A_i x^i \quad (2.2.36b)$$

These equations are applicable to the density ρ calculation by using (2.2.36b) and the mixing ratio calculated by (2.2.36a) when the relative humidity $\eta = a_w$ and $\eta > \text{RHC}$.

B is also calculated using (2.2.34). When the material is the same, B is determined only by η and the increase ratio of the particle size depends only on B ($r = r_0 B$). The aerosol size distribution under hygroscopic growth is expressed by

$$n(r) = \frac{dN}{dr} = \frac{dN}{Bdr_0} = \frac{1}{B}n_0(r_0), \quad r_0 = \frac{r}{B} \quad (2.2.37a)$$

$$\therefore \frac{dN}{d \ln r} = \frac{dN}{d \ln r_0} \quad (2.2.37b)$$

For example, when the number density of the particle size distribution under the dry condition is a lognormal distribution (Appendix A1), the dissolved case of size distribution becomes lognormal and the mode radius is proportional to B . The standard deviation σ is unchanged.

In the case of the refractive index, the molar ratio is expressed using the mixing ratio x :

$$f_s = \frac{xM_w}{(1-x)M_s + xM_w} \quad (2.2.38)$$

where M_w and M_s are the molar weights of the water and dissolved substrate, respectively.

Letting the molar refractions of water and the dissolved substrate be R_w and R_s , respectively, the real part of the refractive index n_r is obtained from

$$\frac{n_r^2 - 1}{n_r^2 + 2} = \rho \frac{(1-f_s)R_w + f_sR_s}{(1-f_s)M_w + f_sM_s} \quad (2.2.39)$$

The molar refractions are calculated from the following relationships:

$$R_w = \frac{M_w}{\rho_w} \frac{n_w^2 - 1}{n_w^2 + 2}, \quad R_s = \frac{M_s}{\rho_s} \frac{n_s^2 - 1}{n_s^2 + 2} \quad (2.2.40)$$

Tang and Munkelwitz (1994, 1996) calculated an accurate value for n_r at $\lambda = 0.633 \mu\text{m}$. By using it, the ratio to interpolate the refractive index is calculated at $\lambda = 0.633 \mu\text{m}$:

$$\alpha = \frac{n_r - n_w}{n_s - n_w} \quad (2.2.41)$$

At this wavelength, $n_w = 1.333$. When this value is applied to the real and imaginary parts of the all wavelengths, the refractive index is interpolated as

$$\mathbf{n} = (1 - \alpha)\mathbf{n}_w + \alpha\mathbf{n}_s \quad (2.2.42)$$

where \mathbf{n}_s and \mathbf{n}_w are complex refractive indices for a dissolved substrate and water, respectively. There are other ways to interpolate the refractive index, using the weighted average of the mass ($\alpha = x$) and weighted average of the volume ($\alpha = 1/B^3$); however, the method just described (2.2.39) is more reasonable. The parameters for typical materials are summarized in Table 2.2.2.

Because Mie scattering of the hygroscopic aerosol depends not only on the radius but also on the refractive index, it is necessary to prepare a 2-D LUT (radius and α). When the particle size distribution and relative humidity are given, x , ρ , and α can be calculated from the relative humidity. Then, the scattering properties of a hygroscopic aerosol are obtained from the

weighted average of the particle size distribution for the interpolated scattering properties from the LUT. The LUT can be prepared for a dry particle radius and relative humidity. However, it is difficult to change the relationship between the relative humidity and radius of the dissolved particles.

Table 2.2.1 Parameters of various hygroscopic materials.

	(NH ₄) ₂ SO ₄	NH ₄ NO ₃	NaCl	H ₂ SO ₄
RHD	0.8	0.62	0.753	NA
RHC	0.4–0.37	0.25–0.32	0.48–0.46	NA
C ₁	-2.715E-1	-3.65E-1	-6.366E-1	-5.196E-1
C ₂	3.113E-1	-9.155E-2	8.624E-1	9.746E-1
C ₃	-2.336E0	-2.826E-1	-1.158E+1	-9.693E0
C ₄	1.412E0	0	1.518E+1	9.405E0
A ₁	5.92E-1	4.05E-1	7.41E-1	7.367E-1
A ₂	-5.036E-2	9.0E-2	-3.741E-1	-4.934E-1
A ₃	1.024E-2	0	2.252E0	1.754E0
A ₄	0	0	-2.06E0	-1.104E0
Dry Density, ρ ₀	1.76	1.725	2.165	1.834
Refractive Index, n _s	1.526	1.554	1.544	1.429
M _s	132.154	80.052	58.44	98.086

$$aEb = a \times 10^b$$

2.3 Radiative properties in plant canopies

We now discuss the photon interaction within a plant canopy. The definitions for the vegetation parameters and the method of forest scene generation are also described.

2.3.1 Optical properties of a leaf

Photons interact with the leaves, stems, and branches within a plant canopy. Because most studies have been dedicated to understanding the influence of environmental conditions on the spectral features of a leaf, we primarily focus on the optical properties of a leaf. Since modeling studies for the optical properties of stems and branches have already been conducted, the observed data from such studies are generally used for radiative transfer simulation. The primary difference between a leaf and stem/branch is the existence of chlorophyll-a and chlorophyll-b.

a. Photon reflection, transmission, and absorption in a leaf

The reflectance and transmittance of a single leaf are determined by the leaf's structure and biochemical composition. Figure 2.3.1 shows an example of simulated single leaf reflectance and transmittance between 400 and 2500 nm. Every leaf has similar spectral reflectance/transmittance patterns.

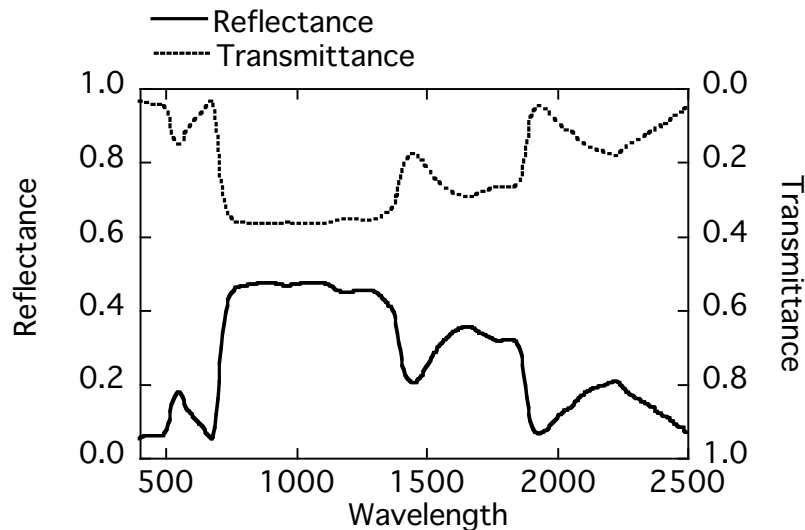


Fig. 2.3.1 Typical single leaf reflectance and transmittance. These are calculated using the LIBERTY model (Dawson et al., 1998) for the biochemical data of a larch needle.

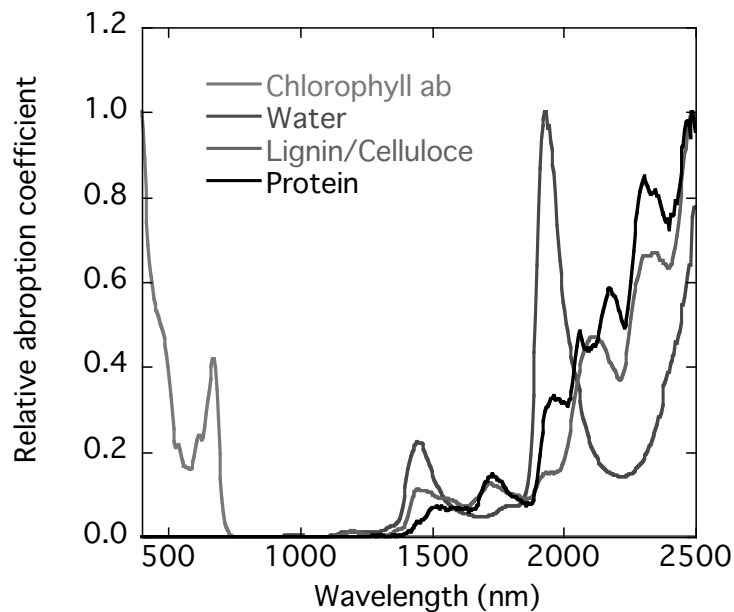


Fig. 2.3.2 Relative absorption coefficient for the pigment in a leaf.

In the visible spectral region, due to the strong absorption of chlorophyll-a and chlorophyll-b and carotenoids, the reflectance and transmittance are low. Chlorophyll-a and chlorophyll-b have strong peaks around 400 nm and 670 nm (Fig. 2.3.2), and the carotenoids have a strong peak at 440–450 nm. Consequently, the reflectance has a convex shape, with a reflectance/transmittance peak around 550 nm. This is the reason why leaves have a dark green color. A fresh leaf has a rather light green color because of lower amounts of chlorophyll-a and chlorophyll-b. In the autumn, the leaf's color becomes red or yellow due to the lack of the pigment required for photosynthesis.

In the near-infrared region (700–1400 nm), there is almost no absorption by the pigment. Therefore the incoming photons are scattered many times within the cell wall before exiting. The intensities of the reflected and transmitted radiation are determined by the leaf structure such as the thickness of the cell and the cell size.

In the shortwave infrared region (1400–2500 nm), there are two strong water absorption bands at 1450 nm and 1900 nm, causing a reduction in the reflectance and transmittance of the leaf. Also, other pigments such as protein, cellulose, and water have a continuous weak absorption, causing a gradual decrease in reflectance and transmittance with longer wavelengths (Fig. 2.3.2).

b. Chlorophyll fluorescence

In the visible spectral region, there is a photon emission process called chlorophyll fluorescence. Chlorophyll fluorescence is a phenomenon that occurs in photosynthesis II. In the photosynthesis cycle, the photon energy absorbed by the plant is converted to organic energy.

However, not all of the photon energy absorbed by the chlorophyll in the leaf is converted. The extra energy that is not converted is dissipated as thermal heat or reemitted. This reemittance process is chlorophyll fluorescence. In chlorophyll fluorescence, chlorophyll molecules in an excited condition emit photons. The peak wavelength of chlorophyll fluorescence is around 680 nm (red). The energy of chlorophyll fluorescence is 0.5–3% of the absorbed energy (Hikosaka, 2003), making it negligibly small in radiative transfer modeling.

c. Xanthophyll cycle and spectral change

The xanthophyll cycle is an energy dissipation process for thermal energy that occurs when the absorbed photosynthetically active radiation is larger than the leaf's photosynthesis ability. In the biochemical reaction processes of the xanthophylls, the absorption peak of the carotenoid moves from 443 nm to 451 nm (Yoshimura, 2001). The reflectance changes caused by this process are generally small at the canopy scale. It may be possible to detect this change with laboratory measurements. However, at the canopy scale, this has a very small effect on canopy reflectance and transmittance because the canopy contains leaves in various conditions (sunlit leaves, shaded leaves with various leaf angles) and the amount of absorbed energy is different for each leaf.

d. Modeling of leaf surface reflectance and transmittance

As described above, a leaf's reflectance and transmittance are determined by the pigment concentration and leaf structure. Several models have been proposed to simulate leaf-level reflectance and transmittance. Jacquemoud and Baret (1990) proposed PROSPECT, a leaf reflectance and transmittance model for broadleaf. Dawson et al. (1998) proposed the LIBERTY model, a reflectance and transmittance model for needle leaves. These models have different assumptions for leaf structures. PROSPECT assumes that the leaf has a layered plate structure, and the LIBERTY model views the leaf as a series of floating spheres regularly positioned in the leaf. Both models simulate the hemispherical reflectance and transmittance of a leaf. Here, the model structure used in PROSPECT is described as an example.

PROSPECT

The PROSPECT model assumes that the leaf is a series of layered plates. This model is an extension of the plate model by Allen et al. (1969). When the maximum incident angle is θ_m , the hemispherical reflectance (R_{N,θ_m}) and transmittance (T_{N,θ_m}) of the N th plate are calculated by

$$R_{N,\theta_m} = xR_{N,90} + y \quad (2.3.1)$$

$$T_{N,\theta_m} = xT_{N,90} \quad (2.3.2)$$

where x and y are given in the following equations:

$$x = \frac{t(\theta_m, n)}{t(90, n)} \quad (2.3.3)$$

$$y = x(t(90,n) - 1) + 1 - t(\theta_m, n) \quad (2.3.4)$$

$t(\theta_m, n)$ is the average transmittance over the incident angle from 0 to θ_m in the boundary layer with the refractive index (n). This is analytically calculated by Fresnel's law and Stern's theory (Stern, 1964). $R_{N,90}$ and $T_{N,90}$ are calculated using the following equations:

$$\frac{R_{N,90}}{b_{90}^N - b_{90}^{-N}} = \frac{T_{N,90}}{a_{90}^N - a_{90}^{-N}} = \frac{1}{a_{90}b_{90}^N - a_{90}^{-1}b_{90}^{-N}} \quad (2.3.5)$$

$$a_{90} = \frac{(1 + \rho_{90}^2 - \tau_{90}^2 + \delta_{90})}{2\rho_{90}} \quad (2.3.6)$$

$$b_{90} = \frac{(1 - \rho_{90}^2 + \tau_{90}^2 + \delta_{90})}{2\tau_{90}} \quad (2.3.7)$$

$$\delta_{90} = \sqrt{(\tau_{90}^2 - \rho_{90}^2 - 1)^2 - 4\rho_{90}^2} \quad (2.3.8)$$

$$\rho_{90} = 1 - t(90, n) + \frac{t(90, n)^2 k^2 (n^2 - t(90, n))}{n^4 - k^2 (n^2 - t(90, n))^2} \quad (2.3.9)$$

$$\tau_{90} = \frac{t(90, n)^2 k n^2}{n^4 - k^2 (n^2 - t(90, n))^2} \quad (2.3.10)$$

k is a parameter related to the pigment absorption and can be converted to K by the following equation:

$$k - (1 - K)e^{-K} - K^2 \int_K^\infty x^{-1} e^{-x} dx = 0 \quad (2.3.11)$$

The leaf absorption coefficient is derived as a weighted average of the content (C) and absorption coefficient (K) of each pigment:

$$K = \sum K_i C_i \quad (2.3.12)$$

The refractive index of the leaf is diverse. However, the values between 1.3 and 1.5 are widely used (Gausman et al., 1974). In the PROSPECT model, the leaf reflectance and transmittance are calculated from the maximum incident angle of the photon (θ_m), refractive index (n), absorption coefficient (K), and leaf thickness (N).

2.3.2 Radiative transfer modeling of leaf canopy

a. Leaf area index and leaf area density

The leaf area density $u(\mathbf{r})$ is defined as half of the total leaf area in the unit volume ($\text{m}^2/\text{m}^3 = \text{m}^{-1}$) at the position \mathbf{r} . The leaf area index (l) is half of the total leaf area in the unit ground area and can be obtained by integrating the leaf area density $u(\mathbf{r})$ from the ground to the top of the canopy height (H):

$$l = \int_0^H u(\mathbf{r}) dz \quad (2.3.13)$$

b. Leaf angle distribution

Generally, plants allocate leaves to gain the maximum photosynthesis. The leaf angle distribution is diverse, varying with the plant species and leaf position in the canopy. It is helpful to use the statistical distribution function. The distribution function $g_L(\mathbf{r}, \mathbf{\Omega}_L)$ is defined as a function of the position \mathbf{r} and the normal vector $\mathbf{\Omega}_L$. $g_L(\mathbf{r}, \mathbf{\Omega}_L)$ is normalized by

$$\frac{1}{2\pi} \int_0^{2\pi} \int_0^{\frac{\pi}{2}} g_L(\mathbf{r}, \mathbf{\Omega}_L) \sin \theta_L d\theta_L d\varphi_L = 1 \quad (2.3.14)$$

In most cases, the leaf angle does not depend on the azimuth angle and (2.3.14) is expressed by

$$\int_0^1 g_L(\mathbf{r}, \theta_L) d\mu_L = 1 \quad (2.3.15)$$

where $\mu_L = \cos \theta_L$. At present, several types of leaf angle distribution functions have been proposed. The simplest function is a uniform leaf distribution:

$$g_L(\mathbf{r}, \theta_L) = 1 \quad (2.3.16)$$

The ellipsoidal distribution is defined by:

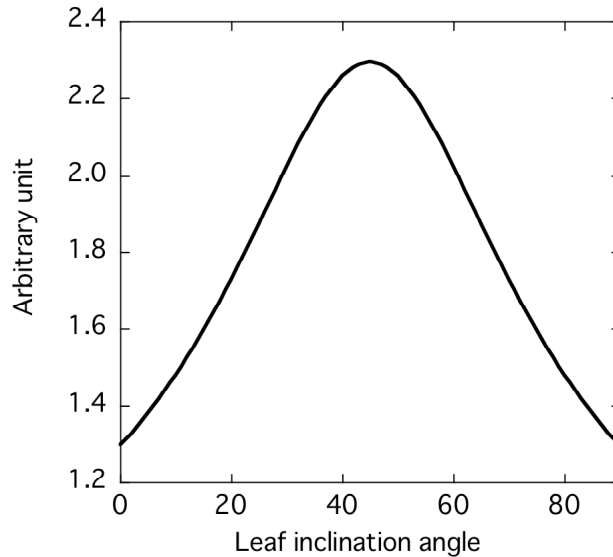


Fig. 2.3.3 Ellipsoidal distribution function ($\theta_m = 45^\circ$, $\varepsilon = 0.9$).

$$g_L(\mathbf{r}, \theta_L) = \frac{B}{\sqrt{1 - \varepsilon^2 \cos^2(\theta_L - \theta_m)}} \quad (2.3.17)$$

where B is a normalization factor. Figure 2.3.3 is an example of the ellipsoidal distribution. This distribution function can be characterized by two parameters (the center of the leaf angle distribution θ_m and eccentricity ε).

c. Extinction coefficient for a leaf canopy

The extinction coefficient for a leaf canopy is described by the projection area in the photon direction Ω . The G -function is expressed by

$$G(\mathbf{r}, \Omega) = \frac{1}{2\pi} \int_0^{2\pi} \int_0^{\pi} g_L(\mathbf{r}, \Omega_L) |\Omega_L \cdot \Omega| \sin \theta_L d\theta_L d\varphi_L \quad (2.3.18)$$

Here, G becomes 1/2 when the leaf angle distribution is uniform. The extinction coefficient in a unit volume β_e is expressed by

$$\beta_e(\mathbf{r}, \Omega) = G(\mathbf{r}, \Omega)u(\mathbf{r}) \quad (2.3.19)$$

The canopy optical thickness can be calculated by integrating (2.3.19) from the ground to the top of the canopy:

$$\tau = \int_0^H \beta_e(\mathbf{r}, \theta = 0) dz \quad (2.3.20)$$

2.3.3 Canopy structure of forest and grassland

a. Modeling of tree structure

There are several ways of modeling a canopy structure for forest light environmental simulation (Fig. 2.3.4). The simplest canopy is a plane-parallel approximation. In this canopy, the leaves, stems, and branches are distributed homogeneously in a layer (Fig. 2.3.4 left). Just as in the case of a plane-parallel atmosphere, it is possible to simulate a multilayer canopy, in which each layer has different optical properties.

A 3-D canopy scene is composed of individual trees, in which all the trees are modeled as geometric objects (Fig. 2.3.4 center). In this case, the leaves and branches are distributed within the canopy objects. Canopies modeled using cones, cylinders, and ellipsoids could be good approximations, and it is possible to make more complicated shapes with combinations of these primitive geometric objects.

In a plane-parallel canopy and 3-D object canopy, the canopy optical and structural conditions can be defined using the leaf area density u and leaf angle distribution g_L . Furthermore, when we need to prepare a more realistic canopy scene, it can be developed by

detailed modeling of the individual leaf, stem, and branch positions and property allocations (Fig. 2.3.4 right). This enables us to conduct very realistic radiative transfer simulations, but the preparation of a canopy scene is not an easy task and the radiative transfer calculation itself requires vast computational resources.

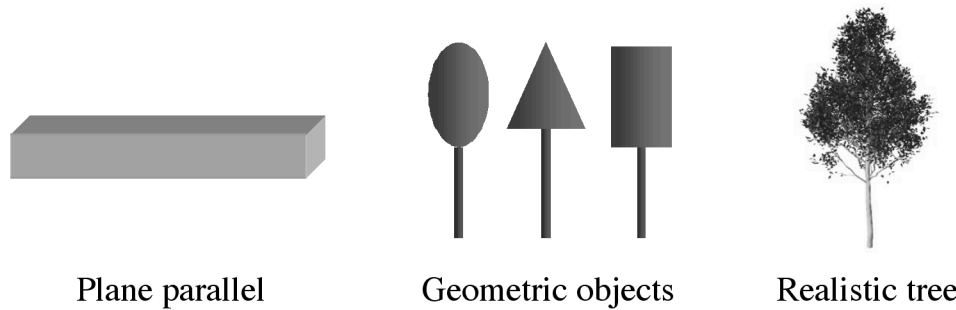


Fig. 2.3.4. Various canopy scenes. Plane parallel (left), 3-D geometric scene (center), very realistic scene (right).

***b.* Preparation of canopy scene**

To determine the 3-D canopy scene, it is necessary to determine the individual tree sizes and positions. When observation data are available, these data could be used to model the canopy scene. In other cases, it is necessary to determine them ecologically. When the output from a dynamic vegetation model is available, it could be another source of information for the canopy structure. Figure 2.3.5 shows an example of a canopy scene.

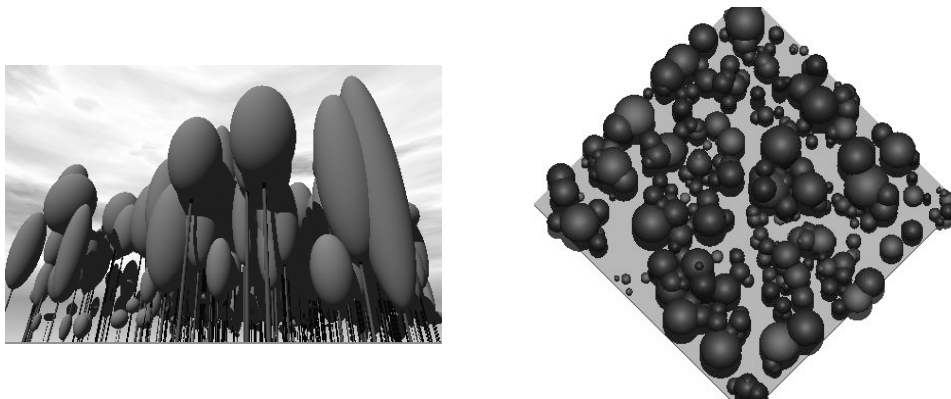


Fig. 2.3.5 Example of a canopy scene.

Chapter 3 Basic algorithms

3.1 Generation of random numbers

We discuss the generation of a uniform pseudorandom number and random numbers that follow the arbitrary distributed probability density function (PDF). Generally, all random numbers that follow the arbitrary distributed PDF can be generated from the uniform pseudorandom number.

3.1.1 Generation of uniform pseudorandom number

There are several methods to generate the uniform pseudorandom number in $[0,1]$. The most common method is a linear congruential generator. In this method, the n th integer is calculated by the following recurrence equation:

$$I_n = aI_{n-1} + b \pmod{m} \quad (3.1.1)$$

where m is a modulus and a is a multiplier. The uniform pseudorandom number in $[0,1]$ is obtained by

$$\rho = I/m \quad (3.1.2)$$

When m is sufficiently large, a long-range random number can be produced. There is a special case ($b = 0$). In this case, the recurrence equation is expressed by

$$I_n = aI_{n-1} \pmod{m} \quad (3.1.3)$$

This is called a multiplicative congruential generator. It has been theoretically and empirically proven that a multiplicative congruential generator has the same accuracy as a linear congruential generator. Note that m and a should be selected carefully. Park and Miller proposed a minimal standard generator (Press et al., 1992: Numerical Recipes (NR)):

$$a = 7^5 = 16807, m = 2^{31} - 1 = 2147483647 \quad (3.1.4)$$

The recurrent cycle of this algorithm is $2^{31} - 2 = 2.1 \times 10^9$.

The use of Eq. (3.1.3) sometimes causes an overflow in a computer simulation, in which the results depend on the computer system. A convenient method to overcome this issue is introduced in NR (“ran0”). The most disadvantageous point of the linear congruential generator is a serious correlation. This problem is well discussed in Fushimi (1989) and NR. (“ran1”) in NR is a method to overcome this problem by shuffling two random numbers.

At present, various criteria and tests have been proposed to measure the robustness of a

random number. The proposed method for generating a random number has been well investigated, and it is known that the maximum-length linearly recurring sequence is one of the best methods: it can generate a long cycle and uniform random numbers. This method is called a shift register with feedback loops. The recurrence equation for the method is expressed by

$$g_n = a_1 g_{n-1} + a_2 g_{n-2} + \dots + a_p g_{n-p} \pmod{2} \quad (3.1.5)$$

The initial value of g_n ($n = 1, 2, \dots, p$) can be selected freely, unless all coefficients are 0. This recurrence equation has 1-bit information (0 or 1) and is defined above the Gallois body (Fushimi, 1989). In a computer, random numbers are generated by an exclusive OR operation. The cycle of this method is $2^p - 1$. An N -bit integer should be N 1-bit numbers. Fushimi (1989) described the following recurrence equation:

$$g_n = g_{n-32} + g_{n-521} \pmod{2} \quad (3.1.6)$$

A 32-bit integer is composed of a series of thirty-two 1-bit integers. The cycle of this equation is $2^{521-32} - 1 \sim 3 \times 10^{147}$, that is, significantly larger than one required for actual applications using a current simulation resource. This method determines a random number by a single exclusive OR operation between two integer numbers. Therefore, this method is very fast compared to others, because it uses the bit operation rather than arithmetic calculation. This method is faster than other methods described in the NR. Other bit operation-based methods like the Mersenne Twister are also good random number generators.

3.1.2 Conversion method (inverse function method)

Let us consider random numbers that follow the general PDF. When the PDF ($g(x)$) is defined in the interval $a-b$, $g(x)$ is normalized by

$$\int_a^b g(x) dx = 1 \quad (3.1.7)$$

The random variable X that follows this PDF is derived from the uniform pseudorandom number ρ in $[0, 1]$:

$$G(X) = \int_a^X g(x) dx = \rho \quad (3.1.8a)$$

$$X = G^{-1}(\rho) \quad (3.1.8b)$$

If (3.1.8) is analytically solved, this method is valid.

a. Exponential distribution

In the case of exponential distribution with an average of 1,

$$g(x) = e^{-x}, \quad x \geq 0 \quad (3.1.9a)$$

$$G(x) = 1 - e^{-x} \quad (3.1.9b)$$

$$G^{-1}(x) = -\log(1-x) \quad (3.1.9c)$$

If we put

$$X = -\log(1-\rho) = -\log \rho', \quad \rho' > 0 \quad (3.1.10)$$

the random number X that follows the exponential function can be generated. If the average is not 1 but μ , then the random number X is derived by

$$X = -\mu \log \rho', \quad \rho' > 0 \quad (3.1.11)$$

b. Gaussian distribution

If we assume a Gaussian distribution with an average of 0 and variance 1, the PDF is expressed by

$$g(x) = \frac{1}{\sqrt{2\pi}} \exp\left(-\frac{x^2}{2}\right) \quad (3.1.12)$$

We can obtain two random numbers that follow the Gaussian (Box-Muller method, NR):

$$\begin{aligned} X_1 &= \sqrt{-2 \log \rho_1} \cos(2\pi\rho_2) \\ X_2 &= \sqrt{-2 \log \rho_1} \sin(2\pi\rho_2) \end{aligned} \quad (3.1.13)$$

However, (3.1.13) is not very fast. The rejection method that is described later is an effective way to improve the speed by avoiding the sine and cosine calculations (Appendix A6).

- 1) Generation of ρ_1, ρ_2 .
- 2) Determination of the position of the point in the quadrant, whose center and area are the origin and 4, respectively.

$$W_1 = 2\rho_1 - 1, \quad W_2 = 2\rho_2 - 1 \quad (3.1.14a)$$

- 3) Calculation of the distance from the origin

$$R^2 = W_1^2 + W_2^2 \quad (3.1.14b)$$

- 4) If $R^2 < 10^{-12}$ or > 1 , then return 1).
- 5) Using the random number, the sine and cosine of the azimuth angle are determined by

$$\rho_1 = R^2, \quad \cos \phi = W_1/R, \quad \sin \phi = W_2/R \quad (3.1.14c)$$

- 6) Finally, the Gaussian random number is determined by

$$X_1 = \frac{W_1}{R} \sqrt{-2 \log R^2}, \quad X_2 = \frac{W_2}{R} \sqrt{-2 \log R^2} \quad (3.1.14d)$$

The arbitrary Gaussian distribution with an average μ and standard deviation σ is derived from

(3.1.13):

$$X' = \sigma X + \mu \quad (3.1.15)$$

c. Gamma distribution: Integer α case

The PDF of the gamma distribution with the structure parameter α and scale parameter 1 is expressed by

$$g(x) = \frac{1}{\Gamma(\alpha)} x^{\alpha-1} e^{-x} \quad (3.1.16)$$

When $\alpha = 1$, (3.1.16) becomes an exponential distribution. The sum of two $g(x)$'s that follow α_1 and α_2 is equal to $g(x)$ with the structure parameter $\alpha_1 + \alpha_2$, that is, the so-called reproductive property.

By using the reproductive property and exponential distribution (3.1.10), the parameter is followed by the gamma distribution if α is an integer:

$$\begin{aligned} X &= -\log \rho_1 - \log \rho_2 - \dots - \log \rho_\alpha \\ &= -\log(\rho_1 \rho_2 \dots \rho_\alpha) \end{aligned} \quad (3.1.17)$$

When α is small, this is the best way. However, when α is large, another method would be desirable. A detailed discussion is provided by Fushimi (1989).

d. Discrete distribution

When the probability parameter X has discrete values x_1, x_2, \dots, x_n and their probabilities are p_1, p_2, \dots, p_n , the random number X that follows this discrete distribution is determined by

$$X = x_k, \text{ if } \sum_{i=1}^{k-1} p_i \leq \rho < \sum_{i=1}^k p_i \quad (3.1.18)$$

3.1.3 LUT method

If Eqs. (3.1.8a) and (3.1.8b) are not analytically solved, a numerical method is required. In this case, a look-up table (LUT) for $X = G^{-1}(\rho)$ should first be analytically computed for various values of ρ . It is possible to prepare the LUT for $\rho = G(X)$. The former method is more effective. X is derived by interpolating from the LUT. Thus, the accuracy depends on the resolution of the LUT. Anyway, it is impossible to obtain an exact solution.

When the number of parameters is less than 2, a solution is easily obtained by linear interpolation or spline interpolation. When the LUT has a larger dimension, the interpolation itself requires vast computation. The fastest method is a nearest-neighbor interpolation. However, that is not reliable and, due to memory limitations, it is impossible to make a

fine-resolution LUT. Therefore, a multidimensional LUT is not effective for improving the speed and accuracy.

3.1.4 Rejection method (selection-rejection method)

Let us consider $f(x)$ that meets the following inequality:

$$f(x) \geq g(x) \quad (3.1.19)$$

$f(x)$ is called a comparison function. Here, $f(x)$ should meet the following conditions: it can be integrated analytically and its inverse function should be easily derived. When $F(x)$ is defined by

$$F(x) = \int_a^x f(x') dx' \quad (3.1.20)$$

the parameter x is randomly determined by the following equations:

$$\frac{\int_a^x f(x') dx'}{\int_a^b f(x') dx'} = \frac{F(x)}{F(b)} = \rho_1 \quad (3.1.21a)$$

$$\therefore x = F^{-1}(\rho_1 F(b)) \quad (3.1.21b)$$

This method is called the rejection method or selection-rejection method (Fushimi, 1989; Press et al., 1992). In von Neumann's method, the random number that follows $f(x)$ is first determined. Then, the rejection or selection is randomly determined. The probability for which x in Eq. (3.1.21b) is followed by the PDF = $g(x)$ is given by $g(x)/f(x)$. In this case, using the newly generated random number, the following criteria are applied:

$$\begin{cases} \text{If } \rho_2 < g(x)/f(x), \text{ finish} \\ \text{If } \rho_2 \geq g(x)/f(x), \text{ rejection} \end{cases} \quad (3.1.22)$$

If rejection is chosen, x is determined by (3.1.21b). The advantage of this method is that it obtains an exact solution, even if the function $g(x)$ is complex. It should be noted that this method requires iterative calculation. When the efficiency is close to 1, we can obtain a good efficiency:

$$\int_a^b f(x) dx = F(b) \quad (3.1.23)$$

Therefore, it is important to find a good comparison function. The typical comparison function is a rectangular, triangular, or trapezoid shape. For example, if $g(x)$ is a smooth function in the given interval $a-b$ and the difference between the maximum and minimum is small, the simplest function is a rectangular distribution function:

$$f(x) = g_{\max} \quad (3.1.24)$$

where g_{\max} is a maximum of g . In this case, $F(x)$ is expressed by

$$F(x) = g_{\max}(x - a) \quad (3.1.25)$$

and x is calculated by

$$x = a + \rho(b - a) \quad (3.1.26)$$

The problem occurs when the function has a strong peak. Under such a condition, the difference between the maximum and minimum is large and the efficiency deteriorates when we use the rectangular function. It is sometimes very difficult to find a good comparison function, and moreover, it is sometimes difficult to find the maximum of the PDF.

As described in 3.1.2, the determination method for the random position in the circle is one example of the rejection method. A randomly-distributed point within a 3-D arbitrarily shaped object can also be determined by the rejection method.

3.1.5 Weighting method

This method adds the weight w to each random number x . If the change in w is allowed, this is a very fast method. Let us consider the PDF $h(x)$ normalized in the same interval with the PDF $g(x)$:

$$\int_a^b h(x) dx = 1 \quad (3.1.27)$$

First, the random number that followed $h(x)$ is determined using one of the previously explained methods (inverse function method, LUT method, rejection method). For this x , the following weight provides the random number that distributes the PDF $g(x)$:

$$w(x) = \frac{g(x)}{h(x)} \quad (3.1.28)$$

$$\begin{aligned} G(x) &= \int_a^x g(x') dx' \\ &= \int_a^x \frac{g(x')}{h(x')} h(x') dx' \\ &= \int_a^x w(x') h(x') dx' \end{aligned} \quad (3.1.29)$$

As an example, when h is a uniform distribution function,

$$h(x) = \frac{1}{b - a} \quad (3.1.30)$$

The random number x is determined by:

$$x = a + \rho(b - a) \quad (3.1.31)$$

Then, the weight is provided by

$$w(x) = (b - a)g(x) \quad (3.1.32)$$

This is just a function proportional to the PDF $g(x)$.

The disadvantage of this method is that the weight may take a large range of values from 0 to infinity. This may cause a large noise in the MC integration. The possible application of this method is as follows: First a value for x that closely follows $g(x)$ is generated using a rejection method and comparison function $h(x)$. Then, the balance of the probability is adjusted by using the weight formulated in (3.1.28).

3.1.6 Metropolis method

The Markov chain Monte Carlo (MCMC) method is an MC method in the narrowest sense. The Metropolis method is a type of MCMC method. It was originally designed for statistical physics but this method can be applied as a general random number generator that follows the general PDF.

A Markov chain is a recurrence formula in which the current state depends only on the value just before the current state. In the Metropolis method, the random number X is determined by the following procedures:

- 1) Next position: the new X' is randomly selected from the current value X_t .
- 2) Calculation of the transition probability: selection of $g(X')/g(X_t)$.
- 3) Renewal of the state: by using the random number, the following value is determined:

$$X_{t+1} = \begin{cases} X' & \text{if } \rho \leq g(X')/g(X_t) \\ X_t & \text{otherwise} \end{cases} \quad (3.1.33)$$

The random series X_1, X_2, \dots generated by this method has a strong correlation. Thus the same value for X is frequently generated. This is a major difference compared with the usual random number sampling methods. Usually, this method is distinguished from other MC methods. It is necessary to investigate the impact of these strong correlations on the accuracy.

3.1.7 Composite method

When a PDF can be expressed by the composition of the PDFs, the PDF is decomposed by

$$g(x) = p_1g_1(x) + p_2g_2(x) + \dots + p_n g_n(x) \quad (3.1.34)$$

$$p_1 + p_2 + \dots + p_n = 1 \quad (3.1.35)$$

$$\int_a^b g_i(x)dx = 1; i = 1, 2, \dots, n \quad (3.1.36)$$

First, the PDF p_i of the discrete distribution is determined by the random integer i . Then, X is determined by $g_i(x)$. The various methods described before can be used for the determination.

3.1.8 Summary of random number generator

In summary, we strongly recommend to using the rejection method because of its applicability to various purposes and efficient speed. This method does not require a large memory and is accurate. It is not necessary to calculate the inverse function. The only requirement is a criterion to reject or select the random number by repeating the rejection criteria. It is also applicable to sample random variables based on a 2-D PDF.

The characteristics of the various methods are summarized in Table 3.1.1.

Table 3.1.1 Advantage and disadvantage for the various random number generators.

	Advantage	Disadvantage
Inverse function method	-Accurate -Fast for a simple function	-Fails to work if inverse function is not available
LUT method	-Approximated value is obtained under an arbitrary PDF	-Large memory is necessary -Bad accuracy for a bad LUT resolution
Rejection method	-Accurate value is obtained under an arbitrary PDF	-Sometimes difficult to find a good comparison function
Weighting method	-Very simple	-May cause a large noise in MC calculation
Metropolis method	-Accurate value is obtained under an arbitrary PDF.	-Series of random numbers is a Markov chain, so it causes a strong correlation with the nearest random number.

3.2 Emissions from radiation source

Let us consider the photon emissions from a radiation source. We will discuss several radiation sources, including solar radiation, thermal radiation from the atmosphere-surface, artificial light, point radiation source like a laser, and radiation from the stars.

3.2.1 Emission energy and distribution of modeled photon

The radiation energy that a single photon conveys in the MC model is generally formulated by the emission energy from the simulation space divided by the total number of photons. The transferred energy by a modeled photon with weight 1 is given by

$$E_1 = \frac{E_{\text{tot}}}{N_{\text{tot}}} \quad (3.2.1a)$$

$$E_{\text{tot}} = \sum_i \sum_j \sum_k E(i, j, k) \quad (3.2.1b)$$

where E is the emission energy from an element (voxel or surface element), (i, j, k) is an element index corresponding to (x, y, z) . In the case of a horizontally uniformly emitted flux in an element, when we assume $A(i, j)$ as a horizontal cross section of the modeled air column (i, j) and $F(i, j, k)$ as the emitted flux from the element (i, j, k) , the following relationship exists:

$$\begin{aligned} E(i, j, k) &= \iint F(x, y, k) dx dy \\ &= F(i, j, k) A(i, j) \end{aligned} \quad (3.2.2)$$

This equation is valid for a radiation source with a finite size, such as solar radiation and thermal emission. We cannot define the emitted flux for a point source because the emitted flux becomes infinite in the emission point. In the point source case, the emitted power is defined as a finite value. If we consider the various radiation sources, the total emission energy is written as

$$E(i, j, k) = E_{\text{solar}}(i, j, k) + E_{\text{thermal}}(i, j, k) + E_{\text{point}}(i, j, k) + \dots \quad (3.2.3)$$

The energy can be simply divided by distributing the number of photons in a way that is proportional to the energy of each component. There are several methods to determine the emission position from the random number. For example, first, we could allocate the same number of photons in a divided subspace and then change the transport energy of a single photon for every subspace. However, the most reasonable method is a method where the photon distribution is determined to follow the 3-D distribution of the energy E . Here, the element of the emission is first determined based on the 3-D distribution of E . Then, the position of the radiation source is determined by the emission energy distribution. Consider that E_{col} is E accumulated in a column; E_{col} can be expressed by

$$E_{\text{col}}(i, j) = \sum_{k=0}^{N+1} E(i, j, k) \quad (3.2.4)$$

where $k = 0$ and $k = N + 1$ represent the surface and the top of the atmosphere, respectively. The average number of modeled photons in the modeled air column (i, j) is

$$\bar{N}_{\text{col}}(i, j) = N_{\text{tot}} \frac{E_{\text{col}}(i, j)}{E_{\text{tot}}} \quad (3.2.5)$$

It should be noted that this value is not an integer. Using an integer for N_{col} , if the following relationship is given:

$$N_{\text{col}} \leq \bar{N}_{\text{col}}(i, j) < N_{\text{col}} + 1 \quad (3.2.6)$$

the number of modeled photons entering the air column (i, j) is determined using the random number ρ :

$$\begin{cases} N_{\text{col}} & \text{if } \rho \geq \bar{N}_{\text{col}} - N_{\text{col}} \\ N_{\text{col}} + 1 & \text{if } \rho < \bar{N}_{\text{col}} - N_{\text{col}} \end{cases} \quad (3.2.7)$$

Using these equations, Eq. (3.2.5) is satisfied.

Next, k , which is an index of vertical number for the column, is determined. From Eq. (3.2.4), the probability of emission from the k th element is expressed by

$$\frac{E(i, j, k)}{E_{\text{col}}(i, j)} \quad (3.2.8)$$

k is determined based on this discrete probability distribution and random number. In the next section, a method to determine the emitted flux for various radiation sources, emission positions, and emission directions is described.

3.2.2 Solar radiation

As well as (3.2.2), the energy of the solar radiation incident at the top of the atmospheric column is expressed by

$$E_{\text{solar}}(k) = \begin{cases} AF_{\text{solar}} & \text{for } k = N + 1 \\ 0 & \text{for } k \neq N + 1 \end{cases} \quad (3.2.9)$$

where A is a column cross section and F_{solar} is the incoming solar flux at the horizontal plane. Strictly speaking, solar radiation is a radiation source that has a strongly-peaked cone-like shape. F_{solar} is a function of the sun-earth distance and solar zenith angle. It annually varies within 3%.

It is easy to determine the emission position when the radiation source is only solar radiation.

The emission flux is independent of the horizontal plane. When the simulation space is defined as $[0, X_{\max}]$, $[0, Y_{\max}]$, $[z_{\text{BOA}}, z_{\text{TOA}}]$, the emission position is determined from two random numbers:

$$\begin{pmatrix} x \\ y \\ z \end{pmatrix} = \begin{pmatrix} \rho_x X_{\max} \\ \rho_y Y_{\max} \\ z_{\text{TOA}} \end{pmatrix} \quad (3.2.10)$$

From Eqs. (3.2.1) and (3.2.9), the energy of the modeled photon is given by:

$$E_1 = \frac{F_{\text{solar}} X_{\max} Y_{\max}}{N_{\text{tot}}} \quad (3.2.11)$$

The direction of the emission is described in 3.2.6.

3.2.3 Point radiation source

Point radiation sources such as artificial lights and lasers are also regarded as cone-shaped radiation sources. The emission point is localized at a point. Therefore, the spatial distribution function of the flux is a delta function. Generally, the emission power should be a known parameter. The emission direction is determined by random selection of a position within the cone angle. The emission point is trivial.

3.2.4 Thermal emission

a. Thermal emission from atmosphere

The thermal emission from the k th atmospheric layer is determined by the temperature distribution and emissivity within the layer. According to Kirchhoff's law, the emission coefficient is equal to the absorption coefficient β_a . The emitted flux is expressed by

$$F_{\text{therm}}(k) = 4\pi \int_{z_{k-1}}^{z_k} \beta_a(z) B(T(z)) dz \quad (3.2.12)$$

where B is a Planck function. It represents the radiance of thermal radiation from a black body:

$$B_\lambda(T) = \frac{c_1}{\lambda^5 [\exp(c_2/\lambda T) - 1]} \quad (3.2.13)$$

where λ and T are the wavelength (μm) and absolute temperature (K), respectively. $c_1 = 1.1910437 \times 10^8$ and $c_2 = 1.438786 \times 10^4$. The emission coefficient is assumed to be constant. The vertical distribution of the Planck function is expressed by the n th order polynomial:

$$B(z) = B(z_{k-1}) + b_1(z - z_{k-1}) + b_2(z - z_{k-1})^2 + \dots + b_n(z - z_{k-1})^n \quad (3.2.14)$$

$n = 0$ or 1 is usually an enough approximation. When the model photon is emitted from this voxel, the vertical coordinate z of an emission point is determined by the random number:

$$\frac{\int_{z_{k-1}}^z B(z)dz}{\int_{z_{k-1}}^{z_k} B(z)dz} = \rho \quad (3.2.15)$$

For example, when the emission coefficient is constant in the voxel and $n = 1$ in (3.2.14), b_1 is expressed by

$$B(z) = B(z_{k-1}) + b_1(z - z_{k-1}) \quad (3.2.16a)$$

$$b_1 = \frac{B(z_k) - B(z_{k-1})}{z_k - z_{k-1}} \quad (3.2.16b)$$

By substituting it to (3.2.12), F_{therm} is obtained

$$F_{\text{therm}}(k) = 4\pi\beta_a(k) \frac{B(z_{k-1}) + B(z_k)}{2} (z_k - z_{k-1}) \quad (3.2.17)$$

Also, the height z of the emission point is obtained by substituting (3.2.15) to (3.2.16.):

$$\begin{aligned} & \frac{2 \int_{z_{k-1}}^z [B(z_{k-1}) + b_1(z - z_{k-1})] dz}{[B(z_{k-1}) + B(z_k)](z_k - z_{k-1})} \\ &= \frac{2 \int_0^{z'} [B(z_{k-1}) + (B(z_k) - B(z_{k-1}))z'] dz'}{B(z_{k-1}) + B(z_k)} \\ &= \frac{2 \int_0^{z'} [1 + \gamma z'] dz'}{2 + \gamma} \\ &= \frac{2z' + \gamma z'^2}{2 + \gamma} = \rho \end{aligned} \quad (3.2.18)$$

Here, z' and γ are assumed:

$$z' = \frac{z - z_{k-1}}{z_k - z_{k-1}} \quad (3.2.19a)$$

$$\gamma = \frac{B(z_k)}{B(z_{k-1})} - 1 \quad (3.2.19b)$$

Finally, by solving the following equation:

$$\gamma z'^2 + 2z' - (2 + \gamma)\rho = 0 \quad (3.2.20)$$

we obtain

$$z' = \begin{cases} \frac{\sqrt{1 + \gamma(\gamma + 2)\rho} - 1}{\gamma} & \text{for } \gamma \neq 0 \\ \rho & \text{for } \gamma = 0 \end{cases} \quad (3.2.21)$$

$$z = z_{k-1} + (z_k - z_{k-1})z' \quad (3.2.22)$$

The angular distribution of emission is isotropic. The determination of the direction is the same as in the isotropic scattering case. The emission direction is determined using the zenith angle θ and the azimuth angle ϕ :

$$\cos\theta = 1 - 2\rho_1 \quad (3.2.23a)$$

$$\phi = 2\pi\rho_2 \quad (3.2.23b)$$

ρ_1 and ρ_2 are random numbers. The derivation of these variables is described in 3.5.2.

b. Thermal emission from horizontal plane

The emissivity of the thermal radiation from the isotropic reflective surface is given by 1 reflectance, which is dependent of the direction of emission. Using the zenith angle μ_0 and albedo α , the emissivity ε and albedo α have the following relationship:

$$\varepsilon(\mu_0) = 1 - \alpha(\mu_0) \quad (3.2.24)$$

The emitted flux from a surface with a temperature T_{sfc} is expressed by

$$\begin{aligned} F_{\text{therm}}(0) &= \int_0^{2\pi} \int_0^1 B(T_{\text{sfc}}) \varepsilon(\mu_0) \mu_0 d\mu_0 d\phi_0 \\ &= 2\pi B(T_{\text{sfc}}) \int_0^1 \varepsilon(\mu_0) \mu_0 d\mu_0 \\ &= \pi B(T_{\text{sfc}}) \left[1 - 2 \int_0^1 \alpha(\mu_0) \mu_0 d\mu_0 \right] \end{aligned} \quad (3.2.25)$$

where B is a Planck function. When average reflectance and emissivity are defined by

$$\bar{\alpha} = 2 \int_0^1 \alpha(\mu_0) \mu_0 d\mu_0 \quad (3.2.26a)$$

$$\bar{\varepsilon} = 1 - \bar{\alpha} \quad (3.2.26b)$$

the emitted flux in (3.2.25) is

$$F_{\text{therm}}(0) = \pi B(T_{\text{sfc}}) \bar{\varepsilon} \quad (3.2.27)$$

Next, let us consider the emission direction. When the emission is isotropic, the direction of the emission can be determined in the same manner as the Lambertian reflection. The cosines of the zenith angle and azimuth angle are determined by

$$\mu_0 = \sqrt{\rho_1} \quad (3.2.28a)$$

$$\phi_0 = 2\pi\rho_2 \quad (3.2.28b)$$

where ρ_1 and ρ_2 are random numbers. The description of the derivation is described in 3.6.3.

The anisotropic emission from the surface is determined by the rejection method. First, as in (3.2.28a), the zenith angle is randomly determined. Next, the emissivity (3.2.24) is calculated and the rejection method is applied to the probability $\mathcal{E}(\mu_0)/\mathcal{E}_{\max}$. \mathcal{E}_{\max} is the maximum emissivity. Since the emissivity is less than 1, the efficiency of the rejection method is good. The azimuth angle can be determined by the same method as (3.2.28b), using a uniform pseudorandom number.

3.2.5 Modification of spatial distribution of radiation source based on importance

As mentioned above, the method of distributing the energy proportionally to the emission energy is the most reasonable method. However, sometimes, we may want to modify the radiation distribution. One example is a case where we need to sample the radiation from an element with low emittance energy. Since the emitted energy is very small in this case, it is necessary to use many photons to reduce noise. Another example is a case where we need a radiation contribution from thermal radiation in the middle infrared, although the solar radiation is greater than the thermal in this spectral domain. In such cases, the photon in the important part is relatively increased, and the weight of the photon is modified. Here we describe a method to overcome it using the importance function defined in the 3-D space.

Consider that the emitted energy $E(i, j, k)$ and importance function $G(i, j, k)$ are given in the element of 3-D space. Here, G should be positive. When we define the total emittance energy as E_{tot} , the emission probability and weight in the element (i, j, k) are usually expressed as

$$p(i, j, k) = E(i, j, k)/E_{\text{tot}} \quad (3.2.29a)$$

$$w(i, j, k) = 1 \quad (3.2.29b)$$

p is normalized by

$$\sum_i \sum_j \sum_k p(i, j, k) = 1 \quad (3.2.30)$$

Here, we modify so that the emission probability distribution is proportional to E and G :

$$p'(i, j, k) = G(i, j, k)E(i, j, k)/E_{\text{tot}} \quad (3.2.31)$$

Then, the new emission probability distribution is

$$p''(i, j, k) = \frac{p'(i, j, k)}{\sum_i \sum_j \sum_k p'(i, j, k)} = \frac{G(i, j, k)E(i, j, k)}{\sum_i \sum_j \sum_k G(i, j, k)E(i, j, k)} \quad (3.2.32)$$

This meets the normalization as

$$\sum_i \sum_j \sum_k p''(i,j,k) = 1 \quad (3.2.33)$$

In each element, the emission probability and weight should be conserved. Hence, these parameters are constrained by the following relationship:

$$p''(i,j,k)w''(i,j,k) = p(i,j,k)w(i,j,k) \quad (3.2.34)$$

Here, the new weight is obtained by substituting (3.2.29) and (3.2.32) to (3.2.34):

$$\begin{aligned} w''(i,j,k) &= \frac{p(i,j,k)w(i,j,k)}{p''(i,j,k)} \\ &= \frac{\sum_i \sum_j \sum_k G(i,j,k)E(i,j,k)}{G(i,j,k)E_{\text{tot}}} \end{aligned} \quad (3.2.35)$$

When we use p'' and w'' , instead of p and w , we can obtain the photon distribution modified by the importance function G . This modification does not give any biases, and this is an effective method to adjust the photon distribution and weight as a variance reduction technique.

3.2.6 Radiation source of isotropic angular distribution

Let us consider the isotropic emission within a finite cone-shaped angular range, like the solar radiation that is incident at the top of the atmosphere. Here, we describe the determination of the direction of radiance and emission based on the MC method. The photon direction should be determined to equalize the horizontal component of irradiance for all photons. This can be analytically calculated in the special cases where the center of the cone is directed to the nadir or zenith direction and the angular range is 0° , 180° , or 360° . If it is not calculated analytically, it is necessary to use the LUT method or rejection method. The following discussion can be applied to solar radiation and artificial light.

a. Definition

The coordinates are defined by the zenith angle θ and azimuth angle ϕ . The center direction of the emission cone angle range is defined by (Θ, Φ) . Then, the zenith angle and azimuth angle relative to this direction (Θ, Φ) are defined by $\hat{\theta}, \hat{\phi}$ (Fig. 3.2.1). Since the direction of emission (θ, ϕ) is derived by rotating (Θ, Φ) with respect to $\hat{\theta}, \hat{\phi}$, (θ, ϕ) is derived from $\hat{\theta}, \hat{\phi}$.

When Δ is defined by a half angle of the cone range, it generally has a range like

$$0 \leq \Delta \leq \pi$$

Here,

$\Delta = 0:$	collimated radiation
$\Delta = \pi/2:$	Lambertian
$\Delta = \pi:$	Spherically isotropic

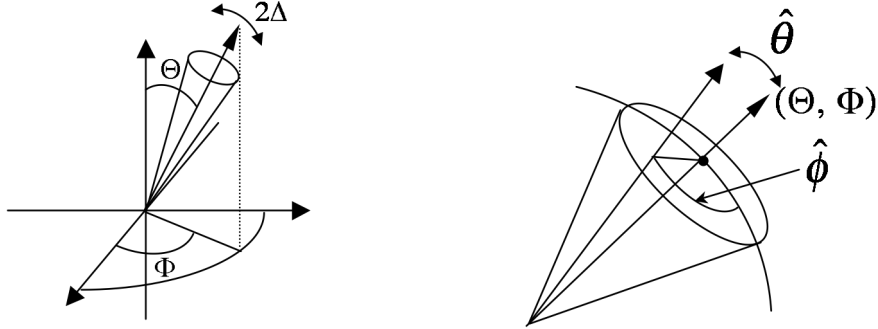


Fig. 3.2.1 Schematics of the cone-shaped angular range and radiation source isotropically emitted.

b. Irradiance and radiance

Let F_0 and R_0 be the irradiance for the horizontal plane to the center of the radiation angular range and the radiance within the angular range. The relationship between F_0 and R_0 is defined by

$$F_0 = \int_0^{2\pi} \int_{\cos\Delta}^1 R_0 |\cos\hat{\theta}| d\cos\hat{\theta} d\hat{\phi} \quad (3.2.36)$$

When we put

$$\begin{aligned} v(\Delta) &= \int_0^{2\pi} \int_{\cos\Delta}^1 |\cos\hat{\theta}| d\cos\hat{\theta} d\hat{\phi} \\ &= \pi(1 - \cos\Delta|\cos\Delta|) \end{aligned} \quad (3.2.37)$$

the relationship between irradiance and radiance is written by

$$F_0 = R_0 v(\Delta) \quad (3.2.38a)$$

$$R_0 = \frac{F_0}{v(\Delta)} \quad (3.2.38b)$$

The radiance is uniquely determined when F_0 and Δ are provided. The spheradiance \hat{F}_0 is

obtained by

$$\begin{aligned}
\hat{F}_0 &= \int_0^{2\pi} \int_{\cos\Delta}^1 R_0 d \cos\hat{\theta} d\hat{\phi} \\
&= 2\pi R_0 (1 - \cos\Delta) \\
&= F_0 \frac{2(1 - \cos\Delta)}{1 - \cos\Delta |\cos\Delta|} \\
&= \begin{cases} F_0 \frac{2}{1 + \cos\Delta} & \text{if } \cos\Delta \geq 0 \\ F_0 \frac{2(1 - \cos\Delta)}{1 + \cos^2\Delta} & \text{if } \cos\Delta < 0 \end{cases}
\end{aligned} \tag{3.2.39}$$

This is also determined uniquely when F_0 and Δ are provided.

The irradiance to the horizontal plane is given by

$$\bar{F}_0(\Theta, \Delta, R_0) = \int_0^{2\pi} \int_{\cos\Delta}^1 R_0 |\cos\theta| d \cos\hat{\theta} d\hat{\phi} \tag{3.2.40}$$

It should be noted that $\cos\theta$ is a function of $\hat{\theta}, \hat{\phi}$:

$$\cos\theta = \sin\Theta \sin\hat{\theta} \cos\hat{\phi} - \cos\Theta \cos\hat{\theta} \tag{3.2.41}$$

The irradiance projection factor to the horizontal plane is defined by

$$\bar{v}(\Theta, \Delta) = \int_0^{2\pi} \int_{\cos\Delta}^1 |\cos\theta| d \cos\hat{\theta} d\hat{\phi} \tag{3.2.42}$$

The difference between (3.2.42) and (3.2.37) is the difference in the projected plane. Using (3.2.38b) and (3.2.42), the irradiance in (3.2.40) is written as

$$\begin{aligned}
\bar{F}_0(\Theta, \Delta, R_0) &= R_0 \bar{v}(\Theta, \Delta) \\
&= F_0 \frac{\bar{v}(\Theta, \Delta)}{v(\Delta)}
\end{aligned} \tag{3.2.43}$$

Generally, it is difficult to obtain the solution of the double integral of (3.2.42). As discussed later, some part of this function can be integrated analytically.

c. Angular distribution function

Using the solid angle ξ , the normalized angular distribution function Ψ is defined as

$$\int_{4\pi} \Psi_0(\theta, \phi) |\cos\theta| d\xi = 1 \tag{3.2.44}$$

This function Ψ_0 is required to calculate the radiance emitted from the radiation source described in 3.9. In the isotropic emission case, the angular distribution function is given by

$$\Psi_0(\theta, \phi) = \begin{cases} \frac{1}{\bar{v}(\Theta, \Delta)} & \text{if } \mathbf{\Omega} \cdot \mathbf{\Omega}_0 > \cos \Delta \\ 0 & \text{if } \mathbf{\Omega} \cdot \mathbf{\Omega}_0 \leq \cos \Delta \end{cases} \quad (3.2.45)$$

$$\mathbf{\Omega} = \begin{pmatrix} \theta \\ \phi \end{pmatrix}, \quad \mathbf{\Omega}_0 = \begin{pmatrix} \Theta \\ \Phi \end{pmatrix}$$

When we apply a judgment of whether the direction is contained in Δ or not, the use of $\sin \Delta$ is better than $\cos \Delta$.

d. Irradiance projection factor for horizontal plane

We discuss the calculation method for the factor in (3.2.42). Three cases exist, as shown in Fig. 3.2.2.

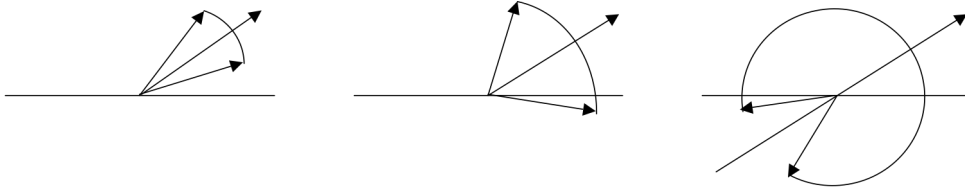


Fig. 3.2.2 Three cases.

1) Emission is always in an up or down direction

In this case, $\Delta \leq |\pi/2 - \Theta|$ ($\cos \Delta \geq \sin \Theta$). Therefore, $\cos \theta$ is always positive or negative in all integral domains.

$$\begin{aligned} \bar{v}(\Theta, \Delta) &= 2 \int_{\cos \Delta}^1 \int_0^\pi |\sin \Theta \sin \hat{\theta} \cos \hat{\phi} - \cos \Theta \cos \hat{\theta}| d\hat{\phi} d \cos \hat{\theta} \\ &= 2\pi |\cos \Theta| \int_{\cos \Delta}^1 \cos \hat{\theta} d \cos \hat{\theta} \\ &= \pi |\cos \Theta| \sin^2 \Delta \end{aligned} \quad (3.2.46)$$

The irradiance to the horizontal plane is derived from (3.2.37) and (3.2.43):

$$\begin{aligned} \bar{F}_0(\Theta, \Delta, R_0) &= F_0 \frac{\pi |\cos \Theta| \sin^2 \Delta}{\pi (1 - \cos \Delta |\cos \Delta|)} \\ &= F_0 |\cos \Theta| \end{aligned} \quad (3.2.47)$$

2) Emission has an up and down direction part 1

In this case, $|\pi/2 - \Theta| < \Delta < \pi - |\pi/2 - \Theta|$ ($-\sin\Theta < \cos\Delta < \sin\Theta$). First, the integration is executed over the condition of $\cos\hat{\theta} \geq \sin\Theta$:

$$\begin{aligned}\bar{v}_a(\Theta, \Delta) &\equiv \int_0^{2\pi} \int_{\sin\Theta}^1 |\cos\theta| d\cos\hat{\theta} d\hat{\phi} \\ &= \pi |\cos\Theta| (1 - \sin^2\Theta) \\ &= \nu\pi |\cos\Theta|^3\end{aligned}\tag{3.2.48}$$

In the other part, the sign of $\cos\theta$ depends on $\cos\hat{\phi}$. It can be written by the single integral

$$\begin{aligned}\bar{v}_b(\Theta, \Delta) &\equiv \int_0^{2\pi} \int_{\cos\Delta}^{\sin\Theta} |\cos\theta| d\cos\hat{\theta} d\hat{\phi} \\ &= 2 \int_{\cos\Delta}^{\sin\Theta} \left[\int_0^{\phi_s} (\sin\Theta \sin\hat{\theta} \cos\hat{\phi} - \cos\Theta \cos\hat{\theta}) d\hat{\phi} \right. \\ &\quad \left. - \int_{\phi_s}^{\pi} (\sin\Theta \sin\hat{\theta} \cos\hat{\phi} - \cos\Theta \cos\hat{\theta}) d\hat{\phi} \right] d\cos\hat{\theta} \\ &= 2 \int_{\cos\Delta}^{\sin\Theta} [2 \sin\Theta \sin\hat{\theta} \sin\phi_s + \cos\Theta \cos\hat{\theta} (\pi - 2\phi_s)] d\cos\hat{\theta}\end{aligned}\tag{3.2.49}$$

where

$$\cos\phi_s = \frac{\cos\Theta \cos\hat{\theta}}{\sin\Theta \sin\hat{\theta}}\tag{3.2.50a}$$

$$\sin\phi_s = \frac{\sqrt{\sin^2\hat{\theta} - \cos^2\Theta}}{\sin\hat{\theta} \sin\Theta}\tag{3.2.50b}$$

When we put

$$t = \cos\hat{\theta}$$

we can obtain an analytical solution for (3.2.49):

$$\begin{aligned}
\bar{v}_b(\Theta, \Delta) &= 4 \int_{\cos \Delta}^{\sin \Theta} \sqrt{\sin^2 \Theta - t^2} dt + 2 \cos \Theta \left[\pi \int_{\cos \Delta}^{\sin \Theta} t dt - 2 \int_{\cos \Delta}^{\sin \Theta} t \phi_s(t) dt \right] \\
&= 2 \left[t \sqrt{\sin^2 \Theta - t^2} + \sin^2 \Theta \sin^{-1} \left(\frac{t}{\sin \Theta} \right) \right]_{\cos \Delta}^{\sin \Theta} \\
&\quad + 2 \cos \Theta \left[\frac{\pi}{2} (\sin^2 \Theta - \cos^2 \Delta) - 2 \int_{\cos \Delta}^{\sin \Theta} t \phi_s(t) dt \right] \\
&= \sin^2 \Theta \left[\pi - 2 \sin^{-1} \left(\frac{\cos \Delta}{\sin \Theta} \right) \right] - 2 \cos \Delta \sqrt{\sin^2 \Theta - \cos^2 \Delta} \\
&\quad + \cos \Theta \left[\pi (\sin^2 \Theta - \cos^2 \Delta) - 4 \int_{\cos \Delta}^{\sin \Theta} t \phi_s(t) dt \right] \\
&= \sin^2 \Theta \left[\pi - 2 \sin^{-1} \gamma \right] - 2 \cos \Delta \sin \Theta \sqrt{1 - \gamma^2} \\
&\quad + \cos \Theta \sin^2 \Theta \left[\pi (1 - \gamma^2) - 4 \int_{\gamma}^1 g \cos^{-1} \sqrt{\frac{g^2 \cos^2 \Theta}{1 - g^2 \sin^2 \Theta}} dg \right]
\end{aligned} \tag{3.2.51}$$

where

$$\phi_s = \cos^{-1} \left(\frac{\cos \Theta}{\sin \Theta} \frac{t}{\sqrt{1 - t^2}} \right) \tag{3.2.52a}$$

$$\gamma = \frac{\cos \Delta}{\sin \Theta} \tag{3.2.52b}$$

Equation (3.2.51) can be calculated numerically by the Gaussian quadrature. The irradiance projection factor is a sum of (3.2.48) and (3.2.51):

$$\bar{v}(\Theta, \Delta) = \bar{v}_a(\Theta, \Delta) + \bar{v}_b(\Theta, \Delta) \tag{3.2.53}$$

3) Emission has both an up and down direction part 2

In this case, $\Delta \geq \pi - |\pi/2 - \Theta|$ ($\cos \Delta \leq -\sin \Theta$). The irradiance projection factor is derived by subtracting (3.2.46) from the spherical integration:

$$\begin{aligned}
\bar{v}(\Theta, \Delta) &= \int_0^{2\pi} \int_{-1}^1 |\cos \theta| d \cos \theta d \phi - \int_0^{2\pi} \int_{-1}^{\cos \Delta} |\cos \theta| d \cos \theta d \hat{\phi} \\
&= 2\pi - 2 \int_0^{\pi} \int_{-\cos \Delta}^1 |\cos \theta| d \cos \theta d \hat{\phi} \\
&= 2\pi - 2 \int_{-\cos \Delta}^1 \int_0^{\pi} |\sin \Theta \sin \hat{\theta} \cos \hat{\phi} - \cos \Theta \cos \hat{\theta}| d \hat{\phi} d \cos \hat{\theta} \\
&= 2\pi \left[1 - |\cos \Theta| \int_{-\cos \Delta}^1 \cos \hat{\theta} d \cos \hat{\theta} \right] \\
&= 2\pi - \pi |\cos \Theta| \sin^2 \Delta
\end{aligned} \tag{3.2.54}$$

Example

Figure 3.2.3 shows the irradiance projection factor for the horizontal plane as a function of Δ with a solar zenith angle of 0° , 30° , 60° , and 90° . The four quadratic points give insufficient accuracy. More than 16 quadratic points give rise to sufficient accuracy. In this figure, $\bar{v}(\Theta, \Delta)/v(\Delta)$ in (3.2.43) is plotted.

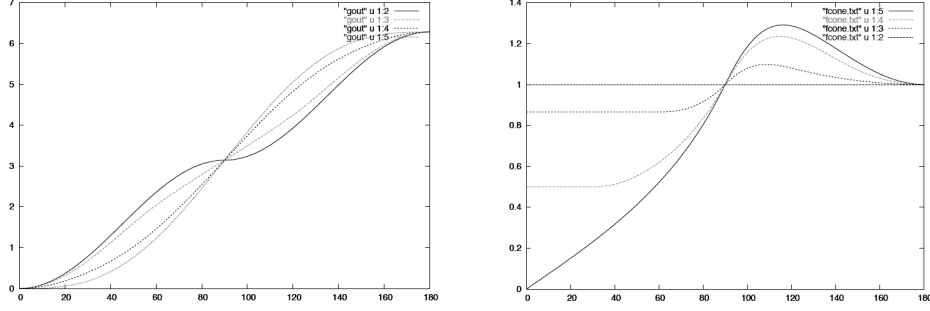


Fig. 3.2.3 Irradiance projection factor for the horizontal plane as a function of Δ with a solar zenith angle of 0° , 30° , 60° , and 90° (left) and $\bar{v}(\Theta, \Delta)/v(\Delta)$ (right).

f. Determination of emission direction: Rejection method

The emission direction is easily determined using the rejection method. First, a direction in the emitted domain is uniformly selected. Since irradiance to the horizontal plane depends on the cosine of the zenith angle, the rejection method is applied to form a zenith angle dependency (a higher zenith angle is likely to be rejected). $\hat{\theta}, \hat{\phi}$ are first determined isotropically:

$$\frac{\int_0^{2\pi} d\hat{\phi} \int_{\cos\Delta}^1 d\cos\hat{\theta}}{\int_0^{2\pi} d\hat{\phi} \int_{\cos\Delta}^1 d\cos\hat{\theta}} = \rho_{\hat{\theta}} \quad (3.2.55)$$

$$\therefore \cos\hat{\theta} = 1 - \rho_{\hat{\theta}}(1 - \cos\Delta) \quad (3.2.56a)$$

$$\therefore \sin\hat{\theta} = \sqrt{\rho_{\hat{\theta}}(1 - \cos\Delta)[2 - \rho_{\hat{\theta}}(1 - \cos\Delta)]} \quad (3.2.56b)$$

Note that $1 - \cos\Delta$ should be very accurate when Δ is very small. Also,

$$\hat{\phi} = 2\pi\rho_{\hat{\phi}} \quad (3.2.57)$$

The better and more powerful way is to use the polar coordinate method (Appendix A6), which can determine $\rho_{\hat{\theta}}, \cos\hat{\phi}, \sin\hat{\phi}$ simultaneously. The emission direction $\mathbf{\Omega} = (\theta, \phi)$ is a direction rotating $\mathbf{\Omega}_0 = (\Theta, \Phi)$ relative to $\hat{\theta}, \hat{\phi}$. This is the same formulation as the scattering

problem. If we put

$$\mathbf{\Omega} = (u_x, u_y, u_z)^T, \mathbf{\Omega}_0 = (u_{0x}, u_{0y}, u_{0z})^T \quad (3.2.58)$$

then

$$\mathbf{\Omega} = \cos \hat{\theta} \mathbf{\Omega}_0 + \sin \hat{\theta} \left[\cos \hat{\phi} \begin{pmatrix} u_{0x} u_{0z} / \sqrt{u_{0x}^2 + u_{0y}^2} \\ u_{0y} u_{0z} / \sqrt{u_{0x}^2 + u_{0y}^2} \\ -\sqrt{u_{0x}^2 + u_{0y}^2} \end{pmatrix} + \sin \hat{\phi} \begin{pmatrix} -u_{0y} / \sqrt{u_{0x}^2 + u_{0y}^2} \\ u_{0x} / \sqrt{u_{0x}^2 + u_{0y}^2} \\ 0 \end{pmatrix} \right] \quad (3.2.59)$$

Here, if $u_{0x}^2 + u_{0y}^2 = 1 - u_{0z}^2 \approx 0$, it is expressed by the more simple form:

$$\mathbf{\Omega} = \text{sign}(u_{0z}) \begin{pmatrix} \sin \hat{\theta} \cos \hat{\phi} \\ \sin \hat{\theta} \sin \hat{\phi} \\ \cos \hat{\theta} \end{pmatrix} \quad (3.2.60)$$

$\text{sign}()$ is a function that has both positive and negative signs.

In an actual case, a z component of (3.2.59) is first derived:

$$\cos \theta = u_z = \cos \hat{\theta} u_{0z} - \sin \hat{\theta} \cos \hat{\phi} \sqrt{u_{0x}^2 + u_{0y}^2} \quad (3.2.61)$$

Next, the rejection method is applied by considering the $\cos \theta$ dependency of the angular distribution:

$$\begin{cases} \text{If } \rho < |\cos \theta| / C_{\max}, \text{ finish} \\ \text{If } \rho \geq |\cos \theta| / C_{\max}, \text{ rejection} \end{cases} \quad (3.2.62)$$

Here, C_{\max} is defined by

$$C_{\max} = \begin{cases} 1 & \text{if } |\cos \Theta| > \cos \Delta \\ \max[|\cos(\Theta - \Delta)|, |\cos(\Theta + \Delta)|] & \text{otherwise} \end{cases} \quad (3.2.63)$$

If the random number is rejected in (3.2.62), the new direction is determined again using (3.2.56–57, 3.2.61). The rejected probability in a single cycle is less than 1/2. Therefore, on average, the direction is determined in two cycles at the worst case. Consequently, the rejection method provides a fast and simple method to determine the direction.

3.3 Ray tracing

The ray tracing method is a visualization method for 3-D graphics that traces the photon trajectory. In the 3-D MC radiative transfer simulation, as shown in Fig 3.3.1, it is necessary to find the nearest intersection point of the photon trajectory with geometric objects in the space. Here, we describe a simulation method for a photon traveling in a simulation space with typical geometric objects (plane parallel, rectangle, cone, cylinder, ellipsoid, and surface with large-scale roughness).

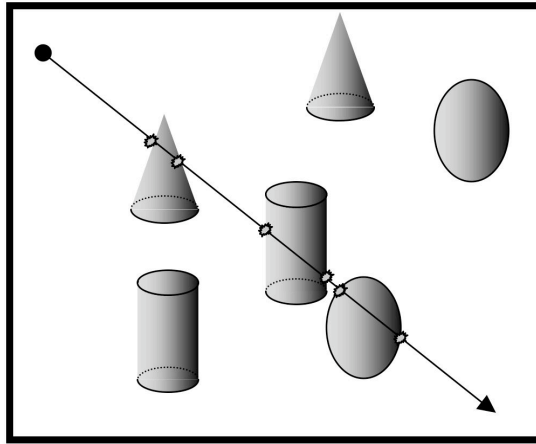


Fig. 3.3.1 Relationship between modeled photon and geometric objects.

3.3.1 Intersection of modeled photon with geometric object

As shown in Fig. 3.3.2, there are three conditions that may exist between the modeled photon and geometric objects such as a rectangle, cone, cylinder, or ellipsoid. In case A (Fig. 3.3.2), there is no intersection. In case B, there are two intersection points between the modeled object and geometric object. If the photon trajectory is a tangent of the object, the intersections are degenerated. In case C, in which the photon is located within the object, there is one intersection. The algorithm to find the intersection points has the following procedures:

Case 1: Starting point of the modeled photon is outside the object

- i) Judgment whether the photon trajectory has intersection points or not
- ii) Extraction of the intersection points of all objects and determination of the appropriate points for each object (b1 of case B in Fig 3.3.2)
- iii) Determination of the nearest point from all candidates selected in procedure ii)

Case 2: Starting point of the modeled photon is inside the object

- i) Extraction of the intersection points of the photon
- ii) Extraction of the intersection point along the photon direction (C2 in case C in Fig. 3.3.2)

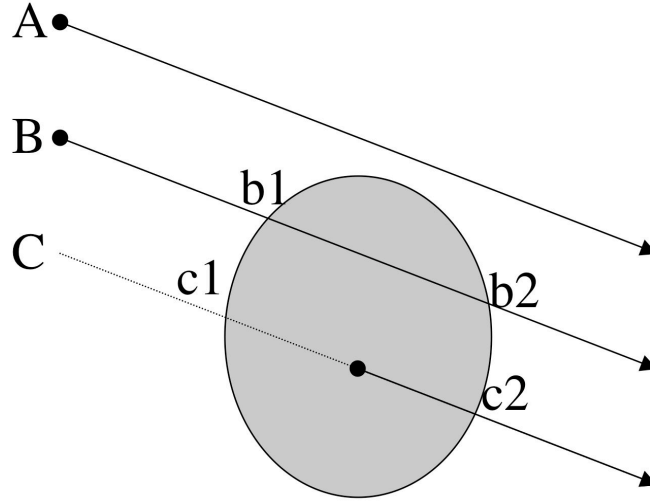


Fig. 3.3.2 Intersection of the modeled photon with the geometric object. A: no intersection point, B: two intersection points with object, and C: one intersection point when the modeled photon is located within the object.

3.3.2 Relationship between modeled photon and geometric object in 3-D scene

a. Equation for modeled photon trajectory

The modeled photon trajectory, which passes through the point $\mathbf{r}_0(x_0, y_0, z_0)$ with the direction vector $\mathbf{\Omega}(v_x, v_y, v_z)$ is expressed by the parameter t :

$$\mathbf{r}(t) = \mathbf{r}_0 + t \mathbf{\Omega} \quad (\text{vector expression}) \quad (3.3.1)$$

x , y , and z of this equation are expressed by

$$x = x_0 + t v_x \quad (3.3.2a)$$

$$y = y_0 + t v_y \quad (3.3.2b)$$

$$z = z_0 + t v_z \quad (3.3.2c)$$

b. Relationship between rectangle and photon

A rectangle is expressed by the six equations for plain surfaces in 3-D space:

$$x = x_1; x = x_1 + r_x \quad (3.3.3a)$$

$$y = y_1; y = y_1 + r_y \quad (3.3.3b)$$

$$z = z_1; z = z_1 + r_z \quad (3.3.3c)$$

In determining the intersection point of the modeled photon with the plain surface (3.3.3a), by substituting (3.3.3a) to (3.3.2a), t is obtained:

$$t = (x_1 - x_0)/v_x; t = (x_1 + r_x - x_0)/v_x \quad (3.3.4)$$

Then, the y and z candidates for the intersection point are derived by substituting t in (3.3.4) to (3.3.2b) and (3.3.2c):

$$y = y_0 + v_y (x_1 - x_0)/v_x; y = y_0 + v_y (x_1 + r_x - x_0)/v_x \quad (3.3.5)$$

$$z = z_0 + v_z (x_1 - x_0)/v_x; z = z_0 + v_z (x_1 + r_x - x_0)/v_x \quad (3.3.6)$$

Furthermore, y and z require the following condition:

$$y_1 \leq y \leq y_1 + r_y, z_1 \leq z \leq z_1 + r_z \quad (3.3.7)$$

If all the above conditions are satisfied, the derived point is an intersection point. If the photon is located within the rectangular object, the following condition should be satisfied:

$$t \geq 0 \quad (3.3.8)$$

The same calculation can be applied to the other planes (y and z).

c. Relationship between plane-parallel layer and photon

In the radiative transfer simulation, it is often necessary to simulate the horizontally infinite plane-parallel layer condition in the finite size of a simulation scene. As shown in Fig. 3.3.3, an outgoing photon from the scene reenters from the opposite side of the face. This calculation can be achieved by the intersection searching problem between a rectangle and photon. When a photon incident from the top of the layer has an intersection at the bottom of the layer $z = z_1$, the intersection point (x', y') is determined by the same method as the rectangular case. Thus, by substituting $z = z_1$ to (3.3.2c), t is obtained by:

$$t = (z_1 - z_0)/v_z \quad (3.3.9)$$

By substituting t to (3.3.2a) and (3.3.2b), (x', y') is obtained by

$$x' = x_0 + tv_x \quad (3.3.10a)$$

$$y' = y_0 + tv_y \quad (3.3.10b)$$

Here, (x', y') may be located outside the simulation scene. When the scene boundary is defined by $[0, x_d]$, $[0, y_d]$, the new photon position in the scene under the periodic boundary conditions is expressed by the following equation:

If v_x is positive,

$$x = x' - \text{integer}(x'/x_d) \times x_d \quad (3.3.11a)$$

If v_x is negative,

$$x = x' - [\text{integer}(x'/x_d) - 1] \times x_d \quad (3.3.11b)$$

Here, an integer indicates the numerical operation to cut after the decimal point. The new position of y is also calculated in the same manner.

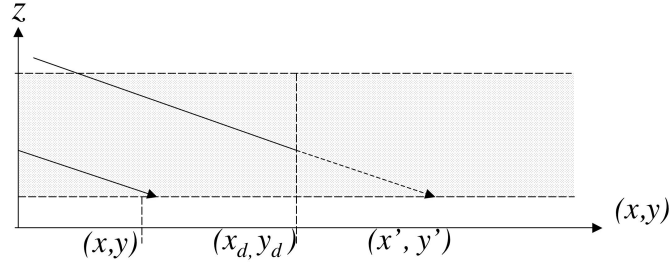


Fig. 3.3.3 Relationship between a plane-parallel layer and photon.

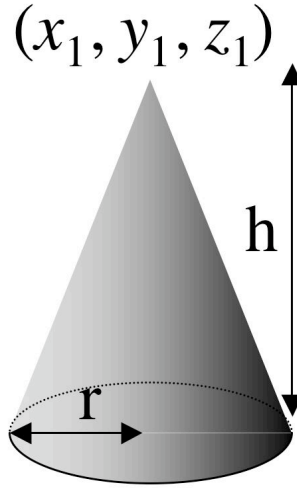


Fig. 3.3.4 Definition of cone parameters.

d. Cone

The equation for a cone is expressed by

$$(x - x_1)^2 + (y - y_1)^2 = c^2 (z - z_1)^2 \text{ (cone side)} \quad (3.3.12)$$

$$z = z_1; (x - x_1)^2 + (y - y_1)^2 < r^2 \text{ (cone bottom)} \quad (3.3.13)$$

where (x_1, y_1, z_1) are the coordinates of the cone apex. Figure 3.3.4 shows the definition of the cone parameters. By substituting (3.3.2) to (3.3.12), we obtain a quadratic equation for t :

$$(v_x^2 + v_y^2 - c^2 v_z^2)t^2 + 2\{v_x(x_0 - x_1) + v_y(y_0 - y_1) - c^2 v_z(z_0 - z_1)\}t + \{(x_0 - x_1)^2 + (y_0 - y_1)^2 - c^2(z_0 - z_1)^2\} = 0 \quad (3.3.14)$$

When the first, second, and third terms of (3.3.14) are expressed by A , B , and C , respectively, D

is defined by

$$D = B^2 - 4AC \quad (3.3.15)$$

D should be ≥ 0 to have intersection points with the cone side. Then, t is determined by

$$t = \frac{-B \pm \sqrt{D}}{2A} \quad (3.3.16)$$

A candidate for the intersection point is determined by substituting t to (3.3.2). However, the intersection is limited to a point with the following condition:

$$z_1 - h \leq z \leq z_1 \quad (3.3.17)$$

The intersection with the bottom face of a cone is calculated by finding the intersection between the plane $z = z_1 - h$ and photon trajectory under the condition in (3.3.13).

When a photon is inside the cone, the solution should meet (3.3.8).

e. Cylinder

As shown in Fig. 3.3.5, the equations for the side and top/bottom of a cylinder are expressed by

$$(x - x_1)^2 + (y - y_1)^2 = r^2; z_2 \leq z \leq z_1 \text{ (cylinder side)} \quad (3.3.18)$$

$$z = z_1; (x - x_1)^2 + (y - y_1)^2 < r^2; z = z_2; (x - x_1)^2 + (y - y_1)^2 < r^2 \text{ (cylinder top and bottom)} \quad (3.3.19)$$

(x_1, y_1, z_1) , and (x_1, y_1, z_2) are counterpoints of the top and bottom circles. By substituting (3.3.2) to (3.3.18), the quadratic equation for t is expressed by

$$(v_x^2 + v_y^2)t^2 + 2\{v_x(x_0 - x_1) + v_y(y_0 - y_1)\}t + \{(x_0 - x_1)^2 + (y_0 - y_1)^2 - r^2\} = 0 \quad (3.3.20)$$

When the first, second, and third terms of (3.3.20) are expressed by A , B , and C , respectively, D is defined by (3.3.15). D should be ≥ 0 to have intersection points with the cylinder side. Since t is calculated from (3.3.16), a candidate for the intersection point is determined by substituting t to (3.3.2). However, the intersection is limited to a point with the following condition:

$$z_2 \leq z \leq z_1 \quad (3.3.21)$$

An intersection with the top and bottom circles is an intersection of the photon trajectory with the plane $z = z_1$; $z = z_2$ under the (3.3.19) condition. When a photon is inside the cylinder, the solution should meet (3.3.8).

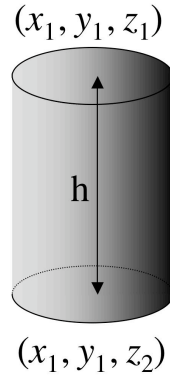


Fig. 3.3.5 Definition of cylinder parameters.

f. Ellipsoid

The equation for an ellipsoid is expressed by

$$\frac{(x - x_1)^2}{a^2} + \frac{(y - y_1)^2}{a^2} + \frac{(z - z_1)^2}{b^2} = 1 \quad (3.3.22)$$

where (x_1, y_1, z_1) is the center point of the ellipsoid. The quadratic equation of t is expressed by substituting (3.3.2) to (3.3.22):

$$(b^2v_x^2 + b^2v_y^2 + a^2v_z^2)t^2 + \{2(x_0v_xb^2 - x_1v_xb^2 + y_0v_yb^2 - y_1v_yb^2 + z_0v_z a^2 - z_1v_z a^2)t + b^2(x_0 - x_1)^2 + b^2(y_0 - y_1)^2 + a^2(z_0 - z_1)^2 - a^2b^2\} = 0 \quad (3.3.23)$$

When the first, second, and third terms of (3.3.23) are expressed by A , B , and C , respectively, D is defined by (3.3.15). D should be ≥ 0 to have intersection points with the ellipsoid. Since t can be derived from (3.3.16), a candidate for the intersection point is determined by substituting t to (3.3.2). Moreover, when a photon is located in the ellipsoid, the photon that meets (3.3.8) is an intersection.

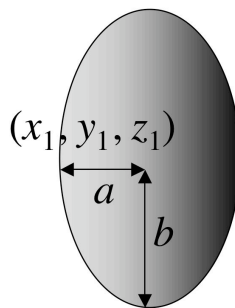


Fig. 3.3.6 Definition of ellipsoid parameters.

3.3.3 Relationship between modeled photon and surface with roughness

When the photon is incident at the ground surface, calculation of the intersection between the photon and ground surface is required. If the surface is perpendicular to the z -axis, the intersection point can be calculated by (3.3.2–6).

In general, the ground surface has large-scale roughness. When we consider it, it is necessary to find the intersection between a sloped surface and the photon. When the surface topography is given by the digital elevation model (DEM), the topographic information is given by a grid point of the quadrate.

First, we describe a method to interpolate the surface elevation z at the arbitrary point (x, y) using the bilinear method, with the nearest four grid points.

In the bilinear method, the surface elevation z is calculated from the nearest four grid points:

$$z = \frac{(y_2 - y)z_a - (y_1 - y)z_b}{(y_2 - y_1)} \quad (3.3.24)$$

Here, z_a , and z_b are calculated by

$$z_a = \frac{(x_2 - x)z_1 - (x_1 - x)z_2}{(x_2 - x_1)} \quad (3.3.25)$$

$$z_b = \frac{(x_2 - x)z_4 - (x_1 - x)z_3}{(x_2 - x_1)} \quad (3.3.26)$$

(3.3.24)–(3.3.26) are equations for a curved ground surface. A quadratic equation for the ground surface is given by substituting (3.3.24)–(3.3.26) to (3.3.2):

$$\begin{aligned} & v_{xv} (z_1 - z_2 + z_3 - z_4) t^2 \\ & + \left\{ \begin{aligned} & y_0 v_x (z_1 - z_2 + z_3 - z_4) + x_0 v_y (z_1 - z_2 + z_3 - z_4) \\ & - y_2 v_x (z_1 - z_2) - y_1 v_x (z_3 - z_4) \\ & - x_2 v_y (z_1 - z_4) - x_1 v_y (-z_2 + z_3) - v_z x_d y_d \end{aligned} \right\} t \quad (3.3.27) \\ & + \left\{ \begin{aligned} & y_0 x_0 (z_1 - z_2 + z_3 - z_4) - y_0 x_2 (z_1 - z_4) - y_0 x_1 (-z_2 + z_3) \\ & - x_0 y_2 (z_1 - z_2) - x_0 y_1 (-z_2 + z_3) \\ & y_2 x_2 z_1 - y_2 x_1 z_2 + y_1 x_1 z_3 - y_1 x_2 z_4 - z_0 x_d y_d \end{aligned} \right\} = 0 \end{aligned}$$

where $x_d = (x_2 - x_1)$, $y_d = (y_2 - y_1)$. t is derived by solving these equations. The intersection point is then obtained from (3.3.2). However, the obtained x, y should meet the following conditions.

$$x_1 \leq x \leq x_2; y_1 \leq y \leq y_2 \quad (3.3.28)$$

To determine the intersection point with the ground surface, it is necessary to examine (3.3.27) and (3.3.28) over all quadrate grids. As shown in photon trajectory A in Fig. 3.3.7 (center), the photon intersection has two solutions: intersection from the top side and bottom

side. In this case, the true intersection point can be determined by selecting the nearest intersection.

When there are $N \times M$ number of grid points in the (x, y) plane, they form $(N - 1) \times (M - 1)$ number of quadrates. Therefore, a large computation time is needed if we employ a finer resolution or large-scale DEM data. In this case, the following method reduces and simplifies the computation:

- i) The maximum and minimum elevations are determined from the DEM before starting the simulation.
- ii) The photon intersections with two planes, which are perpendicular to the z -axis with heights equal to the maximum and minimum of the DEM (Fig. 3.3.7 center), are derived.
- iii) The calculation of the intersection is only conducted in a large rectangular area (Fig. 3.3.7 bottom), which is determined by including the two points calculated from ii).

The efficiency of this method depends on the ratio of the distance between grids to the difference between the maximum and minimum elevations. When the difference in elevation is small and the distance between grids is large, this method drastically improves the computation efficiency. This method is also efficient when the incident angle of the photon is small.

Further improvement can be achieved by the two additional methods described in the next section.

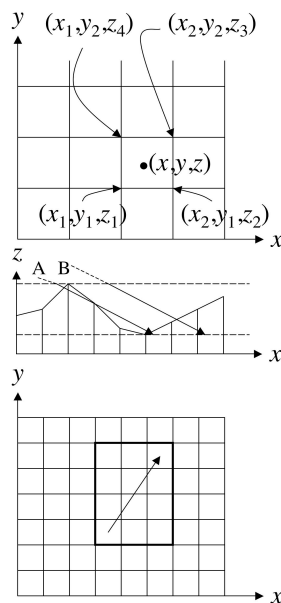


Fig. 3.3.7 Intersection between ground surface and photon. Top: Relationship between arbitrary point (x, y) and four nearest points. Center: Relationship between surface elevation and photon position. Bottom: Calculation area constrained by the maximum and minimum elevations.

3.3.4 Space subdivision method

The space subdivision method divides the simulation space into subdivisions and memorizes where the object in each subdivision is (Araya, 2003). This method reduces the number of intersection calculations. When there are a large number of objects, the computation time improves. Furthermore, hierarchical nesting of the subdivisions is effective.

In the case of a ground surface with large-scale roughness, for example, a simulation scene is divided vertically to include the DEM grid columns. Then, the photon is moved on a subdivision-by-subdivision basis. The photon trajectory is judged by whether the photon reaches the boundary of a subdivision or collides with the ground surface. This method is fairly simple (3.3.2) since there is only one surface object per subdivision. Therefore, it achieves faster computation.

3.3.5 Boundary volume method

The boundary volume method uses simple virtual objects that wrap around complicated objects (Araya, 2003). This method first examines the photon intersection with virtual objects. If the photon has no intersection with a virtual object, the calculation of its intersection with the complicated objects in the virtual object can be skipped. If the photon has an interaction with a virtual point, the calculation of its possible intersection with the complicated object executes. Thus, it reduces the computation time by first determining cases where the photon has no intersection. The hierarchical nesting of subdivisions is also effective in this method.

As an example, it is applicable for fast determination of the photon intersection with the ground surface. When we use a rectangle as a boundary volume that includes the surface elements, the z -axis boundary of this rectangle is determined by the maximum and minimum among the four positions of the surface grids. If the photon has no intersection with this rectangle, it also has no intersection with the ground surface. This method is effective when it is used in combination with the space subdivision method.

As another example, when we examine the intersection with a cone or ellipsoid, it makes it faster to examine a cylinder with an infinite length that contains the object before examining the actual object (cone, ellipsoid). In this case, it is not necessary to consider the z -axis. The problem degenerates to a 2-D (x, y) problem. Examination of the intersection is the same as that of the calculation method for the side of a cylinder. This can be simplified as follows. If we let the photon position $\mathbf{r} = (x, y)^T$, photon direction $\boldsymbol{\Omega} = (u_x, u_y)^T$, and $\mathbf{c} = (p, q)^T$, the radius of the circle R is shown in Fig. 3.3.8. Then, the condition for an intersection between the photon and cylinder is

$$\cos \alpha = \frac{\sqrt{|\mathbf{c} - \mathbf{r}|^2 - R^2}}{|\mathbf{c} - \mathbf{r}|} \geq \boldsymbol{\Omega} \cdot \left(\frac{\mathbf{c} - \mathbf{r}}{|\mathbf{c} - \mathbf{r}|} \right) \quad (3.3.29)$$

When it is expressed by the (x, y) component

$$\sqrt{(p-x)^2 + (q-y)^2 - R^2} \geq (p-x)u_x + (q-y)u_y$$

$$\therefore (p-x)^2 + (q-y)^2 \geq R^2 + [(p-x)u_x + (q-y)u_y]^2 \quad (3.3.30)$$

Evaluation of (3.3.30) can be done more quickly than the cone and ellipsoid described in 3.3.2. This is effective when a single tree consists of a combination of several objects.

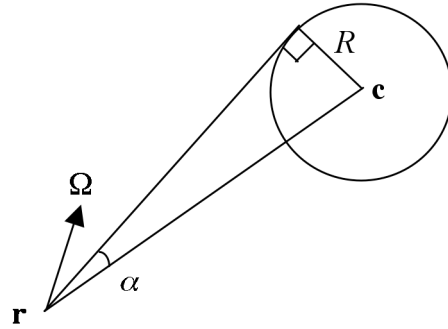


Fig. 3.3.8 Relationship between cylinder and photon trajectory.

3.4 Collision

A photon is scattered or absorbed after collision with a particle in a medium. This collision process can be represented as a simple probabilistic process. However, not only one modeling method but also several modifications can be used. Especially, we should pay attention to how the absorption is treated, how the photon weight is modified at the collision, and how several kinds of media components are treated. This section discusses this topic.

3.4.1 Collision probability and determination of collision point

a. Extinction coefficient and photon path length

Light beam intensity decreases by scattering and absorption in a medium. The radiance of the beam at the distance s from the source at the incident point in a homogeneous volume follows the Lambert-Beer law:

$$I = I_0 \exp(-\beta_e s) \quad (3.4.1)$$

where β_e is the volume extinction coefficient (extinction cross section per unit volume) (m^{-1}), which is closely associated with the photon mean free path length (MFP):

$$\text{MFP} = 1/\beta_e \quad (3.4.2)$$

For inhomogeneous media, when the light transports from \mathbf{r}_0 to \mathbf{r}_1 ,

$$I = I_0 e^{-\tau(\mathbf{r}_0, \mathbf{r}_1)} \quad (3.4.3)$$

$$\tau(\mathbf{r}_0, \mathbf{r}_1) = \int_{\mathbf{r}_0 \rightarrow \mathbf{r}_1} \beta_e(t) dt; \quad t = |\mathbf{r}' - \mathbf{r}_0| \quad (3.4.4)$$

where τ is the optical thickness along the light path. The integral on the right hand side of (3.4.4) can be numerically computed.

b. Collision probability and sampling of collision point

From (3.4.3), the ratio I/I_0

$$T(\tau) = e^{-\tau} \quad (3.4.5)$$

is the transmittance, which can be understood as the probability that no collision occurs until the photon reaches the point with an optical thickness of τ . The contrary probability of this is the collision probability, i.e., the probability that the photon experiences a single collision before its arrival at the point with τ . The collision probability C is written as

$$C(\tau) = 1 - T(\tau) = 1 - e^{-\tau} \quad (3.4.6)$$

This function C is the cumulative distribution function of collision, and its derivative is the PDF:

$$\frac{dC(\tau)}{d\tau} = e^{-\tau} = T(\tau) \quad (3.4.7)$$

It is clear that this PDF is the transmittance itself.

Let us assume that the photon collides once at a random location with a value of optical thickness between 0 and infinity. The sampled random optical thickness is determined by a uniform random number ρ :

$$C(\tau) = \rho; T(\tau) = 1 - \rho = \tilde{\rho} \quad (3.4.8a)$$

$$\therefore \tau = -\ln(1 - \rho) = -\ln \tilde{\rho} \quad (3.4.8b)$$

where $(1 - \rho)$ is still a uniform random number; then, it is replaced with ρ in the 2nd equation above. By substituting the randomly determined τ into (3.4.4), the collision point \mathbf{r}_1 is determined.

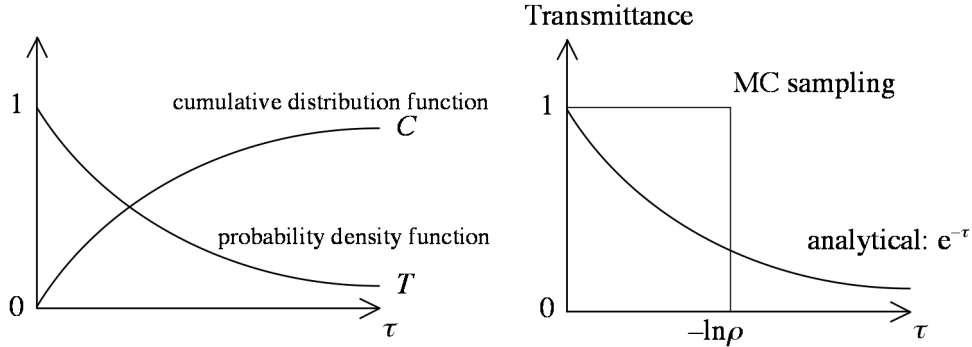


Fig. 3.4.1 Relationships between optical thickness, transmittance, and collision probability

c. Sampling collision point in prescribed limited path

The probability of a collision at a point with an optical thickness between τ_1 and τ_2 is given by the difference in the collision probability C or the transmittance T :

$$\Delta C(\tau_1, \tau_2) = C(\tau_2) - C(\tau_1) = e^{-\tau_1} - e^{-\tau_2} = T(\tau_1) - T(\tau_2) = \Delta T(\tau_1, \tau_2) \quad (3.4.9)$$

This probability can also be written as

$$\begin{aligned}\Delta C(\tau_1, \tau_2) &= e^{-\tau_1} (1 - e^{-(\tau_2 - \tau_1)}) \\ &= T(\tau_1) C(\tau_2 - \tau_1)\end{aligned}\quad (3.4.10)$$

That is, it is the collision probability for the optical thickness of $\tau_2 - \tau_1$ multiplied by the transmittance for τ_1 .

Let us consider about the probability of collision at a point with the optical thickness between τ_1 and τ . For this “limited” collision, the cumulative distribution function is as follows:

$$C'(\tau; \tau_1 \rightarrow \tau_2) = \frac{T(\tau_1) C(\tau - \tau_1)}{T(\tau_1) C(\tau_2 - \tau_1)} = \frac{C(\tau - \tau_1)}{C(\tau_2 - \tau_1)} = \frac{1 - e^{-(\tau - \tau_1)}}{1 - e^{-(\tau_2 - \tau_1)}} \quad (3.4.11)$$

If a collision occurs at a random point with the optical thickness between τ_1 and τ_2 , then the corresponding optical thickness τ is determined by a random number:

$$C'(\tau; \tau_1 \rightarrow \tau_2) = \rho \quad (3.4.12a)$$

$$T(\tau - \tau_1) = 1 - \rho C(\tau_2 - \tau_1) \quad (3.4.12b)$$

$$\therefore e^{-(\tau - \tau_1)} = 1 - \rho (1 - e^{-(\tau_2 - \tau_1)}) \quad (3.4.12c)$$

If

$$\tau_1 = 0, \tau_2 = \infty \quad (3.4.13)$$

then (3.4.12c) is the same as (3.4.8). We have obtained the probability of a collision within an arbitrary segment of the path as (3.4.10), and a random collision point within the segment can be determined by (3.4.12). By applying this, we can, for example, sample the heating rate by forced collision in an arbitrary path segment. The probability of absorption at a random point determined with this method is the collision probability in (3.4.19) multiplied by the single scattering co-albedo:

$$\Delta C(\tau_1, \tau_2)(1 - \omega) = T(\tau_1) C(\tau_2 - \tau_1)(1 - \omega). \quad (3.4.14)$$

3.4.2 Treatment of absorption

The scattering should occur at a randomly determined point, and this is the only method to treat the scattering in the MC model. Absorption can be treated in two different ways. Here, we specify the optical thickness of the media with β_e , β_a , β_s , ω , and P .

a. Absorption at collision point

This method treats the collision as a mixture of absorption and scattering. With the transmittance $T(\tau)$ for the path between the points \mathbf{r}_0 and \mathbf{r}_1 , the optical thickness for the collision will be (see also Fig. 3.4.2)

$$\tau = \tau_e = \int_{\mathbf{r}_0 \rightarrow \mathbf{r}_1} [\beta_s(t) + \beta_a(t)] dt; \quad t = |\mathbf{r}' - \mathbf{r}_0| \quad (3.4.15)$$

If the photon collides, the collision is either of scattering or absorption. The probability that the collision is scattering is given as

$$\omega = \beta_s / \beta_e \quad (3.4.16)$$

Then, the photon weight after the scattering should be

$$w_1 = w_0 \omega \quad (3.4.17)$$

The absorption (heating) weight should be

$$\Delta w = w_0 - w_1 = w_0 (1 - \omega) \quad (3.4.18)$$

This heating should be sampled at the randomly determined collision point.

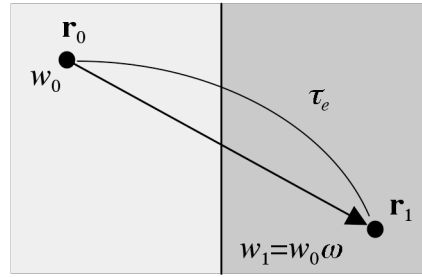


Fig. 3.4.2 Schematic of collision treatment: In the case where absorption is included in the collision.

b. Continuous absorption in path segments

All energy should be scattered if the absorption is treated separately from the collision. Representing the transmission function by $T(\tau)$,

$$\tau = \tau_s = \int_{\mathbf{r}_0 \rightarrow \mathbf{r}_1} \beta_s(t) dt; \quad t = |\mathbf{r}' - \mathbf{r}_0|. \quad (3.4.19)$$

If the photon transports by the path length l' in a medium with a homogeneous absorption coefficient, the photon weight should become

$$w' = w_0 e^{-\beta_a l'} \quad (3.4.20)$$

The weight that should be absorbed in the course of the path is given by

$$\Delta w = w' - w_0 = w_0 (1 - e^{-\beta_a l'}) \quad (3.4.21)$$

Where should the heating of this weight be deposited? If a single point for absorption is being sampled, representing the path length to the point by l_a , using (3.4.12c), we get

$$e^{-\beta_a l_a} = 1 - \rho (1 - e^{-\beta_a l'})$$

$$\therefore l_a = -\frac{\ln[1 - \rho + \rho e^{-\beta_a l'}]}{\beta_a} \quad (3.4.22)$$

In this way, the heating rate is sampled for every voxel that the model photon penetrates. This is a kind of collision-forcing method.

If one tries to calculate heating rates in a medium with a very small extinction coefficient, the method described above is better than the method of sampling the absorption at the collision points. The method in this subsection can sample the heating every time the photon penetrates a voxel, without depending on the degree of absorption. In contrast, with the method of sampling the heating at the collision point, the frequency of sampling is too low if the extinction coefficient is small. However, Iwabuchi (2006) pointed out that the two methods have almost the same efficiency if one uses the collision-forcing method based on the scaling transformation in combination with the method for sampling the heating at collision points. In addition, the method for sampling the heating at collision points is easy to implement in the code and can be used in combination with the maximum cross section (MCS) method (4.1). The method is thus recommended by the authors.

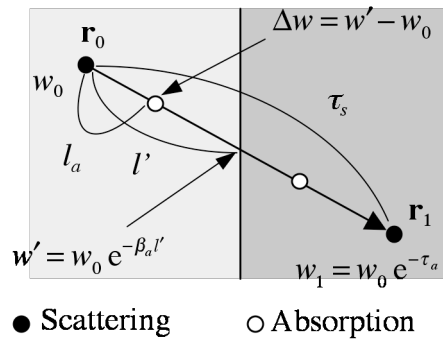


Fig. 3.4.3 Schematic for the treatment of collision: In a case where the absorption is calculated from the path length.

3.4.3 Treatment of mixed media

The actual atmosphere is composed of many component gases and particles. Several scattering/absorption components are mixed together, including Rayleigh scattering by gases, gaseous absorption, Mie scattering by aerosol particles and cloud water/ice particles, and scattering by larger particles such as raindrops, snowflakes, and graupel particles. From the microscale point of view, aerosols and hydrometeors are polydispersions of particles with various sizes, and their size distributions vary spatially and temporarily. As for the forest canopy, several kinds of leaves or leaves of various sizes are mixed together in each tree in the actual forest.

In the case where a medium is composed of N components, the optical properties β_e , β_a , β_s , ω , and P of the mixed media are given as follows:

$$\beta_e = \sum_{i=1}^N \tilde{\beta}_e(i), \beta_a = \sum_{i=1}^N \tilde{\beta}_a(i), \beta_s = \sum_{i=1}^N \tilde{\beta}_s(i) \quad (3.4.23)$$

$$\omega = \frac{\beta_s}{\beta_e} = \frac{\sum_{i=1}^N \tilde{\beta}_s(i)}{\sum_{i=1}^N \tilde{\beta}_e(i)} = \frac{\sum_{i=1}^N \tilde{\omega}(i) \tilde{\beta}_e(i)}{\sum_{i=1}^N \tilde{\beta}_e(i)} \quad (3.4.24)$$

$$P = \frac{\sum_{i=1}^N \tilde{\beta}_s(i) \tilde{P}(i)}{\beta_s} = \frac{\sum_{i=1}^N \tilde{\omega}(i) \tilde{\beta}_e(i) \tilde{P}(i)}{\sum_{i=1}^N \tilde{\omega}(i) \tilde{\beta}_e(i)} \quad (3.4.25)$$

where the following equations are derived for the extinction coefficients:

$$\begin{aligned} \beta_e &= \beta_a + \beta_s \\ \tilde{\beta}_e(i) &= \tilde{\beta}_a(i) + \tilde{\beta}_s(i) \end{aligned} \quad (3.4.26)$$

The determination of the random collision point should be based on the total extinction coefficient β_e , if one tries to model the radiative transfer in the mixed media by the MC method.

It is difficult to determine the scattering direction using the mixed phase function P at the voxel of the collision. This is because a very large amount of computer memory is required if one generates the phase function LUT for each voxel, because each phase function should be tabulated at 10,000 or more points. Note that the number of voxels is usually very large, as large as $200 \times 200 \times 50$ or more in a 3-D atmospheric radiation model! A resolution is to determine randomly a component i for scattering at the collision event using a random number and then to determine the scattering direction using the phase function $\tilde{P}(i)$ of the component. A phase function LUT is required with respect to the component (not to the voxel). The size distribution of particles varies voxel by voxel. Thus, in practice, an LUT is prepared for various components and various size distributions, and indexes for each voxel and each component are saved in

computer memory to refer to the type of phase function. In this case, $\tilde{P}(m(i))$ should be used instead of $\tilde{P}(i)$, where m is the index of the phase function LUT. By selecting the kind of component in the collision (absorption or scattering), for example, it is possible to sample the heating rate for each component.

If scattering and absorption are included in the “collision,” there are two possible ways to randomly determine the component: one is to select the kind of collision (scattering plus absorption), and the other is to select the kind of scattering. Both are physically correct and produce no bias.

a. To select the kind of collision

In this case, a random number determines a component i active for the collision. The probability of i is given as

$$P_{col}(i) = \frac{\tilde{\beta}_e(i)}{\beta_e}, \quad \sum_{i=1}^N P_{col}(i) = 1 \quad (3.4.27)$$

The single scattering albedo can differ by component. The photon weight just after the scattering should become

$$w' = w\tilde{\omega}(i) \quad (3.4.28)$$

The heating rate at this collision is

$$\Delta w = w(1 - \tilde{\omega}(i)) \quad (3.4.29)$$

That is, the heating rate differs by the randomly selected component i . This method results in large noise in heating rates and radiance (sampled by the LEM), because of varying the single scattering albedo by component. For example, let us consider a two-component mixture of gaseous absorption for $i = 1$ with $\tilde{\omega}(1) = 0$ and scattering due to cloud particles for $i = 2$ with $\tilde{\omega}(2) = 0.999999$. The sampled heating should be

$$\Delta w = \begin{cases} w & \text{for } i = 1 \\ w \times 10^{-6} & \text{for } i = 2 \end{cases} \quad (3.4.30)$$

If the scattering due to cloud particles is dominant, the gaseous absorption rarely occurs [$\tilde{\beta}_e(1) \ll \tilde{\beta}_e(2)$]; then, a very small heating due to cloud particles is usually sampled, whereas a significantly larger heating by a factor of 10^6 due to gaseous absorption is sampled rarely. This situation results in a very large noise in the integration result, and the convergence is too slow. That is why the authors do not recommend this method.

b. To select the kind of scattering

The probability of scattering is given simply by ω in (3.4.24). The weight just after the scattering should be

$$w' = w\omega \quad (3.4.31)$$

The heating rate should be

$$\Delta w = w(1 - \omega) \quad (3.4.32)$$

After scaling the weight in this way and sampling the heating, the active scattering component is determined randomly. The scattering probability for the i th component is

$$p_{sca}(i) = \frac{\tilde{\beta}_s(i)}{\beta_s} = \frac{\tilde{\omega}(i)\tilde{\beta}_e(i)}{\omega\beta_e} \text{ where } \sum_{i=1}^N p_{sca}(i) = 1 \quad (3.4.33)$$

The difference from the method using (3.4.27) is the use of a scattering coefficient instead of an extinction coefficient. It is easily understood from (3.4.31–32) that the weight and the heating sampled are always independent of the active component for the scattering. Since ω is uniquely given voxel by voxel, the constant rates for absorption and scattering should always be sampled at every voxel. This method is thus efficient.

3.4.4 Russian roulette method and photon-splitting method

The photon weight decreases at the collision event or in the course of transport in the absorption media. However, tracing photons with a very small weight is not effective for efficient computation. Therefore, the Russian roulette method is useful; the weight is randomly cut off if the weight is smaller than a prescribed threshold (Booth, 1985; Kawrakow and Rogers, 2001).

A random number is generated if the weight w is smaller than an arbitrary value W (can be >1), and then, the weight is modified as

$$w' = \begin{cases} 0 & \text{if } \rho_w \geq w/W \\ W & \text{if } \rho_w < w/W \end{cases} \quad (3.4.34)$$

If the new weight is 0, the model photon is “dead,” so tracing of the model photon terminates. In other words, the survival of the model photon is randomly determined. The probability of survival is w/W , and the total energy is conserved:

$$0 \times (1 - w/W) + W \times w/W = w \quad (3.4.35)$$

where the original energy is w . This method is the so-called Russian roulette method. It is usually reasonable to apply this method under the condition that the photon weight is small enough, e.g., $w < W/2$. This method is energy conservative and unbiased. It can be applied at

any step of the MC simulation and at any location in the model domain.

A similar energy conservative weight control method is the photon-splitting method, which splits a model photon into N model photons with the weight

$$w' = w/N \tag{3.4.36}$$

More generally, the divided weight is not necessarily the same. An application example is to split the model photon (photon packet) at the scattering event and redirect the subpackets into different directions. This photon-splitting method is indeed energy conservative and can be applied at any step of an MC simulation and at any location in the domain, without any bias.

Both methods are methods to control photon population and weights. Table 3.4.1 summarizes the characteristics of these two methods. When do these methods work well? The answer would depend on the importance of the radiative quantities of interest. If one needs to increase the frequency of sampling, then photon splitting works well. In contrast, if one needs to decrease the sampling frequency, the Russian roulette method is useful. If, for example, higher-order scattering is not important, then the Russian roulette method can reduce the photon population by setting W as large enough after the photon packet experiences several scattering events. The photon-splitting method is not required in the usual radiative transfer model for the atmosphere and canopy, and the method could add complexity to the simulation code.

Variance of the photon weight generally results in noise in the integrated quantities. The appropriate value for W used in the Russian roulette method would be between 0.1 and 5.

Table 3.4.1 Changes in the photon weight and population, due to the Russian roulette method and the photon-splitting method.

	Russian roulette	Photon splitting
Weight	increase (if it survives)	decrease
Population	decrease	increase

3.5 Scattering

When a photon enters the atmosphere or a plant, it interacts with atmospheric molecules, cloud particles, aerosols, leaves, stems, etc. The scattering is an electromagnetic interaction between them. We summarize the basic concept of light scattering for atmospheric molecules, aerosols, clouds, and leaves. Then, the MC modeling of these scattering events is described.

3.5.1 Scattering process

The description of atmospheric scattering follows that given by Hansen and Travis (1974) and Shibata (1999) and for leaf scattering follows that given by Shultis and Myneni (1988).

a. Atmospheric scattering processes

The scattering from spherical particles with homogeneous electromagnetic properties, such as a complex refractive index or complex electrical properties can be analytically introduced by Mie theory. The derivation of Mie theory is required to solve Maxwell's equation (differential equation) in 3-D space. The solution is described in the spherical harmonics function. The scattering intensities depend on a complex refractive index and size parameter x . Because details of the derivations of the electrical and magnetic vectors from Mie theory are discussed elsewhere, we skip the details of these derivations.

The size parameter x is defined by the ratio of the wavelength to the sphere's circular perimeter:

$$x = 2\pi a/\lambda \quad (3.5.1)$$

Based on this parameter, the scattering can be divided into three scattering domains: Rayleigh scattering ($x \ll 1$), aerosol and cloud particle scattering ($x \sim 1$), and geometrical optics scattering, such as from soil particles on the planetary surface ($x \gg 1$). As shown in Fig. 3.5.1, the z -axis is defined by the photon direction, and the electrical field vectors of the incident photon and scattering photon are expressed by the vector sum of the parallel direction with a plane included in the scattering angle (p components) and the perpendicular direction with a plane included in the scattering angle (s components). The incident electromagnetic wave is assumed to be a plane wave, and we only discuss the scattered electromagnetic wave that is sufficiently apart from the scattering media. In this case, the scattering electrical vector is expressed using the scattering matrix \mathbf{S} .

$$\begin{pmatrix} E_p \\ E_s \end{pmatrix} = \frac{\exp(-ikr)}{ikr} \begin{pmatrix} S_2 & S_3 \\ S_4 & S_1 \end{pmatrix} \begin{pmatrix} E_{0p} \\ E_{0s} \end{pmatrix} \quad (3.5.2)$$

where k and r are the wave number of the incident wave and distance from the scattering point,

respectively. The ratio of the scattering to incident intensity, or the so-called single scattering albedo ω , is expressed by

$$\omega = \frac{\beta_s}{\beta_e} \quad (3.5.3)$$

where β_s and β_e are the scattering and extinction coefficients in a unit volume (m^{-1}).

Atmospheric molecular scattering (Rayleigh scattering)

The ion radius of an atmospheric molecule is approximately ~ 0.1 nm, which is sufficiently small compared with the photon wavelength (~ 1 μm). In this case, since the electrical vector near a single molecule can be assumed to be spatially homogeneous, the electrical field around the molecule induced by the incident wave becomes a dipole field. Scattered photons by the Rayleigh scattering are a radiation corresponding to the vibration from the time-dependent dipole field. When we use the polarization factor (α_p), the scattering matrix for Rayleigh scattering is written by

$$S = \frac{ik^3\alpha_p}{4\pi\epsilon_0} \begin{pmatrix} \cos\Theta & 0 \\ 0 & 1 \end{pmatrix} \quad (3.5.4)$$

The differential scattering cross section, which is defined by the ratio of the scattering intensity to the incident intensity, is expressed by

$$\frac{d\sigma_s}{d\Omega} = r^2 \frac{|E_p|^2 + |E_s|^2}{|E_{0p}|^2 + |E_{0s}|^2} = \left(\frac{\alpha_p k^2}{4\pi\epsilon_0} \right)^2 \frac{1 + \cos^2\Theta}{2} \quad (3.5.5)$$

We assume that E_{0p} is equal to E_{0s} . The phase function, which is defined by the spatial distribution of the scattering intensity, is expressed using the differential scattering cross section (3.5.5) normalized by the cross section:

$$p(\Theta) = \frac{4\pi}{\sigma_s} \frac{d\sigma_s}{d\Omega} = \frac{3}{4} (1 + \cos^2\Theta) \quad (3.5.6)$$

The phase function requires the following normalization condition:

$$\frac{1}{4\pi} \int_{4\pi} p(\Theta) d\Omega = 1 \quad (3.5.7)$$

In the case of Rayleigh scattering, the phase functions for all molecules are equal. Therefore, the phase function of the ensemble of the molecules is also equal to (3.5.6). Also, since Rayleigh scattering is a perfect elastic scattering, the extinction coefficient is equal to the scattering coefficient, and the single scattering albedo is 1.

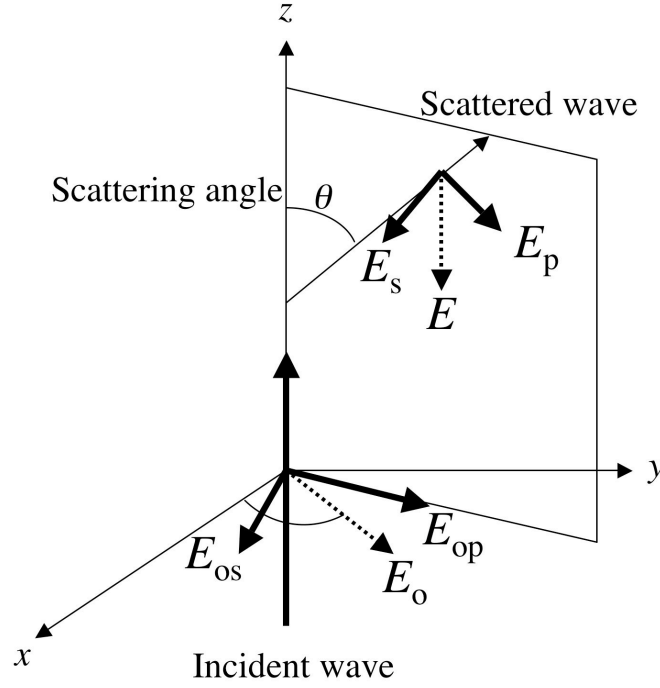


Fig. 3.5.1 Relationship between electrical vectors of incident wave and scattering wave.

Aerosol and cloud scattering

For aerosol and cloud particles, the components S_1 and S_2 in the scattering matrix \mathbf{S} are expressed by

$$S_1(\Theta) = \sum_{n=1}^{\infty} \frac{2n+1}{n(n+1)} \left[a_n(x) \frac{P_n^1(\cos\Theta)}{\sin\Theta} + b_n(x) \frac{dP_n^1(\cos\Theta)}{d\Theta} \right] \quad (3.5.8)$$

$$S_2(\Theta) = \sum_{n=1}^{\infty} \frac{2n+1}{n(n+1)} \left[b_n(x) \frac{P_n^1(\cos\Theta)}{\sin\Theta} + a_n(x) \frac{dP_n^1(\cos\Theta)}{d\Theta} \right] \quad (3.5.9)$$

where P_n^1 is an associated Legendre function and the coefficients a_n and b_n are functions of the size parameter x . When the incident wave is solar radiation and E_{op} is equal to E_{os} , the differential scattering cross section can be calculated by

$$\frac{d\sigma_s}{d\Omega} = r^2 \frac{|E_p|^2 + |E_s|^2}{|E_{op}|^2 + |E_{os}|^2} = \frac{|S_1(\Theta)|^2 + |S_2(\Theta)|^2}{2k^2} \quad (3.5.10)$$

Therefore, the single particle phase function is expressed by

$$P(\Theta) = \frac{4\pi}{\sigma_s} \frac{d\sigma_s}{d\Omega} = \frac{2\pi}{\sigma_s k^2} (|S_1(\Theta)|^2 + |S_2(\Theta)|^2) \quad (3.5.11)$$

The scattering phase function P from the ensemble composed of various sizes of particles is calculated by the weighting average of the phase function corresponding to the particle number density $n(a)$ and scattering cross section as a function of the particle radius (a):

$$P(\Theta) = \frac{1}{\beta_s} \int_{a_{min}}^{a_{max}} p(\Theta) \sigma_s(a) n(a) da \quad (3.5.12)$$

where β_s is calculated by

$$\beta_s = \int_{a_{min}}^{a_{max}} \sigma_s(a) n(a) da \quad (3.5.13)$$

b. Scattering from leaves

There are several ways of modeling the scattering from leaf canopies. We describe the photon scattering phenomenon from a disk-like leaf using the geometrical optics approach. The polarization and diffraction are ignored. The reflectance and transmittance from a leaf are modeled using the Lambertian law (bi-Lambertian). Then, the phase function from a single leaf is expressed using the normal vector of the leaf (Ω_L), vector for the incident direction (Ω'), and vector for the scattering direction (Ω):

$$p(\Omega' \rightarrow \Omega; \Omega_L) = \frac{R_L |\Omega_L \cdot \Omega|}{\omega_0 \pi} \quad \text{if } (\Omega_L \cdot \Omega)(\Omega_L \cdot \Omega') < 0 \quad (3.5.14a)$$

$$p(\Omega' \rightarrow \Omega; \Omega_L) = \frac{T_L |\Omega_L \cdot \Omega|}{\omega_0 \pi} \quad \text{if } (\Omega_L \cdot \Omega)(\Omega_L \cdot \Omega') > 0 \quad (3.5.14b)$$

where the single scattering albedo (ω_0) is expressed by the sum of the spherical reflectance and transmittance of the leaf:

$$\omega_0 = R_L + T_L \quad (3.5.15)$$

The scattering of an ensemble of leaves with different leaf angles is calculated by the weighting average of the single leaf phase function corresponding to the leaf angle distribution function $g_L(\Omega_L)$ and the scattering factor ($|\Omega \cdot \Omega_L|$):

$$P(\Omega' \rightarrow \Omega; \Omega_L) = \frac{2}{G(\Omega')} \int_{4\pi} g_L(\Omega_L) |\Omega' \cdot \Omega_L| p(\Omega' \rightarrow \Omega; \Omega_L) d\Omega_L \quad (3.5.16)$$

Here, $g_L(\Omega_L)$ can be normalized by

$$\frac{1}{2\pi} \int_{2\pi} g_L(\Omega_L) d\Omega_L = 1 \quad (3.5.17)$$

G is a projected area of the leaves toward the Ω' direction for a unit volume and unit leaf area:

$$G(\Omega') = \frac{1}{2\pi} \int_{2\pi} g_L(\Omega_L) |\Omega' \cdot \Omega_L| d\Omega_L \quad (3.5.18)$$

Meanwhile, the phase function is analytically calculated when the leaf angle distribution is constant ($g_L(\Omega_L) = 1$):

$$P(\Theta) = \frac{8}{3\pi} (\sin \Theta - \Theta \cos \Theta) + \frac{8T_L}{3\omega_0} \cos \Theta \quad (3.5.19)$$

The phase function of a spherical atmospheric particle is a function of the scattering angle. In leaf canopies, however, the phase function is generally a function of the incident and scattering directions. The uniform leaf angle distribution case (3.5.19) is the only exception, with the phase function depending only on the scattering angle.

3.5.2 Modeling of scattering by MC method

a. Weight of photon after scattering (analog/non-analog absorption method)

If the absorption of the scattering media is not zero ($1 - \omega$), the photon energy is partially absorbed. In an MC simulation, two methods to express this event exist. In the analog absorption method, the photon tracing will be stopped when the random number $\rho < (1 - \omega)$. In the non-analog absorption method, the weight of the photon is reduced by the rate of absorption. In the latter case, the photon weight is calculated by the single scattering albedo (ω):

$$w_{i+1} = \omega w_i \quad (3.5.20)$$

b. Determination of scattering direction

The scattering direction of the photon should be determined by following the phase function. If the phase function is only a function of the scattering angle (Θ), the azimuth angle Φ relative to the scattering coordinate is expressed using the random number ρ_Φ (see Appendix A6):

$$\Phi = 2\pi\rho_\Phi \quad (3.5.21)$$

The scattering angle is calculated by (for more details, see Appendix A5)

$$\frac{1}{4\pi} \int_{4\pi} P(\Theta) d\Omega = \frac{1}{2} \int_0^\Theta P(\Theta) \sin \Theta d\Theta = \rho_\Theta \quad (3.5.22)$$

(3.5.22) is sometimes calculated (or Θ is sometimes obtained) analytically (e.g., isotropic scattering, Rayleigh scattering).

Generally speaking, it is rare to obtain the form of $\Theta = f(\rho_\Theta)$ analytically. Even if it is feasible to obtain the form of $\Theta = f(\rho_\Theta)$, it may require vast computation. In such cases, the LUT method and rejection method are practical.

In the LUT method, the relationship between ρ_Θ and Θ is prepared prior to starting the MC simulation. Then, the scattering angle Θ is determined by interpolating the LUT values corresponding to ρ_Θ . This method is suitable for the Mie scattering of aerosol and cloud particles and leaf scattering. Figure 3.5.2 shows an example of the relationship between the random number and scattering angles (Rayleigh scattering (3.5.6), aerosol scattering (3.5.12), and leaf scattering (3.5.19)).

In the rejection method, first, the scattering angle Θ is determined by the pseudorandom number, according to a comparison function $R(\Theta)$. Then, the ratio $P(\Theta)/R(\Theta)$ is compared with the pseudorandom number in $[0, 1]$. When the random number is larger than $P(\Theta)/R(\Theta)$, the scattering angle is reflected. This procedure is continued until the scattering direction is accepted (see 3.1). In the rejection method, the computation efficiency depends on the efficiency of the comparison function. The rejection method is an accurate method. When the size of the LUT is constrained by the computational resource, this method would be a good solution.

In leaf scattering, the scattering phase function is a function of the photon incident direction (θ_i, φ_i) and scattering direction, except for some special cases. In this case, the LUT becomes 3-D $(\theta_i, \Theta, \varphi_r)$ when we use the relative azimuth angle $(\varphi_r = \varphi_i - \Phi)$.

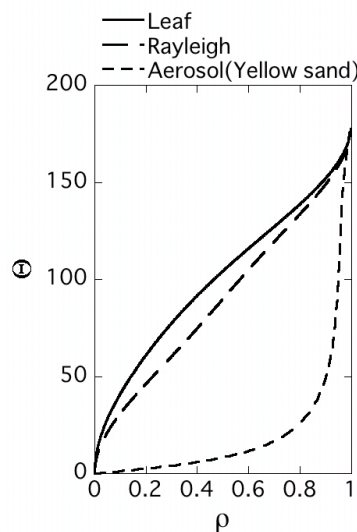


Fig. 3.5.2 Relationship between pseudorandom number and scattering angle. Aerosol (yellow sand, $r_e = 0.375 \mu\text{m}$, $\lambda = 0.575 \mu\text{m}$, $n = 1.54999995 + 0.00433298014i$), leaf (reflectance = 0.2; transmittance = 0.1), and Rayleigh scattering.

Isotropic scattering

In an isotropic scattering case,

$$P(\Theta) = 1 \quad (3.5.23)$$

Therefore, (3.5.22) can be analytically solved. Then, the scattering angle Θ is obtained by

$$\cos\Theta = 1 - 2\rho_{\Theta} \quad (3.5.24)$$

Rayleigh scattering

In a Rayleigh scattering case, the phase function is given by (3.5.6). When $\cos\Theta = \mu$, the relationship between μ and ρ_{Θ} is calculated by

$$\mu^3 + 3\mu - 4 + 8\rho_{\Theta} = 0 \quad (3.5.25)$$

As a solution of the third-order equation, we obtain

$$\begin{aligned} \mu &= X - \frac{1}{X} \\ X &= \sqrt[3]{-(4\rho_{\Theta} - 2) + \sqrt{(4\rho_{\Theta} - 2)^2 + 1}} \end{aligned} \quad (3.5.26)$$

The solution is analytically calculated by (3.5.26). However, it requires time-consuming calculation. On the other hand, the rejection method is efficient. The maximum of the Rayleigh scattering phase function is $3/2$. Therefore, we can use the following comparison function:

$$R(\Theta) = 3/2$$

First, the scattering angle is determined by (3.5.24). The probability to follow the phase function is given by

$$\begin{aligned} \frac{P(\Theta)}{R(\Theta)} &= \frac{3/4(1 + \cos^2 \Theta)}{3/2} \\ &= 1 - 2\rho_{\Theta}(1 - \rho_{\Theta}) \end{aligned}$$

The rejection or selection is determined using another random number ρ_r . Therefore, we use two random numbers every time. One is used to determine the scattering angle, and the other is used to judge the following criteria:

$$\begin{aligned} \rho_r &\leq 1 - 2\rho_{\Theta}(1 - \rho_{\Theta}) \\ \therefore \rho_r' &\geq 2\rho_{\Theta}(1 - \rho_{\Theta}) \end{aligned}$$

On average, the scattering angle is determined by 1.5 iterations.

Leaf scattering: A step-by-step determination method

In this method, the scattering direction is determined by the following three steps:

- 1) Determination of the normal vector $\mathbf{\Omega}_L$ of the leaf surface
- 2) Modification of the probability of the leaf normal vector $\mathbf{\Omega}_L$ to be proportional to $|\mathbf{\Omega} \cdot \mathbf{\Omega}_L|$
- 3) Determination of the scattering angle by $\mathbf{\Omega}_L$ and a random number

This method is also applicable to non-spherical particles, such as ice crystals. This method is similar to the method of Antyufeev and Marshak (1990). In their method, a leaf normal vector is determined by a new probability function, which is easily calculated. Then, the weight of the photon is modified to follow the actual distribution. Here, we describe a method to calculate the scattering angle without any changes in photon weight.

1. Determination of normal vector $\mathbf{\Omega}_L$ of leaf surface using pseudorandom number

In most cases, since the leaf angle distribution is random in the azimuth direction and it only depends on the zenith angle, the azimuth angle φ_L is easily determined by (3.5.21). The zenith angle is determined by the following equation:

$$\frac{1}{2\pi} \int_0^{\theta_L} g_L(\theta_L) \sin \theta_L d\theta_L = \rho_{\theta_L} \quad (3.5.27)$$

In this method, an LUT is first prepared using (3.5.27). Then θ_L is determined by the LUT. Under some conditions, an analytical solution is obtained (e.g., $g_L = \cos(\theta_L)$). Also, it is possible to use the rejection method.

2. Modification of probability of leaf normal vector $\mathbf{\Omega}_L$ to be proportional to $|\mathbf{\Omega} \cdot \mathbf{\Omega}_L|$

The scattering angle determined by step 1 is modified to follow the ratio of the projected area to the leaf normal direction $\mathbf{\Omega}_L$ with respect to $\mathbf{\Omega}'$. In this procedure, the rejection method is the best method. In this case, when θ_p is defined as the angle between the incident direction and leaf normal direction, θ_p is expressed by

$$|\mathbf{\Omega}' \cdot \mathbf{\Omega}_L| = \cos \theta_p \quad (3.5.28)$$

Then, it is compared with the pseudorandom number ρ :

When $\cos \theta_p \geq \rho$, the leaf angle determined by procedure 1 is accepted.

When $\cos \theta_p < \rho$, the leaf angle determined by procedure 1 is rejected and we return to procedure 1.

3. Scattering angle is determined by Ω_L and random number

Once the leaf normal vector Ω_L is determined by procedures 1 and 2, the leaf reflectance and transmittance are determined. The criteria of the reflectance and transmittance are as follows:

$$\text{Reflection } \frac{R_L}{R_L + T_L} \geq \rho; \text{Transmission } \frac{R_L}{R_L + T_L} < \rho \quad (3.5.29)$$

Then, if the leaf is a bi-Lambertian surface, the scattering direction is determined by

$$\mu = \sqrt{\rho_\theta}, \phi = 2\pi\rho_\phi \quad (\mu = \cos(\theta)) \quad (3.5.30)$$

In a reflection case, the scattering angle is accepted if $\Omega' \cdot \Omega_L < 0$. If $\Omega' \cdot \Omega_L \geq 0$, $-\Omega'$ is employed as a scattering direction. In a transmission case, the scattering angle is accepted if $\Omega' \cdot \Omega_L \geq 0$. If $\Omega' \cdot \Omega_L < 0$, $-\Omega'$ is employed.

This method does not require a large LUT. It is effective when the leaf angle distribution depends on the individual tree and position. In the non-Lambertian leaf surface case, the computation is rather complex.

3.6 Reflection

In this section, we describe the general treatment of reflection in bidirectional reflectance distribution function (BRDF) models.

3.6.1 Definitions

a. BRDF

The BRDF is a distribution function for reflectance that depends on the incident and reflected directions. The definition of the BRDF (R) is

$$R(\theta_0, \phi_0, \theta_1, \phi_1) = \frac{dI_1(\theta_1, \phi_1)}{I_0(\theta_0, \phi_0) \cos \theta_0 d\xi} \quad (3.6.1a)$$

where (θ_0, ϕ_0) and (θ_1, ϕ_1) are the incident direction and reflectance direction, respectively. Also, $d\xi$ and I_0, dI_1 are the solid angle, and incident and reflected radiation intensities (Thomas and Stamnes, 1999).

The reflected radiation intensity dI_1 is expressed in the differential form because it corresponds to the solid angle of the incident radiation $d\xi$. When the incident radiation is integrated over all directions, it becomes the radiation intensity for the (θ_1, ϕ_1) direction. Thus,

$$d\xi = d\phi_0 d\cos\theta_0$$

then

$$\begin{aligned} I_1(\theta_1, \phi_1) &= \int dI_1(\theta_1, \phi_1) \\ &= \int_0^{2\pi} d\phi_0 \int_0^1 d\cos\theta_0 R(\theta_0, \phi_0, \theta_1, \phi_1) I_0(\theta_0, \phi_0) \cos\theta_0 \end{aligned} \quad (3.6.1b)$$

As shown in (3.6.1a), the BRDF is defined by the radiance divided by irradiance. Therefore, it is not normalized. Indeed, the BRDF becomes infinite for a flat specular surface. The unit for the BRDF is sr^{-1} .

The BRDF is usually expressed by three parameters, using the relative azimuth angle ϕ :

$$\begin{aligned} R(\theta_0, \phi_0, \theta_1, \phi_1) &= R(\theta_0, \theta_1, \phi) \\ \phi &= \begin{cases} |\phi_0 - \phi_1| & \text{if } |\phi_0 - \phi_1| \leq \pi \\ 2\pi - |\phi_0 - \phi_1| & \text{if } |\phi_0 - \phi_1| > \pi \end{cases} \end{aligned} \quad (3.6.2)$$

It should be noted that the BRDF is sometimes defined in a different form. In particular, the bidirectional reflectance factor (BRF) is defined as the product of (3.6.2) and π . This is sometimes confusing.

b. Relationship between BRDF and albedo

The albedo is defined as the fraction of the reflected irradiance to the incident irradiance. This is a non-dimensional parameter and is always less than zero. The albedo $\alpha(\theta_0, \phi_0)$ depends on the incident direction and is closely related to the BRDF:

$$\alpha(\mu_0, \phi_0) = \int_0^1 \int_0^{2\pi} R(\mu_0, \phi_0, \mu_1, \phi_1) \mu_1 d\phi_1 d\mu_1 \quad (3.6.3)$$

where $\mu_* = \cos \theta_*$.

c. Bidirectional reflectance probability function (BR-PDF)

The following function shows the 2-D PDF of the reflected irradiance in a horizontal BRDF plane:

$$P(\mu_0, \phi_0; \mu_1, \phi_1) \equiv \frac{R(\mu_0, \phi_0, \mu_1, \phi_1) \mu_1}{\alpha(\mu_0, \phi_0)} \quad (3.6.4)$$

We define this function as the “bidirectional reflectance probability density function (BR-PDF).” This function is normalized as

$$\int_0^1 \int_0^{2\pi} P(\mu_0, \phi_0; \mu_1, \phi_1) d\phi_1 d\mu_1 = 1 \quad (3.6.5)$$

d. Isotropic reflection

When the BRDF has no directionality, the reflection is called Lambertian reflection. In this case, the albedo is also constant.

$$R(\mu_0, \phi_0, \mu_1, \phi_1) = R_0 \quad (3.6.6)$$

$$\alpha(\mu_0, \phi_0) = R_0 \int_0^1 \int_0^{2\pi} \mu_1 d\phi_1 d\mu_1 = \pi R_0 \quad (3.6.7a)$$

$$\therefore R_0 = \frac{\alpha}{\pi} \quad (3.6.7b)$$

The BR-PDF becomes

$$P(\mu_0, \phi_0, \mu_1, \phi_1) = \frac{\mu_1}{\pi} \quad (3.6.8)$$

It is easily confirmed that Eq. (3.6.8) meets the normalization (3.6.5).

e. Anisotropy of BRDF

There are several ways to measure the anisotropy of the BRDF. For example, the momentum μ_1 , which is used as an anisotropy factor for the scattering phase function, is one possibility.

However, this factor implicitly assumes the non-anisotropy for the azimuth direction. Here, we introduce χ to measure the anisotropy of the BRDF by calculating the average of the absolute deviation. The average deviation between P (BR-PDF of the BRDF model) and isotropic case (3.6.8) is expressed by

$$\chi = \frac{1}{2} \int_0^1 \int_0^{2\pi} \left| P(\mu_0, \phi_0, \mu_1, \phi_1) - \frac{\mu_1}{\pi} \right| d\phi_1 d\mu_1 \quad (3.6.9)$$

This is a dimensionless parameter with a range of [0–1]. In an isotropic case, $\chi = 0$. In the specular reflection case (BRDF is a Dirac delta function), $\chi = 1$.

f. Azimuthally averaged BRDF

An azimuthally averaged reflection function is defined by

$$\bar{R}(\mu_0, \phi_0, \mu_1) \equiv \frac{1}{2\pi} \int_0^{2\pi} R(\mu_0, \phi_0, \mu_1, \phi_1) d\phi_1 \quad (3.6.10)$$

3.6.2 Reflection from surface with arbitrary BRDF

For simplicity, only a horizontal plane is considered. There are several methods for the treatment of reflection. For example, the reflection direction is first determined and the weight of the photon is then changed (weighting method). However, this method is not cost effective. The change in the photon weight means that the irradiances of the modeled photons differ from each other. After multiple reflections, the weight of the photon disperses from 0 to infinity. That causes large noise in the MC integration.

In the MC simulation discussed in this report, the number of photons in the finite domain is conserved. Each model photon has a constant irradiance for a horizontal plane. Without absorption, the irradiance does not change. In the reflection case, the reflected direction should be determined not to horizontally change the irradiance of a single modeled photon. Here, we consider a method where the weight of the photon does not change after the reflection. In this case, the weight of the photon from the direction (μ_0, ϕ_0) is determined by

$$w' = w\alpha(\mu_0, \phi_0) \quad (3.6.11)$$

This equation indicates that the weight of the photon does not change by the reflected direction. α is always less than 1.

Next, a determination of the reflected direction will be discussed. The reflected direction (μ_1, ϕ_1) is determined by following the BR-PDF. Let μ_1 be

$$p(\mu_1) = \int_0^{2\pi} P(\mu_1, \phi_1) d\phi_1 \quad (3.6.12)$$

Then, from Eq. (3.6.5), $p(\mu_1)$ meets the following normalization:

$$\int_0^1 p(\mu_1) d\mu_1 = 1 \quad (3.6.13)$$

μ_1 is solved by

$$\int_0^{\mu_1} p(\mu'_1) d\mu'_1 = \rho_{\mu_1} \quad (3.6.14)$$

where ρ_{μ_1} is a random number. Generally, the left term of (3.6.14) cannot be analytically solved. Therefore, the LUT method or rejection method can be used. ϕ_1 can be determined by the following equation:

$$\frac{\int_0^{\phi_1} P(\mu_1, \phi'_1) d\phi'_1}{\int_0^{2\pi} P(\mu_1, \phi'_1) d\phi'_1} = \rho_{\phi_1} \quad (3.6.15)$$

Just as is the case with μ_1 , the left term of this equation is not analytically solved. Therefore, the LUT method or rejection method can be used.

It should be noted that the PDF defined in (3.6.15) is a product of Eq. (3.6.4) and μ_1 . Then, (3.6.15) can be only applied to a horizontal surface. When considering a sloped surface, it is necessary to determine the direction using a PDF not multiplied by μ_1 . Then, the rejection method is applied by using the cosine to the horizontal surface (we do not describe this in detail).

The radiance is commonly calculated by the LEM (see 3.9). The scattering, reflection, and emission processes can be sampled by several methods. In this report, we calculate these by the following procedures:

1. Scaling the weight using (3.6.11)
2. Rescaling the weight by Russian roulette
3. Radiance sampling by LEM
4. Determination of direction after events

If the order of these procedures changes, the formulation changes slightly. However, the above order is recommended because it is preferable to execute the Russian roulette before the LEM to reduce the variation in weight. A photon with a weight of 0.01 is clearly less important than that with a weight of 1.0. It is a waste of CPU time to execute the LEM for a photon with a small weight.

In the sloped surface case, first, the reflection direction is determined along coordinates that are normal to the slope; then, the direction is transformed into Cartesian coordinates. For example, let the slope surface normal be $\mathbf{n}(\Theta, \Phi)$ and the incident direction be $\mathbf{\Omega}(\theta, \phi)$. The incident angle relative to the slope surface normal $\mathbf{\Omega}'(\theta', \phi')$ is a vector where $\mathbf{\Omega}(\theta, \phi)$ is rotated $-\Phi$ toward the z -axis and is then rotated $-\Theta$ toward the y -axis. Then, the weight scaling is executed just as on the case for a horizontal surface. Finally, a coordinate transformation in the reverse mode is executed and the direction vector is determined for Cartesian coordinates.

3.6.3 Isotropic reflection: Lambertian reflection

Here, we describe the determination method for the reflection direction in isotropic scattering.

a. Isotropic scattering for horizontal surface

When we consider the isotropic reflection from a horizontal surface with the solid angle ξ , the PDF of the reflected direction is normalized by

$$\frac{1}{\pi} \int_{2\pi} \cos\theta d\xi = \frac{1}{\pi} \int_0^{2\pi} \int_0^1 \cos\theta d\cos\theta d\phi = 1 \quad (3.6.16)$$

The reflected direction for the azimuth direction is uniform. Therefore, ϕ is determined by

$$\phi = 2\pi\rho_\phi \quad (3.6.17)$$

The following is a method to determine the zenith angle.

Analytical method

The zenith angle of the reflection direction θ can be calculated using the random number ρ :

$$\frac{1}{\pi} \int_0^{2\pi} \int_0^{\cos\theta} \cos\theta' d\cos\theta' d\phi = \rho' \quad (3.6.18)$$

$$\therefore \cos^2\theta = 1 - \rho' \equiv \rho_\theta$$

$$\therefore \cos\theta = \sqrt{\rho_\theta} \quad (3.6.19)$$

Rejection method

The direction is first determined isotropically:

$$\frac{1}{2\pi} \int_0^{2\pi} d\phi \int_0^{\cos\theta} d\cos\theta' = \rho_\theta \quad (3.6.20)$$

$$\therefore \cos\theta = \rho_\theta \quad (3.6.21)$$

Then, the $\cos\theta$ dependency of the direction is determined by the rejection method. This can be achieved by using an additional random number:

$$\begin{cases} \text{If } \rho < |\cos\theta|, \text{ finish} \\ \text{If } \rho \geq |\cos\theta|, \text{ rejection} \end{cases} \quad (3.6.22)$$

If rejection is selected, the direction is again calculated by (3.6.21). The rejection probability is 1/2. Therefore, on average, the direction is determined in 2 cycles of the procedures. This method requires more random numbers than the analytical method. However, it does not require

calculating the square root. If the fast algorithm of the random number generator is used, the rejection method may be faster than the analytical method.

Consequently, both the analytical method and rejection method are practical. The rejection method is easily applicable to the arbitrary shape of the BRDF.

b. Isotropic reflection for arbitrary slope surface

In the Lambertian case, the PDF of the reflected direction is independent of the incident angle. Therefore, the same method as for the horizontal surface is used (analytical or rejection method) to calculate the zenith and azimuth angles relative to the normal vector of the slope surface. Then, the direction relative to the Cartesian coordinates is calculated by coordinate transformation.

Let the zenith and azimuth angles of the reflected direction relative to the slope normal $\mathbf{n}(\Theta, \Phi)$ be $\hat{\theta}, \hat{\phi}$, respectively. Then, the PDF of the reflected direction is normalized by

$$\frac{1}{\pi} \int_{2\pi} |\cos \hat{\theta}| d\xi = \frac{1}{\pi} \int_0^{2\pi} \int_0^1 |\cos \hat{\theta}| d \cos \hat{\theta} d\hat{\phi} = 1 \quad (3.6.23)$$

Therefore, $\hat{\theta}, \hat{\phi}$ can be calculated as well as a horizontal surface.

The reflected direction in Cartesian coordinates can be calculated using the same formula as the scattering (Appendix A5.2):

$$\mathbf{\Omega} = \cos \hat{\theta} \mathbf{n} + \sin \hat{\theta} \left[\cos \hat{\phi} \begin{pmatrix} \cos \Theta \cos \Phi \\ \cos \Theta \sin \Phi \\ -\sin \Theta \end{pmatrix} + \sin \hat{\phi} \begin{pmatrix} -\sin \Phi \\ \cos \Phi \\ 0 \end{pmatrix} \right] \quad (3.6.24)$$

c. Isotropic reflection from surface perpendicular to a horizontal surface

A surface that is perpendicular to a horizontal surface is a special case of isotropic reflection for an arbitrary slope surface. In this case, $\Theta = \pi/2$, $\sin \Theta = 1$, $\cos \Theta = 0$ are substituted in (3.6.24). Then, we obtain

$$\begin{aligned} \mathbf{\Omega} &= \cos \hat{\theta} \begin{pmatrix} \cos \Phi \\ \sin \Phi \\ 0 \end{pmatrix} + \sin \hat{\theta} \left[\cos \hat{\phi} \begin{pmatrix} 0 \\ 0 \\ -1 \end{pmatrix} + \sin \hat{\phi} \begin{pmatrix} -\sin \Phi \\ \cos \Phi \\ 0 \end{pmatrix} \right] \\ &= \begin{pmatrix} \cos \hat{\theta} \cos \Phi - \sin \hat{\theta} \sin \hat{\phi} \sin \Phi \\ \cos \hat{\theta} \sin \Phi + \sin \hat{\theta} \sin \hat{\phi} \cos \Phi \\ -\sin \hat{\theta} \cos \hat{\phi} \end{pmatrix} \end{aligned} \quad (3.6.25)$$

3.6.4 Diffuse-specular mixture model: DSM model

Here, we describe the diffuse-specular mixture model (DSM model). The direction of specular reflection is determined from surface roughness, which is derived from the modeled distribution of microfacets. Since surface roughness varies with the surface wind speed in the case of a water surface, it is modeled by the method described here. The BRDF and albedo are expressed by

$$R(\mu_0, \phi_0, \mu_1, \phi_1) = f_d R_d + (1 - f_d) R_s(\mu_0, \phi_0, \mu_1, \phi_1) \quad (3.6.35a)$$

$$\alpha(\mu_0) = f_d \alpha_d + (1 - f_d) \alpha_s(\mu_0) \quad (3.6.35b)$$

where f_d , R_d , and R_s are the fraction of diffuse reflection, and the BRDFs of diffuse and specular reflections. α_d and α_s are the albedos of the diffuse and specular surfaces, respectively.

In the case of diffuse reflection, the following relationship exists:

$$R_d = \frac{\alpha_d}{\pi} \quad (3.6.36)$$

a. Specular reflection with surface roughness

Here, we introduce the water surface reflection model by Nakajima and Tanaka (1983). The angle 2β between the reverse direction of the photon incident direction $\mathbf{\Omega}_0 = (\mu_0, \phi_0)^T$ and reflection $\mathbf{\Omega}_1 = (\mu_1, \phi_1)^T$ is expressed by

$$\cos 2\beta = \mathbf{\Omega}_0 \cdot \mathbf{\Omega}_1 \quad (3.6.37a)$$

$$\cos \beta = \sqrt{\frac{1}{2}(1 + \mathbf{\Omega}_0 \cdot \mathbf{\Omega}_1)} \quad (3.6.37b)$$

Also, the Fresnel reflectance is expressed by $R_F(\beta)$. The direction of a microfacet of $\mathbf{\Omega}_n = (\mu_n, \phi_n)^T$ has the following relationship:

$$\mathbf{\Omega}_n = \frac{\mathbf{\Omega}_0 + \mathbf{\Omega}_1}{\|\mathbf{\Omega}_0 + \mathbf{\Omega}_1\|} \quad (3.6.38a)$$

$$\mu_n = \frac{\mu_0 + \mu_1}{2 \cos \beta} = \frac{\mu_0 + \mu_1}{\sqrt{2(1 + \mathbf{\Omega}_0 \cdot \mathbf{\Omega}_1)}} \quad (3.6.38b)$$

$$\tan^2 \theta_n = \frac{1 - \mu_n^2}{\mu_n^2} = (\partial z / \partial x)^2 + (\partial z / \partial y)^2 \quad (3.6.38c)$$

The slope of the microfacet is given by a 2-D Gaussian distribution and isotropic over the azimuth direction:

$$P\left(\frac{\partial z}{\partial x}, \frac{\partial z}{\partial y}\right) = \frac{1}{\pi \sigma^2} \exp\left[-\frac{(\partial z / \partial x)^2 + (\partial z / \partial y)^2}{\sigma^2}\right] \quad (3.6.39a)$$

$$p(\mu_n) = \frac{1}{\pi\sigma^2\mu_n^3} \exp\left(-\frac{1-\mu_n^2}{\sigma^2\mu_n^2}\right) \quad (3.6.39b)$$

The BRDF is expressed by

$$R_s(\mu_0, \phi_0, \mu_1, \phi_1) = \frac{R_F(\beta)}{4\mu_0\mu_1\mu_n} p(\mu_n) f_s(\mu_0, \mu_1) \quad (3.6.40)$$

where f_s is a shadowing factor:

$$f_s(\mu_0, \mu_1) = \frac{1}{1 + F(\mu_0) + F(\mu_1)} \quad (3.6.41a)$$

$$F(\mu_*) = \frac{1}{2} \left[\frac{\exp(-v_*^2)}{\sqrt{\pi}v_*^2} - \operatorname{erfc}(v_*) \right] \quad (3.6.41b)$$

$$v_* = \frac{\mu_*}{\sigma\sqrt{1-\mu_*^2}} \quad (3.6.41c)$$

erfc is the complementary error function

$$\operatorname{erfc}(v_*) = \frac{2}{\sqrt{\pi}} \int_{v_*}^{\infty} e^{-t^2} dt \quad (3.6.41d)$$

The slope σ is given following the airborne measurements (Nakajima & Tanaka, 1983):

$$\sigma^2 = 0.00534 u_{10} \quad (3.6.42a)$$

Cox & Munk (1954) proposed

$$\sigma^2 = 0.00512 u_{10} + 0.003 \quad (3.6.42b)$$

b. Albedo of DSM model

The albedo of the DSM model can be calculated by Eq. (3.6.35). Here, the unknown parameter is the albedo of the specular reflection. The albedo of a completely flat surface ($\sigma = 0$) is

$$\alpha_s(\mu_0) = R_F(\theta_0) \quad (3.6.43)$$

The albedo of a rough surface ($\sigma > 0$) can be calculated by integrating the solid angle ξ over the direction $(\mu_0, \phi_0 + \pi)$:

$$\begin{aligned} \alpha_s(\mu_0) &= \int_{2\pi} R(\mu_0, \phi_0, \mu_1, \phi_1) \mu_1 d\xi \\ &= \frac{A(\mu_0)}{\mu_0} \end{aligned} \quad (3.6.44)$$

$$A(\mu_0) = \int_{\mu'_{\min}}^1 d\mu' \int_{\phi'_{\min}}^{\pi} d\phi' B(\mu_0, \mu', \phi') \quad (3.6.45a)$$

$$B(\mu_0, \mu', \phi') = \frac{1}{2\pi\sigma^2} \frac{R_F(\beta)}{\mu_n^4} \exp\left(-\frac{1-\mu_n^2}{\sigma^2\mu_n^2}\right) f_s(\mu_0, \mu_1) \quad (3.6.45b)$$

Here, the direction (μ_1, ϕ_1) is given by rotating (μ', ϕ') from $(\mu_0, \phi_0 + \pi)$:

$$\mu_1 = \sin\theta_0 \sin\theta' \cos\phi' - \mu_0\mu' \quad (3.6.46a)$$

Then, β and μ_n are derived from (3.6.37–38). When μ' approaches 1, it is convenient to use the new parameter as follows:

$$\tilde{\mu}' \equiv 1 - \mu' \quad (3.6.46b)$$

Then, it can be expressed by

$$\sin\theta' = \sqrt{1 - \mu'^2} = \sqrt{\tilde{\mu}'(2 - \tilde{\mu}')} \quad (3.6.46c)$$

The lower limitation of ϕ' , in which Eq. (3.6.46c) should have the upper direction, is given by

$$\gamma = \frac{\mu_0\mu'}{\sin\theta_0 \sin\theta'} \quad (3.6.47a)$$

$$\phi'_{\min} = \begin{cases} \pi & \text{if } \gamma < -1 \\ \cos^{-1}\gamma & \text{if } -1 \leq \gamma \leq 1 \\ 0 & \text{if } \gamma > 1 \end{cases} \quad (3.6.47b)$$

When the domain of the integration is assumed to be c times (typically three times) the microfacet slope σ , μ' is expressed by

$$\mu' > \mu'_{\min} = \frac{1 - c^2\sigma^2}{1 + c^2\sigma^2} \quad (3.6.48a)$$

or

$$1 - \mu' < 1 - \mu'_{\min} = \frac{2c^2\sigma^2}{1 + c^2\sigma^2} \quad (3.6.48b)$$

The function A is pre-computed and stored in an LUT before the MC simulation.

c. Calculation of angle distribution function of DSM model

The radiance can be calculated according to the BRDF divided by the albedo (normalized angle distribution function, see 3.9). Based on the definition of (3.6.35),

$$\frac{R(\mu_0, \phi_0, \mu_1, \phi_1)}{\alpha(\mu_0)} = \frac{f_d \alpha_d / \pi + (1 - f_d) R_s(\mu_0, \phi_0, \mu_1, \phi_1)}{\alpha(\mu_0)} \quad (3.6.49a)$$

However, for a smooth surface case ($\sigma \equiv 0$), specular reflection has a strong spike-like peak. Due to its strong peak, it causes a large noise and never converges. Therefore, the slope of the micro-facet σ should be larger than a certain threshold. This causes a small artifact. If the incident direction of the modeled photon is isotropic, the BRDF can be replaced by a smoother function. Here, we introduce an approach to modify the minimum σ closely connected with the isotropic characteristics of the incident light.

However, when σ is set larger than a certain threshold, Eq. (3.6.49a) is not effective in using the radiance calculation. Also, if you use σ with a different value from that in the albedo calculation, this contravenes the conservation law.

Here, we introduce a method that only changes the shape of the angular distribution under the same albedo condition. When the direction of the incident photon is isotropic, the diffuse fraction f_d becomes larger. At the same time, the albedo of the diffuse reflection is modified under conserving the average albedo. From (3.6.35b),

$$\begin{aligned} \alpha(\mu_0) &= f_d \alpha_d + (1 - f_d) \alpha_s(\mu_0) \\ &= f'_d \alpha'_d + (1 - f'_d) \alpha_s(\mu_0) \end{aligned} \quad (3.6.49b)$$

$$\alpha'_d = \frac{f_d}{f'_d} \alpha_d + \left(1 - \frac{f_d}{f'_d}\right) \alpha_s(\mu_0) \quad (3.6.49c)$$

Equation (3.6.49a) can be transformed by

$$\frac{R'(\mu_0, \phi_0, \mu_1, \phi_1)}{\alpha(\mu_0)} = \frac{f'_d \alpha'_d / \pi + (1 - f'_d) R_s(\mu_0, \phi_0, \mu_1, \phi_1)}{\alpha(\mu_0)} \quad (3.6.49d)$$

The peak of this specular function has a weaker and smoother angular distribution than the original one. The average albedo is the same as the original one.

d. Determination of direction in DSM model

First, the reflection pattern (diffuse or specular) is determined. The probability of each reflection is given by

$$f_d \frac{\alpha_d}{\alpha}, \quad (1 - f_d) \frac{\alpha_s}{\alpha}$$

In the case of specular reflection, the reflected direction from a flat surface is

$$\Omega_1 = -\Omega_0 + 2\mu_0 \Omega_n \quad (3.6.50)$$

where Ω_n is a zenith angle.

If the surface is not flat, the direction is determined with the PDF by (3.6.40) and (3.6.44):

$$\begin{aligned} Q_s(\mu_0, \mu_1, \phi_1 - \phi_0) &= \frac{R_s(\mu_0, \phi_0, \mu_1, \phi_1) \mu_1}{\alpha_s(\mu_0)} \\ &= \frac{R_F(\beta) f_s(\mu_0, \mu_1)}{4A(\mu_0) \mu_n^4} P\left(\frac{\partial z}{\partial x}, \frac{\partial z}{\partial y}\right) \end{aligned} \quad (3.6.51)$$

First, the direction of the microfacet Ω_n is randomly determined following P . The rejection method is then applied to make a correct distribution, with an acceptance probability of

$$S(\mu_0, \mu_1, \phi_1 - \phi_0) = \frac{R_F(\beta) f_s(\mu_0, \mu_1)}{\mu_n^4} \quad (3.6.52)$$

Since the slope of the micro-facet follows the 2-D Gaussian distribution with a deviation of $\sigma^2/2$, it can be determined by the two pseudorandom numbers by using the Box-Muller method (see 3.1.2 and NR):

$$\tan^2 \theta_n = \frac{\sigma^2}{2} \left[\left(\frac{\partial Z}{\partial x} \right)^2 + \left(\frac{\partial Z}{\partial y} \right)^2 \right] \quad (3.6.53)$$

$$\frac{\partial Z}{\partial x} = \sqrt{-2 \ln \rho_1} \cos 2\pi \rho_2 \quad (3.6.54a)$$

$$\frac{\partial Z}{\partial y} = \sqrt{-2 \ln \rho_1} \sin 2\pi \rho_2 \quad (3.6.54b)$$

To calculate it effectively, a point within the unit circle is randomly selected by using two random numbers (ρ_3, ρ_4). To avoid a finite slope, the center of the circle should be rejected. This is repeated until it meets the following limitation:

$$W_1 = 1 - 2\rho_3 \quad (3.6.55a)$$

$$W_2 = 1 - 2\rho_4 \quad (3.6.55b)$$

$$r_{\min}^2 \leq r^2 \equiv W_1^2 + W_2^2 \leq 1 \quad r_{\min}^2 \approx 0.001 \quad (3.6.55c)$$

When we put

$$\rho_1 = r^2 \quad (3.6.56a)$$

$$\cos \phi_n = \cos 2\pi \rho_2 = W_1/r \quad (3.6.56b)$$

$$\sin \phi_n = \sin 2\pi \rho_2 = W_2/r \quad (3.6.56c)$$

then

$$\tan^2 \theta_n = -\sigma^2 \ln r^2 \quad (3.6.57a)$$

$$\therefore \mu_n = \frac{1}{\sqrt{1 - 2\sigma^2 \ln r^2}} \quad (3.6.57b)$$

$$\therefore \sin \theta_n = \mu_n \sqrt{-2\sigma^2 \ln r^2} \quad (3.6.57c)$$

Finally, we can avoid the sine and cosine calculations. Then, we can obtain Ω_n . The reflection direction is determined by

$$\Omega_1 = -\Omega_0 + 2 \cos \beta \Omega_n \quad (3.6.58a)$$

$$\cos \beta = \Omega_0 \cdot \Omega_n > 0 \quad (3.6.58b)$$

If the scalar product of (3.6.58b) is negative, reflection does not occur. Therefore, the selected direction should be rejected and a new direction is selected. Also, if the reflected direction is a downward direction, the selected direction should be rejected.

Next, the rejection method is applied based on the function S in (3.6.52). The maximum of S ($S_{\max}(\mu_0)$) should be determined in advance. This is on the principal plane. Because r has a lower limitation constrained by (3.6.55c), the slope of the microfacet has such a limitation:

$$\mu_n \geq \frac{1}{\sqrt{1 - \sigma^2 \ln r_{\min}^2}} \equiv \mu_{\min} \equiv \cos \theta_{\max} \quad (3.6.59)$$

Therefore, the reflected direction is also constrained within a certain range. The “relative zenith angle” is defined by

$$\hat{\theta}_1 \equiv \begin{cases} -\theta_1 & \text{if } |\phi_1 - \phi_0| < \pi/2 \\ \theta_1 & \text{if } |\phi_1 - \phi_0| \geq \pi/2 \end{cases} \quad (3.6.60)$$

The edges of this range can be written by

$$\hat{\theta}_1 = \theta_0 - 2\theta_{\max}, \quad \text{if } |\phi_1 - \phi_0| = 0 \quad (3.6.61a)$$

$$\hat{\theta}_1 = \theta_0 + 2\theta_{\max}, \quad \text{if } |\phi_1 - \phi_0| = \pi \quad (3.6.61b)$$

where

$$\begin{aligned} \cos 2\theta_{\max} &= 1 - 2 \sin^2 \theta_{\max} \\ \sin 2\theta_{\max} &= 2 \sin \theta_{\max} \cos \theta_{\max} \end{aligned}$$

The absolute value of Eq. (3.6.61) is always less than $\pi/2$. S_{\max} can be prepared as an LUT using the golden rule (NR). The reflected direction can be obtained by interpolating with respect to μ_0 . A problem arises when S has a strong peak and the maximum value is located within it. To prevent this problem, S_{\max}/S_0 should be adjusted so as not to become too large. If S_0 is a value of S for a microfacet with a vertical direction ($\mu_n = 1$), then

$$S'_{\max} = \begin{cases} S_{\max} & \text{if } S_{\max} < DS_0 \\ S_0 \left[D - 1 + \left(\frac{S_{\max}}{S_0} - D + 1 \right)^E \right] & \text{if } S_{\max} \geq DS_0 \end{cases} \quad (3.6.62)$$

where D and E are constant values (the preferable values are $D = 4$, $E = 0.5$). Based on this, the rejection method is applied:

$$\frac{S}{S'_{\max}} \quad (3.6.63)$$

Fig. 3.6.1 shows the simulation results of the BRDF for the reflected direction (zenith and azimuth angles) under a solar zenith angle = 0° and a slope dispersion of 0.04.

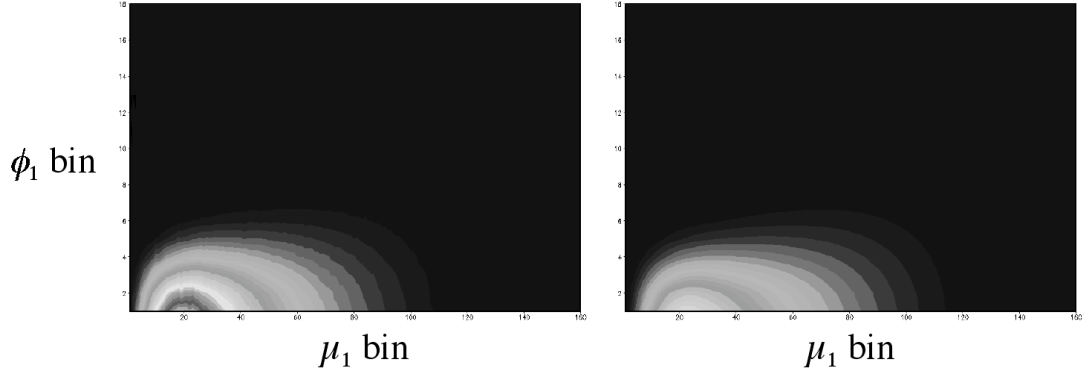


Fig. 3.6.1 BRF from analytical calculation of DSM model (left) and from MC simulation (right).

3.6.5 Rahman-Pinty-Verstraete (RPV) BRDF model

Rahman, Pinty, and Verstraete (1993) (RPV) proposed a semi-empirical model to express the BRDF for vegetation and soil. The RPV model has three geometric parameters (incident zenith, reflected zenith, and relative azimuth), which is the three parameter case in (3.6.2). The BRDF of the RPV model is expressed by

$$R(\theta_0, \theta_1, \phi) = \frac{\rho_0}{\pi} \left\{ \frac{\cos^{k-1} \theta_0 \cos^{k-1} \theta_1}{(\cos \theta_0 + \cos \theta_1)^{1-k}} F(\gamma) [1 + H(G)] + \frac{\sigma}{\cos \theta_0} \right\} \quad (3.6.65)$$

Here, ρ_0 and σ are constant. F is a function similar to the Henyey-Greenstein function:

$$F(\gamma) = \frac{1 - \Theta^2}{[1 + \Theta^2 + 2\Theta \cos \gamma]^{3/2}} \quad (3.6.66)$$

It expresses the anisotropy of the forward and backward scattering. γ is a phase angle (angle between incident $\mathbf{\Omega}_0$ and reflected direction $\mathbf{\Omega}_1$):

$$\cos \gamma = \mathbf{\Omega}_0 \cdot \mathbf{\Omega}_1 = \cos \theta_0 \cos \theta_1 + \sin \theta_0 \sin \theta_1 \cos \phi \quad (3.6.67)$$

The function H expresses the shape of hotspot effects:

$$1 + H(G) = 1 + \frac{1 - \rho_0}{\delta + G} \quad (3.6.68)$$

Generally, $\delta = 1$. In a special case, δ can be used to fit the observation data. G is a geometric factor and is given by

$$G = \sqrt{\tan^2 \theta_0 + \tan^2 \theta_1 - 2 \tan \theta_0 \tan \theta_1 \cos \phi} \quad (3.6.69)$$

The hotspot is located at $\theta_0 = \theta_1$, $\phi = 0$ and has a strong peak. Except for the hotspot effect, the RPV model has a smooth angular distribution.

The RPV model has five parameters (ρ_0 , k , Θ , δ , σ) depending on the vegetation and soil conditions. For the simplicity of the simulation, we use $\sigma = 0$. The BRDF of RPV is then rewritten by:

$$R(\theta_0, \theta_1, \phi) = \frac{\rho_0}{\pi} \frac{\cos^{k-1} \theta_0 \cos^{k-1} \theta_1}{(\cos \theta_0 + \cos \theta_1)^{1-k}} F(\gamma) [1 + H(G)] \quad (3.6.70)$$

Figure 3.6.2 shows an example of this model.

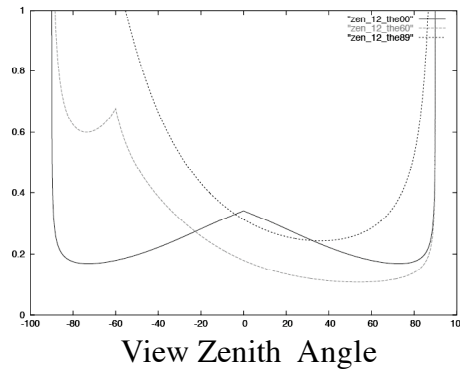


Fig. 3.6.2 BRF (= BRDF* π) calculated by the RPV model for three different incident zenith angles (0° , 60° , 89°).

a. Albedo of RPV model

The albedo is calculated by its definition:

$$\begin{aligned}
\alpha(\mu_0) &= \int_0^1 \int_0^{2\pi} R(\mu_0, \mu_1, \phi) \mu_1 d\phi d\mu_1 \\
&= 2 \int_0^1 \int_0^\pi R(\mu_0, \mu_1, \phi) \mu_1 d\phi d\mu_1 \quad (3.6.71) \\
&= \frac{2\rho_0}{\pi} \mu_0^{k-1} \int_0^1 \left\{ \frac{[\mu_1(\mu_0 + \mu_1)]^k}{(\mu_0 + \mu_1)} \int_0^\pi F(\gamma) \left[1 + \frac{1-\rho_0}{\delta + G} \right] d\phi \right\} d\mu_1
\end{aligned}$$

For simplicity, we put

$$A(\mu_0) = \frac{2\rho_0}{\pi} \int_0^1 B(\mu_0, \mu_1) d\mu_1 \quad (3.6.72a)$$

$$B(\mu_0, \mu_1) = \frac{[\mu_1(\mu_0 + \mu_1)]^k}{(\mu_0 + \mu_1)} \int_0^\pi C(\mu_0, \mu_1, \phi) d\phi \quad (3.6.72b)$$

$$C(\mu_0, \mu_1, \phi) = F(\gamma) \left[1 + \frac{1-\rho_0}{\delta + G} \right] \quad (3.6.72c)$$

Then, the albedo is expressed by

$$\alpha(\mu_0) = \mu_0^{k-1} A(\mu_0) \quad (3.6.73)$$

The function A cannot be solved analytically. The integrand C in (3.6.72b) with respect to ϕ is sufficiently smooth. Therefore, it is possible to integrate using the Gaussian integration method (Press et al., 1992). The integrand with respect to μ_1 is not smooth in the hotspot region ($\mu_1 = \mu_0$). Therefore, to obtain accurate results, it is necessary to use the two integration ranges $0 \leq \mu_1 < \mu_0$ and $\mu_0 \leq \mu_1 \leq 1$.

This requires vast computation if the double integral discussed above is performed at every reflectance event. It is better to prepare an LUT for A with respect to μ_0 . Fortunately, the function A with respect to μ_0 is very smooth, so that we can obtain sufficient accuracy with 4 to 6 quadratic points (the interpolation error is less than 0.3%). When the parameters are dependent on the location (x, y) , the function A becomes a 3-D (x, y, μ_0) LUT.

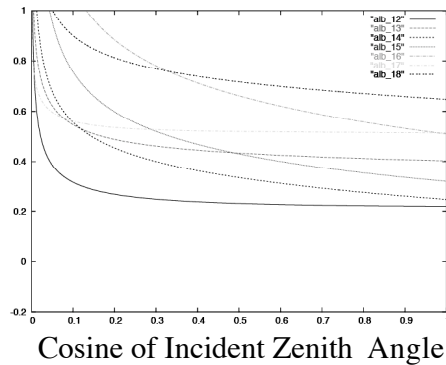


Fig. 3.6.3 Relationship between the albedo and incident zenith angle. Seven different types of surfaces are shown.

The albedo should have the value of [0–1]. The albedo calculated from Eq. (3.6.73) sometimes takes values out of this range (especially in small μ_0 cases). To prevent such abnormal values, we multiply $1/\alpha$ for the BRDF when the albedo is larger than 1. Then, the albedo becomes 1 by compulsion.

Integration of function C

Multiple calculations are required for the integration of $C(\phi)$ over $\phi = 0-\pi$ at a given pair of (μ_1, μ_0) . Therefore, as fast and accurate an integration scheme as possible is necessary. Here, we use the Gaussian integration method.

To achieve effective integration, it would be better to calculate the coefficient with respect to (μ_1, μ_0) . Again, we rewrite the form of function C:

$$C(\mu_0, \mu_1, \phi) = F(\gamma) \left[1 + \frac{1 - \rho_0}{\delta + G} \right] \quad (3.6.74)$$

F and G in (3.6.74) are

$$F(\gamma) = \frac{1 - \Theta^2}{[1 + \Theta^2 + 2\Theta \cos \gamma]^{3/2}} \quad (3.6.75a)$$

$$G = \frac{\sqrt{\mu_0^2 + \mu_1^2 - 2\mu_0\mu_1 \cos \gamma}}{\mu_0\mu_1} \quad (3.6.75b)$$

$$\cos \gamma = \mu_0\mu_1 + \sqrt{(1 - \mu_0^2)(1 - \mu_1^2)} \cos \phi \quad (3.6.75c)$$

Therefore, when we put

$$\begin{cases} d_1 = 1 - \Theta^2 \\ d_2 = 1 + \Theta^2 \\ d_3 = \mu_0\mu_1 \\ d_4 = \sqrt{(1 - \mu_0^2)(1 - \mu_1^2)} \\ d_5 = \mu_0^2 + \mu_1^2 \end{cases} \quad (3.6.76)$$

then F , G , and C are simply expressed by

$$F(\gamma) = \frac{d_1}{[d_2 + 2\Theta \cos \gamma]^{3/2}} \quad (3.6.77)$$

$$G = \frac{\sqrt{d_5 - 2d_3 \cos \gamma}}{d_3} \quad (3.6.78)$$

$$C(\mu_0, \mu_1, \phi) = \frac{d_1}{[d_2 + 2\Theta \cos \gamma]^{3/2}} \left[1 + \frac{(1 - \rho_0)d_3}{\delta d_3 + \sqrt{d_5 - 2d_3 \cos \gamma}} \right] \quad (3.6.79)$$

$$2 \cos \gamma = 2(d_3 + d_4 \cos \phi) \quad (3.6.80)$$

The integration by the Gaussian method is

$$\begin{aligned}\bar{C}(\mu_0, \mu_1) &= \int_0^\pi C(\mu_0, \mu_1, \phi') d\phi' \\ &= \pi \sum_{i=1}^N w_i C(\mu_0, \mu_1, \cos \phi(i))\end{aligned}\quad (3.6.81)$$

where w is a weight of the Gauss-Legendre integration. $\cos \phi$ in each integration point should be prepared by an LUT for effective calculation.

b. BRDF calculation

The BRDF can be directly calculated by the incident and reflected zenith angles and relative azimuth angle. RPV is rewritten by

$$R(\mu_0, \mu_1, \phi) = \frac{\rho_0}{\pi} \frac{F(\gamma)[1+H(G)]}{[\mu_0 \mu_1 (\mu_0 + \mu_1)]^{1-k}} \quad (3.6.82)$$

When it is divided by the albedo, the strong μ_0 dependency is diminished. Using (3.6.73), we obtain

$$\frac{R(\mu_0, \mu_1, \phi)}{\alpha(\mu_0)} = \frac{\rho_0}{\pi A(\mu_0)} \cdot \frac{F(\gamma)[1+H(G)]}{[\mu_1 (\mu_0 + \mu_1)]^{1-k}} \quad (3.6.83)$$

The function H can be rewritten by

$$H(G) = \frac{1 - \rho_0}{\delta + G} \quad (3.6.84a)$$

$$G = \sqrt{\tan^2 \theta_0 + \tan^2 \theta_1 - 2 \tan \theta_0 \tan \theta_1 \cos \phi} \quad (3.6.84b)$$

Here, if we use the following relationship:

$$\mathbf{\Omega}_0 \cdot \mathbf{\Omega}_1 = \mu_0 \mu_1 + \sin \theta_0 \sin \theta_1 \cos \phi \quad (3.6.85)$$

we obtain

$$\tan \theta_0 \tan \theta_1 \cos \phi = \frac{\sin \theta_0 \sin \theta_1 \cos \phi}{\mu_0 \mu_1} = \frac{\mathbf{\Omega}_0 \cdot \mathbf{\Omega}_1}{\mu_0 \mu_1} - 1 \quad (3.6.86)$$

When Eqs. (3.6.86) and (3.6.87) are substituted to (3.6.84b),

$$\begin{cases} \tan^2 \theta_0 = \frac{1-\mu_0^2}{\mu_0^2} = \frac{1}{\mu_0^2} - 1 \\ \tan^2 \theta_1 = \frac{1-\mu_1^2}{\mu_1^2} = \frac{1}{\mu_1^2} - 1 \end{cases} \quad (3.6.87)$$

we obtain

$$G = \sqrt{\frac{1}{\mu_0^2} + \frac{1}{\mu_1^2} - 2 \frac{\mathbf{\Omega}_0 \cdot \mathbf{\Omega}_1}{\mu_0 \mu_1}} = \frac{\sqrt{\mu_0^2 + \mu_1^2 - 2\mu_0 \mu_1 (\mathbf{\Omega}_0 \cdot \mathbf{\Omega}_1)}}{\mu_0 \mu_1} \quad (3.6.88)$$

Finally, we can avoid the sine/cosine/tangent calculation.

$$H(G) = \frac{(1-\rho_0)\mu_0\mu_1}{\delta\mu_0\mu_1 + \sqrt{\mu_0^2 + \mu_1^2 - 2\mu_0\mu_1(\mathbf{\Omega}_0 \cdot \mathbf{\Omega}_1)}} \quad (3.6.89)$$

$$F(\gamma) = \frac{1-\Theta^2}{[1+\Theta^2 + 2\Theta(\mathbf{\Omega}_0 \cdot \mathbf{\Omega}_1)]^{3/2}} \quad (3.6.90)$$

By using the above equations, we can calculate Eq. (3.6.83) from the incident and reflected zenith angles and relative azimuth angle. When μ_1 is nearly 0, we should treat it carefully.

c. Determination of reflection direction in RPV model

When a set of RPV model parameters $(\rho_0, k, \Theta, \delta)$ is given and these parameters are constant in the simulation space, a 3-D LUT is an effective way to simulate. However, if the RPV model parameters $(\rho_0, k, \Theta, \delta)$ vary in space, a seven-dimensional (7-D) LUT is required. This requires a large memory, even for a coarse LUT. Also, the interpolation from a 7-D LUT is numerically very intensive and does not promote accuracy.

At the time of the reflection event, five parameters $(\rho_0, k, \Theta, \delta, \mu_0)$ are already fixed and μ_1 and ϕ should be determined. We propose a method to determine μ_1 and ϕ simultaneously. The comparison function should be a close match to the BR-PDF. Therefore, the μ_1 dependency of the BR-PDF is approximated by a linear function.

Determination of comparison function

The BR-PDF is approximated by a linear function as follows:

$$P(\mu_0, \mu_1, \phi) \approx a_1(\mu_0)\mu_1 + a_0(\mu_0) \quad (3.6.91)$$

In the isotropic case, $P = \mu_1/\pi$, which is well expressed by (3.6.91), a_1 and a_0 are determined by the normalization conditions:

$$\int_0^{2\pi} \int_0^1 [a_1(\mu_0)\mu_1 + a_0(\mu_0)] d\mu_1 d\phi = 2\pi \left(\frac{a_1(\mu_0)}{2} + a_0(\mu_0) \right) = 1 \quad (3.6.92a)$$

$$\therefore a_1(\mu_0) = \frac{1}{\pi} - 2a_0(\mu_0) \quad (3.6.92b)$$

These coefficients can be determined by normalization conditions after regressing to the function B (average BRDF over the azimuth angle ϕ) (see 3.6.71–72).

It is necessary to obtain the coefficient of the following parameters:

$$B(\mu_0, \mu_1) \approx \bar{a}_1(\mu_0)\mu_1 + \bar{a}_0(\mu_0) \quad (3.6.93a)$$

It should be noted that the comparison function always takes positive values for the range of $\mu_1 = 0-1$. Finally, it becomes

$$a_1(\mu_0) = \frac{\bar{a}_1(\mu_0)}{\pi(\bar{a}_1(\mu_0) + 2\bar{a}_0(\mu_0))} \quad (3.6.93b)$$

where the comparison function should be positive; therefore, it is forced by

$$-\frac{1}{\pi} < a_1(\mu_0) < \frac{1}{\pi} \quad (3.6.93c)$$

a_0 can be determined by

$$a_0(\mu_0) = \frac{1}{2} \left(\frac{1}{\pi} - a_1(\mu_0) \right) \quad (3.6.93d)$$

Here, we can find a comparison function that is “larger than the original BR-PDF in all points”:

$$P(\mu_0, \mu_1, \phi) \equiv \frac{R(\mu_0, \mu_1, \phi)\mu_1}{\alpha(\mu_0)} \quad (3.6.94)$$

We can find the above equation divided by (3.6.91). To meet the criteria for a comparison function that is larger than the original BR-PDF in all points, we multiply the following equation by (3.6.91):

$$b(\mu_0) = \max \left\{ \frac{\mu_1}{[a_1(\mu_0)\mu_1 + a_0(\mu_0)]} \cdot \frac{R(\mu_0, \mu_1, \phi)}{\alpha(\mu_0)} \right\} \quad (3.6.95)$$

The function $\max\{\}$ is a maximum of all μ_1, ϕ . R/α can be calculated by (3.6.83). In the case of the RPV model, it is located on the principal plane ($\phi = 0$ or π). When the BR-PDF is a linear function such as (3.6.91a), the factor b becomes 1. If the BRDF has a strong peak, multiple iterations are necessary. Instead of b , we use the following equations:

$$b'(\mu_0) = \begin{cases} b(\mu_0) & \text{if } b(\mu_0) < b_{\min} \\ b_{\min} - 1 + [b(\mu_0) - b_{\min} + 1]^S & \text{if } b(\mu_0) \geq b_{\min} \end{cases} \quad (3.6.96)$$

S is a tuning parameter. That is, if the BR-PDF is far from the linear function, it should be approximated by a similar angular distribution shape to the BR-PDF. $b_{\min} = 4$, $S = 0.5$ are the best values for most cases. In the case of the RPV model, there is no prominent peak and $b =$ usually 1–5. Consequently, the comparison function becomes

$$f(\mu_0, \mu_1, \phi) = b'(\mu_0)[a_1(\mu_0)\mu_1 + a_0(\mu_0)] \quad (3.6.97)$$

The coefficients a_1 and b' should be prepared as a 3-D LUT. If the reflection event occurs, it is interpolated by the LUT with respect to μ_0 . Since the comparison function is usually estimated roughly, it is not necessary to derive these coefficients accurately. We evaluate a_0 from Eq. (3.6.97).

Use of rejection method

In the following description, we ignore the argument μ_0 . The comparison function in Eq. (3.6.97) can be written as

$$f(\mu_1, \phi) = b'(a_1\mu_1 + a_0) \quad (3.6.98)$$

μ_1 that follows this equation can be determined by solving:

$$2\pi \int_0^{\mu_1} (a_1\mu' + a_0)d\mu' = \rho_{\mu_1} \quad (3.6.99)$$

Therefore, this is a problem to solve a quadratic equation:

$$a_1\mu_1^2 + 2a_0\mu_1 - \frac{\rho_{\mu_1}}{\pi} = 0 \quad (3.6.100)$$

The solution of this equation within the range of $\mu_1 = 0-1$ is

1) If $a_1 \neq 0$

$$\mu_1 = \frac{-a_0 + \sqrt{a_0^2 + a_1 \rho_{\mu_1} / \pi}}{a_1} \quad (3.6.101a)$$

2) Else if $a_1 = 0$

$$\mu_1 = \rho_{\mu_1} \quad (3.6.101b)$$

The azimuth angle can easily be determined by

$$\phi = 2\pi\rho_{\phi} \quad (3.6.102)$$

The probability that the above direction is followed by the BR-PDF in the RPV model is given by

$$\gamma = \frac{P(\mu_1, \phi)}{f(\mu_1, \phi)} = \frac{\mu_1}{b'(a_1\mu_1 + a_0)} \cdot \frac{R(\mu_0, \mu_1, \phi)}{\alpha(\mu_0)} \quad (3.6.103)$$

Therefore, we use the additional random number and apply the following criteria:

$$\begin{cases} \text{If } \rho < \gamma, \text{ finish} \\ \text{If } \rho \geq \gamma, \text{ rejection} \end{cases} \quad (3.6.104)$$

If rejected, the new direction is selected again by (3.6.101–102). The reflected direction followed by the RPV model can be determined by the above prescribed method.

c. Simulation example

Several test simulations were performed. The prescribed method had enough speed (using a Pentium IV 3.6 GHz PC, we could achieve a reflection simulation with over 6,000,000 events). Figure 3.6.4 shows the validation results for the exact BRF and the BRF calculated by the MC method. The results have a fairly good accordance.

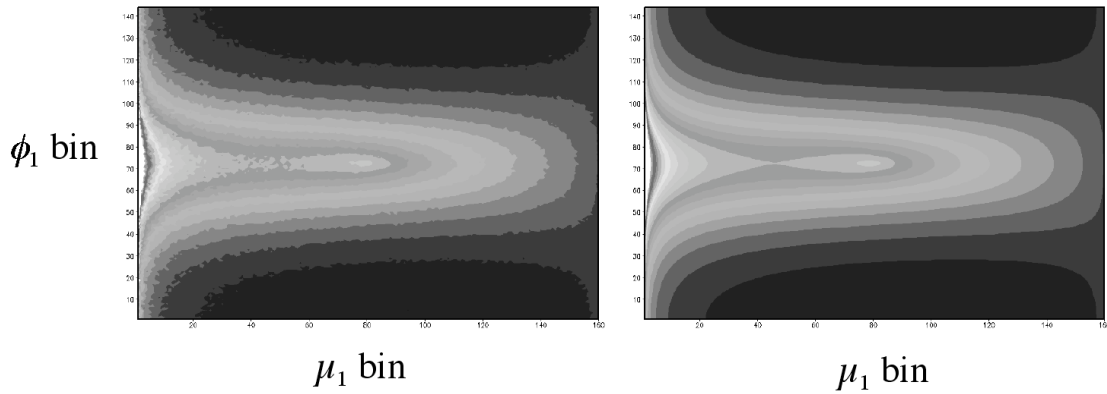


Fig. 3.6.4 Analytical BRF calculation of RPV (left) and BRF by MC simulation (right).

3.6.6 Li-Sparse-Ross-Thick (LSRT) BRDF model

Lucht et al. (2000) proposed a semi-empirical model to express a land surface BRDF, called the Li-Sparse-Ross-Thick (LSRT) linear kernel model. This model is employed to estimate the retrieval of land surface parameters from MODIS and MISR data. Also, it is combined with the SHARM model by Lyapustin (2000).

Here, we describe a method to include the LSRT model in the MC simulation.

a. Original formulas of LSRT BRDF

Let the incident direction be $\mathbf{\Omega}_0$ (this is a different definition than in the previous section). The zenith angle, its cosine, and azimuth angle are expressed by θ_0 , $\cos\theta_0 = \mu_0$, and ϕ_0 , respectively. The reflected direction is also defined by $\mathbf{\Omega}_1$ and its components are θ_0, μ_0 , and ϕ_0 . The LSRT model is a three-parameter BRDF model (3.6.2). The hotspot direction is expressed by $-\mu_0 = \mu_1$, $\phi = \pi$.

The BRDF can be expressed by the combination of the reflectance contributions from Lambertian, geometric-optics, and volume scatterings:

$$\pi R(\mu_0, \mu_1, \phi) = k_L + k_g f_g(\mu_0, \mu_1, \phi) + k_v f_v(\mu_0, \mu_1, \phi) \quad (3.6.106)$$

Here, the kernel function is expressed by

$$f_v(\mu_0, \mu_1, \phi) = \frac{(\pi/2 - \gamma) \cos \gamma + \sin \gamma}{-\mu_0 + \mu_1} - \frac{\pi}{4} \quad (3.6.107)$$

$$f_g(\mu_0, \mu_1, \phi) = \frac{1}{\pi} (t - \sin t \cos t) (\mu_1'^{-1} - \mu_0'^{-1}) - (\mu_1'^{-1} - \mu_0'^{-1}) - \frac{(1 + \cos \gamma')}{2\mu_0' \mu_1'} \quad (3.6.108)$$

These functions have negative values in some directions. γ is a phase angle (inverse direction of incident direction and reflected direction) given by

$$\cos \gamma = \mathbf{\Omega}_0 \cdot \mathbf{\Omega}_1 = -(\mu_0 \mu_1 + \sqrt{1 - \mu_0^2} \sqrt{1 - \mu_1^2} \cos \phi) \quad (3.6.109a)$$

$$\cos \gamma' = \mathbf{\Omega}'_0 \cdot \mathbf{\Omega}'_1 = -(\mu'_0 \mu'_1 + \sqrt{1 - \mu_0'^2} \sqrt{1 - \mu_1'^2} \cos \phi) \quad (3.6.109b)$$

Here, the angle t is expressed by

$$\cos t = \frac{h \sqrt{\tan^2 \theta'_0 + \tan^2 \theta'_1 - 2 \tan \theta'_0 \tan \theta'_1 \cos \phi + \tan^2 \theta'_0 \tan^2 \theta'_1 \sin^2 \phi}}{b (\mu_1'^{-1} - \mu_0'^{-1})} \quad (3.6.110)$$

Here, it is constrained by $|\cos t| \leq 1$. The angle of the prime parameters in (3.6.108–110) is defined by

$$\tan \theta'_0 = \frac{b}{r} \tan \theta_0 \quad (3.6.111a)$$

$$\tan \theta'_1 = \frac{b}{r} \tan \theta_1 \quad (3.6.111a)$$

The ratio of the canopy structural parameters is assumed by (Lucht et al., 2000)

$$b/r = 1 \text{ and } h/b = 2 \quad (3.6.112)$$

Finally, the BRDF is determined by the three parameters k_L , k_g , and k_v .

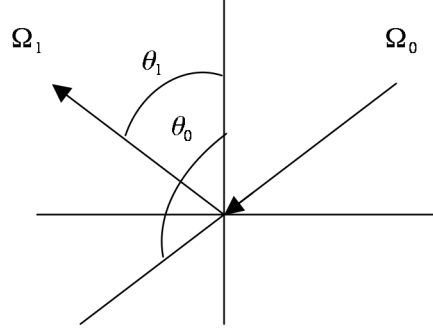


Fig. 3.6.5 Definition of direction and angles

b. Modifications

When the incident direction is nearly horizontal, the LSRT model outputs a negative value or infinity. If the value is negative, it is reset to 0. If the albedo is larger than 1, it is reset to 1 and the BRDF is rescaled as a small value.

The original form of the LSRT model has many trigonometric functions, which requires rather extensive computation. Therefore, we change the form of (3.6.108) (3.6.110) as an expression of the direction cosine. The geometric kernel in (3.6.108) is written as

$$f_g(\mu_0, \mu_1, \phi) = \frac{1}{\mu'_0 \mu'_1} \left[\left(1 - \frac{t - \sin t \cos t}{\pi} \right) (\mu'_1 - \mu'_0) - \frac{1}{2} (1 + \cos \gamma') \right] \quad (3.6.113)$$

Here, we summarize the following function by substituting to (3.6.110):

$$\tan \theta'_0 \tan \theta'_1 \cos \phi = \frac{\sin \theta'_0 \sin \theta'_1 \cos \phi}{\mu'_0 \mu'_1} = -\frac{\cos \gamma'}{\mu'_0 \mu'_1} - 1 \quad (3.6.114)$$

$$\tan^2 \theta'_0 = \frac{1 - \mu_0'^2}{\mu_0'^2}; \tan^2 \theta'_1 = \frac{1 - \mu_1'^2}{\mu_1'^2} \quad (3.6.115)$$

Then, we obtain

$$\cos t = \frac{h}{b} \frac{\sqrt{1 - \cos^2 \gamma'}}{\mu'_1 - \mu'_0} \quad (3.6.116)$$

f_g and t become easier to compute. In the hotspot direction, the following relationship exists:

$$\Omega'_0 = -\Omega'_1; \mu'_0 = -\mu'_1; \cos t = 0; f_g(\mu_0, \mu_1, \phi) = \frac{1 - \mu_1'}{\mu_1'^2}$$

The direction cosine in (3.6.113) and (3.6.116) can be derived as follows. First, the following relationship is found from (3.6.111):

$$\mu'_0 = \mu_0 / \sqrt{B + (1-B)\mu_0^2}; B = \left(\frac{b}{r}\right)^2 \quad (3.6.117)$$

$$\mathbf{\Omega}_0 = \begin{pmatrix} \mu_{x0} \\ \mu_{y0} \\ \mu_{z0} \end{pmatrix}; \mathbf{\Omega}'_0 = \frac{1}{\sqrt{B + (1-B)\mu_0^2}} \begin{pmatrix} \mu_{x0} \cdot b/r \\ \mu_{y0} \cdot b/r \\ \mu_{z0} \end{pmatrix} \quad (3.6.118)$$

The variables indicated by the subscript 1 are expressed in the same manner. Therefore, we obtain

$$\cos \gamma' = \mathbf{\Omega}'_0 \cdot \mathbf{\Omega}'_1 = \frac{B(\mathbf{\Omega}_0 \cdot \mathbf{\Omega}_1) + (1-B)\mu_0\mu_1}{\sqrt{[B + (1-B)\mu_0^2][B + (1-B)\mu_1^2]}} \quad (3.6.119)$$

For the calculation, we first calculate the scalar product $\mathbf{\Omega}_0 \cdot \mathbf{\Omega}_1$ in (3.6.119). From (3.6.118), the two directions expressed by the prime parameters are determined and the scalar products are then determined. These values are substituted to (3.6.116) and we obtain $\cos t$; $\sin t$, t , and f_g are obtained by (3.6.113). Also, f_v is calculated from (3.6.107). Finally, the BRDF is calculated by (3.6.106).

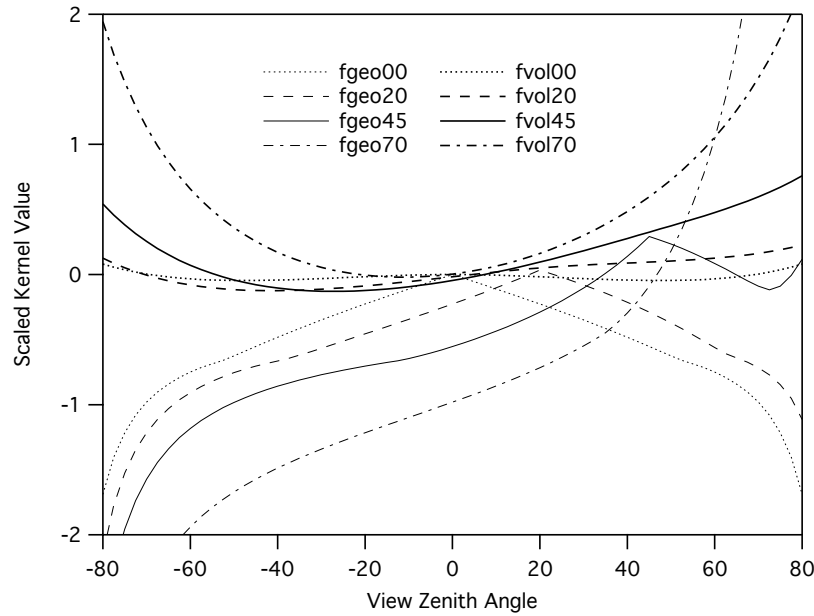


Fig. 3.6.6 Kernel function (same as Fig. 2 in Lucht et al. 2000).

c. Albedo of LSRT model

The albedo can be written as

$$\begin{aligned}
 \alpha(\mu_0) &= \int_0^1 d\mu_1 \int_0^{2\pi} d\phi R(\mu_0, \mu_1, \phi) \mu_1 \\
 &= 2 \int_0^1 d\mu_1 \mu_1 \int_0^\pi d\phi R(\mu_0, \mu_1, \phi) \\
 &= \frac{2}{\pi} \int_0^1 d\mu_1 \mu_1 \int_0^\pi d\phi (k_L + k_g f_g(\mu_0, \mu_1, \phi) + k_v f_v(\mu_0, \mu_1, \phi)) \\
 &= k_L + k_g A_g(\mu_0) + k_v A_v(\mu_0)
 \end{aligned} \tag{3.6.120}$$

It should be restricted within [0–1]. Here, A_g and A_v are the kernel functions of the geometrical optics and volume scatterings, respectively:

$$\begin{aligned}
 A_g(\mu_0) &= \frac{2}{\pi} \int_0^1 d\mu_1 \mu_1 \int_0^\pi d\phi f_g(\mu_0, \mu_1, \phi) \\
 A_v(\mu_0) &= \frac{2}{\pi} \int_0^1 d\mu_1 \mu_1 \int_0^\pi d\phi f_v(\mu_0, \mu_1, \phi)
 \end{aligned} \tag{3.6.121}$$

As shown in Fig. 3.6.7, these functions sometimes take negative values. These functions are prepared as an LUT with respect to μ_0 . Unlike the RPV model, the LSRT model does not require an LUT for each pixel.

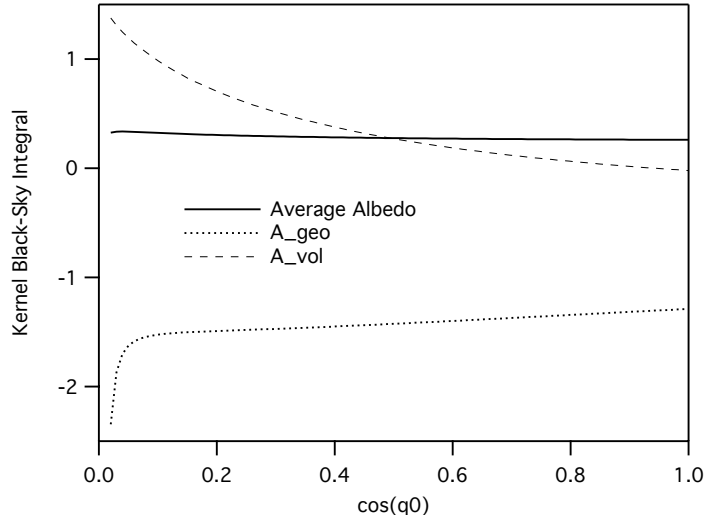


Fig. 3.6.7 Kernel function of the albedo (same as Fig. 4 in Lucht et al. 2000), with average albedo for $(k_L, k_g, k_v) = (0.3, 0.07, 0.03)$.

d. Determination of reflected direction for LSRT model

Here, we determine μ_1 and ϕ simultaneously. The following procedure is the same as in the RPV model. As much as possible, the comparison function should be selected to have a shape similar to the original BR-PDF.

Determination of comparison function

The BR-PDF can be approximated by the linear function like

$$P(\mu_0, \mu_1, \phi) \equiv R(\mu_0, \mu_1, \phi) \mu_1 / \alpha(\mu_0) \quad (3.6.122a)$$

$$P(\mu_0, \mu_1, \phi) \approx a_1(\mu_0) \mu_1 + a_0(\mu_0) \quad (3.6.122b)$$

In the isotropic case, $P = \mu_1 / \pi$, which is well expressed by (3.6.91), a_1 and a_0 are determined by the normalization conditions:

$$\int_0^{2\pi} \int_0^1 [a_1(\mu_0) \mu_1 + a_0(\mu_0)] d\mu_1 d\phi = 2\pi \left(\frac{a_1(\mu_0)}{2} + a_0(\mu_0) \right) = 1 \quad (3.6.123a)$$

$$\therefore a_0(\mu_0) = \frac{1}{2} \left(\frac{1}{\pi} - a_1(\mu_0) \right) \quad (3.6.123b)$$

To obtain the coefficients of this function, we first solve the following equation:

$$\begin{aligned} \bar{P}(\mu_0, \mu_1) &\equiv \mu_1 \int_0^\pi R(\mu_0, \mu_1, \phi) d\phi \\ &= \mu_1 \int_0^\pi (k_L + k_g f_g(\mu_0, \mu_1, \phi) + k_v f_v(\mu_0, \mu_1, \phi)) d\phi \\ &= \mu_1 \left[k_L \pi + k_g \int_0^\pi f_g(\mu_0, \mu_1, \phi) d\phi + k_v \int_0^\pi f_v(\mu_0, \mu_1, \phi) d\phi \right] \\ &\approx \bar{a}_1(\mu_0) \mu_1 + \bar{a}_0(\mu_0) \end{aligned} \quad (3.6.124)$$

where these functions are prepared as an LUT:

$$\begin{aligned} \bar{f}_g(\mu_0, \mu_1) &= \int_0^\pi f_g(\mu_0, \mu_1, \phi) d\phi \\ \bar{f}_v(\mu_0, \mu_1) &= \int_0^\pi f_v(\mu_0, \mu_1, \phi) d\phi \end{aligned} \quad (3.6.125)$$

The regression function is written as

$$\mu_1 [k_L \pi + k_g \bar{f}_g(\mu_0, \mu_1) + k_v \bar{f}_v(\mu_0, \mu_1)] \approx \bar{a}_1(\mu_0) \mu_1 + \bar{a}_0(\mu_0) \quad (3.6.126)$$

From this equation, we obtain the ratio of

$$\frac{a_0(\mu_0)}{a_1(\mu_0)} = \frac{\bar{a}_0(\mu_0)}{\bar{a}_1(\mu_0)} \quad (3.6.127)$$

From normalization conditions (3.6.123) and (3.6.127), we obtain

$$a_1(\mu_0) = \frac{\bar{a}_1(\mu_0)}{\pi(\bar{a}_1(\mu_0) + 2\bar{a}_0(\mu_0))} \quad (3.6.128)$$

Here, when (3.6.122) is used as a comparison function, μ_1 should be [0–1] and positive. In this case, the albedo should be within (based on the authors' experience, it would be better if it was narrower than this range)

$$-\frac{1}{\pi} < a_1(\mu_0) < \frac{1}{\pi} \quad (3.6.129)$$

On the other hand, a_0 is calculated by (3.6.123b). To meet the criteria that the comparison function is larger than the original BR-PDF in all points, we multiply the following equation by (3.6.122):

$$b(\mu_0) = \max \left\{ \frac{\mu_1}{[a_1(\mu_0)\mu_1 + a_0(\mu_0)]} \cdot \frac{R(\mu_0, \mu_1, \phi)}{\alpha(\mu_0)} \right\} \quad (3.6.130)$$

The function $\max\{\}$ is applied to all μ_1, ϕ in (3.6.130). b in the BRDF, which has a strong peak, becomes large and many iterations are necessary in the rejection method. Instead of b , we use b' :

$$b'(\mu_0) = \begin{cases} b(\mu_0) & \text{if } b(\mu_0) < b_{\min} \\ b_{\min} - 1 + [b(\mu_0) - b_{\min} + 1]^S & \text{if } b(\mu_0) \geq b_{\min} \end{cases} \quad (3.6.131)$$

where S is a tuning parameter. When the BR-PDF is far from a linear regression, we use the BR-PDF, which has a similar shape to the original BR-PDF. $b_{\min} = 4, S = 0.5$ are better values in most cases. In the case of the LSRT model, there is usually no prominent peak and $b = 1-5$. Consequently, the comparison function becomes

$$h(\mu_0, \mu_1, \phi) = b'(\mu_0)[a_1(\mu_0)\mu_1 + a_0(\mu_0)] \quad (3.6.132)$$

When k_* varies by pixel, the coefficient should be determined pixel by pixel. The parameters a_1 and b' are prepared by a 3-D LUT (x, y, μ_0). When the reflectance event occurs, a_1 and b' are determined by interpolating from the LUT with respect to μ_0 . Since the comparison function is usually estimated roughly, it is not necessary to derive these coefficients accurately.

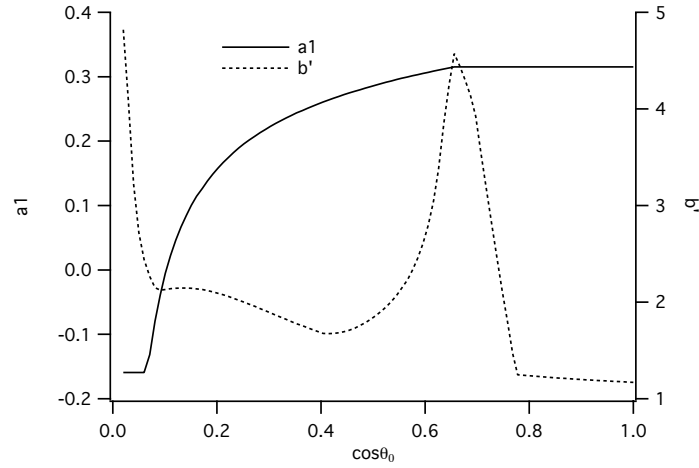


Fig. 3.6.8 Incident angle dependency of a_1, b' . This is an example where $(k_L, k_g, k_v) = (0.3, 0.07, 0.03)$.

Use of rejection method

In the following description, we ignore the argument μ_0 . The comparison function in Eq. (3.6.132) can be written by

$$h(\mu_1, \phi) = b'(a_1\mu_1 + a_0) \quad (3.6.133)$$

Since $a_1\mu_1 + a_0$ is normalized as shown in (3.6.123), μ_1 that follows this equation can be determined by solving:

$$2\pi \int_0^{\mu_1} (a_1\mu_1 + a_0) d\mu_1 = \rho_{\mu_1} \quad (3.6.134)$$

Therefore, this is a problem to solve a quadratic equation:

$$a_1\mu_1^2 + 2a_0\mu_1 - \frac{\rho_{\mu_1}}{\pi} = 0 \quad (3.6.135)$$

The solution of this equation within the range of $\mu_1 = 0-1$ is

1) If $a_1 \neq 0$

$$\mu_1 = \frac{-a_0 + \sqrt{a_0^2 + a_1 \rho_{\mu_1} / \pi}}{a_1} \quad (3.6.136a)$$

2) Else if $a_1 = 0$

$$\mu_1 = \rho_{\mu_1} \quad (3.6.136b)$$

On the other hand, the azimuth angle can be easily determined by

$$\phi = 2\pi\rho_{\phi} \quad (3.6.137)$$

The probability that the above direction is followed by the BR-PDF in the LSRT model is given by

$$\eta = \frac{P(\mu_1, \phi)}{h(\mu_1, \phi)} = \frac{\mu_1}{b'(a_1\mu_1 + a_0)} \cdot \frac{R(\mu_0, \mu_1, \phi)}{\alpha(\mu_0)} \quad (3.6.138)$$

Therefore, we use the additional random number and apply the following criteria:

$$\begin{cases} \text{If } \rho < \eta, \text{ finish} \\ \text{If } \rho \geq \eta, \text{ rejection} \end{cases} \quad (3.6.139)$$

If rejected, the new direction is selected again by (3.6.136–137). The reflected direction followed by the LSRT model can be determined by the above prescribed method.

e. Simulation example

The following is the simulation procedure:

- 1) Preparation: Development of LUT
 - Development of LUT with respect to the albedo kernel functions A_g, A_v
 - Development of the coefficients a_1, b' for comparison function
 - Calculation of average surface emission if thermal emission exists
- 2) MC simulation: Reflectance event
 - Determination of A_g, A_v and a_1, b' by interpolation of LUT
 - Calculation of albedo
 - Scaling of photon weight (albedo should be less than 1)
 - LEM: calculation of R/α
 - Determination of reflected direction
- 3) MC simulation: Thermal emission events
 - LEM: Emissivity is determined by interpolating the LUT.
 - Determination of reflected direction

Several test simulations were performed. The prescribed method had enough speed (using a Pentium IV 3.6 GHz PC, we could achieve a reflectance simulation with over 6,000,000 events). Figure 3.6.9 shows the validation results for the exact BRF and BRF calculated by the MC method. The results had fairly good accordance.

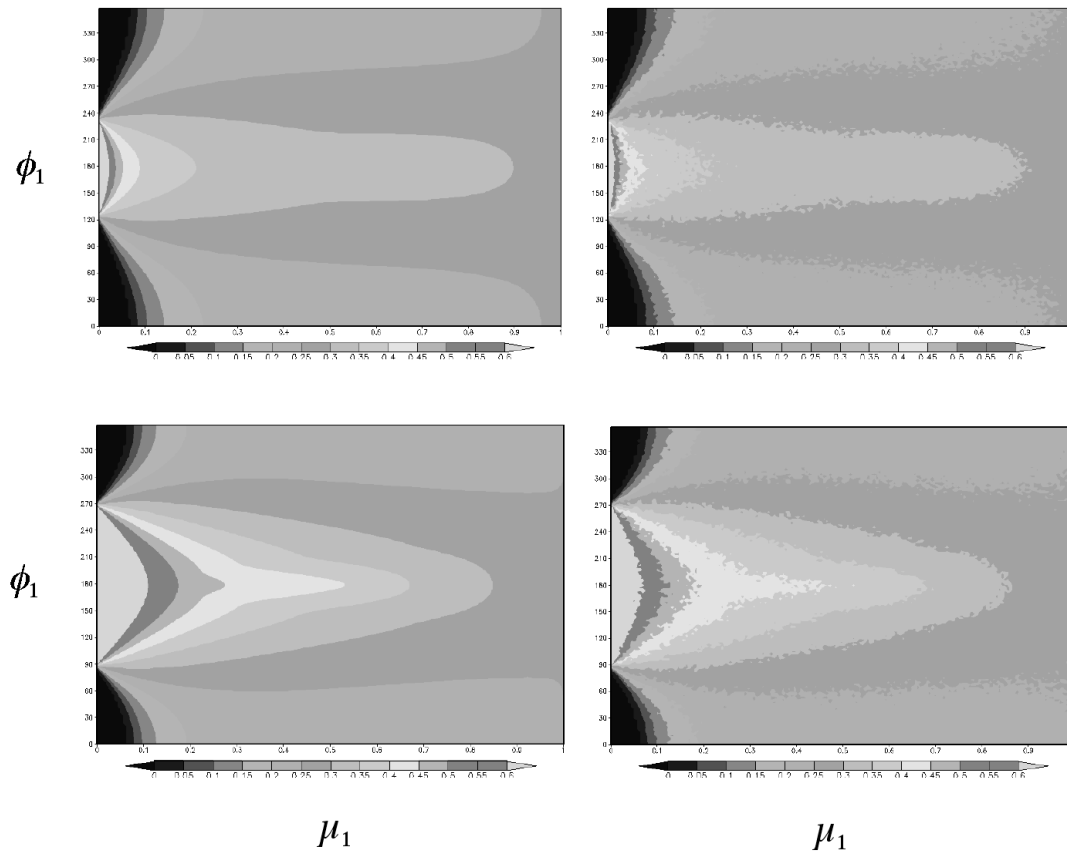


Fig. 3.6.9 Angular dependency of the BRF. The upper two examples are for a solar zenith angle of 45° and the bottom two examples are for a solar zenith angle of 60° . Left: exact simulation; right: MC simulation.

3.7 Refraction

The refraction occurs at a boundary surface where different compositions and/or different densities meet. The same phenomenon appears when light is transported in a medium in which the refractive index changes continuously. Refraction is important for describing the reflection at the ocean surface and light path bending in the atmosphere. For example, a mirage is the result of refraction. These phenomena are basically explained by Snell's law and the Fresnel equations. In this section, algorithms for simulating non-polarized intensity with a MC model are described.

3.7.1 Snell's law and Fresnel equations

Figure 3.7.1 illustrates the transmission and reflection at a boundary surface. The incident vector is Ω_0 with a zenith angle of θ_0 and $\cos\theta_0 = \mu_0$. The reflection and transmission vectors are respectively expressed by Ω_R and Ω_T . Snell's law is represented as

$$m = \frac{n_1}{n_0} = \frac{\sin\theta_0}{\sin\theta_T} \quad (3.7.1)$$

where m is the ratio of refractive indexes. For the reflection and transmission vectors,

$$\Omega_R = 2 \cos\theta_0 \mathbf{N} + \Omega_0, \quad (3.7.2a)$$

$$\Omega_T = \frac{n_0}{n_T} (\Omega_0 + \cos\theta_0 \mathbf{N}) - \cos\theta_T \mathbf{N} \quad (3.7.2b)$$

All of the energy is reflected if the light is incident from a low density medium to a high density medium, with no transmission, under the condition

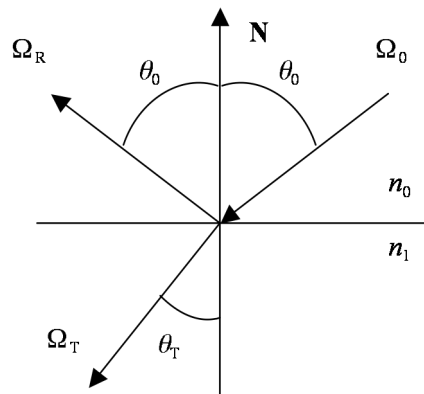


Fig. 3.7.1 Definition of vectors and angles

$$\sin \theta_0 > m \quad (3.7.3)$$

The Fresnel reflectance R_F for non-polarized incident light is given as

$$R_F = \frac{1}{2}(r_{\parallel}^2 + r_{\perp}^2) \quad (3.7.4)$$

The Fresnel coefficients modified to account for absorption are given as follows (Liou, 1992):

$$r_{\parallel}^2 = \frac{[(n^2 - k^2)\cos\theta_0 - U]^2 + [2nk\cos\theta_0 - V]^2}{[(n^2 - k^2)\cos\theta_0 + U]^2 + [2nk\cos\theta_0 + V]^2} \quad (3.7.5a)$$

$$r_{\perp}^2 = \frac{(\cos\theta_0 - U)^2 + V^2}{(\cos\theta_0 + U)^2 + V^2}, \quad (3.7.5b)$$

where n and k are respectively the real and imaginary parts of the refractive index:

$$m = n + ik \quad (3.7.6)$$

$$U^2 = \frac{1}{2}(\sqrt{G^2 + 4n^2k^2} + G) \quad (3.7.7a)$$

$$V^2 = \frac{1}{2}(\sqrt{G^2 + 4n^2k^2} - G) \quad (3.7.7b)$$

$$G = n^2 - k^2 - \sin^2 \theta_0 \quad (3.7.8c)$$

In a case with no absorption, (3.7.5) is simplified as

$$r_{\parallel} = \frac{n^2 \cos\theta_0 - \sqrt{n^2 - \sin^2 \theta_0}}{n^2 \cos\theta_0 + \sqrt{n^2 - \sin^2 \theta_0}}, \quad (3.7.9a)$$

$$r_{\perp} = \frac{\sqrt{n^2 - \sin^2 \theta_0} - \cos\theta_0}{\sqrt{n^2 - \sin^2 \theta_0} + \cos\theta_0} \quad (3.7.9b)$$

$$\frac{r_{\parallel}}{r_{\perp}} = \frac{\cos\theta_0 \sqrt{n^2 - \sin^2 \theta_0} - \sin^2 \theta_0}{\cos\theta_0 \sqrt{n^2 - \sin^2 \theta_0} + \sin^2 \theta_0} \quad (3.7.9c)$$

3.7.2 Treatment of refraction in atmosphere

The absorption can be neglected in the earth's atmosphere ($k = 0$). The refractive index anomaly from unity is proportional to the air density. The refractive index n is nearly 1, and $n - 1$ is in the order of 0.0001, for the near-surface atmosphere. Continuous change in the refractive index can be treated, but in this subsection, the atmosphere is divided into homogeneous layers, and the refraction is considered only at the layer boundaries. In the following, the previous equations are modified so as to be suitable for the MC model. Similar equations are also described in Marchuk et al. (1980).

From (3.7.2a), the reflection vector is given as

$$\begin{pmatrix} u_{xR} \\ u_{yR} \\ u_{zR} \end{pmatrix} = \begin{pmatrix} u_{x0} \\ u_{y0} \\ -u_{z0} \end{pmatrix} \quad (3.7.10)$$

With the ratio of the refractive index

$$n = \frac{n_1}{n_0} \quad (3.7.11)$$

the transmission vector is given from (3.7.2b) as

$$\begin{pmatrix} u_{xT} \\ u_{yT} \\ u_{zT} \end{pmatrix} = \frac{1}{n} \begin{pmatrix} u_{x0} \\ u_{y0} \\ \sqrt{u_{z0}^2 + n^2 - 1} \end{pmatrix} \quad (3.7.12)$$

If from (3.7.3),

$$u_{z0}^2 + n^2 - 1 < 0 \quad (3.7.13)$$

then transmission is absent, with a reflectance of 1. If the light is incident to a dense layer from a thin layer ($n > 1$), the reflectance is derived from (3.7.9) and (3.7.12):

$$R_F = \left(\frac{u_{z0} - B}{u_{z0} + B} \right)^2 \frac{u_{z0}^2 B^2 + A^2}{(u_{z0} B + A)^2} \quad (3.7.14)$$

$$A = 1 - u_{z0}^2 = u_{x0}^2 + u_{y0}^2 \quad (3.7.15)$$

$$B = \sqrt{u_{z0}^2 + n^2 - 1}$$

In contrast, if the light is incident to a thin layer from a dense layer ($n < 1$),

$$R'_F = \frac{n^2 - 1 + R_F}{n^2} \quad (3.7.16)$$

With attention to the fact that the refractive index is nearly unity, the anomaly from 1 is more useful on the numerical side:

$$n = 1 + \Delta n \quad (3.7.17)$$

Then, the following are useful:

$$\begin{aligned}\frac{1}{n} &\cong 1 - \Delta n(1 - \Delta n) \\ \frac{1}{n^2} &\cong 1 - \Delta n(2 - 3\Delta n) \\ n^2 - 1 &= \Delta n(2 + \Delta n)\end{aligned}$$

These can be used in the calculations of (3.7.12–16).

In the MC model, the reflectance is first evaluated by (3.7.14) and (3.7.16). However, the reflectance is usually very small in the earth's atmosphere. Then, a random number determines whether the light transmits or reflects. The direction after the transmission or reflection is given by (3.7.10) or (3.7.12).

3.7.3 Refractive index in earth's atmosphere

The refractive index of the atmosphere is generally a function of atmospheric composition and number density of atmospheric molecules:

$$\begin{aligned}\Delta n &\cong n - 1 \\ &= (n_s - 1) \frac{N}{N_s} = (n_s - 1) \frac{P}{P_s} \frac{T_s}{T}\end{aligned}\quad (3.7.18)$$

where N , P , and T are respectively the number density, pressure, and temperature of the atmosphere. The subscript s denotes the standard status of the atmosphere. Let us consider a dry atmosphere. The number density is represented as

$$N_s = \frac{N_A}{R^*} \cdot \frac{P_s}{T_s}\quad (3.7.19)$$

where $N_A = 6.0221367 \times 10^{23} \text{ mol}^{-1}$ is Avogadro's number and R^* is the universal gas constant.

Empirical equations of the refractive index, based on experiments, are available for dry standard atmosphere at wavelength λ (μm):

Edlén (1953):

$$\begin{aligned}(n_s - 1) \times 10^8 &= 6432.8 + \frac{2949810}{146 - \lambda^{-2}} + \frac{25540}{41 - \lambda^{-2}} \\ P_s &= 1013.25 \text{ hPa}, T_s = 288.15 \text{ K}, 300 \text{ ppm CO}_2\end{aligned}\quad (3.7.20)$$

Peck and Reeder (1972):

$$\begin{aligned}(n_s - 1) \times 10^8 &= 8060.51 + \frac{2480990}{132.274 - \lambda^{-2}} + \frac{17455.7}{39.32957 - \lambda^{-2}} \\ P_s &= 1013.25 \text{ hPa}, T_s = 288.15 \text{ K}, 300 (330?) \text{ ppm CO}_2\end{aligned}\quad (3.7.21)$$

The correction formula for CO_2 concentration (parts per volume, e.g., 360×10^{-6} for 360 ppm) is given as (Edlén (1953))

$$\frac{(n_s - 1)_{\text{CO}_2}}{(n_s - 1)_{300}} = 1 + 0.54(\text{CO}_2 - 0.0003) \quad (3.7.22)$$

Dry atmosphere is usually considered, neglecting the effect of water vapor.

3.8 Calculation of irradiance and heating rate

The forward-propagating MC model can estimate subarea-averaged irradiances and voxel-averaged heating rates at all regions in the domain, from a single simulation.

3.8.1 Definition of radiative quantities and sampling of quantities by MC method

Irradiance

The irradiance F (W m^{-2}) at a location \mathbf{r} on a plane with normal direction $\mathbf{\Omega}_c$ is the integral of the radiance I ($\text{W m}^{-2} \text{sr}^{-1}$) perpendicular component on the plane over the hemisphere:

$$F(\mathbf{\Omega}_c, \mathbf{r}) = \int_{2\pi} I(\mathbf{\Omega}, \mathbf{r}) |\mathbf{\Omega} \cdot \mathbf{\Omega}_c| d\mathbf{\Omega} \quad (3.8.1)$$

A special case of this is the irradiance on a horizontal plane:

$$F^\pm(\mathbf{r}) = \int_{2\pi} I^\pm(\mathbf{\Omega}, \mathbf{r}) |\cos \theta| d\mathbf{\Omega} \quad (3.8.2)$$

where θ is the zenith angle, and the plus/minus superscript denotes upward/downward.

Spheradiance

The spheradiance (W m^{-2}) at a location \mathbf{r} is defined as the integral of the radiance I ($\text{W m}^{-2} \text{sr}^{-1}$) over the sphere. It is the same as the so-called actinic flux or mean radiance. The spheradiance is more effective for the evaluation of the photosynthesis for vegetation and the ultraviolet radiation on a creature's body surface. The spheradiance is defined as

$$S(\mathbf{r}) = \int_{4\pi} I(\mathbf{\Omega}, \mathbf{r}) d\mathbf{\Omega} \quad (3.8.3)$$

A difference from (3.8.1) is that the spheradiance is not the integral of the perpendicular component of radiance, but simply the integral of the radiance.

Radiative heating rate

The radiative heating rate $H(\mathbf{r})$ (W m^{-3}) is the convergence of the radiative energy, with a negative value for cooling.

Area-averaged irradiance and volume-averaged radiative heating rate

The area-averaged irradiance over an area \mathbf{R}_A with a finite section of A and the volume-averaged heating rate over a region \mathbf{R}_V with a volume V are given, respectively, as

$$\bar{F}^\pm(\mathbf{R}_A) = \frac{1}{A} \int F^\pm(\mathbf{r}) dA \quad (3.8.4)$$

$$\bar{H}(\mathbf{R}_V) = \frac{1}{V} \int H(\mathbf{r}) dV \quad (3.8.5)$$

In the following, methods for calculating these quantities with the MC model are described.

Sampling of radiative quantities

When calculating the quantities of (3.8.4–5) by the MC model, estimates are integrated if the photon location is included in the region \mathbf{R}_A or \mathbf{R}_V . The irradiance and heating rate are calculated by integrating the contribution functions ψ and η :

$$\bar{F}^\pm(\mathbf{R}_A) = \frac{E_1}{A} \sum_{p=0}^N \sum_{s=0}^{\alpha(p)} \psi_{p,s}(\boldsymbol{\Omega}, \mathbf{r}) \quad (3.8.6)$$

$$\bar{H}(\mathbf{R}_V) = \frac{E_1}{V} \sum_{p=0}^N \sum_{s=0}^{\beta(p)} \eta_{p,s}(\boldsymbol{\Omega}, \mathbf{r}), \quad (3.8.7)$$

where N is the total number of model photons, α and β are the maximum number of samples, and E_1 is the radiative energy (W) transported by a single model photon:

$$E_1 = \frac{E_{\text{tot}}}{N} \quad (3.8.8)$$

where E_{tot} is the total energy emitted by all radiation sources. Several methods exist, with different points of view on the conditions and target radiative quantities.

In the following, we limit our discussion to the irradiance on a horizontal plane and heating rate. The irradiance on a non-horizontal plane and spheradiance can be calculated in a similar way.

3.8.2 Method I: Random sampling of transmittance

The optical thickness to a collision point is determined by a randomly determined transmittance. If the collision is treated, including absorption and scattering, then the MC model interprets the transmittance as 1 up to the collision point, and the transmittance changes suddenly to 0 from the point. In other words, the analytical transmittance

$$T(\mathbf{r}_0, \mathbf{r}_1) = e^{-\tau(\mathbf{r}_0, \mathbf{r}_1)} \quad (3.8.10)$$

is modified to

$$T(\mathbf{r}_0, \mathbf{r}_1) = \begin{cases} 1 & \text{for } \tau(\mathbf{r}_0, \mathbf{r}_1) \leq -\ln \rho \\ 0 & \text{for } \tau(\mathbf{r}_0, \mathbf{r}_1) > -\ln \rho \end{cases} \quad (3.8.11)$$

The absorption (heating) probability at the collision point is given as $1 - \omega$, where ω is the single scattering albedo.

When calculating the irradiance and heating rate, one choice is to use the method based on the randomly determined transmittance, as above. As for irradiance, if the model photon is incident at a sampling region \mathbf{R}_A , the model samples the following quantity:

$$\psi = w \quad (3.8.12)$$

where the photon weight is taken at the initial point of the path. For the heating rate, if the collision point is included in a region \mathbf{R}_V , the model samples

$$\eta = w(1 - \omega). \quad (3.8.13)$$

However, one might try to calculate heating rates for each component of mixed media (gases, aerosols, and clouds). In this case, the weight of (3.8.13) is subdivided into components in proportion to their respective absorption coefficients, or a randomly chosen component can be used by using a random number.

This method is simple to implement. Its deficiency is that the heating is only at collision points, and thus, the sampling frequency can be too low at optically thin regions. In such a case, the collision forcing method in 4.2 is useful.

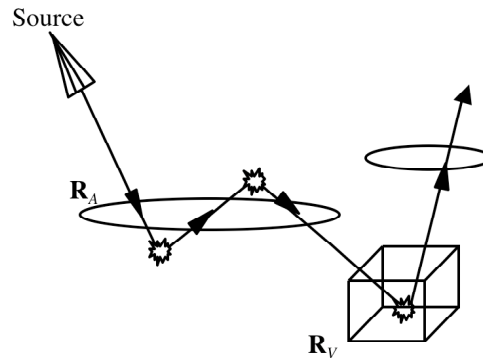


Fig. 3.8.1 Schematic of sampling method I for irradiance and heating rate.

3.8.3 Method II: Analytical sampling of transmittance

One can use just the analytical transmittance in (3.8.10) for sampling radiative quantities. This method traces a virtual trajectory from the initial point \mathbf{r}_0 for an emission/scattering/reflection event to the upper/lower boundary surface of the domain, sampling radiative quantities in the course of the ray path. The transmittance is the function of the optical thickness integrated from the initial point \mathbf{r}_0 , and the contribution function of irradiance is given as

$$\psi(\mathbf{r}) = wT(\mathbf{r}) = w e^{-\tau(\mathbf{r})} \quad (3.8.14)$$

If the ray penetrates a sampling volume for the heating rate, from a location \mathbf{r} to \mathbf{r}' , the contribution function for heating rate is

$$\begin{aligned}\eta(\mathbf{r} \rightarrow \mathbf{r}') &= w[T(\mathbf{r}) - T(\mathbf{r}')][1 - \omega(\tilde{\mathbf{r}})] \\ &= w e^{-\tau(\mathbf{r})} C(\tau(\mathbf{r}') - \tau(\mathbf{r}))[1 - \omega(\tilde{\mathbf{r}})]\end{aligned}\quad (3.8.15)$$

where $\tilde{\mathbf{r}}$ is the point of sampling the heating, and $C(x)$ is the probability of the collision within a path segment to a point with optical thickness x :

$$C(x) = 1 - e^{-x} \quad (3.8.16)$$

The sampling point $\tilde{\mathbf{r}}$ is determined randomly:

$$C(\tau(\tilde{\mathbf{r}}) - \tau(\mathbf{r})) = \rho C(\tau(\mathbf{r}') - \tau(\mathbf{r})) \quad (3.8.17)$$

It should be noted that there is no need to determine this point if the single scattering albedo is constant within the path segment between \mathbf{r} and \mathbf{r}' .

The physical trajectory of the photon packet terminates at the randomly chosen collision point, whereas the model should trace a virtual trajectory extended to the domain boundary (Fig. 3.8.2). Because with this method the model can trace the virtual trajectory up to the domain boundary, this method is useful for the frequent sampling of radiative quantities at points with very large optical thicknesses compared to the emission point.

High accuracy can be expected for this method due to the analytical calculation of the sampled energy. On the other hand, this method requires time-consuming ray tracing and the evaluation of a numerically intensive function, the exponential function, many times. When comparing its numerical efficiency with method I, which is better one depends on the problem, extinction coefficient, inhomogeneity, geometrical complexity, and radiative quantity of the interest. Method I samples energy only at the collision points, whereas method II samples many points within the path. Method II is efficient for calculating heating rates in optically thin media.

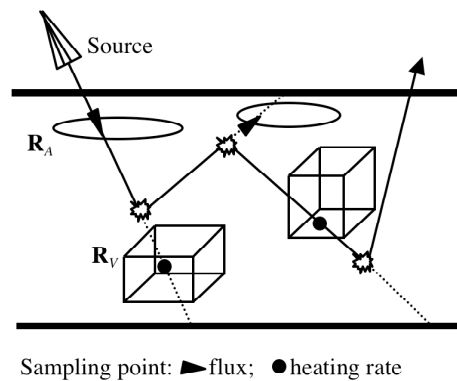


Fig. 3.8.2 Schematic of sampling method II for irradiance and radiative heating rate.

Method II requires the calculation of the geometrical and optical path lengths every time the photon packet penetrates a voxel. Therefore, the MCS method (described in 4.1) cannot be used with method II. This is the reason that the method is inefficient in a case where the domain is divided into many small volume elements.

3.8.4 Method III: Hybrid method

Another possible choice is a hybrid of methods I and II. The transmittance is treated analytically up to a threshold T_{\min} and by the MC method subsequently for larger optical thicknesses:

$$T(\mathbf{r}) = \begin{cases} e^{-\tau(\mathbf{r})} & \text{for } \tau(\mathbf{r}) \leq \tau_{\max} \\ e^{-\tau_{\max}} & \text{for } \tau_{\max} < \tau(\mathbf{r}) \leq \tau_{\max} + \tau_{\text{free}} \\ 0 & \text{for } \tau_{\max} + \tau_{\text{free}} < \tau(\mathbf{r}) \end{cases} \quad (3.8.18)$$

where

$$T_{\min} = e^{-\tau_{\max}} \quad (3.8.19a)$$

$$\tau_{\text{free}} = -\ln \rho \quad (3.8.19b)$$

Figure 3.8.3 shows the transmittance schematically. The model should always trace the photon packet up to the point with an optical thickness of τ_{\max} . However, it is not necessary to trace the photon packet up to the domain boundary.

Sampled contributions of irradiance and heating rate are respectively

$$\psi(\mathbf{r}) = wT(\mathbf{r}) \quad (3.8.20)$$

$$\eta(\mathbf{r} \rightarrow \mathbf{r}') = w[T(\mathbf{r}) - T(\mathbf{r}')][1 - \omega(\tilde{\mathbf{r}})] \quad (3.8.21)$$

The sampling point for the heating could be determined in a way similar to method II:

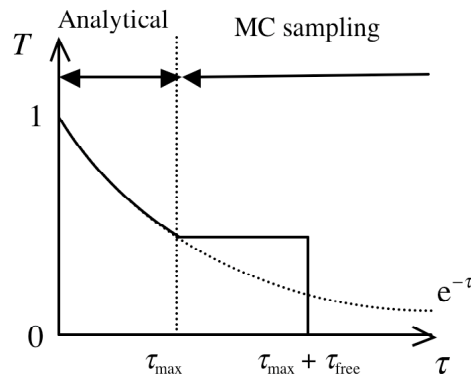


Fig. 3.8.3 Transmittance in method III

$$T(\tau(\mathbf{r})) - T(\tau(\tilde{\mathbf{r}})) = \rho [T(\tau(\mathbf{r})) - T(\tau(\mathbf{r}'))] \quad (3.8.22)$$

There is no requirement to determine the point $\tilde{\mathbf{r}}$ if the single scattering albedo is constant between \mathbf{r} and \mathbf{r}' .

Different sampling methods could be used for respective orders of scattering. For example, a possible method would be to use the hybrid method for a direct beam and first-order scattering light and subsequently use method I for multiple scattering light.

3.8.5 Method IV: Use of equivalence theorem for absorption

As previously noted, it is possible to treat the scattering as a random process by the MC method and to treat the absorption continuously by analytical expression. This is an application of the equivalence theorem. In this case, the collision point is solely determined by the distribution of the scattering coefficient, and the photon weight is scaled by the transmittance due to the continuous absorption within the path the photon penetrated. The transmittance is solely a function of the absorption optical thickness τ_a (see Fig. 3.8.4):

$$T(\mathbf{r}) = \begin{cases} e^{-\tau_a(\mathbf{r})} & \text{for } \tau_s(\mathbf{r}) \leq \tau_{\text{free}} \\ 0 & \text{for } \tau_s(\mathbf{r}) > \tau_{\text{free}} \end{cases} \quad (3.8.23)$$

The optical thicknesses for the absorption and scattering are respectively

$$\tau_a(\mathbf{r}) = \int_{\mathbf{r}_0 \rightarrow \mathbf{r}} \beta_a(t) dt; \quad t = |\mathbf{r}' - \mathbf{r}_0| \quad (3.8.24a)$$

$$\tau_s(\mathbf{r}) = \int_{\mathbf{r}_0 \rightarrow \mathbf{r}} \beta_s(t) dt; \quad t = |\mathbf{r}' - \mathbf{r}_0| \quad (3.8.24b)$$

The irradiance and heating rate are sampled at many points on the photon path for $\tau < \tau_{\text{free}}$. Each sampled contribution is given as follows:

$$\psi(\mathbf{r}) = wT(\mathbf{r}) \quad (3.8.25)$$

$$\eta(\mathbf{r} \rightarrow \mathbf{r}') = w[T(\mathbf{r}) - T(\mathbf{r}')] \quad (3.8.26)$$

This method has good efficiency for calculating the heating rate, compared with method I. However, this method requires multiple calculations of the computationally intensive exponential function, as in methods II and III, making the computation time longer than method I. In addition, this method requires the calculation of the geometrical and optical path lengths every time the photon packet penetrates a voxel, as in methods II and III. Therefore, the MCS method (described in 4.1) cannot be used, which is a deficiency of method IV.

An advantage of this method is that simultaneous calculations for many different wavelengths (with different absorption coefficients) are easy. If the scattering properties are the same for different wavelengths, the photon path could be common for all wavelengths, with the only difference being the transmittance of (3.8.23). The scattering properties of clouds, aerosols,

and gases are usually functions that change slowly with wavelength and could be approximated as constant within a narrow band. On the other hand, gaseous absorption coefficients can vary significantly, even within a narrow band. If the photon weight is calculated according to (3.8.23), simultaneous calculations for multiple wavelengths are possible and efficient. This method is efficient also when calculating band-averaged radiative quantities.

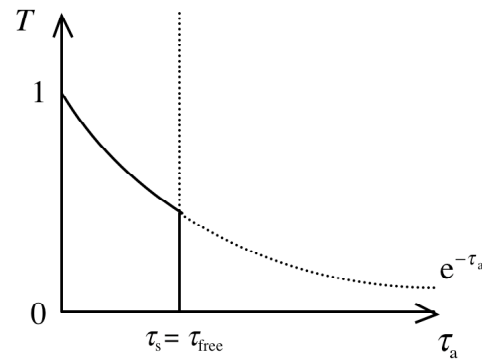


Fig. 3.8.4 Transmittance in method IV: Absorption is continuously treated, and the scattering event occurs at a point with τ_{free} .

3.9 LEM

The LEM (Marchuk et al., 1980; Evans and Marshak, 2005) calculates the analytical energy that is scattered at the collision point and transmitted to a certain point of interest. The following quantities could be calculated by the LEM, for example:

- Area-averaged radiance in a specific direction on a plane with arbitrary orientation
- Angular-averaged radiative quantities (radiance and irradiance) at a point

3.9.1 Formulas for local estimate

The LEM samples analytical contribution functions at each instance of source emission, scattering, or reflection, from the event point to the detector surface of the sensor of interest. Area-averaged radiance on an arbitrary plane and angular-averaged radiance on a point, or irradiance and spheradiance at a point, could be calculated by this method.

The method samples the contribution function of an event at a location \mathbf{r}_0 :

$$\zeta(\mathbf{\Omega}_1, \mathbf{r}_1) = w\Psi(\mathbf{\Omega}_0, \mathbf{\Omega}_1)T(\mathbf{r}_0, \mathbf{r}_1), \quad (3.9.1)$$

where w is the photon weight just after the emission/scattering/reflection event, Ψ is the PDF for angular distribution, and T is the transmittance between the point \mathbf{r}_0 and the detector location \mathbf{r}_1 . The transmittance is a function of the optical thickness:

$$T(\mathbf{r}_0, \mathbf{r}_1) = e^{-\tau(\mathbf{r}_0, \mathbf{r}_1)}, \quad (3.9.2a)$$

$$\tau(\mathbf{r}_0, \mathbf{r}_1) = \int_{\mathbf{r}_0 \rightarrow \mathbf{r}_1} \beta_e(t) dt; \quad t = |\mathbf{r}' - \mathbf{r}_0|. \quad (3.9.2b)$$

Ray tracing is required to calculate the optical thickness in (3.9.2b), for the path between \mathbf{r}_0 and \mathbf{r}_1 . The PDF for the angular distribution is normalized as

$$\int_{4\pi} \Psi(\mathbf{\Omega}_0, \mathbf{\Omega}_1) |\cos\theta_1| d\mathbf{\Omega} = 1. \quad (3.9.3)$$

The detection point \mathbf{r}_1 should be on the line oriented to the direction $\mathbf{\Omega}_1$ from the event point \mathbf{r}_0 . Thus,

$$\mathbf{\Omega}_1 = \frac{\mathbf{r}_1 - \mathbf{r}_0}{|\mathbf{r}_1 - \mathbf{r}_0|} \quad (3.9.4)$$

Generally, radiative quantities can be written in the form of the sum of the contribution functions for all events:

$$Q = \sum_{p=0}^{N_p} \sum_{s=0}^{N_s(p)} E_1 \psi_{p,s}(\boldsymbol{\Omega}_1, \mathbf{r}_1) \Xi_{p,s}(\boldsymbol{\Omega}_1, \mathbf{r}_1) \quad (3.9.5a)$$

$$\Xi_{p,s}(\boldsymbol{\Omega}_1, \mathbf{r}_1) = \begin{cases} 1 & \text{if } \boldsymbol{\Omega}_1 \in \mathbf{U} \text{ and } \mathbf{r}_1 \in \mathbf{R} \\ 0 & \text{otherwise} \end{cases} \quad (3.9.5b)$$

where N_p is the total number of model photons, N_s is the maximum order of scattering, \mathbf{U} is the volume of the direction vectors within the sensor field of view, and \mathbf{R} is the volume of the location vectors for the incident points at the detector surface. E_1 denotes the radiative energy (W) transported by a single model photon with a weight of 1:

$$E_1 = \frac{E_{\text{tot}}}{N_p} \quad (3.9.6)$$

where E_{tot} is the total source energy.

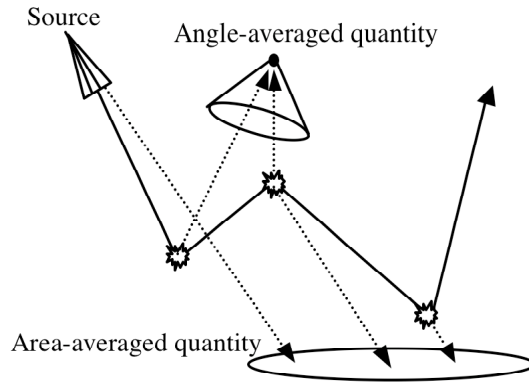


Fig. 3.9.1 Schematic of sampling by local estimation.

Area-averaged radiance

The area-averaged radiance ($\text{W m}^{-2} \text{sr}^{-1}$) for a direction $\boldsymbol{\Omega}_1$ in an arbitrary horizontal area \mathbf{R} with a cross section A is defined as

$$\bar{I}(\boldsymbol{\Omega}_1, \mathbf{R}) = \frac{\int_{\mathbf{R}} I(\boldsymbol{\Omega}_1, \mathbf{r}_1) dA}{\int_{\mathbf{R}} dA} = \frac{1}{A} \int_{\mathbf{R}} I(\boldsymbol{\Omega}_1, \mathbf{r}_1) dA \quad (3.9.7)$$

Using the LEM, the function of (3.9.5) for this kind of averaged radiance is written as

$$\psi(\boldsymbol{\Omega}_1, \mathbf{r}_1) = \frac{\zeta(\boldsymbol{\Omega}_1, \mathbf{r}_1)}{A} \quad (3.9.8)$$

Local radiance averaged over solid angle

The local radiance ($\text{W m}^{-2} \text{sr}^{-1}$) at a point \mathbf{r}_1 averaged over an angular region \mathbf{U} with a solid angle of ξ is defined as

$$\tilde{I}(\mathbf{U}, \mathbf{r}_1) = \frac{\int_{\mathbf{U}} I(\boldsymbol{\Omega}_1, \mathbf{r}_1) d\xi}{\int_{\mathbf{U}} d\xi} = \frac{1}{\xi} \int_{\mathbf{U}} I(\boldsymbol{\Omega}_1, \mathbf{r}_1) d\xi \quad (3.9.9)$$

The small cross section dA at the point \mathbf{r}_0 is associated with a small solid angle $d\xi$ at another point \mathbf{r}_1 as follows:

$$d\xi = dA \cdot \frac{|\cos \theta_1|}{|\mathbf{r}_1 - \mathbf{r}_0|^2} \quad (3.9.10)$$

Using this, the function ψ for calculating the angular-averaged radiance by the LEM is derived as

$$\psi(\boldsymbol{\Omega}_1, \mathbf{r}_1) = \frac{\zeta(\boldsymbol{\Omega}_1, \mathbf{r}_1)}{\xi} \frac{|\cos \theta_1|}{|\mathbf{r}_1 - \mathbf{r}_0|^2} \quad (3.9.11)$$

MC integration of this type is difficult, because theoretically, the variance could become infinite due to the dependence of ψ on the distance $|\mathbf{r}_1 - \mathbf{r}_0|$. A large number of photons do not help to get convergence. For example, a 100 times larger contribution is sampled if a scattering event occurs at a point 10 times closer to the detector of interest. Variance reduction methods for this kind of problem are discussed in Marchuk et al. (1980).

Local irradiance and spheradiance

The irradiance (W m^{-2}) at a point \mathbf{r}_1 on a plane oriented in a direction $\boldsymbol{\Omega}_c$ integrated over an angular region \mathbf{U} in the hemisphere is defined as

$$\bar{F}(\mathbf{U}, \mathbf{r}_1) = \int_{2\pi} I(\boldsymbol{\Omega}_1, \mathbf{r}_1) |\boldsymbol{\Omega}_1 \cdot \boldsymbol{\Omega}_c| d\boldsymbol{\Omega}_1 \quad (3.9.12)$$

The sampled contribution by the LEM is:

$$\psi(\boldsymbol{\Omega}_1, \mathbf{r}_1) = \zeta(\boldsymbol{\Omega}_1, \mathbf{r}_1) \frac{|\cos \theta_1|}{|\mathbf{r}_1 - \mathbf{r}_0|^2} |\boldsymbol{\Omega}_1 \cdot \boldsymbol{\Omega}_c| \quad (3.9.13)$$

Radiative quantities integrated over an arbitrary angular region (not just for the hemisphere) could be similarly derived.

A special case is the irradiance on a horizontal plane:

$$\bar{F}(\mathbf{U}, \mathbf{r}_1) = \int_{2\pi} I(\boldsymbol{\Omega}_1, \mathbf{r}_1) |\cos \theta_1| d\boldsymbol{\Omega}_1 \quad (3.9.14)$$

For this quantity, the contribution by the LEM becomes

$$\psi(\boldsymbol{\Omega}_1, \mathbf{r}_1) = \zeta(\boldsymbol{\Omega}_1, \mathbf{r}_1) \frac{|\cos \theta_1|^2}{|\mathbf{r}_1 - \mathbf{r}_0|^2} \quad (3.9.15)$$

The spheradiance (or actinic flux) (W m^{-2}) at a point \mathbf{r}_1 is defined as

$$\hat{F}(\mathbf{r}_1) = \int_{4\pi} I(\boldsymbol{\Omega}_1, \mathbf{r}_1) d\boldsymbol{\Omega}_1 \quad (3.9.16)$$

This quantity is defined as a simple integration of the radiance with an equal weight given to all directions, being different from the projection to a specific plane as the irradiance in (3.9.12). For example, the spheradiance is more important for the evaluation of plant photosynthesis or the ultraviolet radiation absorbed by a living body. The contribution for this quantity when using the LEM should be

$$\psi(\boldsymbol{\Omega}_1, \mathbf{r}_1) = \zeta(\boldsymbol{\Omega}_1, \mathbf{r}_1) \frac{|\cos \theta_1|}{|\mathbf{r}_1 - \mathbf{r}_0|^2} \quad (3.9.17)$$

3.9.2 Definition of PDF for angular distribution

Scattering by particles in the atmosphere

$$\Psi(\theta_0, \phi_0, \theta_1, \phi_1) = \frac{P(\theta_0, \phi_0, \theta_1, \phi_1)}{4\pi |\cos \theta_1|} \quad (3.9.18)$$

where P is the scattering phase function normalized as:

$$\frac{1}{4\pi} \int_{4\pi} P(\theta_0, \phi_0, \theta_1, \phi_1) d\boldsymbol{\Omega}_1 = 1 \quad (3.9.19)$$

For isotropic scattering, $P = 1$.

Reflection at surface

$$\Psi(\theta_0, \phi_0, \theta_1, \phi_1) = \frac{R(\theta_0, \phi_0, \theta_1, \phi_1)}{\alpha(\theta_0, \phi_0)} \quad (3.9.20)$$

where R is the BRDF, and α is the black-sky albedo. The BRDF is normalized as

$$\int_{2\pi} R(\theta_0, \phi_0, \theta_1, \phi_1) |\cos \theta_1| d\Omega = \alpha(\theta_0, \phi_0) \quad (3.9.21)$$

For Lambertian reflection, $R = \alpha/\pi$.

Emission of thermal radiation in atmosphere

$$\Psi(\theta_0, \phi_0, \theta_1, \phi_1) = \frac{1}{4\pi |\cos \theta_1|} \quad (3.9.22)$$

This is the same as the case for isotropic scattering.

Emission of thermal radiation from surface

$$\Psi(\theta_0, \phi_0, \theta_1, \phi_1) = \frac{\varepsilon(\theta_0)}{\pi \varepsilon}, \quad (3.9.23)$$

where ε is the emissivity, which is represented by the reflectance (albedo) α :

$$\varepsilon(\mu_0) = 1 - \alpha(\mu_0). \quad (3.9.24)$$

The mean reflectance and mean emittance are respectively

$$\bar{\alpha} = 2 \int_0^1 \alpha(\mu_0) \mu_0 d\mu_0 \quad (3.9.25a)$$

$$\bar{\varepsilon} = 1 - \bar{\alpha} \quad (3.9.25b)$$

For example, $\Psi = 1/\pi$ for a Lambertian surface.

Isotropic source emission in conical angular region (as in solar incidence from above)

$$\Psi(\theta_0, \phi_0, \theta_1, \phi_1) = \begin{cases} \frac{1}{\bar{v}(\Theta, \Delta)} & \text{if } \mathbf{\Omega}_1 \cdot \mathbf{\Omega}_0 > \cos \Delta \\ 0 & \text{if } \mathbf{\Omega}_1 \cdot \mathbf{\Omega}_0 \leq \cos \Delta \end{cases} \quad (3.9.26)$$

where Δ is the half cone angle for the angular region, and Θ is the zenith angle for the center direction:

$$\bar{v}(\Theta, \Delta) = \int_0^{2\pi} \int_{\cos \Delta}^1 |\cos \theta| d \cos \hat{\theta} d \hat{\phi} \quad (3.9.27a)$$

$$\cos \theta = \sin \Theta \sin \hat{\theta} \cos \hat{\phi} - \cos \Theta \cos \hat{\theta} \quad (3.9.27b)$$

If the angular region does not include the horizontal directions ($\cos \Delta > \sin \Theta$),

$$\bar{v}(\Theta, \Delta) = \pi |\cos \Theta| \sin^2 \Delta.$$

In a special case where $|\cos \Theta| = 1$ and $\Delta = \pi/2$,

$$\Psi(\theta_0, \phi_0, \theta_1, \phi_1) = \begin{cases} \frac{1}{\pi} & \text{if } \mathbf{\Omega}_1 \cdot \mathbf{\Omega}_0 > 0 \\ 0 & \text{if } \mathbf{\Omega}_1 \cdot \mathbf{\Omega}_0 \leq 0 \end{cases} \quad (3.9.28)$$

which is the same as for a Lambertian surface. In general cases, the calculation method for the function in (3.9.27a) is described in 3.2.

3.10 Treatment of atmospheric sphericity

The radiative transfer in a planetary atmosphere should generally be treated as a spherical shell on a sphere or spheroid surface. Usually, the atmosphere could be approximated as plane-parallel. An exception is the case where the light travels in near-horizontal directions. For example, the sphericity is very important when simulating light intensity at sunrise or sunset with a low sun altitude, or when the instrument views a near-horizontal direction. The ray bending due to refraction in the atmosphere is also important in these cases.

This section gives a correction of the atmospheric sphericity for calculating the radiances using the LEM. In particular, a correction is discussed for the line of sight (from the scattering event point to the detector surface).

3.10.1 Characteristics of sphericity effect

When calculating the radiance by the LEM in 3.9, the following contribution function is sampled:

$$\zeta(\mathbf{\Omega}_1, \mathbf{r}_1) = w\Psi(\mathbf{\Omega}_0, \mathbf{\Omega}_1)T(\mathbf{r}_0, \mathbf{r}_1) \quad (3.10.1)$$

where w is the photon weight just after the scattering (or reflection) event, Ψ is the normalized PDF (sr^{-1}) for the angular distribution, and T is the transmittance between the scattering point \mathbf{r}_0 and the detection point \mathbf{r}_1 . The transmittance is a function of the optical thickness:

$$T(\mathbf{r}_0, \mathbf{r}_1) = e^{-\tau(\mathbf{r}_0, \mathbf{r}_1)}. \quad (3.10.2a)$$

$$\tau(\mathbf{r}_0, \mathbf{r}_1) = \int_{\mathbf{r}_0 \rightarrow \mathbf{r}_1} \beta_e(t) dt; \quad t = |\mathbf{r}' - \mathbf{r}_0| \quad (3.10.2b)$$

The function Ψ is given, for the scattering by a particle in the atmosphere, as

$$\Psi(\mathbf{\Omega}_0, \mathbf{\Omega}_1) = \frac{P(\mathbf{\Omega}_0, \mathbf{\Omega}_1)}{4\pi|\cos\theta_1|} \quad (3.10.3)$$

where P is the scattering phase function. For surface reflection,

$$\Psi(\mathbf{\Omega}_0, \mathbf{\Omega}_1) = \frac{R(\mathbf{\Omega}_0, \mathbf{\Omega}_1)}{\alpha(\mathbf{\Omega}_0)} \quad (3.10.4)$$

where R is the BRDF, and α is the black-sky albedo.

If the atmosphere is plane-parallel and the refraction is neglected, then the line of sight is a straight line. The scattering direction is equal to the direction at the detection point (left side of Fig. 3.10.1). For a spherical atmosphere with refraction, the light bends in the line of sight, and the direction at the detection point differs from the scattering direction (right side of Fig. 3.10.1).

The function Ψ of (3.10.1) should be different between plane-parallel and spherical atmospheres. In addition, the transmittance is also different because optical and geometrical path lengths are different between plane-parallel and spherical atmospheres.

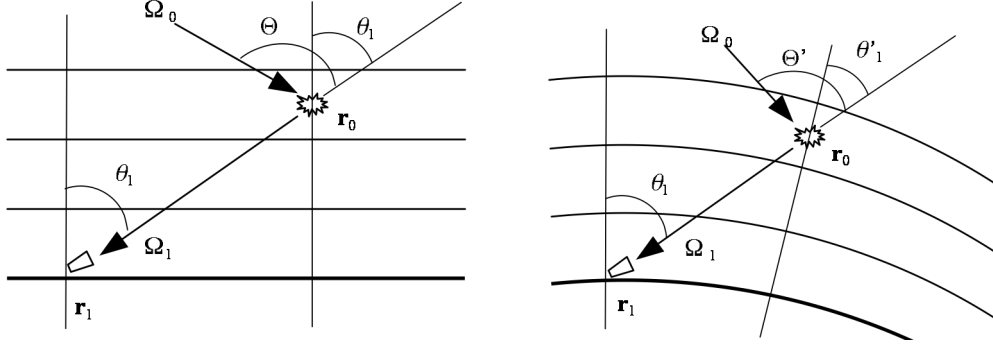


Fig. 3.10.1 Schematic of radiance sampling. Left: plane-parallel atmosphere, right: spherical-shell atmosphere.

3.10.2 Correction of sphericity effect for line of sight

Let us derive a path length a that corresponds to the height difference Δ , in the spherical atmosphere, and the angle A between the path direction and the local normal vector (from the zero point at the center of the planet). The beginning and end points are respectively C and B , and the corresponding distances from the planet center are b and c (see Fig. 3.10.2 for definitions). By representing the planet radius with R_p ,

$$c = R_p + c' \quad (3.10.5a)$$

$$b = R_p + b' \quad (3.10.5b)$$

The height difference is given as

$$\Delta = c - b = c' - b' \quad (3.10.6)$$

The light path has a cross point on the line of sight under the following condition:

$$-\Delta < b(1 - \sin C) = b \frac{\cos^2 C}{1 + \sin C} = (R_p + b') \frac{\cos^2 \theta_1}{1 + \sin \theta_1} \quad (3.10.7)$$

If this condition is false, no light trajectory is possible to travel from point C to point B (in the spherical atmosphere). This could be possible if the ray is downward with a negative Δ .

From the law of cosines, the path length a is given by

$$\begin{aligned} a^2 &= b^2 + c^2 - 2bc \cos A \\ &= 2(1 - \cos A)c(c - \Delta) + \Delta^2 \end{aligned} \quad (3.10.8)$$

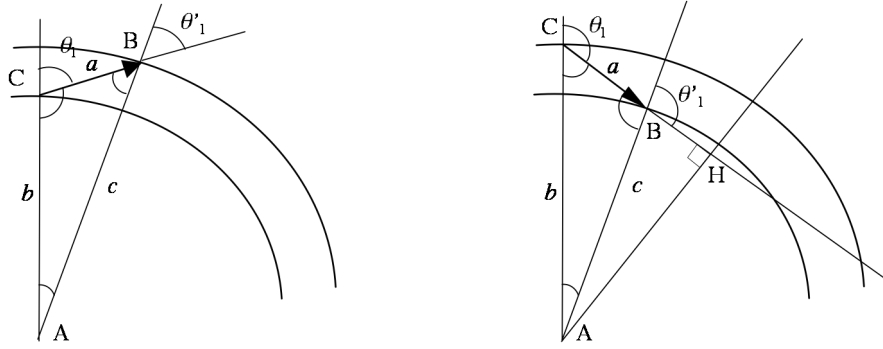


Fig. 3.10.2 Geometry in the spherical-shell atmosphere. Left: upward ray, right downward ray.

The law of sines determines the angle A , using $B = \pi - A - C$

$$b \sin C = c \sin B \quad (3.10.9a)$$

$$= c \sin(A+C)$$

$$\sin(A+C) - \frac{b}{c} \sin C = 0 \quad (3.10.9b)$$

$$\sin(A+C) - (1-\delta) \sin C = 0 \quad (3.10.9c)$$

This could be solved for A . In the above,

$$\delta = \frac{\Delta}{c} = \frac{\Delta}{R_p + c'} \quad (3.10.10)$$

Because the planet is large compared with the atmospheric depth, δ is usually very small. We should exercise special caution on this point because of the numerical problem of calculating a very small A :

$$A = \sin^{-1}((1-\delta) \sin C) - C \quad (3.10.11)$$

It is problematic to compute this formula with a computer because it rounds off. In practice, accurate calculation is possible using the following method.

a. Calculation of A by numerical method

Let us derive first the term

$$\sin^{-1}((1-\delta) \sin C) \quad (3.10.12)$$

in (3.10.11). This is the solution of

$$f(x) = \sin x - (1 - \delta) \sin C = 0 \quad (3.10.13)$$

The derivative is

$$f'(x) = \cos x \quad (3.10.14)$$

Using the Newtonian method, a sequence of numbers could be derived:

$$x_{i+1} = x_i - \Delta x_i \quad (3.10.15a)$$

$$\Delta x_i = \frac{f(x_i)}{f'(x_i)} \quad (3.10.15b)$$

With an initial estimate

$$x_0 = C \quad (3.10.16)$$

the solution of (3.10.9) is

$$x = C - \sum_{i=0}^{\infty} \Delta x_i \quad (3.10.17)$$

From (3.10.15b) and (3.10.16),

$$\Delta x_0 = \frac{f(C)}{f'(C)} = \delta \frac{\sin C}{\cos C} \quad (3.10.18)$$

Finally, the angle A of (3.10.11) can be computed by

$$A = -\sum_{i=0}^{\infty} \Delta x_i = -\delta \frac{\sin C}{\cos C} - \sum_{i=1}^{\infty} \Delta x_i \quad (3.10.19)$$

The first-order approximation is as follows:

$$A \approx -\delta \frac{\sin C}{\cos C} \geq 0 \quad (3.10.20)$$

The calculation algorithm for (3.10.19) is as follows:

1) Compute the initial estimate A_0 :

$$A_0 = -\delta \frac{\sin C}{\cos C} \quad (3.10.21)$$

2) Compute the following:

$$p = \sin A_i \approx A_i - \frac{1}{6} A_i^3 + \frac{1}{120} A_i^5 - \dots \quad (3.10.22a)$$

$$q = \cos A_i \approx 1 - \frac{1}{2} A_i^2 + \frac{1}{24} A_i^4 - \dots \quad (3.10.22b)$$

$$r = 1 - \cos A_i = \frac{\sin^2 A_i}{1 + \cos A_i} = \frac{p^2}{1 + q} \quad (3.10.23c)$$

3) Compute Δx_i :

$$\begin{aligned} f(C + A_i) &= \sin(C + A_i) - (1 - \delta) \sin C \\ &= p \cos C - (r - \delta) \sin C \end{aligned} \quad (3.10.24a)$$

$$f'(C + A_i) = q \cos C - p \sin C \quad (3.10.24b)$$

$$\therefore \Delta x_i = \frac{f(C + A_i)}{f'(C + A_i)} = \frac{(p \cos C - r \sin C) + \delta \sin C}{q \cos C - p \sin C} \quad (3.10.24c)$$

$$4) A_{i+1} = A_i - \Delta x_i \quad (3.10.25)$$

5) If Δx_i is small enough compared with A_i , then finish, else return to (2).

This iteration usually converges within two cycles.

b. Correction of geometrical and optical path lengths

The path length is derived substituting (3.10.22c) into (3.10.8)

$$a = \sqrt{2rc(c - \Delta) + \Delta^2} \quad (3.10.26)$$

This equation gives a better result than using the law of sines. The corresponding path length in the plane-parallel geometry is

$$\frac{\Delta}{-\cos C}. \quad (3.10.27)$$

Therefore, by the spherical effect, the path length is factored by

$$\frac{-a \cos C}{\Delta} \quad (3.10.28)$$

c. Correction of local zenith angle

The local zenith angle for the line of sight rotates by the angle A up to the end of a path of length a . Only the zenith angle changes, with the azimuth unaltered. With the zenith angle θ for the ray,

Upward tracing: $\cos \theta > 0$

Downward tracing: $\cos \theta < 0$

In both cases, the local zenith angle at the terminal point is determined using (3.10.22a,b):

$$\theta' = \theta - A \quad (3.10.29a)$$

$$\sin \theta' = \sin \theta \cos A - \cos \theta \sin A = q \sin \theta - p \cos \theta \quad (3.10.29b)$$

$$\cos \theta' = \cos \theta \cos A + \sin \theta \sin A = q \cos \theta + p \sin \theta \quad (3.10.29c)$$

The angle A is always larger than 0 , and the zenith angle should decrease, not depending on the upward or downward direction.

d. Implementation algorithm

In practice, the refraction in the multilayered atmosphere should be included. For simplicity, the refraction occurs only at the layer boundaries. The sphericity correction, modification of the zenith angle by (3.10.29), is applied every time the photon packet penetrates a layer in the line of sight. The direction is modified at layer boundaries due to refraction. The following is a possible algorithm:

- 1) First, one should know the direction Ω'_1 at the last scattering point, when the direction of the radiance of interest is Ω_1 . For this, the ray is traced in the backward trajectory from the detector to the altitude of the scattering event at \mathbf{r}_0 , and the direction Ω'_1 is obtained. The refraction and sphericity should be included when tracing the backward trajectory.
- 2) Determine the PDF $\Psi(\Omega_0, \Omega'_1)$ for the angular distribution at the scattering point \mathbf{r}_0 .
- 3) Start the ray tracing from the scattering point to the detection point \mathbf{r}_1 . The optical thickness and geometrical path lengths at each layer are computed. The refraction and sphericity should be included in this step.

To accelerate the calculation of (1), an LUT would be useful. The LUT should tabulate the directions at the initial points at various altitudes.

It should be noted that a light path may not always reach the destination altitude from an arbitrary altitude, if the refraction and sphericity are included.

Figure 3.10.3 shows the effects of refraction and sphericity for the radiance at the surface and normalized average path length (air mass factor, AMF).

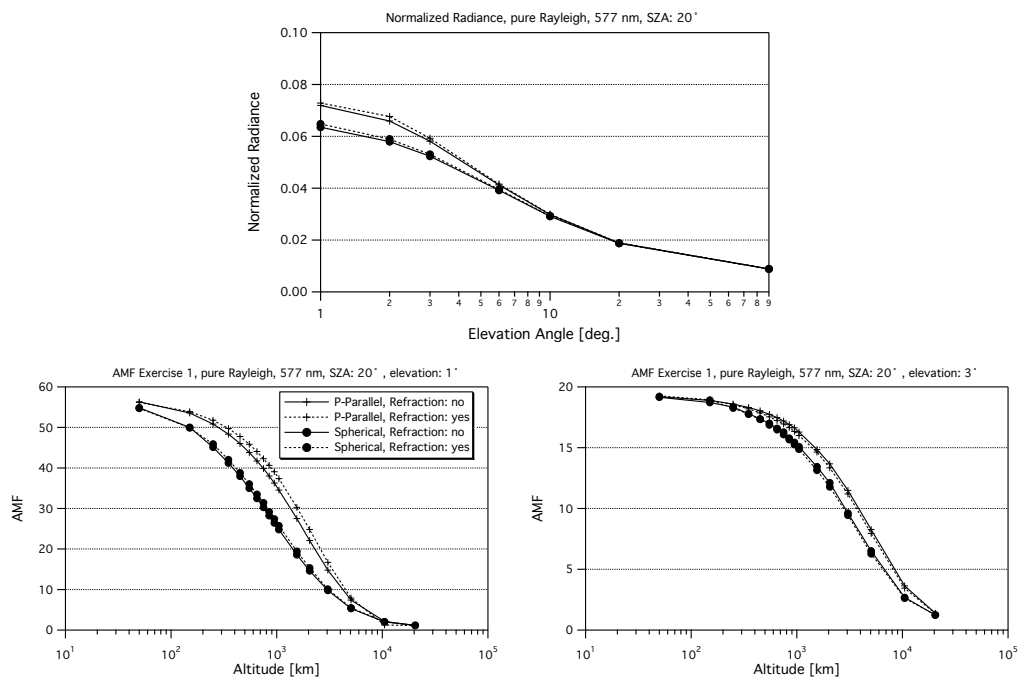


Fig. 3.10.3 Effects of refraction and sphericity for the radiance at the surface and normalized average path length (air mass factor, AMF).

3.11 Spectral integration

Here, we describe an integration method for the physical quantity over a broad wavelength domain. In the MC method, it is possible to achieve the same computation time as for a monochromatic wavelength. This is one of the advantages of the MC method.

In this section, two different meanings of “photon” are mixed: a light photon (or light quantum) and the modeled photon as a sampling unit in the MC method. We should clearly distinguish these two.

3.11.1 Extraterrestrial solar irradiance and photon flux density

Figure 3.11.1(a) shows a spectral solar irradiance at the top of the atmosphere F_λ ($\text{W m}^{-2} \mu\text{m}^{-1}$). The incoming solar irradiance with the solar zenith angle θ_s is $F_\lambda \cos(\theta_s)$. Figure 3.11.1(b) shows a spectral solar photon flux density Q_λ ($\mu\text{mol m}^{-2} \text{s}^{-1} \mu\text{m}^{-1}$). The photon flux density Q_λ can be derived from the irradiance F_λ . The energy of the single light photon E_p is expressed by

$$E_p = ch/\lambda \quad (3.11.1)$$

where c ($= 2.997 \times 10^8 \text{ m s}^{-1}$) is the velocity of light and h ($= 6.626 \times 10^{-34}$) is Planck’s constant. The irradiance F_λ can be converted to photon flux density N :

$$N = F_\lambda / E_p \quad (3.11.2)$$

Hence, when (3.11.2) is rewritten using the mol unit ($\mu\text{mol m}^{-2} \text{s}^{-1} \mu\text{m}^{-1}$), Q_λ becomes

$$Q_\lambda = N / N_A = \frac{1}{chN_A} \lambda F_\lambda \quad (3.11.3)$$

where N_A is Avogadro’s number. The energy of a single light photon is inversely proportional to the wavelength. Therefore, the energy of a single photon becomes smaller at longer wavelengths. In other words, the number of photons increases with longer wavelengths at the same energy level. When we compare the extraterrestrial spectral solar irradiance and photon flux density (Fig. 3.11.1 (c)), the photon flux density peak is located at a longer wavelength than the solar irradiance.

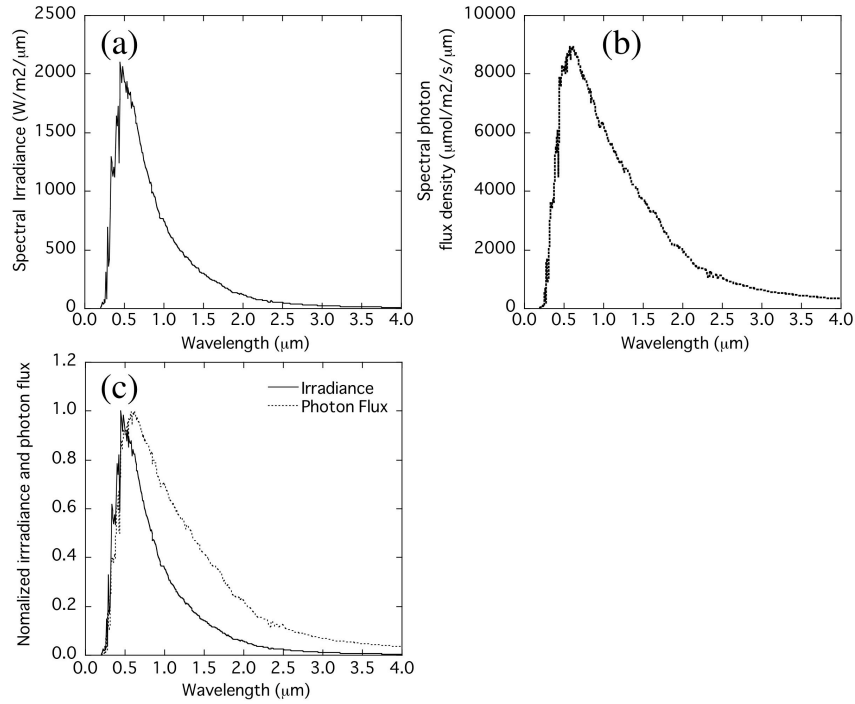


Fig. 3.11.1 (a) Extraterrestrial spectral solar irradiance, (b) extraterrestrial spectral solar photon flux density, and (c) comparison between irradiance and photon flux (The values are normalized).

3.11.2 Calculation of spectral integration

In MC calculation, we divide the wavelength domain into subdomains, in which the optical properties in the atmosphere and plant canopy are assumed to be constant. The spectral integration of the radiative quantity is derived by counting the sampling quantities in the subdomains. In an actual simulation, the spectral integration is achieved by adding the spectral integration loop as an outer loop (Fig. 3.11.2).

a. Approach to use same number of modeled photons in all spectral subdomains

Let us consider dividing the wavelength domain $[\lambda_{\min}, \lambda_{\max}]$ into M subdomains. Then, spectral integration is performed as a sum of the M subdomains. When the total number of modeled photons is N and $N_i (= N/M)$ modeled photons are used in each subdomain, the intensity (energy or photon flux density) of a single modeled photon is expressed by

$$\frac{M}{N} F_i \text{ or } \frac{M}{N} Q_i \quad (3.11.4)$$

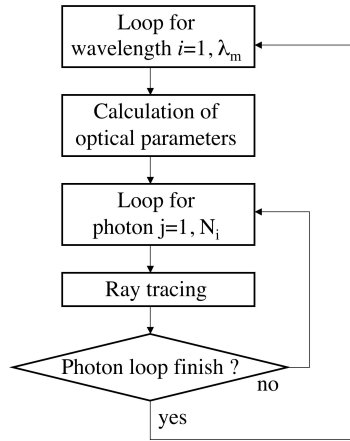


Fig. 3.11.2 Flowchart of the spectral integration.

where F_i and Q_i are the spectrally integrated incident irradiance and photon flux density within the i th subdomain. F and Q can be calculated by

$$F = \sum_{i=1}^M F_i, F_i = \int_{\lambda_{i-1}}^{\lambda_i} F_{\lambda} d\lambda \quad (3.11.5a)$$

$$Q = \sum_{i=1}^M Q_i, Q_i = \int_{\lambda_{i-1}}^{\lambda_i} Q_{\lambda} d\lambda \quad (3.11.5b)$$

This is a simple, stable, and accurate method to calculate the average radiative quantity within subdomains. However, it is necessary to allocate the same number of modeled photons as the most contributing spectral subdomain over all the subdomains. Therefore, this method requires a vast computation time compared with a monochromatic wavelength simulation. The method described in the next section has a better performance.

b. Approach using photon population proportional to incident solar radiation intensity

The accuracy of radiative quantities sampled by the MC method depends on the sampling number. It is possible to simulate a physical quantity with the same accuracy as the monochromatic wavelength simulation using the same number of modeled photons when the modeled photons are allocated to be proportional to the spectral solar radiation intensity. And, as shown in Fig. 3.11.1, the spectral distributions of irradiance and photon flux density are similar. Thus, the irradiance and photon flux density can be calculated simultaneously. When we use a total of N modeled photons for the spectral integration in the domain $[\lambda_{\min}, \lambda_{\max}]$, the weight of the i th subdomain with respect to the incident spectral radiation intensity is

$$w_i = F_i/F, \sum_{i=1}^M w_i = 1 \quad (3.11.6)$$

where F and F_i are derived from (3.11.5a). The number of modeled photons N_i in the i th subdomain is

$$N_i = w_i N \quad (3.11.7)$$

In this case, the intensity of the i th subdomain is expressed in the irradiance unit:

$$\Delta F_i = \frac{F_i}{N_i} = \frac{F}{N} \quad (3.11.8)$$

This is constant over all subdomains, when we use the photon flux density:

$$\Delta Q_i = \frac{Q_i}{N_i} \quad (3.11.9)$$

In the wavelength, where the thermal emission effect is not negligible, the total intensity is expressed by

$$F_i = F_{\text{solar},i} + F_{\text{thermal},i} \quad (3.11.10)$$

Here, $F_{\text{thermal},i}$ is an average thermal irradiance, which is defined as the total thermal radiative energy normalized by the total area in the simulation space.

3.12 Canopy photosynthesis

We describe a method to calculate canopy photosynthesis using a radiative quantity derived from MC simulation.

3.12.1 Single leaf photosynthesis rate

There are several biochemical models for the simulation of photosynthesis. Here, we briefly introduce Farquhar's model (Farquhar et al., 1980), which is widely used. A detailed description is provided in (Farquhar et al., 1980; de Pury and Farquhar, 1997). When the photosynthetically active radiation absorbed by a single leaf is defined by I_l ($\mu\text{mol s}^{-1} \text{m}^{-2}$), the absorbed radiation in photosynthesis II is expressed by

$$I_{lc} = I_l(1 - f)/2 \quad (3.12.1)$$

where f is an absorbed energy other than chloroplast (Farquhar et al., 1980). Strictly speaking, the parameter f depends on the leaf thickness. de Pury and Farquhar (1997) proposed $f = 0.15$.

The electron transfer rate in a unit leaf area J can be derived as a solution of the quadratic equation

$$\theta_1 J^2 - (I_{lc} + J_m)J + I_{lc}J_m = 0 \quad (3.12.2)$$

where J_m and θ_1 are maximum J and empirical parameters to determine the electron transfer response to absorbed photosynthetically active radiation (APAR), respectively. In de Pury and Farquhar (1997), $\theta_1 = 0.7$ is used. J_m is a function of temperature. Using J , the photosynthesis rate A_j under the electron transfer limitation can be calculated by

$$A_j = J \frac{p_i - \Gamma^*}{4(p_i + 2\Gamma^*)} \quad (3.12.3)$$

where Γ^* and p_i are a CO_2 compensation point Γ (Pa) in the absence of mitochondrial respiration and partial CO_2 pressure in the leaf.

The photosynthesis rate A_v under the Rubisco-limited condition can be calculated by

$$A_v = V_l \frac{p_i - \Gamma^*}{p_i + 2K'}, \quad (3.12.4)$$

where K' is an effective Michaelis-Menten constant of Rubisco. Finally, the photosynthesis rate A_l can be derived by taking the minimum between A_j (3.12.3) and A_v (3.12.4):

$$A_l = \min(A_j, A_v) - R_l \quad (3.12.5)$$

where R_l is a leaf respiration rate.

3.12.2 APAR calculation

In a 3-D canopy radiative transfer model, the following three radiative quantities can be calculated:

- Total APAR in each voxel ($\mu\text{mol s}^{-1} \text{m}^{-2} \text{m}^{-3}$) or ($\text{W m}^{-2} \text{m}^{-3}$)
- Diffuse APAR in each voxel ($\mu\text{mol s}^{-1} \text{m}^{-2} \text{m}^{-3}$) or ($\text{W m}^{-2} \text{m}^{-3}$)
- Number of modeled photons of first-order scattering in each voxel

a. Calculation of sunlit leaf area in each voxel

The sunlit leaf area can be calculated by counting the number of modeled photons of first-order scattering in the voxel. The number of incident modeled photons in a unit voxel N_d (m^{-2}) at the top of a canopy is

$$N_d = N/(x_d y_d) \quad (3.12.6)$$

where N and x_d, y_d are the total modeled photons and the length of a voxel on the x and y -axes. The projected sunlit leaf area in the unit voxel u_p (m^2) is calculated by

$$u_p = (x_d y_d) N_a/N_d \quad (3.12.7)$$

where N_a is the number of absorbed direct modeled photons in the voxel.

Since, as described in 2.3, the projected leaf area G toward $\mathbf{\Omega}(\theta, \phi)$ is expressed by

$$G(\mathbf{\Omega}) = \frac{1}{2\pi} \int_0^{2\pi} \int_0^{\pi/2} g_L(\theta_L) |\mathbf{\Omega} \cdot \mathbf{\Omega}_L| d\theta_L d\phi_L \quad (3.12.8)$$

the total sunlit leaf area can be calculated using G (3.12.8) and u_p (3.12.7):

$$u_s = u_p/G \quad (3.12.9)$$

b. Photosynthesis calculation for each voxel

The photosynthesis rate in each voxel can be calculated using physical quantities derived from the MC radiative transfer simulation and single leaf photosynthesis model. We assume that the voxel size is sufficiently small, the spatial heterogeneity of the diffuse PAR flux is negligible, and the diffuse flux is incident from the upper hemisphere and is uniform over all directions within the voxel. Equation (3.12.5) is a function of I_l , which is defined as an APAR in a unit leaf area. On the other hand, the APAR calculated from radiative transfer simulation is the APAR normalized in a unit volume. The simulated APAR (unit volume) can be converted to the APAR in a unit leaf area ($I_{l,\text{sun}}, I_{l,\text{shade}}$) using the following equations:

$$I_{l,sun} = I_{dir}(\Omega_s \cdot \Omega_L)(1 - \omega) + \frac{APAR_{dif}}{u} \quad (3.12.10)$$

$$I_{l,shade} = \frac{APAR_{dif}}{u} \quad (3.12.11)$$

where I_{dir} is a direct PAR flux incident at the top of the canopy. Therefore, photosynthesis in a voxel can be calculated by

$$A_{vox} = \frac{u_s}{2\pi} \int_{2\pi} A_l(I_{l,sun})g_L(\Omega_L)d\Omega_L + \frac{(u - u_s)}{2\pi} \int_{2\pi} A_l(I_{l,shade})g_L(\Omega_L)d\Omega_L \quad (3.12.12)$$

where the first term is a contribution from a sunlit leaf and the second term is a contribution from a shaded leaf. It should be noted that (3.12.12) does not distinguish between the adaxial and abaxial sides of a leaf. Generally speaking, the photosynthesis abilities for the adaxial and abaxial sides are not equal. Thus, it is necessary to consider the adaxial and abaxial sides of a leaf if it is necessary to perform a more detailed analysis, by changing the constant parameters in Farquhar's model.

Chapter 4

Improvement of numerical efficiency

4.1 MCS method

The MC atmospheric radiative transfer model usually treats the atmosphere as divided into a large number of voxels, representing the fine-scale structure of the atmosphere. Each voxel has specific optical properties (extinction coefficient, single scattering albedo, and phase function). Each voxel is homogeneous, but different voxels can have different properties. In these circumstances, photon tracing requires that every crossing point at each voxel boundary be found to compute the optical path length in the voxel (Fig. 4.1.1). This calculation can be very time consuming if there are too many voxels. For example, the earth's upper atmosphere is optically thin. If the mean free path in the upper part is 100 km, and if there are 1,000 layers of 0.1 km thickness, then how many numerical instructions are required? Calculations for the crossing points on the order of 1,000 are required to find the next collision point!

The MCS method (Marchuk et al., 1980) is useful to avoid this problem. This method is implemented in many MC radiative transfer models.

4.1.1 Base of MCS method

Any inhomogeneous field with a varying extinction coefficient can be considered as equivalent to a homogeneous field with a constant extinction coefficient that is the maximum β_{\max} of the extinction coefficients in the domain, using the scaling transformation based on the similarity relations (e.g., Liou, 1992). The medium in the voxel can be considered to be a mixed medium of two components: one is the original, and the other is a medium that has pure forward scattering with a scattering angle of 0 (equivalent to transmission). In other words, the transmission in the original medium is treated as virtual forward scattering. By using the MCS method, there are two kinds of collision processes:

- 1) Real collision: a physical collision as in the original
- 2) Virtual collision: mathematical scattering due to the scaling transformation

By the MCS method, the extinction coefficient becomes as large as β_{\max} , originally from β_e . The number of collisions should thus increase. However, the virtual scattering is relatively easy to treat in the model, compared to the physical scattering. The reason is that no absorption is included for the virtual scattering ($\omega = 1$) and that a direction change never occurs in the virtual

scattering. A possible algorithm for the MCS method is as follows:

- 1) Determination of the collision location, based on the maximum extinction coefficient β_{\max} .
- 2) Determination of the kind of collision: “virtual” or “real”? The probability of the real scattering is β_e/β_{\max} , so that a random number determines the kind.
- 3) Iterate the above until the real scattering is detected. If virtual, return to 1.
- 4) If real scattering occurs, then the direction changes as usual.

Using this method, there is no requirement to determine the crossing points at every voxel boundary, because the extinction coefficient is constant throughout the domain. The model photon can thus jump to the net collision point from the current point. A schematic of photon tracing using this method is shown in Fig. 4.1.1.

Table 4.1.1 Optical property changes due to the MCS method

Medium	Extinction coefficient	Single scattering albedo	Scattering phase function
1	β_e	ω	$P(\Theta)$
2	$\beta_{\max} - \beta_e$	1	$2\delta(\Theta)$
1 + 2	β_{\max}	$(\omega\beta_e + \beta_{\max} - \beta_e)/\beta_{\max}$ $= 1 - (1 - \omega)\beta_e/\beta_{\max}$	$\frac{\omega\beta_e P(\Theta) + 2(\beta_{\max} - \beta_e)\delta(\Theta)}{\omega\beta_e + \beta_{\max} - \beta_e}$

δ is Dirac’s delta function

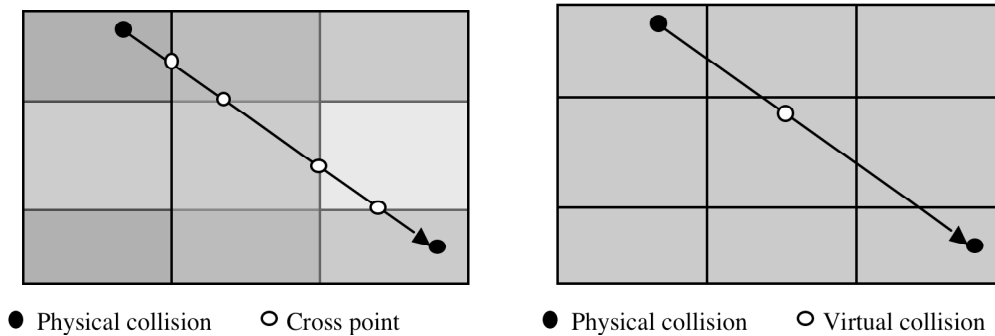


Fig. 4.1.1 Schematic of photon tracing. Left: usual method, right: using the MCS method.

4.1.2 Discussion on efficiency of MCS method

The MCS method does not always improve the efficiency. What about with a significantly larger maximum extinction coefficient than the average extinction coefficient? The efficiency will be worse because too many virtual scattering events occur before reaching the real

scattering point. Figure 4.1.2 shows an extreme case.

The MCS method does not work effectively if the average probability of a physical collision, β_e/β_{\max} , is low. Városi and Dwek (1999) discussed a similar point. The MCS method works effectively under the following conditions:

- 1) The size of the voxel is small compared with the average free path length: the extinction coefficient is small.
- 2) The medium is relatively homogeneous: the inhomogeneity of the extinction coefficient is small.

The extinction coefficient is at a maximum in clouds and the value is relatively large. If the maximum is used for the MCS method for the whole domain, the efficiency would be bad. The MCS method is thus used for each of the subdomains (or super-voxel) that make up the entire domain. Therefore, it is important to adaptively construct the super-voxels before the radiative transfer calculation.

With thresholds related to the above two conditions, the voxels are hierarchically merged into super-voxels in the pre-process until the following condition is broken:

- 1) The maximum extinction in the super-voxel is less than the average by a factor of A.
- 2) The inverse of the maximum extinction is larger than the voxel size by a factor of B.

The creation of super-voxels that are as large as possible under the above conditions would improve the efficiency of the MCS method.

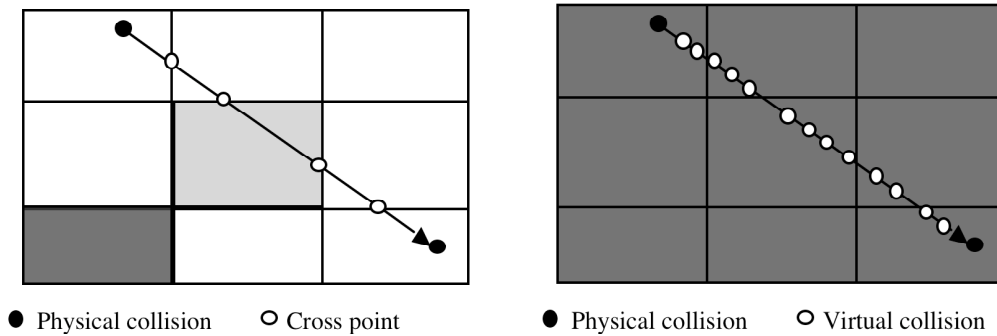


Fig. 4.1.2 Schematic of photon tracing in a case where the MCS method is not efficient: (Left) usual method, (right) using the MCS method.

4.2 Variance reduction methods

MC integration results in little variance (noise) if the number of samples is large. However, the computation time is generally proportional to the number of samples. Variance reduction methods seek to obtain results with little noise in a limited computation time; that is, they are a method for improving numerical efficiency. Several methods have already been described in previous sections (e.g., the Russian roulette method). This section describes other methods for variance reduction. Marchuk et al. (1980), Booth (1985), and Iwabuchi (2006) also presented good methods for variance reduction. The MCML code of the Los Alamos National Laboratory X-5 Monte Carlo Team also uses good methods.

4.2.1 Exponential transformation method

In the usual method for the determination of the collision point, the optical path length to the collision point follows the exponential distribution with an average of 1. The transmittance is

$$T(\tau) = e^{-\tau} \quad (4.2.1)$$

The randomly chosen optical path length to the collision point is determined by a uniform random number ρ :

$$\int_0^{\tau} e^{-\tau} d\tau = \rho; \quad \tau = -\ln(1-\rho) \quad (4.2.2)$$

In this method, the photon weight is unchanged.

The PDF (transmittance) of the collision can be modified as

$$T'(\tau) = \frac{1}{S} e^{-\tau/S} \quad (4.2.3)$$

with an average for the optical thickness of S . This is properly normalized to 1. If the PDF is modified as this form, the random optical thickness to the collision point should be

$$\frac{1}{S} \int_0^{\tau'} e^{-\tau'/S} d\tau' = \rho \quad (4.2.4a)$$

$$\tau' = -S \ln(1-\rho) = -S \ln \tilde{\rho} \quad (4.2.4b)$$

For energy conservation, the following equation should be true:

$$w'T'(\tau') = wT(\tau) = w e^{-\tau} \quad (4.2.5)$$

Thus, the weight is given as

$$w' = w \frac{S e^{-\tau'}}{e^{-\tau'/S}} = w S \exp \left[-\tau' \left(1 - \frac{1}{S} \right) \right] = w S \exp[(S-1) \ln \bar{\rho}] \quad (4.2.6)$$

By this modification, the average optical thickness is modified to an arbitrary value for S instead of 1. When $S > 1$, then the photon will fly to a far point. In contrast, when $S < 1$, the collision will occur at a closer point.

Using this method, the model photon is forced to escape from the domain even when too many scattering events should usually occur, by setting $S > 1$. However, it should be noted that the photon weight varies due to (4.2.6). The Russian roulette method is easier to use for reducing the multiple scattering. Another application is to force many scattering events when the media is too thin to sample enough scattering events, by setting $S < 1$ (4.2.4).

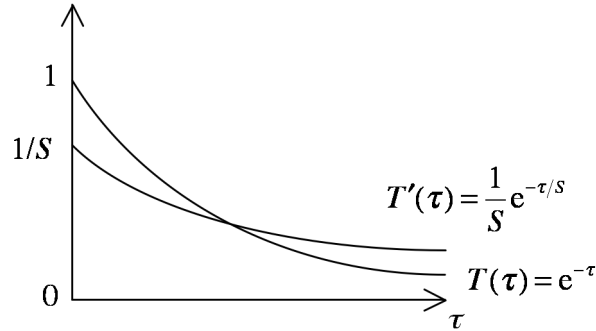


Fig. 4.2.1 Schematic of the exponential transformation: PDF of the collision (transmission function).

4.2.2 Modification of contribution function

The LEM samples the following contribution function for radiance:

$$\zeta(\mathbf{\Omega}_1, \mathbf{r}_1) = w \Psi(\mathbf{\Omega}_0, \mathbf{\Omega}_1) T(\mathbf{r}_0, \mathbf{r}_1) \quad (4.2.7)$$

where w is the weight just after the scattering (or reflection), Ψ is the normalized PDF (sr^{-1}), and T is the transmittance between the event point \mathbf{r}_0 and the detection point \mathbf{r}_1 . The transmittance is the function of the optical thickness:

$$T(\mathbf{r}_0, \mathbf{r}_1) = e^{-\tau(\mathbf{r}_0, \mathbf{r}_1)} \quad (4.2.8a)$$

$$\tau(\mathbf{r}_0, \mathbf{r}_1) = \int_{\mathbf{r}_0 \rightarrow \mathbf{r}_1} \beta_e(t) dt; \quad t = |\mathbf{r}' - \mathbf{r}_0| \quad (4.2.8b)$$

The function of (4.2.7) varies significantly sample-by-sample, especially when the phase function is anisotropic, as in cloud particles or ocean reflection. It is important to reduce the variance of the contribution function ζ to reduce the radiance noise.

a. Modification of small ζ

The function ζ is frequently small. We are trying to present a method to modify ζ so as to keep it larger than a threshold. If $\zeta < \zeta_{\min}$ in the original form, a method such as the Russian roulette method can be applied to modify (4.2.7). First, the following modification is valid:

$$\begin{aligned} &\text{If } w\Psi < \zeta_{\min} \text{ and } \rho < w\Psi/\zeta_{\min}, \text{ then } w\Psi \rightarrow \zeta_{\min} \\ &\text{Otherwise} \qquad \qquad \qquad w\Psi \rightarrow 0 \end{aligned} \quad (4.2.9)$$

Denoting

$$\zeta_{\min} = w\Psi e^{-\tau_{\max}} \quad (4.2.10)$$

the transmittance T is modified, using the random sampling method for the collision, to

$$\begin{aligned} T &= e^{-\tau} = e^{-\tau_{\max}} e^{-(\tau-\tau_{\max})} \\ \rightarrow &\begin{cases} e^{-\tau} & \text{if } \tau \leq \tau_{\max} \\ e^{-\tau_{\max}} & \text{if } \tau > \tau_{\max} \text{ and } \rho < e^{-(\tau-\tau_{\max})} \\ 0 & \text{otherwise} \end{cases} \end{aligned} \quad (4.2.11)$$

where $\tau > \tau_{\max}$ and ρ is a uniform random number. No sampling is needed if $T = 0$, of course. Figure 4.2.2 shows schematically the transmittance modified in this method.

Combining (4.2.9) and (4.2.11), the following equation is derived (Iwabuchi, 2006):

$$\begin{aligned} &\text{When } w\Psi \leq \zeta_{\min}, \\ &\zeta' = \begin{cases} \zeta_{\min} & \text{if } \rho_1 \leq w\Psi/\zeta_{\min} \text{ and } \tau \leq \tau_{\text{free}} \\ 0 & \text{otherwise} \end{cases} \end{aligned} \quad (4.2.12a)$$

$$\begin{aligned} &\text{When } w\Psi > \zeta_{\min}, \\ &\zeta' = \begin{cases} \zeta & \text{if } \tau \leq \tau_{\max} \\ \zeta_{\min} & \text{if } \tau_{\max} < \tau \leq \tau_{\max} + \tau_{\text{free}} \\ 0 & \text{if } \tau > \tau_{\max} + \tau_{\text{free}} \end{cases} \end{aligned} \quad (4.2.12b)$$

where

$$\tau_{\text{free}} = -\ln \rho_2 \quad (4.2.13a)$$

$$\tau_{\max} = -\ln \left(\frac{\zeta_{\min}}{w\Psi} \right) \quad (4.2.13b)$$

Before the tracing between the scattering point and the detector, τ_{free} and τ_{\max} are determined. Tracing can terminate as soon as it is known that the photon energy is 0 ($\zeta' = 0$) for that sample, which could be known before the tracing or at some point between the scattering point and the detector.

This method has two advantages. One is a reduction of computation time because of the reduction in the number of tracings. The other is a variance reduction in the contribution function due to the fact that the sampled functions are all larger than the threshold. Iwabuchi (2006) found that $\zeta_{\min} = 0.3$ has the best performance for calculating reflectance from a cloud deck.

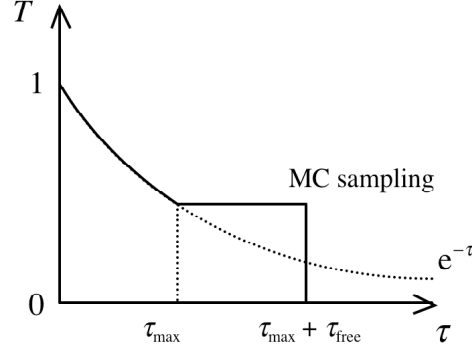


Fig. 4.2.2 Schematic of the transmittance modification

b. Use of MCS method

The analytical transmittance in (4.2.7) requires time-consuming ray tracing between the scattering point \mathbf{r}_0 and the detection point \mathbf{r}_1 , to calculate the optical thickness between the two points. The optical thickness integrating is a numerically heavy procedure if there are many voxels in the atmosphere. Let us consider a use of the MCS method for calculating the transmittance.

In (4.2.10), the threshold τ_{\max} is associated with ζ_{\min} . Similarly, introducing another parameter ζ_{\max} ,

$$\zeta_{\max} = w\Psi e^{-\tau_{\max}} \quad (4.2.14)$$

$$\tau_{\max} = \begin{cases} -\ln\left(\frac{\zeta_{\max}}{w\Psi}\right) & \text{if } w\Psi > \zeta_{\max} \\ 0 & \text{otherwise} \end{cases} \quad (4.2.15)$$

Using these, we can derive the following:

$$\text{When } w\Psi \leq \zeta_{\min}, \quad \zeta' = \begin{cases} \zeta_{\min} T'(\tau) & \text{if } \rho_1 \leq w\Psi/\zeta_{\min} \\ 0 & \text{otherwise} \end{cases} \quad (4.2.16a)$$

$$\text{When } \zeta_{\min} < w\Psi \leq \zeta_{\max}, \quad \zeta' = w\Psi T'(\tau) \quad (4.2.16b)$$

$$\text{When } w\Psi > \zeta_{\max},$$

$$\zeta' = \begin{cases} \zeta & \text{if } \tau \leq \tau_{\max} \\ \zeta_{\max} T'(\tau - \tau_{\max}) & \text{otherwise} \end{cases} \quad (4.2.16c)$$

The modified transmittance is determined randomly:

$$T'(\tau) = \begin{cases} 1 & \text{if } \tau \leq \tau_{\text{free}} = -\ln \rho_2 \\ 0 & \text{otherwise} \end{cases} \quad (4.2.17)$$

This formulation is useful for applying the MCS method. Using the MCS method for calculating T' , the transmittance is 1 if a physical collision does not occur between the two points. If a physical collision does occur, the transmittance is 0, and the ray tracing can terminate immediately.

Using this method, an algorithm follows:

- 1) If Ψ is small, the contribution function is modified as larger than ζ_{\min} , following (4.2.16a). Else, $\tau_{\max} = 0$.
- 2) Start the tracing from \mathbf{r}_0 .
- 3) Analytical transmittance is calculated until τ is smaller than τ_{\max} . If the photon packet reaches \mathbf{r}_1 , then the transmittance is determined by the first equation of (4.2.16c) and the sampling for the local estimate finishes. Else, the MCS method is applied from the point with $\tau = \tau_{\max}$.
- 4) Randomly determined collision is due to mathematical scattering or physical collision. A random number can determine the kind of collision.
- 5) If a physical collision is detected, then the transmittance becomes 0, and the tracing terminates. Else, the photon reaches \mathbf{r}_1 , and the transmittance with $T' = 1$ is substituted into (4.2.16a,b,c). Finally, the sampled contribution function should be

$$\zeta' = \begin{cases} \zeta_{\min} & \text{if } w\Psi \leq \zeta_{\min} \\ w\Psi & \text{if } \zeta_{\min} < w\Psi \leq \zeta_{\max} \\ \zeta_{\max} & \text{if } w\Psi > \zeta_{\max} \end{cases} \quad (4.2.18)$$

4.2.3 Truncation approximations for anisotropic scattering

The contribution function sampled by the LEM in (4.2.7) contains the PDF Ψ for angular distribution, which is associated with the phase function for the scattering. If the phase function contains sharp peaks, the contribution function sometimes becomes significantly large. Thus, the convergence of the integral of (4.2.7) is very slow, with significant noise (Barker et al., 2003). The forward scattering peak for cloud particles and large aerosol particles is significantly sharp, and the phase function is 10^4 or more at the peak.

Truncation approximations are effective for this problem (Iwabuchi, 2006). Commonly, the method approximates the original phase function P by

$$P(\Theta) \approx 2f_{\delta}\delta(\Theta) + (1 - f_{\delta})\hat{P}(\Theta) \quad (4.2.19)$$

where \hat{P} is the truncated phase function and f_δ is the delta fraction. The forward scattering with zero scattering angle is equivalent to the transmission. By the similarity relations (e.g., Liou, 1992), the extinction coefficient and single scattering albedo are scaled as

$$\hat{\beta}_e = \beta_e(1 - f_\delta\omega) \quad (4.2.20)$$

$$\hat{\omega} = \omega \frac{1 - f_\delta}{1 - f_\delta\omega} \quad (4.2.21)$$

The radiative transfer can be calculated for a system with scaled properties $\hat{\beta}_e$, $\hat{\omega}$, and \hat{P} .

Various definitions of \hat{P} can be possible (e.g., Nakajima and Tanaka, 1988; Antyufeev, 1996; Thomas and Stamnes, 1999; Modest, 2003). All of the proposed methods are approximations because the real forward peak is not exactly the same as the delta function. Bias is thus imposed on the calculation results. A method with as small a bias as possible is preferable.

Table 4.2.1 Changes in optical properties due to the truncation approximation.

Media	Extinction coefficient	Single scattering albedo	Scattering phase function
Original	β_e	ω	$P(\Theta)$
Approximated	β_e	ω	$2f_\delta\delta(\Theta) + (1 - f_\delta)\hat{P}(\Theta)$
Transformed	$\hat{\beta}_e$	$\hat{\omega}$	$\hat{P}(\Theta)$

a. Delta-isotropic approximation

The delta-isotropic approximation (transport approximation) uses the isotropic phase function as the truncated phase function:

$$\hat{P}(\Theta) = 1 \quad (4.2.22)$$

Calculations become very simple. For accurately approximating the original radiative transfer, it is important for the moments of the approximated phase function (right hand side of 4.2.19) to be close to the original. The first-order moment (asymmetry factor) g_1 is defined as

$$g_1 = \frac{1}{2} \int_0^\pi P(\Theta) \cos \Theta \sin \Theta d\Theta \quad (4.2.23)$$

Conservation of the first-order moment

$$g_1 = \frac{1}{2} \int_0^\pi [2f_\delta\delta(\Theta) + (1 - f_\delta)\hat{P}(\Theta)] \cos \Theta \sin \Theta d\Theta \quad (4.2.24)$$

is the prerequisite. Then,

$$g_1 = f_\delta \int_{-1}^1 \delta(\cos\Theta - 1) \cos\Theta d\cos\Theta + (1 - f_\delta) \frac{1}{2} \int_{-1}^1 \hat{P}(\Theta) \cos\Theta d\cos\Theta \quad (4.2.25)$$

$$= f_\delta + (1 - f_\delta) \times 0$$

$$\therefore f_\delta = g_1 \quad (4.2.26)$$

That is, the delta fraction is determined uniquely from this equation.

This method is not appropriate for radiance calculations because of very large bias. However, the radiative flux and heating rate may be accurately calculated using this method, if the method is applied only to multiple scattering. This method reduces the extinction coefficient and the number of scattering events, and the method is useful for optically-thick atmosphere. When $g_1 = 0.86$, for example, substituting (4.2.26) into (4.2.20), the extinction coefficient is decreased by a fraction of 0.14. The number of scattering events is almost proportional to the extinction coefficient, so that the computation time is significantly reduced.

b. Delta-Heyney-Greenstein approximation

In this method, the truncated phase function is expressed by the Heyney-Greenstein function. For the first-order moment \hat{g}_1 ,

$$\hat{P}(\Theta) = \frac{1 - \hat{g}_1^2}{[1 - 2\hat{g}_1 \cos\Theta + \hat{g}_1^2]^{3/2}} \quad (4.2.27)$$

As in (4.2.24), equating the first-order moment of the approximated function to the original,

$$g_1 = f_\delta + (1 - f_\delta)\hat{g}_1 \quad (4.2.28)$$

$$\therefore \hat{g}_1 = \frac{g_1 - f_\delta}{1 - f_\delta} \quad (4.2.29)$$

where

$$\begin{aligned} &\text{if } 0 \leq \hat{g}_1, \text{ then } f_\delta \leq g_1 \\ &\text{if } -1 \leq \hat{g}_1, \text{ then } f_\delta \leq \frac{1}{2}(g_1 + 1) \end{aligned} \quad (4.2.30)$$

Eq. (4.2.28) is true for an arbitrary f_δ under the condition of (4.2.30), so that the user can freely set f_δ .

Although this method has better accuracy than the delta-isotropic approximation, it is not applicable to calculating radiance (because of large bias).

c. Forward-end truncation approximation (FTA)

Let us consider the truncated phase function as a geometrically truncated and renormalized one without the forward peak part in the original:

$$\hat{P}(\Theta) = \begin{cases} P(\Theta)/f_t & \text{for } \Theta \geq \Theta_f \\ 0 & \text{for } \Theta < \Theta_f \end{cases} \quad (4.2.31)$$

where

$$f_t = \frac{1}{2} \int_{\Theta_f}^{\pi} P(\Theta) \sin \Theta d\Theta \quad (4.2.32)$$

The truncation angle Θ_f is determined from the conservation of the asymmetry factor (4.2.24):

$$\begin{aligned} \hat{g}_1 &\equiv \frac{1}{2} \int_0^{\pi} \hat{P}(\Theta) \cos \Theta \sin \Theta d\Theta \\ &= \frac{1}{2f_t} \int_{\Theta_f}^{\pi} P(\Theta) \cos \Theta \sin \Theta d\Theta \end{aligned} \quad (4.2.33)$$

We obtain

$$g_1 = f_\delta + (1 - f_\delta) \hat{g}_1 \quad (4.2.34)$$

$$\int_{\Theta_f}^{\pi} P(\Theta) \cos \Theta \sin \Theta d\Theta = \frac{g_1 - f_\delta}{1 - f_\delta} \int_{\Theta_f}^{\pi} P(\Theta) \sin \Theta d\Theta \quad (4.2.35)$$

The angle Θ_f can be determined by numerically solving the above equation. f_δ is a free parameter. In Iwabuchi (2006), the parameter is set so as to increase with the isotropy of the photon packet (with multiple scattering).

This method is significantly better than the two methods previously described. The form of (4.2.31) is the same as the original function, except for the forward part, and this similarity of the phase function form is a key for achieving high accuracy. This method can be applicable to radiance calculations with small bias (usually less than 0.5%), except for the solar aureole simulation.

The form of (4.2.31) has another merit for the MC model. LUTs for the original phase functions and associated cumulative distribution functions can be reused even for the truncated phase functions. The LUT is usually tabulated for a very large number of grid points, requiring the use of a large memory. The form of (4.2.31) does not require new tables for truncated functions. This point is especially important when setting different approximation degrees with different f_δ values for each scattering order.

d. Dual-end truncation approximation

This method is similar to the previous one, but truncates both ends of the phase function. The truncation of the backward part introduces another free parameter and results in better calculation results in some situations. The truncated phase function is

$$\hat{P}(\Theta) = \begin{cases} P(\Theta)/f_t & \text{for } \Theta_f \leq \Theta \leq \Theta_b \\ 0 & \text{for } \Theta < \Theta_f \text{ or } \Theta > \Theta_b \end{cases} \quad (4.2.36)$$

where

$$f_t = \frac{1}{2} \int_{\Theta_f}^{\Theta_b} P(\Theta) \sin \Theta d\Theta \quad (4.2.37)$$

For first and second moments,

$$g_1 \equiv \frac{1}{2} \int_0^\pi P(\Theta) \cos \Theta \sin \Theta d\Theta \quad (4.2.38a)$$

$$g_2 \equiv \frac{1}{2} \int_0^\pi P(\Theta) \cos^2 \Theta \sin \Theta d\Theta \quad (4.2.38b)$$

Similarly, for an approximated function,

$$\hat{g}_1 \equiv \frac{1}{2} \int_0^\pi \hat{P}(\Theta) \cos \Theta \sin \Theta d\Theta = \frac{1}{2f_t} \int_{\Theta_f}^{\Theta_b} P(\Theta) \cos \Theta \sin \Theta d\Theta \quad (4.2.39a)$$

$$\hat{g}_2 \equiv \frac{1}{2} \int_0^\pi \hat{P}(\Theta) \cos^2 \Theta \sin \Theta d\Theta = \frac{1}{2f_t} \int_{\Theta_f}^{\Theta_b} P(\Theta) \cos^2 \Theta \sin \Theta d\Theta \quad (4.2.39b)$$

Prerequisite conditions are the conservations of these two moments:

$$g_1 = f_\delta + (1 - f_\delta) \hat{g}_1 \quad (4.2.40a)$$

$$g_2 = f_\delta + (1 - f_\delta) \hat{g}_2 \quad (4.2.40b)$$

By numerically solving the system of equations

$$\int_{\Theta_f}^{\Theta_b} P(\Theta) \cos \Theta \sin \Theta d\Theta = \frac{g_1 - f_\delta}{1 - f_\delta} \int_{\Theta_f}^{\Theta_b} P(\Theta) \sin \Theta d\Theta \quad (4.2.41a)$$

$$\int_{\Theta_f}^{\Theta_b} P(\Theta) \cos^2 \Theta \sin \Theta d\Theta = \frac{g_2 - f_\delta}{1 - f_\delta} \int_{\Theta_f}^{\Theta_b} P(\Theta) \sin \Theta d\Theta \quad (4.2.41b)$$

the two angles Θ_f and Θ_b are determined.

The user can freely set the fraction f_δ . If the parameter is set so as to increase with the isotropy of the photon packet (with multiple scattering), then higher accuracy is obtained (Iwabuchi, 2006). This method is slightly better than the previous one. The bias in radiance is less than 0.2%, except for the solar aureole. By using this method, the numerical efficiency for radiance calculation is significantly improved. In addition, as in the previous method, any LUT related to the original phase functions can be used even for the truncated phase functions.

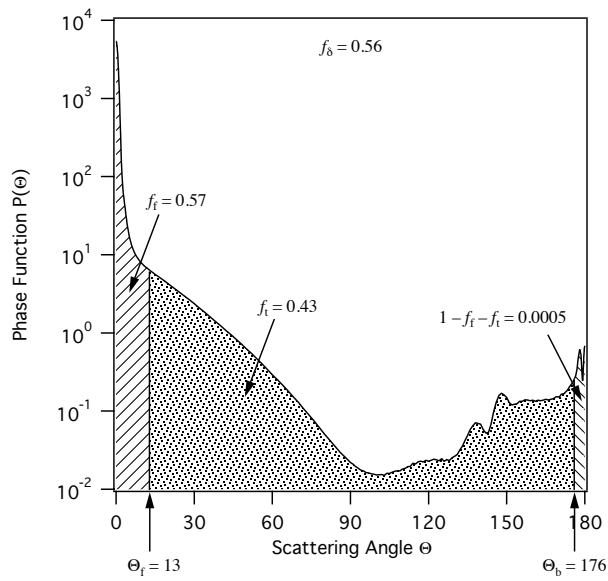


Fig. 4.2.3 Example of the dual-end truncation approximation (DTA). Effective radius of $10 \mu\text{m}$, wavelength at $0.67 \mu\text{m}$.

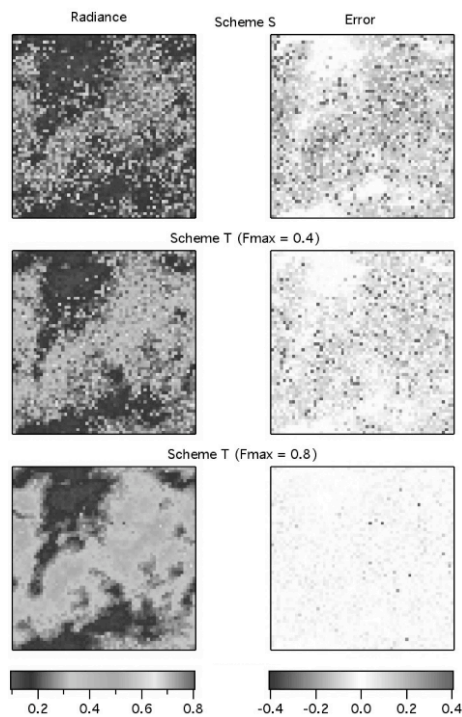


Fig. 4.2.4 Radiance images computed without DTA (scheme S) and with DTA (scheme T). A thousand photons are incident per pixel. Right images show noise error. Note that a large F_{max} corresponds to a large delta fraction.

4.2.4 Collision-forcing method

Collisions rarely occur in optically thin media. This causes rare sampling of heating rate and radiance calculated using the LEM, both of which are sampled at collision events. To improve the numerical efficiency for these quantities, collision-forcing methods are useful. Three methods are introduced in the following.

a. Method using scaling transformation

The scaling transformation based on the similarity relations (e.g., Liou, 1992) can easily increase the extinction coefficient (Iwabuchi, 2006). Increasing the extinction coefficient by a factor of $1/f_e$,

$$\beta'_e = \frac{\beta_e}{f_e} \quad (4.2.42)$$

The transformed single scattering albedo and scattering phase function are as follows:

$$\omega' = 1 - (1 - \omega)f_e \quad (4.2.43)$$

$$P'(\Theta) = 2f_d\delta(\Theta) + (1 - f_d)P(\Theta) \quad (4.2.44)$$

where

$$f_d = \frac{1 - f_e}{1 - (1 - \omega)f_e} = (1 - f_e)/\omega' \quad (4.2.45)$$

In other words, the transmission in the original medium is treated as forward scattering with a scattering angle of zero. The same theory is also used in the MCS method. The extinction coefficient increases, and the amount of scattering increases with a single scattering albedo close to 1 (weak absorption) and a phase function with the forward scattering peak. Optical properties are summarized in Table 4.2.2. The original medium (1) is equivalent to the mixed media (1 + 2). This transformation is mathematically correct and results in no bias.

Table 4.2.2 Changes in optical properties due to the collision-forcing method based on the scaling transformation

Medium	Extinction coefficient	Single scattering albedo	Scattering phase function
1	β_e	ω	$P(\Theta)$
2	$\frac{\beta_e}{f_e} - \beta_e$	1	$2\delta(\Theta)$
1+2	$\beta'_e = \frac{\beta_e}{f_e}$	$\omega' = 1 - (1 - \omega)f_e$	$P'(\Theta) = 2f_d\delta(\Theta) + (1 - f_d)P(\Theta)$

Calculation using this method is done with parameters given in (4.2.42–44). The phase function for the local estimate should be $(1 - f_d)P(\Theta)$ from (4.2.44). When determining the scattering direction, a random number first determines whether the event is mathematical scattering (due to the forward scattering) with a probability of f_d or the physical scattering. The photon direction is not altered for the mathematical scattering.

Using this method, the extinction coefficient increases to an arbitrary (possibly large) value, and collisions should occur frequently enough. This method is the simplest and most efficient for forcing collisions.

b. Forced sampling of collision in path segments

As mentioned in 3.4, virtual collisions can be sampled in arbitrary path segment(s). The probability of a collision in a path segment with an optical thickness of $\Delta\tau$ is

$$C(\Delta\tau) = 1 - e^{-\Delta\tau} \quad (4.2.46)$$

To determine a random collision point in this path segment, the optical thickness up to the point is given as

$$\frac{C(\tau)}{C(\Delta\tau)} = \rho \quad (4.2.47)$$

$$\therefore e^{-\tau} = 1 - \rho(1 - e^{-\Delta\tau}) \quad (4.2.48)$$

The photon weight is w_0 at the initial point of this path segment, and the single scattering albedo at the collision point is $\omega(\tau)$. The photon weights for absorption and scattering are respectively

$$w_{\text{abs}} = w_0(1 - e^{-\Delta\tau})[1 - \omega(\tau)] \quad (4.2.49a)$$

$$w_{\text{sca}} = w_0(1 - e^{-\Delta\tau})\omega(\tau) \quad (4.2.49b)$$

These weights can be used for sampling the heating rate and radiance. A random number determines whether the photon collides at the point or transmits up to the terminal point of the path segment. As noted in 3.4 (sampling absorption based on path length), one can force to sample only absorption or scattering.

This method is useful for sampling frequent collisions at specific volume elements of interest.

c. Exponential transformation method

As described in 4.2.1, collisions occur frequently with $S < 1$. However, with such a method, the photon weight can vary significantly between 0 and (possibly) infinity. This causes large noise in calculated radiative quantities. Therefore, the authors do not recommend this method.

4.2.5 Numerical diffusion

The usual MC models sample the radiative flux, heating rate, and radiance at local points. If these local samples are distributed in non-local regions (area or volume), then sampling noise could be reduced. Each sample is subdivided into subsamples and distributed in a horizontal area. The photon trajectory is not altered, but at each sampling process, the photon energy is divided and replaced in subpixels. The domain average of the calculated quantity has no bias if each sampling conserves the total of the original contribution.

For example, Iwabuchi (2006) proposed a method to distribute the contribution in a rectangular region (diffusion area) with uniform spatial distribution. The size of the region was determined according to the number of photon packets incident to the domain, diffusivity diagnostics of the photon packet, and sampled contribution function.

This method is purely technical, and the optimal redistribution region size cannot be determined theoretically. The optimal size should be determined by tests. The noise should be reduced with a wide diffusion area, and the spatial distribution of the calculated quantity should become smooth. However, artifacts will increase if the diffusion area is too large, and there will also be an increase in the computation time that is not negligible.

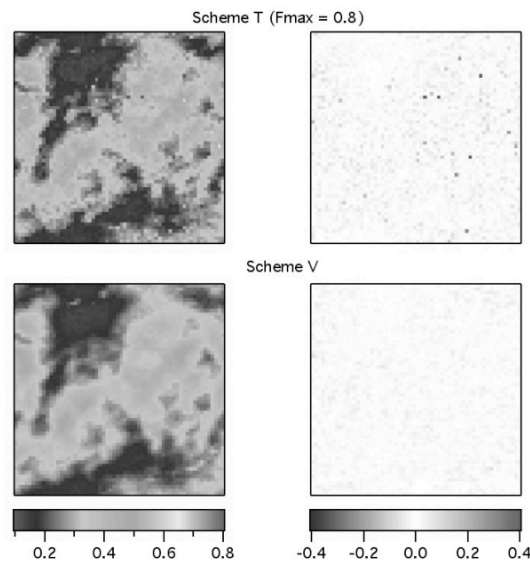


Fig. 4.2.5 Examples of computed radiance without using the numerical diffusion (scheme T) and with (scheme V). 1000 photon packets were incident. Right images show the error.

4.2.6 Semi-analytical calculation of direct-beam and single-scattering components

It is important for noise reduction with MC integration to use analytical calculation for the part where this is possible. As for solar radiative transfer, the direct-beam and single-scattering components can be calculated semi-analytically. The direct beam flux can be determined at local points by tracing the direct-beam ray from each point of interest for obtaining the optical

thickness for the beam. The direct beam flux should be $\exp(-\tau)$ multiplied by the solar incident flux. However, spatial averaging is required for obtaining the area-averaged irradiance and volume-averaged heating rate (due to the initial scattering). This averaging requires numerical integration because the optical thickness for the direct beam is not given in analytical forms for 3-D inhomogeneous fields. Therefore, the area-averaged direct-beam irradiance and first-order scattering heating rate should be calculated semi-analytically.

Two methods can be considered. One is to trace the backward trajectories from the target region of interest. The other is to trace the forward trajectories from the radiation source. The forward-type algorithm is better when one tries to calculate radiative quantities at many regions. Several options could be used for spatial integration. The simplest one is to distribute uniformly many rays at the top of the atmosphere. This seems very similar to the MC algorithm. However, they are different in two points: 1) The MC method has a random distribution of photon packets at the top of the atmosphere, but the semi-analytical algorithm has uniform distribution, and the same number of rays penetrates areas with constant cross sections. 2) The MC method determines a random initial collision point, but the semi-analytical method always traces the ray to the bottom of the atmosphere. Therefore, the semi-analytical method has better accuracy than the MC method. The number of rays determines the trade-off between computation time and accuracy. Methods of spatial interpolation and integration are important for achieving better accuracy with a small number of rays. Calculation algorithms for calculating the direct beam irradiance and first-order scattering heating rate are similar to those described in 3.8.3.

The ray tracing is relatively time consuming, especially if the atmosphere contains a large number of cells. The analytical calculation method cannot use the tricks for increasing efficiency, such as the MCS method in 4.1. Several techniques may improve the calculation efficiency. For example, if the integrated direct-beam optical thickness is large enough, it is efficient to switch to MC sampling of the random collision point, as described in 3.8.2, and to terminate the ray tracing at the initial collision point. In addition, if the ray penetrates many optically-thin, small cells, the MC method with the MCS method can be used to accelerate the calculation.

Another advantage of the semi-analytical calculation is that radiative quantities for all spectral wavelength (or bands) of interest could be obtained from one ray tracing. If there are many target wavelengths, the method is useful.

The first-order scattering radiance, too, can be calculated semi-analytically. There are also forward and backward-type algorithms for the method.

4.3 Parallelization

Since the MC method traces many photons, it takes a large amount of computation time. Parallelization, which divides the simulation tasks into several CPUs, is an effective tool for MC simulation. We next describe a parallelization method for MC radiative transfer simulation.

4.3.1 Parallel programming

So far, several hardware and software architectures have been proposed. With respect to the dependency between the memory and processor, two types of architecture exist: the distributed memory type and shared memory type. The shared memory type consists of memories and processors directly connected with each other in a computer network. On the other hand, processors have their own memories in the distributed memory type.

The message passing method is widely employed in the distributed memory type for sharing and exchanging data. A message passing interface (MPI) is commonly used to achieve the data sharing and exchange.

There are two approaches to designing the parallel programming. The data parallel approach distributes the same data source to all processors to execute the same type of calculations. The controlled parallel approach divides the simulation task between the processors. Each processor executes a different type of simulation.

Hereafter, we will mainly describe MPI-based programming. In particular, the data parallel approach has the advantage of easy programming and expansion from single processor code. The details of parallel programming can be found in Pacheco, (1997) etc.

4.3.2 Parallel computing by MC method I: Photon split method

Let us consider that the MC simulation is performed using N modeled photons with N_{prc} processors. When the MC simulation is conducted in the N_{prc} independent processors, independent random number sequences are required for each processor. This can be achieved by preparing independent initial seeds for the random number sequences for each processor.

In the basic parallel programming, the MC simulation is first performed using N/N_{pr} photons. Then, the results obtained in each processor are assembled in one processor and the physical quantities are calculated. The following is a detailed procedure for the photon split method.

- i) Determination of the initial random number seed and photon number for each processor
(= N/N_{prc})
- ii) Execution of the MC simulation
- iii) Wait until all processors finish their simulations
- iv) Gather the results from all processors and calculate the physical quantities

In this approach, data are exchanged only at the beginning and end of the simulation. The

amount of exchanged data is small. When the number of photons is sufficiently large, the computation time becomes almost equal for all processors. Therefore, it is efficient. This method is very simple, and it is easy to modify the program with less work. On the other hand, since all the processors have all of the data required in the simulation, it consumes a large amount of memory.

One idea to reduce the required memory resources is to consolidate the 3-D data for the optical properties in one or a few parent processors, which work as a data transfer system. Child processors perform the simulation, and if it is necessary to use or save the data, the child processor requests that the parent processors exchange the data. The information exchanged between the parent and child processors would include the extinction coefficient, single scattering albedo, phase function, and so on. In this idea, it is necessary to exchange the data for every scattering event. The maximum cross section method described in 4.1 will help to reduce the data exchange.

4.3.3 Parallel computing by MC method II: Space split method

Another method for efficient parallel programming is a space split method, which divides the simulation space so that each processor performs a simulation in their allocated space. This method reduces the amount of memory used. Therefore, it enables a simulation using a large number of simulation grids, compared with the single processor simulation. This means that it is possible to conduct a larger spatial-scale simulation or finer spatial resolution simulation.

On the other hand, this approach is rather complicated. Assuming that the modeled photon enters the (i, j) space, and emits to the $(i+1, j)$ space after the photon tracing, it is necessary to transfer the photon information such as position, weight, and direction. The processor simulation for the (i, j) space may receive the modeled photon from the nearest space. The number of modeled photons used in the MC simulation is very large. Therefore, the computation for the simulation requires frequent exchanges of data between processors.

To reduce the photon exchanges among processors, it is necessary to set the space as large as possible. It is not efficient to exchange small amounts of data many times due to the latency issue (Pacheco, 1997). Therefore, it is preferable to exchange the data when some amount of photon data, for photons emitted from the current space, are stored in the current space. In this method, photon data are stored in the local memories and the next simulation then starts. This procedure is continued until the stored data reaches some predetermined volume.

Another problem with this method is that if a simulated space, which is composed of a severe heterogeneous medium, is divided with the same spatial scale between all the processors, it cause a computational imbalance between processors: some processors are required to handle many photon tracings, while others handle only a few. To prevent this imbalance, it is necessary to achieve equal computation time for all the processors. For example, the simulation space is first divided into many small spatial areas. Then, the simulation space for each processor is randomly determined, or if some processors finish their simulation, they help with the simulation of another processor (though it may be difficult to create programming for this).

The method described above is an example for parallel computing. An efficient method should be designed by considering the spatial homogeneity/heterogeneity of the optical

properties.

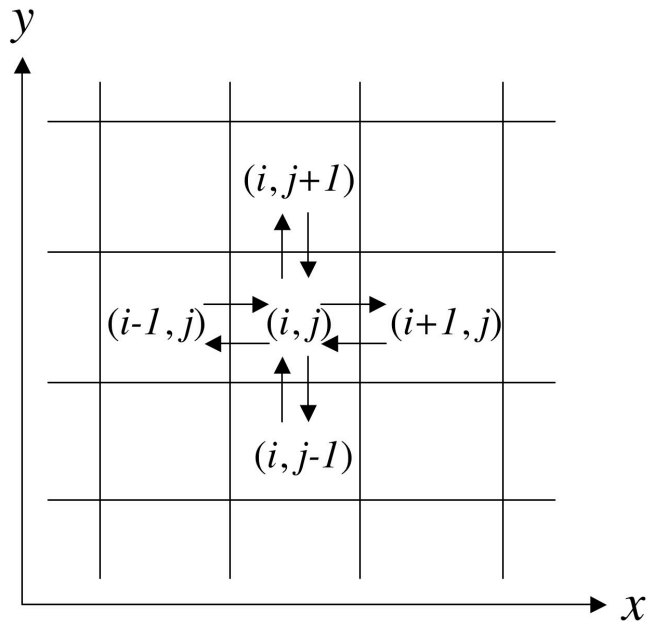


Fig. 4.3.1 Data exchange in the simulation space.

Chapter 5 Introduction of radiative transfer models and examples of applications

5.1 Simple code for MC radiation

The radiative transfer in a simple system can be easily modeled in code. For example, consider the code for the MC radiative transfer model for a plane-parallel atmosphere on a flat Lambertian surface. The atmosphere is plane-parallel, it is not necessary to calculate the photon's horizontal location coordinates (x and y), which makes the code simple. Isotropic scattering is assumed. The code computes reflectance, transmittance, and absorptance, in addition to the nadir-looking radiance at the top of the atmosphere, by using the LEM. The Russian roulette method is applied each time after a scattering or reflection event.

Although the code shown here is very short, with this alone, we can accurately calculate radiative flux and radiance under arbitrary conditions for the solar zenith angle, optical thickness, single scattering albedo, and surface reflectance. Using a modern personal computer, 200,000 photon packets can be simulated in a second for an optical thickness of 10. The accuracy of such a simulation would be approximately 0.3%. In addition, the code can be easily modified as follows:

- to compute separately the direct-beam and diffuse components for irradiance and heating rate, respectively
- to compute the radiance for an arbitrary direction
- to model vertically inhomogeneous layers
- to treat scattering with an arbitrary phase function
- to treat the medium as a mixture of gases, aerosols, and cloud particles and sample the heating rates separately for each component

The function `rand()` can usually be used in a UNIX/Linux system, although the function can be replaced by any good random number generator. Table 5.1.1 shows the results for various optical thicknesses.

Sample code, mcpp.f

```

program mcpp
!*****
! Demo program of Monte Carlo radiative transfer model for
! plane-parallel homogeneous atmosphere on Lambertian surface
!****
  implicit none
! Input
  integer iseed, nph, nsmax
  real the0, tau, omg, alb, dz, wrt
! Work
  integer iph, is
  real ext, afp, uz0, w, z, uz, ftau, znew, rad, pi
  real rand
  parameter (pi = 3.141592653, rad = pi/180.0)
! Work/Output
  double precision r, t, a, eu

! User variables
  iseed = 11           ! initial seed for random number generator
  nph = 100000        ! # of photons
  nsmax = 1000        ! max # of collisions
  the0 = 60.0*rad     ! solar zenith angle
  tau = 2.0           ! optical thickness of the atmosphere
  omg = 0.99          ! single scattering albedo
  alb = 0.2           ! surface albedo
  dz = 1000.0        ! geometrical thickness (m) of the atmosphere
  wrt = 0.5

! Initializations
  w = rand(iseed)     ! dummy for random number initialization
  ext = tau/dz        ! extinction coefficient (/m)
  afp = 1.0/ext       ! average free path (m)
  uz0 = -cos(the0)    ! downward incidence
  r = 0.0
  t = 0.0
  a = 0.0
  eu = 0.0

! Monte Carlo simulation
  do iph = 1, nph
    w = 1.0
    z = dz             ! source from top
    uz = uz0
    do is = 0, nsmax
      ftau = -log(max(1.0e-35, rand(0))) ! free optical thickness
      znew = z + uz * ftau * afp
      if (znew .ge. dz) then           ! escape
        r = r + w
        exit
      else if (znew .le. 0.0) then ! Lambertian reflection
        t = t + w
        z = 0.0
        uz = sqrt(rand(0))
        w = w * alb
        eu = eu + w * exp(-dz*ext)
      else                               ! isotropic scattering
        a = a + w * (1.0 - omg)
        z = znew
        uz = 1.0 - 2.0 * rand(0)
        w = w * omg
        eu = eu + w / 4.0 * exp(-(dz - z)*ext)
      end if
      if (w .lt. wrt*0.5) then          ! Russian roulette
        if (w .gt. wrt*rand(0)) then
          w = wrt
        else
          w = 0.0
          exit
        end if
      end if
    end do
  end do
end do

```

```

! Results (normalized quantities)
  r = r/real(nph)      ! TOA upward flux
  t = t/real(nph)      ! BOA downward flux
  a = a/real(nph)      ! Absorptance
  eu = eu/real(nph)    ! pi*(TOA nadir radiance)
  write (*,*) r, t, a, eu

end

```

Table 5.1.1 Simulation results using the mcpp code

τ	R	T	A	Nadir BRF
0.1	0.2589	0.9232	0.00253	0.2267
0.5	0.4267	0.7009	0.01267	0.3369
1	0.5451	0.5387	0.02396	0.4411
2	0.6614	0.3695	0.04295	0.5647
4	0.7511	0.2184	0.07415	0.6729

5.2 Introduction of atmospheric radiative transfer model

5.2.1 Radiative transfer model MCARaTS

The radiative transfer model MCARaTS (Monte Carlo atmospheric radiative transfer simulator) is a multipurpose model to treat the 3-D radiative transfer in a system composed of the atmosphere, ocean, and land. The model can simulate detailed spatial and angular distributions of the radiative energy in a cloudy atmosphere. Such a model is important for realistically simulating the 3-D distribution of radiative heating in cloud-resolving model simulations. For remote sensing purposes, too, the model is useful for relating the observable spectral radiances, which could be available from satellite observations, to the parameters for clouds, aerosols, gases, and land.

The forward-type MC method is used for the radiative transfer calculations. Many model photons are emitted from the radiation sources, scattering in the atmosphere and surface reflection are simulated by using random numbers, and the simulation for each single model photon is continued until the model photon's energy is completely absorbed in the system or escapes from the system (to space). In addition to several standard variance reduction methods such as the Russian roulette method, the truncation approximation of Iwabuchi (2006), the collision-forcing method, the MCS method, the numerical diffusion, and the methods described in this report are implemented in the model. This model was originally developed for the purpose of studying 3-D radiative effects in a field with inhomogeneous clouds. Especially, the problems of satellite remote sensing of the physical properties of boundary layer clouds have been studied (Iwabuchi and Hayasaka, 2002, 2003). Efforts now continue for model development and improvements for the purpose of online coupling with the cloud/large eddy resolving model.

The 3-D atmosphere is defined in the Cartesian coordinate system, and the 3-D distribution of clouds, aerosols, and gases (scattering and absorption) is taken into account. Several typical models for the aerosol mixture, such as Hess et al. (1998), can be selected by the user. The surface is defined in two dimensions, and its BRDF can vary spatially. Semi-empirical BRDF models of water and land are incorporated. BRDF models can be selected from the Lambertian, DSM, RPV, and LSTR models. At present, the surface is macroscopically flat, whereas the water surface model has microscopic roughness due to wind velocity. The applicable spectral bands include solar spectra, infrared, and microwave in a wavelength range of 0.2–2000 μm . The radiation source can be the solar incidence, thermal emission, or artificial light.

The model's outputs are the irradiance (averaged over pixel cross section, local irradiance on a horizontal plane, or local spheradiance), radiative heating rate, radiance (averaged over area or angular region with arbitrary solid angle), and average photon path length distribution. The direct beam and total irradiance are separately computed. Because the model employs the forward-type MC algorithm, from a single simulation, one can derive 3-D distributions of irradiance, heating rate, and radiance. The radiance can be computed at arbitrary locations and for arbitrary directions. It could be applied to the generation of photo-realistic computer graphics (Fig. 5.2.4). Lidar signal simulation is another application.

Three solver modes are implemented in the model, for the purpose of studying the 3-D radiative transfer effects. One is used to solve fully the 3-D transfer (F3D). Another is the independent column approximation (ICA, Cahalan et al., 1994b), which applies the 1-D transfer independently to every atmospheric column. The ICA is used in the current climate/weather prediction models and in the remote sensing of the atmosphere and land. The other computation mode is the partly-3-D (P3D) scheme, which uses the 3-D transfer for low-order scattering and 1-D for higher-order scattering.

The model's code is written in Fortran 77 and runs on many common computers under the UNIX/Linux OS. The radiative transfer code can be parallized with an MPI, and the code can run on large-scale parallel computers. The code is open and distributed for free (GPL license), with associated code and some example files, on the Web: <http://www.geocities.co.jp/null2unity/mcarats/>.

This model has been used in several model comparison projects such as I3RC (Cahalan et al., 2005), Wagner et al. (2006), and Ishida (2006), and several reasonable agreements have been obtained.

Figure 5.2.2 shows the algorithm flowchart. Due to the MCS method, a collision is categorized as a mathematical collision or a physical one, and the model photon moves only when a physical collision occurs. The photon tracing for a model photon terminates if the photon weight is zero or the photon escapes from the system into space. The irradiance and heating rate are calculated by method I in 3.8 (random sampling of the transmittance). The radiance and local flux are calculated by the LEM in 3.9, being sampled at every scattering event.

Figure 5.2.3 shows the grid system for the model. The atmosphere is divided into horizontally homogeneous and inhomogeneous layers. This is a numerically efficient way to realize the atmosphere by treating the cloudy layers as 3-D inhomogeneous layers and the clear layers as possibly homogeneous layers. The optical properties (extinction coefficient, single scattering albedo, and phase function) are constant within each cell (voxel). Cyclic boundary conditions are assumed for the horizontal domain boundary. The radiative quantities are computed at layer boundary surfaces, except for the heating rate, which is a cell-averaged quantity. The domain subdivision method is used for the photon tracing, and the model photon is tracked, traveling voxel-by-voxel.

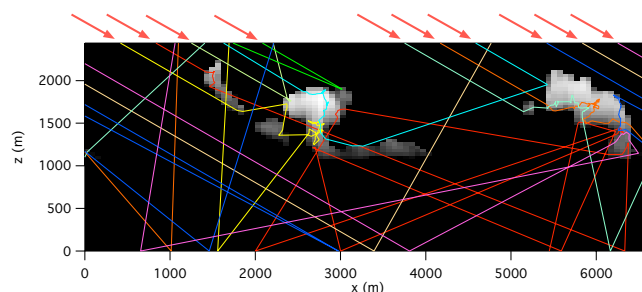


Fig. 5.2.1 Examples of photon trajectories in the MC simulation.

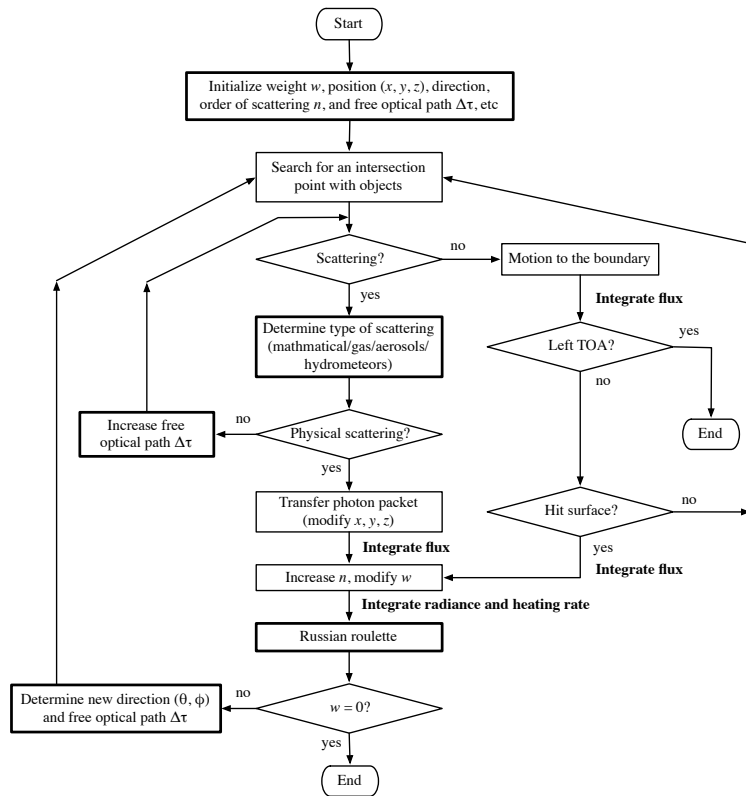


Fig. 5.2.2 Algorithm flowchart for the MCARaTS model. The algorithm for a single photon packet is illustrated.

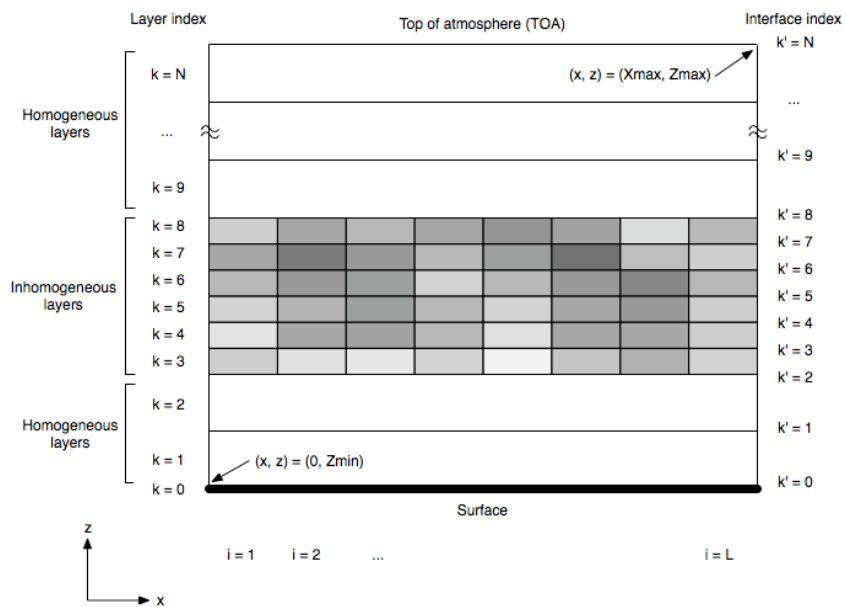


Fig. 5.2.3 Grid system used in the MCARaTS model

5.2.2 Calculation examples using MCARaTS

Calculation examples for the MCARaTS are shown in the following. Figures 5.2.4–5 show the angular distribution of computed radiances at a local point at the surface or above the clouds, using a 3-D distribution of cloud water simulated by large eddy simulation (LES). The surface is assumed to be an ocean with a wind velocity of 7 m s^{-1} . The model successfully simulated the reflection at the ocean surface, cloud shadows, and multiple scattering among broken clouds.

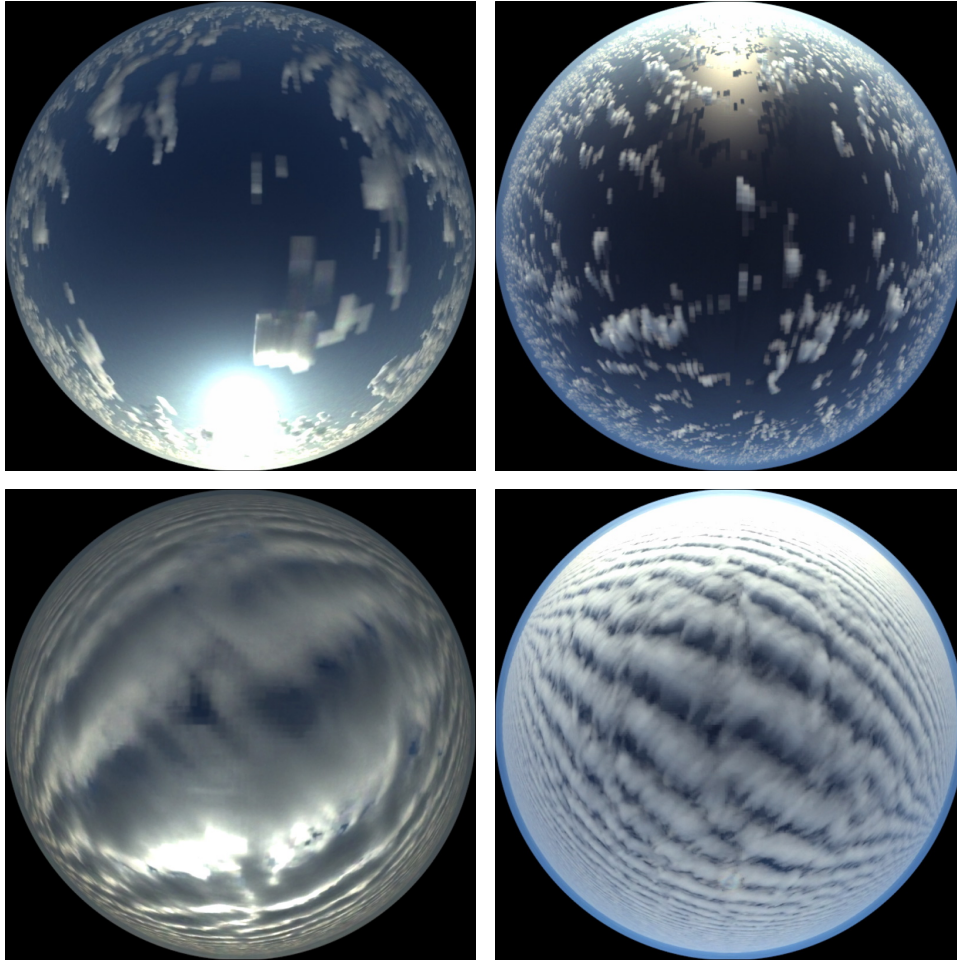


Fig. 5.2.4 Photorealistic computer graphics generated by using the MCARaTS model. Local radiances were plotted in the hemispheric angular region, and a true-color RGB composite was made. The 3-D distribution of the amount of cloud water was obtained from the LES simulation.



Fig. 5.2.5 Photorealistic computer graphics generated by using the MCARaTS model for sunset scenes over an ocean. A true-color RGB composite was made. The 3-D distribution of the amount of cloud water was obtained from the LES simulation. Left images show moderate amounts of aerosol (moderately clean atmosphere), and right images show large amounts of aerosol (realizing a dirty atmosphere).

Figure 5.2.6 shows horizontal-vertical cross sections of irradiance and radiance in a scene with two cumulus-type clouds. The forward-type MC algorithm makes it easy to estimate the spatial distribution of radiative energy from one simulation.

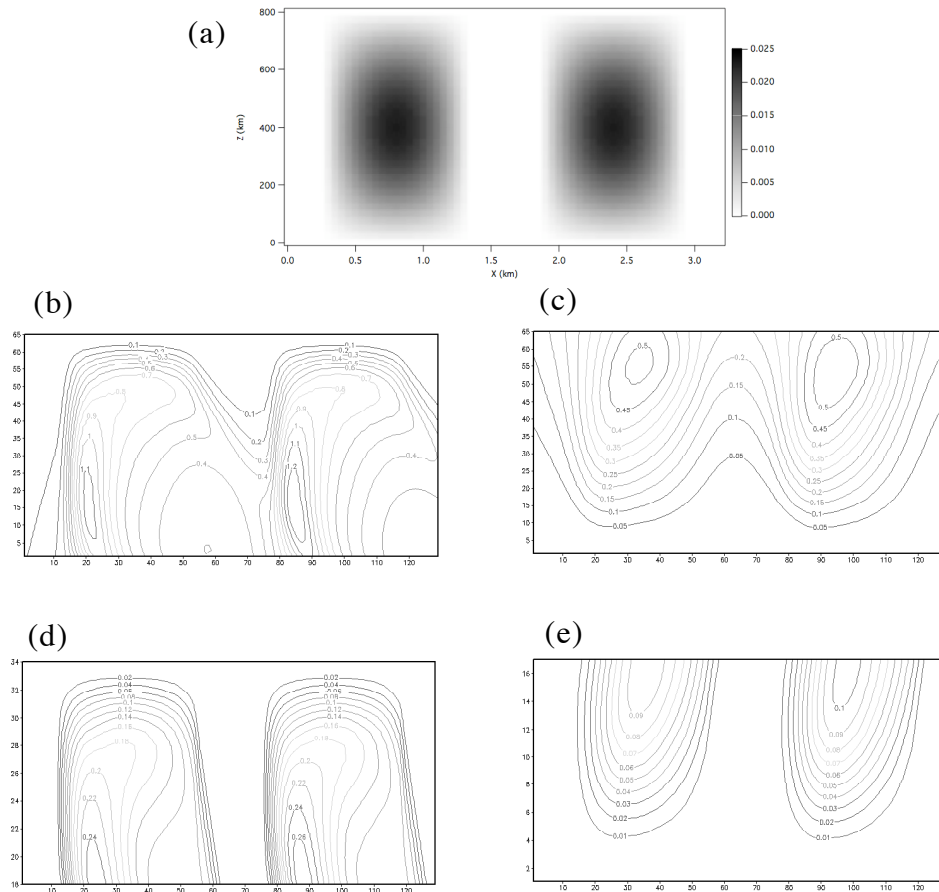


Fig. 5.2.6 Calculation example for a wavelength of 500 nm, in a case with two cumulus clouds (x - z cross section): (a) extinction coefficient; (b) downward irradiance; (c) upward irradiance; (d) downward radiance for $\mu_1 = -0.95$, $\phi_1 = 0^\circ$; and (e) upward radiance with $\mu_1 = 0.95$, $\phi_1 = 0^\circ$. The solar zenith angle is 53° , and the sun is on the left side.

Figure 5.2.7 shows simulation results for radiance, which could be obtained from satellite observation. Figure 5.2.8 shows simulation results for the multiple-scattering lidar signals. The radiation model can be used as a tool for the remote sensing of cloud properties.

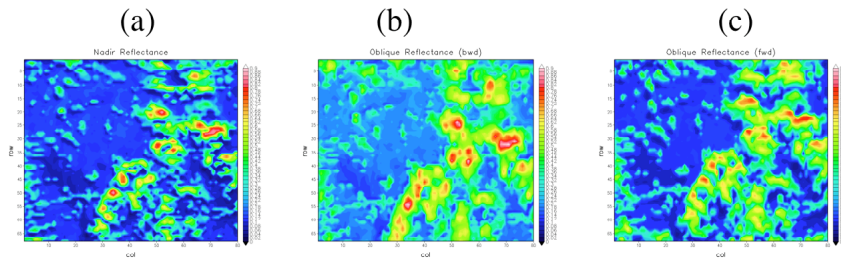


Fig. 5.2.7 Simulation results of satellite observation radiance: (a) BRF for nadir looking, (b) backward viewing (geometry of the backscattering), and (c) forward viewing (geometry of the forward scattering). These are from case 6 of I3RC phase III.

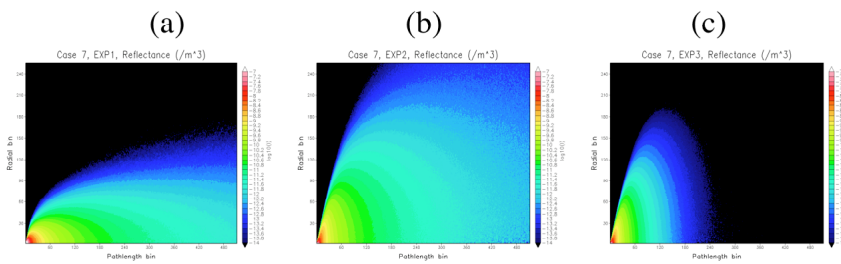


Fig. 5.2.8 Simulation results of the multiple-scattering lidar: 2-D plot of irradiance frequency as a function of flight path length in the cloud (bottom axis) and beam emission direction (right axis). The laser beam light is emitted, scattered in the cloud many times, and detected at the receiver near the emitter. (a) Infinitely thick layer with isotropic scattering, (b) as (a) but with Heyney-Greenstein phase function, and (c) thickness of 300 m with Mie scattering phase function. These are from case 7 of I3RC phase III.

5.3 Introduction of plant canopy radiative transfer model

A plant canopy radiative transfer model is important for evaluating forest and grassland light environments. The light environment is one of the primary environmental parameters for plant photosynthesis. Plant canopy photosynthesis can be simulated using the method described in 3.12 when the spatial distribution of the plant canopy light environment, such as the APAR, and incident irradiance at the top of the understory layer from radiative transfer simulation is available. Also, the simulated spectral reflectance at the top of a plant canopy is helpful in analyzing the relationship between the observed spectral reflectance and forest structures.

We introduce the plant canopy radiative transfer model based on the method described in Chapter 2 to Chapter 4. Then, some examples of the simulation are shown.

5.3.1 Plant canopy radiative transfer model

a. Simulation scene

It is necessary to prepare the simulation scene for radiative transfer calculation. Figure 5.3.1 shows the forest scene and individual tree and forest floor conditions. As described in 2.3, several representations of the forest scene can potentially be used for the radiative transfer simulation. We use the geometrical representation of individual trees (see center image in Fig. 2.3.4 in 2.3).

Each tree canopy is modeled as an ellipsoid (Fig. 5.3.1(a)). The leaves are distributed uniformly within this geometric object (leaf angle distribution = constant). Stems are modeled as cylinders. A photon does not enter the stem. The photon is reflected at the surface of the stem. The forest floor is assumed to be a plane-parallel layer (see left image in Fig. 2.3.4 in 2.3), and under the forest floor vegetation, a soil layer exists.

Trees are distributed in a 30×30 m simulation scene. Figures 5.3.1(b) and (c) are the simulation scenes used in this example. A total of 100 trees are randomly positioned in this 30×30 m area. The heights of the trees, lengths of the canopies, and radii of the canopies are determined to be in the range of $15.0 \text{ m} \pm 7.5 \text{ m}$, $5.0 \text{ m} \pm 1.2 \text{ m}$, $1.5 \text{ m} \pm 0.3 \text{ m}$, respectively.

In the plant canopy radiative transfer model, a simulation is conducted in this defined scene by tracing the photon and sampling the radiative quantities.

b. Preparation of optical properties of plant canopy element

The optical properties of the forest elements are required to perform the radiative transfer simulation. The parameters required in the simulation are the reflectance and transmittance of the forest elements (canopy leaf, forest floor plant leaf, stem, soil), canopy leaf area index, forest floor leaf area index, and leaf angle distribution of the canopy and forest floor.

As described in 2.3, the reflectance and transmittance for a single leaf are calculated from the leaf radiative transfer model or they can be obtained from measured data. As an example, we

use the parameters summarized in Table 5.3.1 and Table 5.3.2.

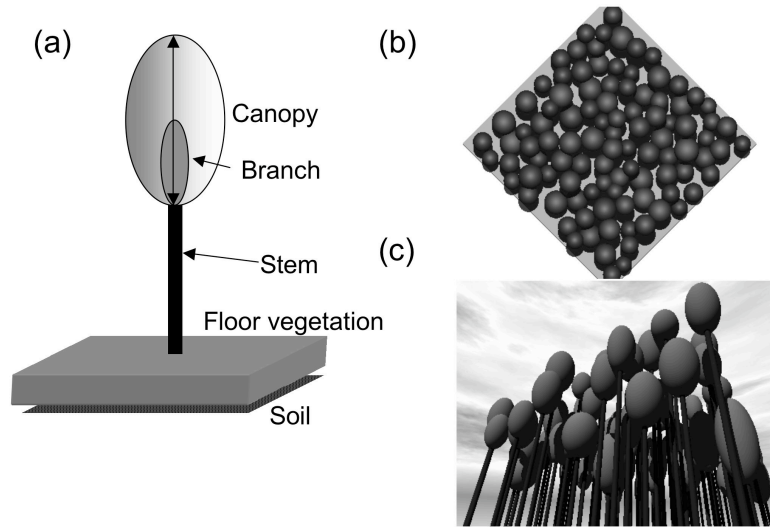


Fig 5.3.1 Forest canopy scene used in the simulation: (a) Modeled single tree, (b) nadir view of the modeled forest scene, and (c) modeled forest scene.

Table 5.3.1 Optical properties of canopy and forest floor elements.

	450 nm	550 nm	650 nm	800 nm	PAR
Canopy leaf reflectance	0.038	0.110	0.046	0.502	0.065
Canopy leaf transmittance	0.017	0.038	0.021	0.190	0.025
Floor leaf reflectance	0.050	0.186	0.075	0.420	0.100
Floor leaf transmittance	0.136	0.272	0.131	0.560	0.180
Stem	0.142	0.175	0.247	0.428	0.190
Soil	0.085	0.115	0.149	0.268	0.120

Table 5.3.2 Other parameters.

Solar zenith angle	40°
Canopy leaf area density	0.5, 2.0
Canopy branch area density	0.5
Floor leaf area index	0.5

c. MC simulation in forest scene

Figure 5.3.2 shows a flowchart for the canopy radiative transfer model. In the forest scene, this model traces the photon trajectory, which is input at the top of the canopy with an initial weight w_0 . Then, scattering events are generated within the canopy and for forest floor objects or on the stem and ground surfaces. The non-analog method (see 3.5) is employed to evaluate the

radiative quantities from sampled photons. The scattering direction is determined using the LUT method (see 3.5). The photon tracing will be stopped when the photon exits the simulation scene or the weight of the photon w becomes 0 after the Russian roulette. Then, the next photon tracing will start.

There are no universal criteria to determine the threshold ε of the Russian roulette. The accuracy becomes worse when we use larger values for ε , and the computation time becomes longer when we use smaller values for ε . In plant canopies, leaf reflectance and transmittance have lower values in the visible region and higher values in the near-infrared region, as shown in 2.3. Therefore, ε should be determined empirically by trial and error. Here, we use the following threshold ε , which is defined using the single scattering albedo ω :

$$\varepsilon = 0.1\omega^2 \quad (5.3.1)$$

By using this equation, the Russian roulette is executed after third-order scattering on average in the visible region ($\omega \sim 0.1$). In the near-infrared region ($\omega \sim 0.9$), the Russian roulette is executed after twentieth-order scattering on average if all scattering occurs in the leaf surface. However, in an actual forest scene, the Russian roulette is executed after fifth- to tenth-order scattering because of the existence of the stem and soil, the single scattering albedo of which is less than that of a leaf. We employ the spectral integration method described in 3.11 for integrating the radiative quantities for all of the solar radiation and the photosynthetically active radiation.

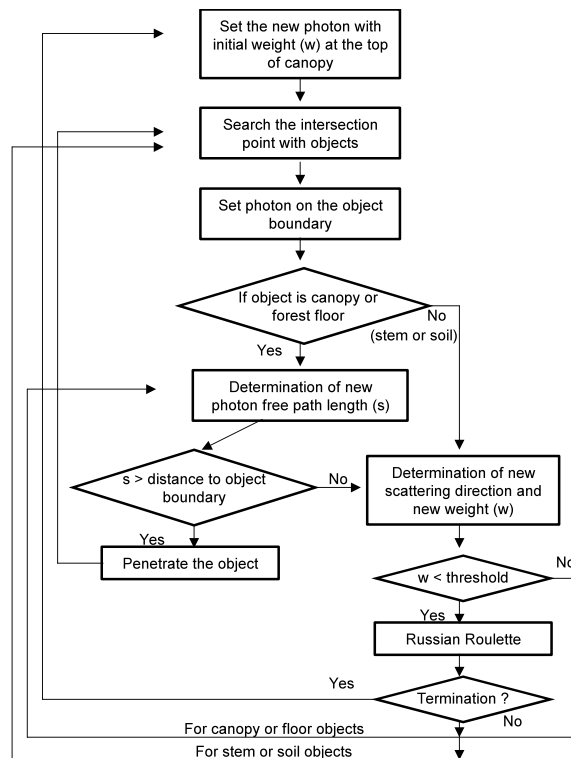


Fig. 5.3.2 Flowchart for the plant canopy radiative transfer model.

d. Sampling of radiative quantities

The radiative quantities are sampled by tracing photons in the forest. In remote sensing and terrestrial carbon cycle studies, the following five parameters are important:

1. Bidirectional reflectance factor (BRF)
2. Downward irradiance at the forest floor
3. Total APAR in the voxel ($\mu\text{mol s}^{-1} \text{m}^{-2} \text{m}^{-3}$) or ($\text{W m}^{-2} \text{m}^{-3}$)
4. Diffuse APAR in the voxel ($\mu\text{mol s}^{-1} \text{m}^{-2} \text{m}^{-3}$) or ($\text{W m}^{-2} \text{m}^{-3}$)
5. Number of direct photons first scattered in the voxel

We employ the LEM for BRF sampling. The downward irradiance at the forest floor is an important parameter to evaluate the light environment for the forest floor vegetation. We sample it by counting the weight crossing over the horizontal plane at the forest floor. The parameters from 3 to 5 are required to calculate the canopy photosynthesis. The parameters 3 and 4 are equivalent to the heating rate in the atmospheric radiative transfer model. These parameters can be sampled by counting the absorbed energy $w_i(1 - \omega)$ after the scattering events.

In the springtime, deciduous forests have little leaf canopy (low leaf area density), causing a difficulty in sampling the APAR accurately, due to few scattering events. In this case, the scaling method described in 4.2 (collision-forcing method) is effective to improve the computation time and accuracy.

5.3.2 Simulated results

Figure 5.3.3 shows the simulated BRF in the blue, green, red, and near infrared spectral regions. The x -axis indicates the observation angle over the principal plane. The negative angle indicates the solar direction (backscattering direction). The BRF in the backscattering direction is larger than that in forward scattering. In the forward scattering direction, the BRF gradually decreases with an increase in the observation angle. In the solar direction (backscattering direction), strong BRF peaks are found. This is called the hotspot or opposition effect, which occurs when all of the shadows are hidden from the observation view.

Figure 5.3.4 shows the nadir view simulated RGB images in a forest landscape. The left image shows the lower leaf area index case and the right image is the higher leaf area index case. When the leaf coverage in the canopy is low, the forest floor can be identified. Also, we can clearly identify the dark shadows caused by the stems and solar geometry (solar radiation is incident from the right side of these images).

Figure 5.3.5 shows the results of the 3-D distribution of the APAR at three different canopy height levels. As shown on the right side of Fig. 5.3.5, we can identify the effect of the stem shadow at a low canopy level. Figure 5.3.6 shows the spatial distribution of the downward irradiance at the forest floor. Even if the canopy leaf area index is low (leaf area index = 0.5), the irradiance in the shaded area is only 20% of the sunlit area.

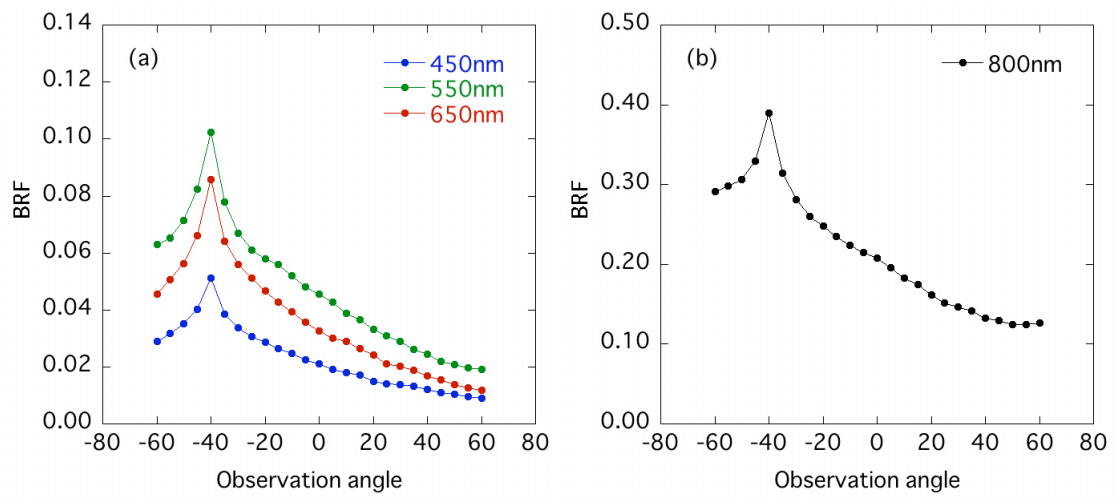


Fig. 5.3.3 Bidirectional reflectance factor at the top of the canopy (principal plane): (a) 450 nm, 550 nm, 650 nm and (b) 800 nm.

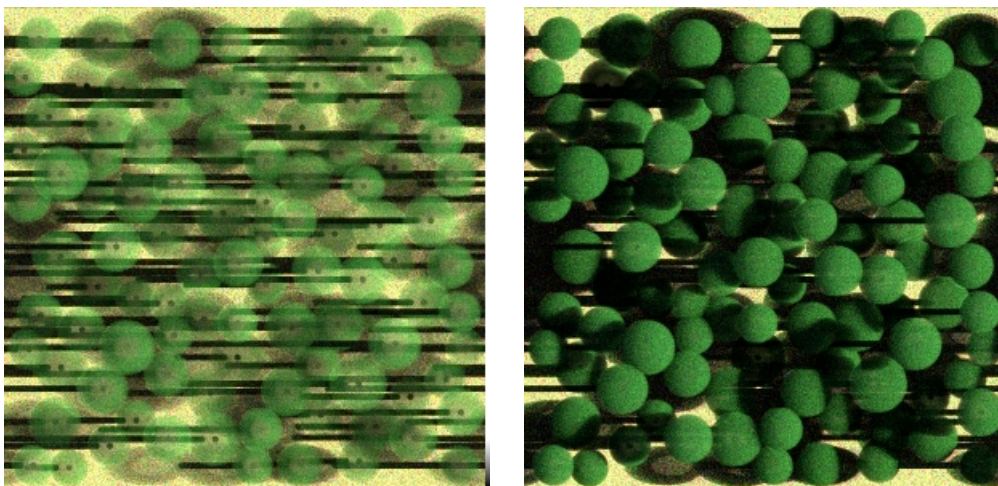


Fig. 5.3.4 Nadir view of the simulated forest landscape. Left: leaf area index = 0.5; right: leaf area index = 2.0.

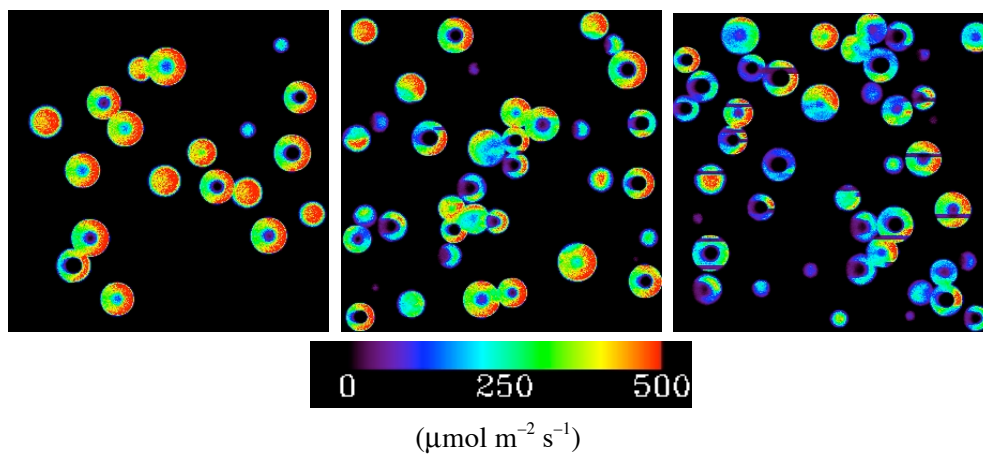


Fig. 5.3.5 3-D APAR distribution in the forest canopy (leaf area index = 0.5). Left: average for 19–20 m height, middle: average for 14–15 m height, right: average for 9–10 m.

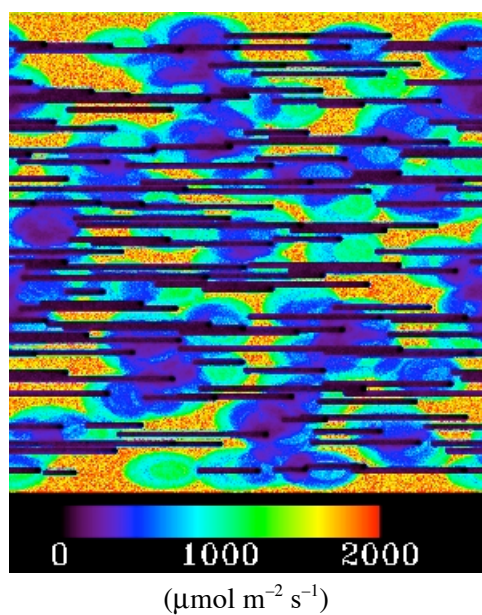


Fig. 5.3.6 Downward PAR irradiance at the forest floor (leaf area index = 0.5).

Chapter 6 Conclusion

This report described three-dimensional (3-D) radiative transfer models based on Monte Carlo (MC) methods. The fundamental theory of the model and the physical and optical properties of the atmosphere and plant canopy were described, and details of the algorithms used for the model were also described with significant emphasis. Recently, computing power using large-scale computers has been rapidly growing, at a factor of 400 per 10 years. This tendency can be expected to continue in the future (at least the near future). With the aid of this computing power, the realism of the models used for scientific studies will improve, accurately depicting physical processes that could not be treated explicitly in the past. As for radiation models, more realistic processes could be included in the model in the future. As described in this report, the MC methods enable the accurate and efficient calculation of 3-D radiative transfer in a cloudy atmosphere and plant canopy. The model can precisely treat complicated mixed media and a bidirectional reflectance distribution function, compute the radiative quantity for each scattering order, and treat arbitrary objects with complicated geometrical shapes in an arbitrary coordinate system. In addition, the MC model is very efficient for calculating the radiative quantities averaged over a spectral band.

Although in this report, discussions were limited to a cloudy atmosphere and plant canopy, the algorithms described in this report are not limited to these problems. For example, they can be applied to the radiative transfer in city canopies, mountains (rough surfaces), or astrophysics, as well as in medical sensing or mechanical engineering. The authors will be pleased if these algorithms help the reader to develop new models when studying new problems.

Marchuk et al. (1980) described very good calculation methods for atmospheric optics using the MC methods. Even though 25 years have passed since these were published, they remain the best for an MC radiative transfer model. For a plant canopy, too, the algorithms of Marchuk et al. would be useful, because the theory behind the problem is very similar.

Acknowledgements

The authors are grateful to Prof. K. Tsuboki of Nagoya University and Dr. A. T. Noda of FRCGC, JAMSTEC, for providing the large eddy simulation data for boundary layer clouds used in 5.2.

This work was partly supported by KAKENHI (Wakate-Kenkyu B, No. 18710020) of the Ministry of Education, Culture, Sports, Science and Technology (MEXT).

This work was supported by Japan EOS (Earth Observation System) Promotion Program of the Ministry of Education, Culture, Sports, Science and Technology (MEXT).

Appendix

A1 Analytical functions for size distribution

Size distribution for cloud and aerosol particles is often expressed in analytical form. In the following, common distribution functions are introduced, along with the relationships between their parameters and M , V , and N . See also 2.1 for the representations of parameters.

A1.1 Power-law distribution

The size distribution of ice particles could be expressed as a combination of the power-law functions (OPAC, Hess et al., 1998; Heymsfield and Platte, 1984):

$$n(r) = NMf \times \begin{cases} 0 & \text{for } r < r_0 \text{ or } r_2 < r \\ a_1 r^{b_1} & \text{for } r_0 < r < r_1 \\ a_2 r^{b_2} & \text{for } r_1 < r < r_2 \end{cases} \quad (\text{A1.1})$$

Eight parameters other than M and N are required.

A1.2 Gamma distribution

The gamma distribution is often used for approximating the cloud particle size distribution:

$$n(r) = N \frac{r^{\alpha-1}}{\beta^\alpha \Gamma(\alpha)} \exp\left(-\frac{r}{\beta}\right) \quad (\text{A1.2})$$

where $\alpha > 0$ is the scale parameter. The mode radius r_{mod} is

$$r_{\text{mod}} = (\alpha - 1)\beta, \quad \alpha \geq 1 \quad (\text{A1.3})$$

The moment (about zero) of the p th-order is given by

$$\frac{\beta^p \Gamma(\alpha + p)}{\Gamma(\alpha)} \quad (\text{A1.4})$$

Using this, various definitions of average radius and variance could be derived:

$$r_{\text{geo}} = \beta\alpha \quad (\text{A1.5a})$$

$$r_{sec}^2 = \beta^2 \alpha (\alpha + 1) \quad (A1.5b)$$

$$r_{vol}^3 = \beta^3 \alpha (\alpha + 1) (\alpha + 2) \quad (A1.5c)$$

$$v_{geo} = \beta^2 \alpha \quad (A1.5d)$$

where v_{geo} is the variance. The standard deviation normalized by the average is

$$\tilde{\sigma} \equiv \frac{\sqrt{v_{geo}}}{r_{geo}} = \frac{1}{\sqrt{\alpha}} \quad (A1.6)$$

The effective radius and variance are respectively

$$r_{eff} = (\alpha + 2)\beta = (\alpha + 2) \frac{r_{mod}}{\alpha - 1} = \frac{r_{geo}}{1 - 2v_{eff}} \quad (A1.7a)$$

$$v_{eff} = \frac{1}{\alpha + 2} \quad (A1.7b)$$

The parameter κ of (2.2.23) is derived from (A1.5c) and (A1.7a) as

$$\kappa = \frac{(\alpha + 1)\alpha}{(\alpha + 2)^2} \quad (A1.8)$$

By representing β with M and N , the following equation is derived:

$$\beta = \left[\frac{3}{4\pi(\alpha + 2)(\alpha + 1)\alpha} \cdot \frac{M}{\rho N} \right]^{1/3} \quad (A1.9)$$

By substituting this to (A1.7a), the effective radius can be written as a function of M (or V) and N .

To determine the parameters α and β from the effective radius and the volume mean radius, the following can be used:

$$\beta = \frac{r_{eff}}{4} \left[3 - \sqrt{1 + 8(r_{vol}/r_{eff})^3} \right] \quad (A1.10a)$$

$$\alpha = \frac{r_{eff}}{\beta} - 2. \quad (A1.10b)$$

Using r_{geo} or r_{mod} for representing the size distribution, instead of using β ,

$$n(r) = N \left(\frac{\alpha}{r_{geo}} \right)^\alpha \frac{r^{\alpha-1}}{\Gamma(\alpha)} \exp\left(-\frac{\alpha}{r_{geo}} r\right) \quad (A1.11a)$$

$$n(r) = N \left(\frac{\alpha - 1}{r_{mod}} \right)^\alpha \frac{r^{\alpha-1}}{\Gamma(\alpha)} \exp\left(-\frac{\alpha - 1}{r_{mod}} r\right) \quad (A1.11b)$$

Note that the mode radius is defined only when $\alpha > 1$.

A1.3 Modified/generalized gamma distribution

The modified/generalized gamma distribution is also frequently used for expressing the cloud particle size distribution:

$$n(r) = N \frac{r^{\alpha\gamma-1}}{\beta^{\alpha\gamma}\Gamma(\alpha)} \exp\left[-\left(\frac{r}{\beta}\right)^\gamma\right] \quad (\text{A1.12})$$

where α , β , and γ are parameters. The mode radius is

$$r_{mod} = \beta \left(\frac{\alpha\gamma-1}{\gamma}\right)^{1/\gamma} \text{ for } \alpha > \frac{1}{\gamma} \quad (\text{A1.13})$$

The moment of p th order is given as

$$\frac{\beta^p \Gamma\left(\alpha + \frac{p}{\gamma}\right)}{\Gamma(\alpha)} \quad (\text{A1.14})$$

As for the gamma distribution, this can be used to derive various average radii:

$$r_{geo} = \beta \Gamma\left(\alpha + \frac{1}{\gamma}\right) / \Gamma(\alpha) \quad (\text{A1.15a})$$

$$r_{sec}^2 = \beta^2 \Gamma\left(\alpha + \frac{2}{\gamma}\right) / \Gamma(\alpha) \quad (\text{A1.15b})$$

$$r_{vol}^3 = \beta^3 \Gamma\left(\alpha + \frac{3}{\gamma}\right) / \Gamma(\alpha) \quad (\text{A1.15c})$$

$$r_{eff} = \beta \Gamma\left(\alpha + \frac{3}{\gamma}\right) / \Gamma\left(\alpha + \frac{2}{\gamma}\right) \quad (\text{A1.15d})$$

The size distribution of (A1.12) could be expressed using r_{geo} or r_{mod} , instead of β :

$$n(r) = N \frac{X^\alpha}{r \Gamma(\alpha)} \exp(-X) \quad (\text{A1.16a})$$

$$X = \left(\frac{\Gamma(\alpha+1/\gamma)}{\Gamma(\alpha)} \frac{r}{r_{geo}}\right)^\gamma = \frac{\alpha\gamma-1}{\gamma} \left(\frac{r}{r_{mod}}\right)^\gamma \quad (\text{A1.16b})$$

where the mode radius exists only when $\alpha > 1/\gamma$.

A1.4 Lognormal distribution (number density)

Size distribution of number density for cloud and aerosol particles is often expressed by the lognormal distribution (Nakajima and King, 1990; Hess et al., 1998):

$$n(r) = N \frac{1}{\sqrt{2\pi r \ln s}} \exp\left[-\frac{1}{2} \left(\frac{\ln r - \ln r_{mod}}{\ln s}\right)^2\right] \quad (\text{A1.17})$$

where r_{mod} corresponds to the mode in the logarithmic scale (the mode of $dN/d\ln r$). The moment of p th-order is

$$(\ln r_{mod})^p \exp\left(\frac{1}{2} p^2 \ln^2 s\right) \quad (\text{A1.18})$$

Using this, the following are derived:

$$r_{geo} = r_{mod} \exp\left(\frac{1}{2} \ln^2 s\right) \quad (\text{A1.19a})$$

$$r_{sec} = r_{mod} \exp(\ln^2 s) \quad (\text{A1.19b})$$

$$r_{vol} = r_{mod} \exp\left(\frac{3}{2} \ln^2 s\right) \quad (\text{A1.19c})$$

$$v_{geo} = r_{mod}^2 \exp(\ln^2 s) [\exp(\ln^2 s) - 1] \quad (\text{A1.19d})$$

$$r_{eff} = r_{mod} \exp\left(\frac{5}{2} \ln^2 s\right) \quad (\text{A1.19e})$$

$$v_{eff} = \exp(\ln^2 s) - 1 \quad (\text{A1.19f})$$

$$\kappa = \exp(-3 \ln^2 s) \quad (\text{A1.19g})$$

By substituting (A1.19g) into (2.2.25), the effective radius and the mode radius are written as functions of M and N :

$$r_{eff} = \left[\frac{3M}{4\pi N\rho}\right]^{1/3} \exp(\ln^2 s) \quad (\text{A1.20a})$$

$$r_{mod} = \left[\frac{3M}{4\pi N\rho}\right]^{1/3} \exp\left(-\frac{3}{2} \ln^2 s\right) \quad (\text{A1.20b})$$

Additionally, the mode radius and the standard deviation (s) are expressed as follows:

$$r_{mod} = r_{vol} \left(\frac{r_{vol}}{r_{eff}}\right)^{3/2} = r_{vol} \sqrt{\kappa} \quad (\text{A1.21a})$$

$$\ln^2 s = \ln\left(\frac{r_{eff}}{r_{vol}}\right) = -\frac{1}{3} \ln \kappa \quad (\text{A1.21b})$$

A1.5 Lognormal distribution (volume density)

The volume size distribution could be assumed to be expressed by the lognormal function (Hayasaka et al., 1994; Higurashi and Nakajima, 1999):

$$v(r) \equiv \frac{dV}{dr} = V \frac{1}{\sqrt{2\pi r \ln s}} \exp \left[-\frac{1}{2} \left(\frac{\ln r - \ln r_{\text{mod}}}{\ln s} \right)^2 \right] \quad (\text{A1.22})$$

In this case, the number density is written as

$$\begin{aligned} n(r) &= \frac{dV}{dr} \times \frac{3}{4\pi r^3} \\ &= N \frac{r_{\text{vol}}^3}{\sqrt{2\pi r^4 \ln s}} \exp \left[-\frac{1}{2} \left(\frac{\ln r - \ln r_{\text{mod}}}{\ln s} \right)^2 \right] \end{aligned} \quad (\text{A1.23})$$

Various radius averages are as follows:

$$r_{\text{geo}} = r_{\text{mod}} \exp \left(-\frac{5}{2} \ln^2 s \right) \quad (\text{A1.24a})$$

$$r_{\text{sec}} = r_{\text{mod}} \exp \left(-2 \ln^2 s \right) \quad (\text{A1.24c})$$

$$r_{\text{vol}} = r_{\text{mod}} \exp \left(-\frac{3}{2} \ln^2 s \right) \quad (\text{A1.24c})$$

$$r_{\text{eff}} = r_{\text{mod}} \exp \left(-\frac{1}{2} \ln^2 s \right) \quad (\text{A1.24d})$$

$$\kappa = \exp \left(-3 \ln^2 s \right). \quad (\text{A1.24e})$$

By substituting (A1.24e) into (2.2.25), the effective radius and the mode radius are written with M (or V) and N :

$$r_{\text{eff}} = \left[\frac{3M}{4\pi N \rho} \right]^{1/3} \exp \left(\ln^2 s \right) \quad (\text{A1.25a})$$

$$r_{\text{mod}} = \left[\frac{3M}{4\pi N \rho} \right]^{1/3} \exp \left(\frac{1}{2} \ln^2 s \right) \quad (\text{A1.25b})$$

The mode radius and the standard deviation (s) are expressed as

$$r_{\text{mod}} = r_{\text{vol}} \left(\frac{r_{\text{eff}}}{r_{\text{vol}}} \right)^{3/2} = \frac{r_{\text{vol}}}{\sqrt{\kappa}} \quad (\text{A1.26a})$$

$$\ln^2 s = \ln \left(\frac{r_{\text{eff}}}{r_{\text{vol}}} \right) = -\frac{\ln \kappa}{3} \quad (\text{A1.26b})$$

A2 Optical properties of mixed media

Let us consider a mixed medium with several kinds of aerosol, cloud water, and ice particle dispersions. The optical and physical properties of each component are already known. If the absolute amounts ($N(i)$ or $V(i)$ or $q(i)$ for i th component) of the respective components are known, the optical properties of the mixed medium are calculated, for a wet status with hygroscopic aerosols, as follows:

$$\bar{\beta}_e = \sum_i \sigma_e(i)N(i) = \sum_i Q_e(i)\pi(r_{sec}^{wet}(i))^2 N(i) \quad (\text{A2.1a})$$

$$\bar{\beta}_s = \sum_i \sigma_s(i)N(i) = \sum_i Q_s(i)\pi(r_{sec}^{wet}(i))^2 N(i) \quad (\text{A2.1a})$$

$$\bar{\omega} = \frac{\bar{\beta}_s}{\bar{\beta}_e} \quad (\text{A2.1c})$$

$$\bar{P}(\Theta) = \frac{\sum_i \sigma_s(i)N(i)P(i,\Theta)}{\sum_i \sigma_s(i)N(i)} = \frac{1}{\bar{\beta}_s} \sum_i Q_s(i)\pi(r_{sec}^{wet}(i))^2 N(i)P(i,\Theta) \quad (\text{A2.1d})$$

Another case is where the absolute amounts are unknown but the mixing ratio is known. With the number density mixing ratio α_N ,

$$\sum_i \alpha_N(i) = 1 \quad (\text{A2.2a})$$

$$\alpha_N(i) = \frac{N(i)}{\bar{N}} \quad (\text{A2.2b})$$

where the total number density of the mixed medium is

$$\bar{N} = \sum_i N(i) \quad (\text{A2.3})$$

The cross-section-mean radius, the volume-mean radius, and the internal mass density of the wet/dry polydispersion are given as

$$\bar{r}_{sec}^{dry/wet} = \left[\sum_i (r_{sec}^{dry/wet}(i))^2 \alpha_N(i) \right]^{1/2} \quad (\text{A2.4a})$$

$$\bar{r}_{vol}^{dry/wet} = \left[\sum_i (r_{vol}^{dry/wet}(i))^3 \alpha_N(i) \right]^{1/3} \quad (\text{A2.4b})$$

$$\bar{\rho}^{dry/wet} = \frac{\sum_i (r_{vol}^{dry/wet}(i))^3 \rho^{dry/wet}(i) \alpha_N(i)}{\sum_i (r_{vol}^{dry/wet}(i))^3 \alpha_N(i)} \quad (\text{A2.4c})$$

The optical properties of wet polydispersion are calculated by

$$\bar{Q}_e = \frac{\sum_i Q_e(i) \pi(r_{sec}^{wet}(i))^2 \alpha_N(i)}{\sum_i \pi(r_{sec}^{wet}(i))^2 \alpha_N(i)} \quad (\text{A2.5a})$$

$$\bar{Q}_s = \frac{\sum_i Q_s(i) \pi(r_{sec}^{wet}(i))^2 \alpha_N(i)}{\sum_i \pi(r_{sec}^{wet}(i))^2 \alpha_N(i)} \quad (\text{A2.5b})$$

$$\bar{w} = \frac{\bar{Q}_s}{\bar{Q}_e} \quad (\text{A2.5c})$$

$$\bar{P}(\Theta) = \frac{\sum_i Q_s(i) \pi(r_{sec}^{wet}(i))^2 \alpha_N(i) P(i, \Theta)}{\sum_i Q_s(i) \pi(r_{sec}^{wet}(i))^2 \alpha_N(i)} \quad (\text{A2.5d})$$

Using these formulas, the extinction and scattering coefficients are calculated from the total number density:

$$\bar{\beta}_e = \bar{N} \times \bar{Q}_e (\bar{r}_{sec}^{wet})^2, \quad \bar{\beta}_s = \bar{N} \times \bar{Q}_s (\bar{r}_{sec}^{wet})^2 \quad (\text{A2.6})$$

Instead of the number density mixing ratios, the volume density mixing ratios at the dry/wet status or the mass mixing ratios could be the known parameters. In such a case, the number mixing ratios can be converted from the known ratios if the volume-mean radius and internal mass density of each component are known. For various mixing ratios,

$$\sum_i \alpha_V^{dry}(i) = \sum_i \alpha_M^{dry}(i) = \sum_i \alpha_V^{wet}(i) = \sum_i \alpha_M^{wet}(i) = 1 \quad (\text{A2.7})$$

The relationship with the number mixing ratio is as follows:

$$\alpha_V^{dry/wet}(i) \propto \alpha_N(i) \times (r_{vol}^{dry/wet}(i))^3 \quad (\text{A2.8a})$$

$$\alpha_M^{dry/wet}(i) \propto \alpha_N(i) \times (r_{vol}^{dry/wet}(i))^3 \rho^{dry/wet}(i) \quad (\text{A2.8b})$$

Using this and (A2.7), any mixing ratios can be converted to number mixing ratios. Table A1 lists the optical properties of typical aerosol mixtures, calculated according to Hess et al. (1998).

Table A1 Optical properties of typical aerosol mixtures: wavelength of 0.55 μm , relative humidity of 80%, asymmetry parameter g .

Aerosol type	r_{eff} (μm)	ρ (10^2 kg m^{-3})	Q_e	ω	g
Continental clean	0.23	15.1	0.941	0.973	0.710
Continental average	0.21	14.9	0.893	0.930	0.706
Continental polluted	0.18	14.3	0.853	0.899	0.700
Urban	0.18	14.6	0.796	0.828	0.692
Desert	1.28	25.5	1.92	0.889	0.729
Maritime clean	1.07	12.2	1.94	0.997	0.768
Maritime polluted	0.69	12.2	1.49	0.976	0.753
Maritime tropical	1.13	12.2	2.02	0.998	0.770
Arctic	0.29	12.4	1.00	0.893	0.721
Antarctic	0.46	11.2	2.33	1.000	0.776
Mineral transported	2.37	26.0	2.34	0.820	0.782
Yellow dust	2.19	20.0	2.43	0.871	0.738
Stratosphere	0.44	11.0	2.33	1.000	0.776
Volcanic ash	0.44	10.0	2.50	0.930	0.707

A3 Spectrally averaged optical properties

Optical properties spectrally averaged over a spectral band are required for the radiative transfer calculation for the band. The spectral averaging is usually performed with weighting by the spectral source flux $S(\lambda)$ (solar incident flux or the Planck function for the thermal emission):

$$\tilde{Q}_e = \frac{\int_{\lambda_{\min}}^{\lambda_{\max}} Q_e(\lambda) S(\lambda) d\lambda}{\int_{\lambda_{\min}}^{\lambda_{\max}} S(\lambda) d\lambda} \quad (\text{A3.1a})$$

$$\tilde{Q}_s = \frac{\int_{\lambda_{\min}}^{\lambda_{\max}} Q_s(\lambda) S(\lambda) d\lambda}{\int_{\lambda_{\min}}^{\lambda_{\max}} S(\lambda) d\lambda} \quad (\text{A3.1b})$$

$$\tilde{Q}_a = \frac{\int_{\lambda_{\min}}^{\lambda_{\max}} Q_a(\lambda) S(\lambda) d\lambda}{\int_{\lambda_{\min}}^{\lambda_{\max}} S(\lambda) d\lambda} \quad (\text{A3.1c})$$

$$\tilde{P}(\Theta) = \frac{\int_{\lambda_{\min}}^{\lambda_{\max}} P(\Theta, \lambda) Q_s(\lambda) S(\lambda) d\lambda}{\int_{\lambda_{\min}}^{\lambda_{\max}} Q_s(\lambda) S(\lambda) d\lambda} \quad (\text{A3.1d})$$

These could result in an inconsistent balance between the scattering and absorption efficiency factors:

$$\tilde{Q}_e \neq \tilde{Q}_s + \tilde{Q}_a \quad (\text{A3.2})$$

This causes many possibilities to define the spectrally averaged single scattering albedo:

$$\bar{\omega}(0) = \frac{\int_{\lambda_{\min}}^{\lambda_{\max}} \omega(\lambda) S(\lambda) d\lambda}{\int_{\lambda_{\min}}^{\lambda_{\max}} S(\lambda) d\lambda} \quad (\text{A3.3a})$$

$$\bar{\omega}(1) = \bar{Q}_s / \bar{Q}_e \quad (\text{A3.3b})$$

$$\bar{\omega}(2) = (\bar{Q}_e - \bar{Q}_a) / \bar{Q}_e \quad (\text{A3.3c})$$

$$\bar{\omega}(3) = \bar{Q}_s / (\bar{Q}_s + \bar{Q}_a) \quad (\text{A3.3d})$$

$$\bar{\omega}(4) = \frac{1}{2} (\bar{\omega}(1) + \bar{\omega}(2)) \quad (\text{A3.3e})$$

There are also other definitions (e.g., Fu, 1996; Nakajima et al., 2000). The differences between these definitions are especially large near a wavelength where the absorption coefficient varies rapidly with wavelength. The best choice for the definition would depend on the problem: the strength of the absorption and shape of the source flux spectrum.

A4 Vertical profile of aerosols

The vertical profile of aerosols is often expressed, as a first-order approximation, by an exponential function. If the compositions of the medium, size distributions, mixing ratios, and (for hygroscopic aerosols) the relative humidity are constant for a vertical column, then the aerosol extinction coefficient should solely follow the profile of the number density. If the relative humidity is not constant, then the proportionality becomes invalid.

Let us assume an exponential vertical profile for the number density:

$$N(z) = N(0) \exp(-sz), \quad s = \frac{1}{Z_s}. \quad (\text{A4.1})$$

With bottom and top altitudes (Z_{\min} and Z_{\max} , respectively), the vertically integrated number concentration per unit cross section of the column is

$$\begin{aligned} N_{col} &= \int_{Z_{\min}}^{Z_{\max}} N(z) dz \\ &= N(0) \frac{[\exp(-sZ_{\min}) - \exp(-sZ_{\max})]}{s} \end{aligned} \quad (\text{A4.2a})$$

If s is nearly equal to 0,

$$N_{col} \approx N(0)(Z_{\max} - Z_{\min}) \quad (\text{A4.2b})$$

From (A4.2a) or (A4.2b), the vertical profile is uniquely determined by $N(0)$ or N_{col} . Eq. (A4.1) becomes

$$N(z) = N_{col} \frac{s \exp(-sz)}{\exp(-sZ_{min}) - \exp(-sZ_{max})} \quad (A4.3)$$

The vertical profile of the extinction coefficient is

$$\begin{aligned} \beta_e(z) &= N(z)\sigma_e(z) \\ &= Q_e(z)\pi r_{sec}^2(z)N_{col} \frac{s \exp(-sz)}{\exp(-sZ_{min}) - \exp(-sZ_{max})} \end{aligned} \quad (A4.4)$$

where the average extinction efficiency $Q_e(z)$ should be calculated for the wet status of the mixed medium, using the method described in the previous subsection. The average extinction efficiency is constant within the layer and could be written as $Q_e(j)$. The optical thickness for the vertical column (integral of the extinction coefficient) is given as

$$\begin{aligned} \tau &= \int_{Z_{min}}^{Z_{max}} \beta_e(z) dz \\ &= N_{col} \frac{s}{\exp(-sZ_{min}) - \exp(-sZ_{max})} \int_{Z_{min}}^{Z_{max}} Q_e(z)\pi r_{sec}^2(z) \exp(-sz) dz \\ &= N_{col} \frac{s}{\exp(-sZ_{min}) - \exp(-sZ_{max})} \sum_j \left[Q_e(j)\pi r_{sec}^2(j) \int_{z_{j-1}}^{z_j} \exp(-sz) dz \right] \\ &= N_{col} \frac{1}{\exp(-sZ_{min}) - \exp(-sZ_{max})} \sum_j \left\{ Q_e(j)\pi r_{sec}^2(j) [\exp(-sz_{j-1}) - \exp(-sz_j)] \right\} \end{aligned} \quad (A4.5)$$

From this, N_{col} can be calculated if τ is given. In addition, using the volume-mean radius averaged over all components, $V(z)$ can be calculated from $N(z)$. The vertically integrated volume density ($\text{m}^3 \text{m}^{-2}$) is

$$\begin{aligned} V_{col} &= \int_{Z_{min}}^{Z_{max}} V(z) dz = \int_{Z_{min}}^{Z_{max}} N(z) \frac{4}{3} \pi r_{vol}^3(z) dz \\ &= N_{col} \frac{1}{\exp(-sZ_{min}) - \exp(-sZ_{max})} \sum_j \left\{ \frac{4}{3} \pi r_{vol}^3(j) [\exp(-sz_{j-1}) - \exp(-sz_j)] \right\} \end{aligned} \quad (A4.6)$$

Thus, N_{col} can be derived from V_{col} . Similarly, N_{col} can be derived from the vertically integrated mass density M_{col} (kg m^{-2}). Furthermore, the volume and mass could be formulated for both the dry and wet statuses. Finally, a single parameter out of τ , V_{col} , and M_{col} at the dry/wet status is enough to derive all of the other parameters.

Let us assume that the mixing ratios of aerosol species and relative humidity are all constant. Eqs. (A4.5–6) can be reduced to

$$\tau^{dry/wet} = N_{col} Q_e^{dry/wet} \pi (r_{sec}^{dry/wet})^2 \quad (A4.7a)$$

$$V_{col}^{dry/wet} = N_{col} \frac{4\pi}{3} (r_{vol}^{dry/wet})^3 \quad (\text{A4.7b})$$

$$M_{col}^{dry/wet} = N_{col} \frac{4\pi}{3} (r_{vol}^{dry/wet})^3 \rho^{dry/wet} \quad (\text{A4.7c})$$

Observations using an instrument such as lidar show that the vertical profile of the extinction coefficient is roughly exponential and that the extinction coefficient is somewhat large in the planetary boundary layer. If a more complicated profile shape is needed, a combination of several functions (e.g., the gamma distribution) would be a choice.

A5 Representation of photon transport by direction vector

The transport direction of the photon can be expressed by a unit vector with (x, y, z) components. For the zenith angle θ and azimuth angle ϕ , the direction vector is

$$\mathbf{\Omega} = \begin{pmatrix} u_x \\ u_y \\ u_z \end{pmatrix} = \begin{pmatrix} \sin\theta \cos\phi \\ \sin\theta \sin\phi \\ \cos\theta \end{pmatrix} \quad (\text{A5.1})$$

where

$$u_x^2 + u_y^2 + u_z^2 = 1 \quad (\text{A5.2})$$

$$\sin\theta = \sqrt{u_x^2 + u_y^2} = \sqrt{1 - u_z^2} \quad (\text{A5.3})$$

A5.1 Movement of photon

When the photon travels in the direction $\mathbf{\Omega}$ by a path length l , the coordinates of the photon become

$$\begin{pmatrix} x' \\ y' \\ z' \end{pmatrix} = \begin{pmatrix} x \\ y \\ z \end{pmatrix} + l\mathbf{\Omega} \quad (\text{A5.4})$$

A5.2 Rotation of direction due to scattering

When scattering occurs, the photon transport direction rotates. The unit vector $\mathbf{\Omega}$ rotates by an angle Θ to increase the zenith angle and subsequently rotates by an azimuth angle Φ about the original vector $\mathbf{\Omega}$. The new direction is

$$\mathbf{\Omega}' = \cos \Theta \mathbf{\Omega} + \sin \Theta \left[\cos \Phi \begin{pmatrix} u_x u_z / \sin \theta \\ u_y u_z / \sin \theta \\ -\sin \theta \end{pmatrix} + \sin \Phi \begin{pmatrix} -u_y / \sin \theta \\ u_x / \sin \theta \\ 0 \end{pmatrix} \right] \quad (\text{A5.5})$$

The numerical evaluation of this formula fails if $\sin^2 \theta = u_x^2 + u_y^2 = 1 - u_z^2 \approx 0$. In such a case, the new direction can be calculated by

$$\mathbf{\Omega}' = \text{sign}(u_z) \begin{pmatrix} \sin \Theta \cos \Phi \\ \sin \Theta \sin \Phi \\ \cos \Theta \end{pmatrix} \quad (\text{A5.6})$$

where $\text{sign}(\cdot)$ is a function to return +1 or -1 depending on the sign of the argument.

A5.3 Angle between two vectors

For the angle between two vectors $\mathbf{\Omega}_1$ and $\mathbf{\Omega}_2$,

$$\cos \alpha = \mathbf{\Omega}_1 \cdot \mathbf{\Omega}_2. \quad (\text{A5.7})$$

The angle can be derived from this formula. However, it is numerically difficult if α is nearly 0 or π , because of the round-off error. This problem is especially important for the simulation of a lidar signal, for example. The following gives an algorithm for accurate calculation of the angle even when α is nearly 0 or π .

First, let us derive $\sin \alpha$ for a small α . For the narrow triangle with the two vectors $\mathbf{\Omega}_1$ and $\mathbf{\Omega}_2$, the length of the other side is

$$a^2 = |\mathbf{\Omega}_1 - \mathbf{\Omega}_2|^2 \quad (\text{A5.8})$$

From the law of cosines,

$$a^2 + 1 - 2a \cos \beta = 1 \quad (\text{A5.9})$$

$$\therefore \sin \beta = \sqrt{1 - a^2/4} \quad (\text{A5.10})$$

From this and the law of sines,

$$\sin \alpha = a \sin \beta = a \sqrt{1 - a^2/4} \quad (\text{A5.11})$$

Next, from

$$y = \sin \alpha - C = 0 \quad (\text{A5.12})$$

and using the first-order Newtonian formula,

$$\alpha = C - \frac{y(\alpha = C)}{y'(\alpha = C)} = C - \frac{\sin C - C}{\cos C} \quad (\text{A5.13})$$

Expanding $\sin C$ and $\cos C$ by the Taylor series, truncating at the second term, and substituting it to the above formula, we get

$$\alpha = C \frac{6 - 2C^2}{6 - 3C^2}. \quad (\text{A5.14})$$

The solution is obtained by substituting $C = \sin \alpha$ into this equation.

A6 Determination of random point in a circle: Polar coordinate method

At a scattering or reflection event, a random number and the sine and cosine of a random azimuth angle are needed. A possible method to get the random azimuth is to compute

$$\Phi = 2\pi\rho_\Phi \quad (\text{A6.1})$$

using a random number uniformly distributed in $[0, 1]$. However, the required values are its sine and cosine, both of which are numerically heavy functions. A better method is the polar coordinate method, which directly determines $\rho, \cos \Phi, \sin \Phi$ (Fushimi, 1989). From two random numbers, ρ_1 and ρ_2 ,

$$\begin{aligned} W_1 &= 1 - 2\rho_1, W_2 = 1 - 2\rho_2 \\ r^2 &= W_1^2 + W_2^2 \end{aligned} \quad (\text{A6.2})$$

are computed. This is iterated until

$$10^{-12} \leq r^2 \leq 1 \quad (\text{A6.3})$$

Such an iteration converges fast because the probability that (A6.3) is true is large as $\pi/4 \sim 0.785$, for one iteration cycle. Finally, random points in a circle in two dimensions are determined, and such points should be distributed uniformly within the circle. The coordinates of the points are given by W_1 and W_2 . Then,

$$\begin{aligned} \rho &= r^2 \\ \cos \Phi &= W_1/r \\ \sin \Phi &= W_2/r \end{aligned} \quad (\text{A6.4})$$

This method does not require the evaluation of the sine and cosine!

For example, let us consider the Lambertian reflection. The azimuth angle after the reflection should be distributed isotropically and $\cos^2\theta$ should be uniform, so that the following is derived using (A6.4):

$$\begin{aligned}\cos\theta &= \sqrt{\rho} = r \\ \cos\phi &= W_1/r \\ \sin\phi &= W_2/r\end{aligned}\tag{A6.5}$$

The reflection vector becomes

$$\mathbf{\Omega} = \begin{pmatrix} W_1\sqrt{1-r^2}/r \\ W_2\sqrt{1-r^2}/r \\ r \end{pmatrix}\tag{A6.6}$$

A7 Mathematical functions

A7.1 $\cos^{-1}x$

The solution of this function should be in a range between 0 and π . This function is numerically very heavy, so that an LUT is useful for $-0.99 < x < 0.99$. If x is nearly 1, then the following approximate calculation is useful.

Let us try to solve the following equation:

$$y = \cos\alpha - x = 0\tag{A7.1}$$

The initial guess by first-order approximation is

$$\alpha \approx \sqrt{2(1-x)}\tag{A7.2}$$

Applying the Newtonian method and using the Taylor series expansion,

$$\begin{aligned}\alpha &= \sqrt{2(1-x)} - \frac{y(\alpha = \sqrt{2(1-x)})}{y'(\alpha = \sqrt{2(1-x)})} \\ &= \sqrt{2\delta} \frac{60 - 15\delta + 2\delta^2}{60 - 20\delta + 2\delta^2}\end{aligned}\tag{A7.3}$$

where $\delta = 1 - x$. If x is nearly equal to -1 , then the solution is $\alpha = \pi - \cos^{-1}(-x)$.

A7.2 $\exp(-x)$

This function is frequently used for the radiative transfer for calculating the transmittance, usually with an optical thickness x between 0 and $x_{\max} = 80$. The transmittance $\exp(-x)$ for an x larger than 80 is almost equal to 0, with single precision. This function is tabulated in an LUT with about 10000 grid points. For evaluating the function, the following are computed:

$$i = \text{int}\left(\frac{N}{x_{\max}}x + 0.5\right) \quad (\text{A7.4a})$$

$$\delta = x - \frac{x_{\max}}{N}i. \quad (\text{A7.4b})$$

Using the Taylor series expansion,

$$\exp(-x) \approx \text{LUT}(i)[1 - \delta(1 - \delta/2)] \quad (\text{A7.5})$$

With $N = 10000$, and $x_{\max} = 80$, the accuracy of the above approximation is 0.00001% or better. If $x < 0.01$, more simply

$$\exp(-x) \approx 1 - x(1 - x/2) \quad (\text{A7.6})$$

can be used.

A7.3 $1 - \exp(-x)$

This function is used for calculating the collision probability and heating rate. When x is large (0.03 or more), the above function $\exp(-x)$ could be used. However, caution should be paid for a small x because of the round-off error. Using the Taylor series expansion,

$$1 - \exp(-x) \approx x \left[1 - x \left(\frac{1}{2} - \frac{x}{6} \right) \right] \quad (\text{A7.7})$$

The maximum error for this is less than 0.0001% for $x < 0.03$.

A7.4 $\sin(x)$ and $\cos(x)$

These functions are numerically time-consuming. Let us assume that the argument x is between 0 and 2π . An LUT of about 10,000 grid points is useful. For evaluating the sine and cosine,

$$i = \text{int}\left(\frac{N}{2\pi}x + 0.5\right) \quad (\text{A7.8})$$

$$\delta = x - \frac{2\pi}{N}i \quad (\text{A7.9})$$

are computed. Representing the sine and cosine LUT values S and C , respectively, using the Taylor series expansion, we get

$$\sin(x) \approx S(i) + \delta C(i) \quad (\text{A7.10a})$$

$$\cos(x) \approx C(i) - \delta S(i) \quad (\text{A7.10b})$$

If $N = 10000$, the error of the above is less than 0.00001%.

References

-in Japanese-

- Araya, S., 2003: 明解 3次元コンピュータグラフィックス. 共立出版 (Kyoritsu-shuppan), pp. 191 (in Japanese).
- Shibata, K., 1999: 光の気象学, 朝倉書店 (Asakura-shoten), pp. 182 (in Japanese).
- Taniguchi, H., W-J. Yang, K. Kudoh, A. Kuroda, A. Mochida, 1994: パソコン活用のモンテカルロ法による放射伝熱解析. コロナ社 (Konona-sya), pp. 231 (in Japanese).
- Fushimi, M., 1989: 乱数. UP 応用数学選書 12 (UP Applied Mathematics Series 12), 東京大学出版会 (Tokyo-daigaku-shuppan-kai), pp. 164 (in Japanese).
- Hikobasa, K., 2003: 光合成機能の評価2 クロロフィル蛍光, in 光と水と植物のかたち, edited by Muraoka & Kachi, 文一総合出版 (Bun-itsu-sogo-syuppan), p. 319 (in Japanese).
- Yoshimura, H., 2001: キサントフィル・サイクル色素とスペクトル変化, 日本リモートセンシング学会誌 (Journal of the Remote Sensing Society of Japan), **21**, **4**, 373–376 (in Japanese).

-in English-

- Aida, M., 1977: Scattering of solar radiation as a function of cloud dimensions and orientation. *J. Quant. Spectrosc. Radiat. Transfer*, **17**, 303–310.
- Allen, W. A., H. W. Gausman, A. J. Richardson, and J. R. Thomas, 1969: Interaction of isotropic light with a compact plant leaf. *J. Opt. Soc. Am.*, **59**(10), 1376–1379.
- d’Almeida, G. A., P. Koepke, and E. P. Shettle, 1991: *Atmospheric Aerosols. Global Climatology and Radiative Characteristics*. A. Deepak Publishing, pp. 561.
- Antyufeev V. S., and A. Marshak, 1990: Monte Carlo method and transport equation in plant canopies, *Remote Sens. Environ.*, **31**, 183.4.23.2091.
- Antyufeev, V. S., 1996: Solution of the generalized transport equation with a peak-shaped indicatrix by the Monte Carlo method. *Russ. J. Numer. Anal. Math. Modeling*, **11**, 113–137.
- Barker, H. W., and J. A. Davies, 1992: Solar radiative fluxes for stochastic, scale-invariant broken cloud fields. *J. Atmos. Sci.*, **49**, 1115–1126.
- Barker, H. W., J.-J. Morcrette, and G. D. Alexander, 1998: Broadband solar fluxes and heating

- rates for atmospheres with 3D broken clouds. *Q. J. R. Meteorol. Soc.*, **124**, 1245–1271.
- Barker, H. W., R. K. Goldstein, and D. E. Stevens, 2003: Monte Carlo simulation of solar reflectances for cloudy atmospheres. *J. Atmos. Sci.*, **60**, 1881–1894.
- Bates, D. R., 1984: Rayleigh scattering by air. *Planet. Space Sci.*, **32**, 785–790.
- Bodhaine, B. A., N. B. Wood, E. G. Dutton, and J. R. Slusser, 1999: On Rayleigh optical depth calculations. *J. Atmos. and Oceanic Tech.*, **16**, 1854–1861.
- Bohren, C. F., and D. R. Huffman, 1983: *Absorption and Scattering by Small Particles*, J. Wiley & Sons, NY, pp. 530.
- Booth, T. E., 1985: *A Sample Problem for Variance Reduction in MCNP*. Los Alamos National Laboratory report LA-10363-MS, pp. 68 (available from Los Alamos National Laboratory Research Library).
- Cahalan, R. F., W. Ridgway, and W. J. Wiscombe, 1994a: Independent pixel and Monte Carlo estimates of the stratocumulus albedo. *J. Atmos. Sci.*, **51**, 3776–3790.
- Cahalan, R. F., W. Ridgway, W. J. Wiscombe, T. L. Bell, and J. B. Snider, 1994b: The albedo of fractal stratocumulus clouds. *J. Atmos. Sci.*, **51**, 2434–2455.
- Cahalan, R. F., et al., 2005: The International Intercomparison of 3D Radiation Codes (I3RC): Bringing together the most advanced radiative transfer tools for cloudy atmospheres, *Bull. Am. Meteorol. Soc.*, **86**, 1275–1293.
- Chou, M.-D., and K.-T. Lee, 1996: Parameterizations for the absorption of solar radiation by water vapor and ozone. *J. Atmos. Sci.*, **53**, 1203–1208.
- Cox, C., and W. Munk, 1954: Measurements of the roughness of the sea surface from photographs of the Sun's glitter. *J. Opt. Society Am.*, **44**, 838–850.
- Davies, R., 1984: Reflected solar radiances from broken cloud scenes and the interpretation of scanner measurements. *J. Geophys. Res.*, **89**, 1259–1266.
- Dawson, T. P., P. J. Curran, and S. E. Plummer, 1988: LIBERTY: Modeling the effects of leaf biochemical concentration on reflectance spectra. *Remote. Sens. Environ.*, **65**, 50–60.
- de Pury, D., and G., Farquhar, 1997: Simple scaling of photosynthesis from leaves to canopies without the errors of big-leaf models. *Plant Cell Environment*, **20**, 537–557.
- Downing, H. D., and D. Williams, 1975: Optical constants of water in the infrared. *J. Geophys. Res.*, **80**, 1656–1661.
- Edlén, B., 1953: The dispersion of standard air. *J. Opt. Soc. Amer.*, **43**, 339–344.
- Evans, K. F., 1998: The spherical harmonics discrete ordinate method for three-dimensional atmospheric radiative transfer. *J. Atmos. Sci.*, **55**, 429–446.
- Evans, K. F., and A. Marshak, 2005: Numerical Methods. *3D Radiative Transfer for Cloudy*

Atmospheres, A. B. Davis and A. Marshak, Ed., Springer-Verlag, 243–281.

- Farquhar, G. D., S. von Caemmerer, and J. A. Berry, 1980: A biochemical model of photosynthetic CO₂ assimilation in leaves of C3 species. *Planta*, **149**, 78–90.
- Fu, Q., and K.-N. Liou, 1992: On the correlated k-distribution method for radiative transfer in nonhomogeneous atmospheres. *J. Atmos. Sci.*, **49**, 2130–2156.
- Fu, Q., 1996: An accurate parameterization of the solar radiative properties of cirrus clouds for climate models. *J. Climate*, **9**, 2058–2082.
- Fu, Q., M. C. Caribb, H. W. Barker, S. K. Krueger, and A. Grossman, 2000: Cloud geometry effects on atmospheric solar absorption. *J. Atmos. Sci.*, **57**, 1156–1168.
- Gastellu-Etchegorry, J.-P., V. Demarez, V. Pinel, and F. Zagolski, 1996: Modeling radiative transfer in heterogeneous 3-D vegetation canopies. *Remote Sensing of Environment*, **58**, 131–156.
- Gausman, H. W., W. A. Allen, and D. E. Ecobar, 1974: Refractive index of plant cell walls. *App. Opt.*, **13(1)**, 109–111.
- Govaerts, Y., and M. M. Verstraete, 1998: Raytran: A Monte Carlo ray tracing model to compute light scattering in three-dimensional heterogeneous media. *IEEE Transaction on Geoscience and Remote Sensing*, **36**, 493–505.
- Hale, G. M., and M. R. Query, 1973: Optical constants of water in the 200-nm to 200 μ m wavelength region, *Appl. Optics*, **12**, 555–563.
- Hansen, J. E., and L. D. Travis, 1974: Light scattering in planetary atmosphere. *Space Sci. Rev.*, **16**, 527–610.
- Hayasaka, T., M. Kuji, and M. Tanaka, 1994: Air truth validation of cloud albedo estimated from NOAA advanced very high resolution radiometer data. *J. Geophys. Res.*, **99**, 18685–18693.
- Hess, M., P. Koepke, and I. Schult, 1998: Optical properties of aerosols and clouds: The software package OPAC. *Bull. Amer. Meteorol. Soc.*, **79**, 831–844.
- Heymsfield, A. J., and C. M. R. Platte, 1984: A parameterization of the particle size spectrum of ice clouds in terms of the ambient temperature and the ice water content. *J. Atmos. Sci.*, **41**, 846–855.
- Higurashi, A., and T. Nakajima, 1999: Development of a two-channel aerosol retrieval algorithm on a global scale using NOAA AVHRR. *J. Atmos. Sci.*, **56**, 924–941.
- Ishida, H., 2006: Personal communications.
- Iwabuchi, H., and T. Hayasaka, 2002: Effects of cloud horizontal inhomogeneity on the optical thickness retrieved from moderate-resolution satellite data. *J. Atmos. Sci.*, **59**, 2227–2242.

- Iwabuchi, H., and T. Hayasaka, 2003: A multi-spectral non-local method for retrieval of boundary layer cloud properties from optical remote sensing data. *Remote Sens. Environ.*, **88**, 294–308.
- Iwabuchi, H., and K. Tsuboki, 2004: Camera visualization of cloud fields simulated by non-hydrostatic atmospheric models. *Journal of Visualization (Frontispiece)*, **7**, 272.
- Iwabuchi, H., 2006: Efficient Monte Carlo methods for radiative transfer modeling. *J. Atmos. Sci.*, **63**, 2324–2339.
- Jacquemoud, S., and F. Baret, 1990: PROSPECT: A model of leaf optical properties spectra. *Remote Sens. Environ.*, **34**, 75–91.
- Kato, S., T. P. Ackerman, J. H. Mather, and E. E. Clothiaux, 1999: The k-distribution method and correlated-k approximation for a shortwave radiative transfer model. *J. Quant. Spectrosc. Radiat. Transfer*, **62**, 109–121.
- Kawrakow, I., and D. W. O. Rogers, 2001: *The EGSnrc Code System: Monte Carlo Simulation of Electron and Photon Transport*, NRCC Report PIRS-701, pp. 287 (revised in 2003).
- Kneizys, F. X., E. P. Shettle, L. W. Abreu, J. H. Chetwynd, G. P. Anderson, W. O. Gallery, J. E. A. Selby, and S. A. Clough, 1988: *Users Guide to LOWTRAN 7*. AFGL-TR-88-0177, pp. 137.
- Liou, K. N., 1992: *Radiation and Cloud Processes in the Atmosphere*. Oxford University Press, pp. 473.
- Liou 2002: *An Introduction to Atmospheric Radiation. Second Edition*. Academic Press, NY, pp. 583.
- List, R. J., 1968: *Smithsonian Meteorological Tables*. Smithsonian, pp. 527.
- Lucht W., C. B. Schaaf, and A. H. Strahler, 2000: An algorithm for the retrieval of albedo from space using semiempirical BRDF models. *IEEE Trans. Geosci. Remote Sens.* **38**, 977–998.
- Lyapustin, A., 2002: Radiative transfer code SHARM-3D for radiance simulations over a non-Lambertian nonhomogeneous surface: Intercomparison Study, *Appl. Optics*, **41**, 5607–5615.
- Macke, A., D. L. Mitchell, and L. V. Bremen, 1999: Monte Carlo radiative transfer calculations for inhomogeneous mixed phase clouds. *Phys. Chem. Earth (B)*, **24**, 237–241.
- Marchuk, G., G. Mikhailov, M. Nazarialiev, R. Darbinjan, B. Kargin, and B. Elepov, 1980: *The Monte Carlo Methods in Atmospheric Optics*. Springer-Verlag, pp. 208.
- Marshak, A., and A. B. Davis (Eds), 2005: *Three-Dimensional Radiative Transfer in Cloudy Atmospheres*. Springer, pp. 686.
- Martin, G. M., D. W. Johnson, and A. Spice, 1994: The measurement and parameterization of

- effective radius of droplets in warm stratocumulus clouds. *J. Atmos. Sci.*, **51**, 1823–1842.
- McKee, T. B., and S. K. Cox, 1974: Scattering of visible radiation by finite clouds. *J. Atmos. Sci.*, **31**, 1885–1892.
- Modest, M. F., 2003: *Radiative Heat Transfer. Second Edition*. Academic Press, NY, pp. 822.
- Nakajima, T., and M. Tanaka, 1983: Effect of wind-generated waves on the transfer of solar radiation in the atmosphere-ocean system. *J. Quant. Spectrosc. Radiat. Transfer*, **29**, 521–537.
- Nakajima, T., and M. Tanaka, 1988: Algorithms for radiative intensity calculations in moderately thick atmospheres using a truncation approximation. *J. Quant. Spectrosc. Radiat. Transfer*, **40**, 51–69.
- Nakajima, T., and M. D. King, 1990: Determination of the optical thickness and effective particle radius of clouds from reflected solar radiation measurement. Part I: Theory. *J. Atmos. Sci.*, **47**, 1878–1893.
- Nakajima, T., M. Tsukamoto, Y. Tsushima, A. Numaguti, and T. Kimura, 2000: Modeling of the radiative process in an atmospheric general circulation model. *Appl. Opt.*, **39**, 4869–4878.
- North, P. R., 1996: Three-dimensional forest light interaction model using a Monte Carlo method. *IEEE Transactions on Geoscience and Remote Sensing*, **34(4)**, 946–956.
- Oikawa, T., and T. Saeki, 1977: Light regime in relation to plant population geometry. I. A Monte Carlo simulation of light microclimate within a random distribution foliage. *Bot. Mag. Tokyo*, **90**, 1–10.
- O'Hirok, W., and C. Gautier, 1998: A three-dimensional radiative transfer model to investigate the solar radiation within a cloudy atmosphere. Part I: Spatial effects. *J. Atmos. Sci.*, **55**, 2162–2179.
- Pacheco, P. S., 1997: *Parallel Programming with MPI*. Morgan Kaufmann Publishers.
- Palmer, K. P., and D. Williams, 1974: Optical properties of water in the near infrared. *J. Opt. Soc. Am.*, **64**, 1107–1110.
- Peck., E. R., and K. Reeder, 1972: Dispersion of air. *J. Opt. Soc. Amer.*, **62**, 958–952.
- Penndorf, R., 1957: Tables of the refractive index for standard air and the Rayleigh scattering coefficient for the spectral region between 0.2 and 20.0 μm and their application to atmospheric optics. *J. Opt. Soc. Amer.*, **47**, 176–182.
- Press, W. H., S. A. Teukolsky, W. T. Vetterling, and B. P. Flannery, 1992: *Numerical Recipes in Fortran 77: The Art of Scientific Computing. Second Edition*. Cambridge University Press, pp. 933.
- Rahman, H., B. Pinty, and M. M. Verstraete, 1993: Coupled surface-atmosphere reflectance (CSAR) model. 2. Semiempirical surface model usable with NOAA advanced very high

- resolution radiometer data. *J. Geophys. Res.*, **98**, 20, 791–20, 801.
- Ross, J. K., and A. L. Marshak, 1988: Calculation of canopy bidirectional reflectance using the Monte Carlo method. *Remote Sens. Environ.*, **24**, 213–225.
- Shettle, E. P., and R. W. Fenn, 1979: *Models for the Aerosols of the Lower Atmosphere and the Effects of Humidity Variations on Their Optical Properties*. AFGL-TR-79-0214.
- Shultis, J. K., and R. Myneni, 1988: Radiative transfer in vegetation canopies with anisotropic scattering. *J. Quant. Spectrosc. Radiat. Transfer*, **39**, 115–129.
- Stern, F., 1964: Transmission of isotropic radiation across an interface between two dielectrics. *Appl. Opt.*, **3**(1), 111–113.
- Tang, I. N., and H. R. Munkelwitz, 1994: Water activities, densities, and refractive indices of aqueous sulfates and sodium nitrate droplets of atmospheric importance. *J. Geophys. Res.*, **99**, 18801–18808.
- Tang, I. N., and H. R. Munkelwitz, 1996: Chemical and size effects of hygroscopic aerosols on light scattering coefficients. *J. Geophys. Res.*, **101**, 19245–19250.
- Thomas, G. E., and K. Stamnes, 1999: *Radiative Transfer in the Atmosphere and Ocean*. Cambridge University Press, Cambridge, UK, pp. 517.
- Városi, F., and E. Dwek, 1999: Analytical approximations for calculating the escape and absorption of radiation in clumpy dusty atmosphere. *The Astrophys. J.*, **523**, 265–305.
- Wagner, T., J. P. Burrows, T. Deutschmann, B. Dix, C. von Friedeburg, U. Frieß, F. Hendrick, K.-P. Heue, H. Irie, H. Iwabuchi, Y. Kanaya, J. Keller, C. A. McLinden, H. Oetjen, E. Palazzi, A. Petritoli, U. Platt, O. Postyyakov, J. Pukite, A. Richter, M. van Roozendaal, A. Rozanov, V. Rozanov, R. Sinreich, S. Sanghavi, F. Wittrock, 2006: Comparison of box-air-mass-factors and radiances for multiple-axis differential optical absorption spectroscopy (MAX-DOAS) geometries calculated from different UV/visible radiative transfer models. *Atmos. Chem. Phys.* (submitted).
- X-5 Monte Carlo Team, 2003 (Revised 6/30/2004): *MCNP—A General Monte Carlo N-Particle Transport Code, Version 5. Volume I: Overview and Theory*. Los Alamos National Laboratory report LA-UR-03-1987, (available from Los Alamos National Laboratory Research Library).
- Young, A. T., 1981: On the Rayleigh-scattering optical depth of the atmosphere. *J. Appl. Meteor.*, **20**, 328–330.